

**Titre:** Substrate Integrated Waveguide Devices and Receiver Systems for  
Title: Millimeter-Wave Applications

**Auteur:** Zhenyu Zhang  
Author:

**Date:** 2011

**Type:** Mémoire ou thèse / Dissertation or Thesis

**Référence:** Zhang, Z. (2011). Substrate Integrated Waveguide Devices and Receiver Systems  
Citation: for Millimeter-Wave Applications [Thèse de doctorat, École Polytechnique de  
Montréal]. PolyPublie. <https://publications.polymtl.ca/675/>

 **Document en libre accès dans PolyPublie**  
Open Access document in PolyPublie

**URL de PolyPublie:** <https://publications.polymtl.ca/675/>  
PolyPublie URL:

**Directeurs de  
recherche:** Ke Wu  
Advisors:

**Programme:** génie électrique  
Program:

UNIVERSITÉ DE MONTRÉAL

SUBSTRATE INTEGRATED WAVEGUIDE DEVICES AND RECEIVER  
SYSTEMS FOR MILLIMETER-WAVE APPLICATIONS

ZHENYU ZHANG

DÉPARTEMENT DE GÉNIE ÉLECTRIQUE

ÉCOLE POLYTECHNIQUE DE MONTRÉAL

THÈSE PRÉSENTÉE EN VUE DE L'OBTENTION  
DU DIPLÔME DE PHILOSOPHIAE DOCTOR (Ph.D.)

(GÉNIE ÉLECTRIQUE)

SEPTEMBRE 2011

© Zhenyu Zhang, 2011.

UNIVERSITÉ DE MONTRÉAL

ÉCOLE POLYTECHNIQUE DE MONTRÉAL

Cette thèse intitulée:

SUBSTRATE INTEGRATED WAVEGUIDE DEVICES AND RECEIVER SYSTEMS FOR  
MILLIMETER-WAVE APPLICATIONS

présentée par: ZHANG Zhenyu

en vue de l'obtention du diplôme de: Philosophiae Doctor

a été dûment accepté par le jury d'examen constitué de:

M. Caloz Christophe, Ph. D., président

M. Wu Ke, Ph. D., membre et directeur de recherche

M. Cardinal Christian, Ph. D., membre

M. Park Chan-Wang, Ph. D., membre externe

## DEDICATION

*To my family*

## ACKNOWLEDGMENT

I would like to thank all the persons who have given me their help during my study at Ecole Polytechnique Montreal.

First of all, I am extremely grateful for my supervisor, Dr. Ke Wu. Over the past five years, I have benefited much from his invaluable and patient instructions. His supervision and right altitude to life will be valuable assets for my whole life.

My sincere appreciation extends to the member of my doctoral committee: Dr. Christophe Caloz, Dr. Christian Cardinal and Dr. Chan-Wang Park, for their insightful comments and constructive suggestions.

I am very thankful to Anthony Ghiotto for his help in the French section of this thesis.

I thank my former colleagues in the Poly-Grames Research Center. In particular, Yingrao Wei, Ning Yang, Lin Li, Duochuan Li, Wenrui Li, Xiaoping Chen, Fanfan He, Sulav Adhikari and Tristan Dubois have provided me with many helpful discussions for my research work. I also thank Jules Gauthier, Steve Dude, Traian Antonescu, and Maxime Thibault for their kind assistance in my circuit fabrication.

Finally, I wish to express my gratitude to my family—my parents and my wife, for their continuous love, support, encouragement and sacrifice. Thanks to my daughter, who was born in the summer of 2010 and brings me so much joy and true happiness.

## RÉSUMÉ

La très forte congestion du spectre radiofréquence alloué aux fréquences RF et micro-ondes pour les communications sans fil d'aujourd'hui motive ce travail de recherche qui se consacre aux bandes millimétriques pour lesquelles d'avantages d'allocations spectrales sont disponibles, et qui est particulièrement intéressante pour le transfert à très haut débit. Comparé aux autres technologies de ligne de transmission, le Guide Intégré au Substrat (GIS) montre des avantages très attractifs comme un faible profil, un faible coût, un haut facteur de qualité (facteur Q), de faibles pertes d'insertion... Ce dernier a gagné beaucoup d'attention récemment grâce à ces caractéristiques favorables pour la conception de circuits et systèmes millimétriques.

Le sujet de ce doctorat concerne deux tâches de recherche distinctes : la première est dédiée à l'investigation et à la conception de composants et d'antennes GIS innovants pour une possible application en ondes millimétriques; la seconde se consacre à la mise au point et à la démonstration de systèmes de réceptions millimétriques de tailles compactes, faibles pertes, à haut niveau d'intégration et hautes performances.

Les chapitres 1 à 4 se concentrent sur l'exploitation et l'investigation, un à un, de composants GIS pour lesquels un nombre de concepts originaux et innovants de structures est proposé et démontré. Dans le chapitre 5, les architectures classiques et les paramètres des systèmes de réception sont introduits, puis utilisés pour la conception de systèmes de réceptions millimétriques dans les chapitres suivants. Du chapitre 6 au chapitre 8, des systèmes submillimétriques et millimétriques basés sur le GIS sont démontrés.

Les contributions majeures de cette thèse sont les suivantes :

- Une structure balancée large bande inhérente peut être obtenue en imprimant un circuit sur deux faces d'un substrat GIS. Ainsi, un balun planaire large bande GIS implémenté sur un circuit imprimé (ou PCB, pour *Printed Circuit Board*) simple couche est proposé et présenté suite auquel une nouvelle transition large bande de ligne microruban à ligne parallèle est démontrée. Avec cette transition proposée comme réseau d'alimentation, une nouvelle antenne large bande quasi-Yagi planaire est développée.
- Les techniques du Guide Intégré au Substrat à Demi-Mode (GISDM) et du Guide Intégré au Substrat à Quart de Mode (GISQM) sont introduites dans le but de miniaturiser les circuits

GIS et d'améliorer la bande passante. Les structures GISDM et GISQM sont générées en bisectant les structures GIS avec des murs magnétiques fictifs. Un diviseur de puissance GISDM de type Wilkinson est mis au point avec l'intégration réussie d'une branche résistive avec la structure GIS, ce afin de garantir une bonne isolation ainsi qu'une bonne adaptation en sortie. De plus, deux filtres GISQM de type Chebychev sont proposés et démontrés pour des applications à large bande.

- Un décaleur de phase à large bande qui met à profit des fentes longitudinales non radiatives sur les murs larges d'un GIS est présenté. Le décaleur de phase à large bande est conçu sur la base d'un phénomène de dispersion du GIS et de la ligne GIS à fentes. Le concept est développé à partir de la différence des constantes de propagation du mode  $TE_{10}$  et du mode quasi TEM, qui sont les modes fondamentales respectifs de la ligne GIS et de notre ligne GIS à fentes proposés.
- Une nouvelle topologie de Mélangeur auto-Oscillant à Sous-harmonique (MOS) qui met à profit les caractéristiques de transmission de deux modes opérants dans une cavité GIS est proposée. Le MOS est constitué d'un filtre passe-bande GIS à deux modes, d'un transistor à effet de champ (ou FET, pour *Field Effect Transistor*) à source commune et d'un filtre passe-bas. Le mode fondamental  $H_{101}$  de la cavité GIS est utilisé comme mode RF alors que le mode  $H_{202}$  est utilisé pour générer l'oscillation locale.
- Un mélangeur large bande millimétrique basé sur une diode qui met en œuvre un circuit hybride 180 degrés GIS est présenté. De plus, un frontal (ou front-end) de réception qui intègre une antenne à haute performance constituée d'un réseau de fentes et du mélangeur proposé est conçu. Subséquemment, un système sans fil avec une modulation de type M-QAM (pour *M-ary Quadrature Amplitude Modulation*) est démontré pour un canal à vision direct (ou LOS, pour *Line-Of-Sight*).
- Un nouveau frontal de réception basé sur un MOS est proposé. Il emploie une architecture à verrouillage par injection afin d'améliorer la stabilité en fréquence et le bruit de phase de l'oscillateur local. Le MOS proposé met à profit les caractéristiques de transmission de deux modes opérant dans une cavité GIS. Ainsi, le frontal de réception proposé a les avantages de procurer un faible bruit de phase et une bonne isolation entre l'entrée RF et le signal de l'oscillateur local (LO).

Un émetteur/récepteur GIS opérant à 60 GHz avec une large bande d'opérations de 3 GHz est présenté. La technique d'intégration proposée de structure planaire et non-planaire permet la conception de composants passifs et d'éléments actifs dans un même et unique boîtier. Les circuits passifs et les antennes à haut gain sont intégrés ensemble avec des circuits monolithiques intégrés micro-ondes (ou MMICs pour *Monolithic Microwave Integrated Circuits*) par le procédé de câblage filaire (ou *wire-bonding*).



## ABSTRACT

The heavily congested condition at the existing radio frequency (RF)/microwave spectra allocated for the today's wireless communications motivates and expedites the research work at millimeter-wave bands where more spectrum space is available for massive data rate delivery. Compared with other transmission line techniques, the substrate integrated waveguide (SIW) platform shows attractive advantages of low profile, low-cost, high Q-factor, and low insertion loss, etc. It has gained a lot of attention recently due to its favorable features in millimeter-wave circuit/system design.

The topic of this doctoral dissertation are concerned with two distinct research tasks: (1) investigating and designing innovative SIW components and antennas for possible millimeter-wave applications; (2) developing and demonstrating geometry-compact, low cost, high level of integration and high performance millimeter-wave receiver systems.

Chapters 1 to 4 focus on the exploitation and investigation of individual SIW devices, in which a number of original concepts and innovative structures are proposed and demonstrated. In Chapter 5, generic architectures and parameters of receiver systems are discussed and used as a guideline for the millimeter-wave system design in the next chapters. From Chapter 6 to Chapter 8, sub-millimeter/millimeter wave systems based on SIW technique are demonstrated.

The major contributions of this thesis work can be highlighted as follows:

- An inherent broadband balanced structure can be achieved by printing circuits on two opposite sides of an SIW substrate. According to this feature, a broadband SIW planar balun implemented on a single layer printed circuit board (PCB) is proposed and presented, following which another newly proposed broadband microstrip-to-broadside parallel stripline transition is demonstrated. With the proposed transition as the feeding network, a novel broadband printed quasi-Yagi antenna is developed.
- Half-mode substrate integrated waveguide (HMSIW) and quarter-mode substrate integrated waveguide (QMSIW) techniques are introduced for the purpose of miniaturizing SIW circuits and enhancing the bandwidth. The HMSIW and QMSIW structures are generated by bisecting SIWs with fictitious magnetic walls. A broadband HMSIW Wilkinson power divider is developed, which successfully integrates a resistor branch with the SIW structure to guarantee

good output matching and isolation. Furthermore, two C-band QMSIW Chebychev filters are proposed and demonstrated for wide band applications.

- A broadband phase shifter that makes use of non-radiating longitudinal slots in the broad wall of an SIW is presented. The proposed broadband phase shifter is developed on the basis of a dispersive phenomenon of SIW and slotted SIW lines. The design concept is developed on different propagation constants of  $TE_{10}$  mode and quasi-TEM mode, which are the fundamental modes of SIWs and our proposed slotted SIWs, respectively.
- A novel sub-harmonic self-oscillating mixer (SOM) topology that makes use of the transmission characteristics of two operating modes in an SIW cavity is proposed. The SOM circuit consists of a dual-mode SIW band-pass filter, a common source hetero-junction FET and a low-pass filter. The fundamental mode ( $H_{101}$ ) of the SIW cavity is used for RF mode operation while the  $H_{202}$  mode is used for local oscillation.
- A broadband millimeter-wave single balanced diode mixer that makes use of an innovative SIW based 180-degree hybrid is presented. Furthermore, a receiver front-end that integrates a high-performance SIW slot array antenna and the proposed mixer is developed. Subsequently, a wireless communication system with M-ary quadrature amplitude modulation (M-QAM) is demonstrated for line-of-sight (LOS) channels.
- A novel SOM-based receiver front-end is proposed, which deploys an injection locking scheme in order to improve the frequency stability and phase noise of the oscillating signal. The proposed SOM makes use of the transmission characteristics of two operating modes in an SIW cavity. As such, the proposed receiver front-end has the advantages of low phase noise and decent isolation between RF and local oscillator (LO) signals.
- A 60 GHz substrate integrated transceiver system with a broad bandwidth up to 3 GHz is presented. The proposed integration technique of planar and non-planar structures allows the design of passive components and active devices within a single package. The passive circuits and high-gain antennas are integrated together with monolithic microwave integrated circuits (MMICs) by simple wire-bonding process.

## CONDENSÉ EN FRANÇAIS

### Introduction

Les systèmes millimétriques ont un considérable intérêt grâce à leurs avantages tels que la bande passante disponible, l'amélioration de la résolution, et le faible poids. Aussi, les hautes fréquences ont de plus courtes longueurs d'onde et donc une plus petite taille de circuits. La plupart des modules en ondes millimétriques sont réalisés en utilisant des technologies de circuits intégrés (ou IC, pour *integrated circuits*). Cependant le coût de la conception et de la fabrication de tels circuits peut être considérablement élevé si on considère un volume de production limité. De plus, les antennes et les filtres passe-bandes à haut facteur de qualité sont difficiles à intégrer dans les boîtiers d'un point de vue de la conception système. Ainsi le développement de modules compacts et faible coût en ondes millimétriques est nécessaire pour les systèmes millimétriques.

Une plateforme candidate pour répondre à ce besoin est offerte par le concept d'une nouvelle génération de circuits intégrés haute fréquence appelé Circuits Intégrés au Substrat (CISs). Fondamentalement, le concept des CISs consiste en la synthèse de structures non-planaires à partir d'un substrat diélectrique planaire et d'intégrer ces dernières dans une plateforme unique avec d'autres structures planaires. Cela peut être accompli de façon générale en créant des canaux artificiels guidant les ondes. Les CISs peuvent grandement faciliter les interconnexions et intégrations entre des circuits plans et non-plans. Il est un fait qu'ils donnent des avantages sans précédent pour la conception de composants micro-ondes et millimétriques, de systèmes et application photonique sans fil, en considérant sa contribution à offrir une solution potentiellement faible coût et performante pour des applications de production de masse.

Le concept des CISs peut être utilisé pour synthétiser une variété de guides d'ondes basés sur des matériaux diélectriques et/ou conducteurs en utilisant des trous métallisés ou non dans le procédé conventionnel faible coût des circuits imprimés simples ou multicouches. Également, cette technologie est compatible avec de nombreux autres procédés de fabrication tels que le procédé en couche mince (ou *thin film*), HTCC (pour *High Temperature Co-fired Ceramic*), LTCC (pour *Low Temperature Co-fired Ceramic*) et possiblement les procédés basés sur les semi-conducteurs tels que MMIC (pour *Microwave Monolithic Integrated Circuit*) ou CMOS, et donc occasionne un intérêt grandissant dans les communautés scientifiques et technologiques. Il y a plusieurs structures CIS populaires incluant le Guide Intégrés au Substrat (GIS), le SISW (pour *Substrate Integrated Slab Waveguide*), le SINRD (pour *Substrate Integrated Non-Radiating Dielectric*), le

SIIDG (pour *Substrate Integrated Image Dielectric Guide*), le SIINDG (pour *Substrate Integrated Inset Dielectric Guide*), et le SIIG (pour *Substrate Integrated Insular Guide*).

Les GISs sont des structures intégrées similaires aux guides d'ondes. Ils consistent en un substrat diélectrique compris entre deux plans conducteurs et des lignes périodiques de trous ou fentes métallisés connectant ces deux plans conducteurs. Comparé aux autres technologies CISs, le GIS présente la plateforme la plus développée, étant donné qu'il est relativement facile de reproduire en technologie GIS des conceptions existantes et matures réalisées en guide d'onde rectangulaire conventionnel. La recherche sur les guides d'onde conventionnels a ouvert la voie à l'exploration des conceptions GIS pour la mise au point de composants passifs à haut facteur de qualité tels que les résonateurs, les filtres, les coupleurs, les diviseurs de puissance, les circulateurs et les antennes.

Le sujet de ce doctorat concerne deux tâches de recherche distinctes : la première est dédiée à l'investigation et à la conception de composants et d'antennes GIS innovants pour une possible application en ondes millimétriques; la seconde se consacre à la mise au point et à la démonstration de systèmes de réceptions millimétriques de tailles compactes, faibles pertes, à haut niveau d'intégration et hautes performances.

Les chapitres 1 à 4 se concentrent sur l'exploitation et l'investigation, un à un, de composants GIS pour lesquels un nombre de concepts originaux et innovants de structures est proposé et démontré. Dans le chapitre 5, les architectures classiques et les paramètres des systèmes de réception sont introduits, puis utilisés pour la conception de systèmes de réceptions millimétriques dans les chapitres suivants. Du chapitre 6 au chapitre 8, des systèmes submillimétriques et millimétriques basés sur le GIS sont démontrés.

### **Balun GIS à large bande**

Un balun est un élément ou un circuit qui convertit des signaux entre une structure non balancée et une structure balancée. Deux catégories de balun planaires peuvent être définies en fonction de leurs applications. La première catégorie de balun peut être appelée micro-ruban à micro-ruban, car les interfaces des ports non balancé et balancé sont des micros rubans. La seconde catégorie se réfère aux transitions entre une ligne non balancée (tel que micro-ruban ou coplanaire) et une ligne balancée telle qu'une ligne parallèle ou parallèle coplanaire.

Une structure balancée large bande inhérente peut être obtenue en imprimant un circuit sur deux

faces d'un substrat GIS. Basé sur cette structure, deux différents types de balun sont proposés et présentés dans le chapitre 1. Le premier balun consiste en un diviseur de puissance GIS à 3 dB et de ligne micro-rubans qui sont placés sur les deux côtés d'un substrat diélectrique afin d'obtenir des ports balancés déphasés de  $180^\circ$ . Ce diviseur GIS présentant une caractéristique large bande, la nouvelle structure de balun peut fournir une réponse large bande, ce qui est une caractéristique critique pour de nombreux systèmes de communication sans fil. D'un autre côté, les ports balancés peuvent se retrouver sur un même plan en utilisant un trou métallisé pour amener un des signaux différentiels d'un côté à l'autre du circuit. De cette façon, le nouveau balun peut être facilement conçu et fabriqué sur un circuit imprimé double coté. Comparé aux autres structures rapportées dans la littérature, le balun proposé peut être facilement utilisé aux fréquences millimétriques et de plus cette structure ne nécessite pas de section avec un couplage demandant une géométrie très précise comme c'est généralement le cas pour de nombreuses structures de balun MMIC.

Deuxièmement, une nouvelle transition de ligne micro-ruban à ligne parallèle basée sur le GIS est proposée. Elle offre des performances large bande avec de nombreux avantages tels que de faibles pertes d'insertion, de bonnes tolérances de fabrication et une taille compacte aux fréquences millimétriques. Une caractéristique majeure de la transition proposée est que la ligne balancée est créée par la géométrie et non par une structure sensible à la fréquence. Ainsi elle peut fournir de bonnes performances sur une bande très large. Avec cette transition proposée comme réseau d'alimentation, une nouvelle antenne large bande quasi-Yagi planaire est développée. Un système à deux antennes quasi-Yagi GIS est conçu et mesuré afin de démontrer les performances de l'antenne proposée.

### **Miniaturisation et élargissement de bande de circuits GIS**

À cause de la demande grandissante dans les communications sans fil durant les dernières décades, des efforts ont été menés afin de réduire la taille et le coût des circuits micro-ondes. En général, la taille des circuits GIS est plus grande que leur contrepartie micro-ruban ou coplanaire. Cela pourrait être avantageux pour les applications millimétriques puisque les tolérances de fabrication sont moins contraignantes pour le GIS. Cependant, la taille des composants GIS pose un problème pour leurs applications aux fréquences plus basses. Récemment, des structures GIS à demi mode, ou GISDM, générées en bisectant les structures GIS avec des murs magnétiques

fictifs et préservant la distribution de champs original d'une ligne GIS, ont été reportées.

### **Diviseur de puissance GISDM de type Wilkinson**

Les diviseurs de puissance conventionnels en plan H souffrent de ne pas être adaptés à tous les ports et également de ne pas offrir une bonne isolation entre les ports de sortie. Dans de nombreuses applications, l'adaptation en sortie et l'isolation des diviseurs de puissance doivent être considérées afin d'améliorer les performances. Par exemple, dans les applications aux réseaux d'antennes, les sorties d'un diviseur de puissance sont généralement directement connectées aux éléments d'antennes. Et une bonne isolation peut éviter à ces éléments d'interférer entre eux.

Le diviseur de puissance de Wilkinson présente un réseau ayant de fortes pertes à en juger par la branche résistive utilisée afin d'isoler les ports de sortie. Un tel diviseur est tout particulièrement utile, car les ports de sortie peuvent être simultanément adaptés et isolés. Ce principe, qui a été implémenté dans la conception d'une jonction en T micro-ruban il y a plusieurs années n'a jamais été utilisé dans la conception d'une jonction en T en guides d'onde. Cela peut être attribué à la difficulté dans la façon de concevoir un réseau à perte et aussi de l'intégrer dans la structure à guide d'onde.

Dans le chapitre 2, un diviseur de puissance GIS de type Wilkinson en plan H réalisé sur un circuit simple couche est proposé et présenté pour la première fois. Dans notre nouvelle structure proposée, le GISDM est utilisé non seulement afin de réduire la taille, mais aussi afin de rendre le champ E maximum sur le bord où est intégré un réseau à perte. Comparé aux autres structures reportées, le diviseur de puissance proposé présente une bonne adaptation en sortie et une bonne isolation, ce pour une large bande. De plus, cette mise en œuvre prend les avantages des GIS, à savoir : un bas profil, de faibles pertes d'insertion, et une bonne immunité aux interférences, mais pour une taille encore plus réduite. Il faut aussi mentionner que la configuration ne supporte pas le mode supérieur  $TE_{20}$  comme c'est le cas pour le GIS. Ainsi, une plus grande largeur de bande résulte pour la structure proposée comparativement à ses contreparties. Le diviseur de puissance GIS de Wilkinson peut facilement être utilisé aux fréquences millimétriques.

### **Filtre passe-bande GISQM**

Le filtre GIS à cavité est une des applications les plus populaires de cette technologie émergente. Comparés aux autres filtres planaires basés sur les lignes micro-rubans, ou les lignes coplanaires, les filtres GIS ont démontré d'excellentes performances en terme de facteurs de qualité et de pertes d'insertion. En général, la taille des filtres GIS est beaucoup plus grande que leurs contreparties micro-ruban ou coplanaire, ce qui posent un problème et restreint leurs applications en basses fréquences. En fait, la conception de filtre intégré présentant le plus de difficulté se trouve être pour les fréquences de l'ordre de quelques GHz.

De façon à obtenir une taille plus compacte, le guide d'onde intégré à quart de mode, ou GISQM, est proposé et appliqué à la conception de nos filtres. Le GISQM est généré en bisectant un GISDM avec un second mur magnétique fictif. Le maximum du champ E du mode dominant  $TE_{101}$  est ainsi localisé à l'angle de la cavité GISQM. La dimension totale de cette cavité est de près du quart de la dimension de sa contrepartie GIS. Ainsi, le GISQM proposé démontre un excellent potentiel pour les applications en basse fréquence (de l'ordre de quelques GHz).

Le facteur de qualité Q de la structure GISQM proposée est moindre que celui de ses contreparties GIS car les deux côtés ouverts ne représentent pas des murs magnétiques parfaits et qu'une partie de l'énergie est radiée. Cependant, la ligne GISQM proposée peut permettre d'obtenir un coefficient de couplage plus important entre deux sections voisines. Ainsi, elle peut être utilisée pour obtenir un filtre à bande passante large ce qui ne peut être facilement accompli avec les filtres GIS conventionnels. Pour démontrer le concept en détail, deux filtres en bande C à quatre pôles de type Chebychev sont conçus et fabriqués pour différentes bandes d'applications. Un premier filtre opère à la fréquence centrale de 5.85 GHz avec une bande d'opérations fractionnelle de 14%. Le second opère à la fréquence centrale de 5.5 GHz avec une bande d'opérations fractionnelle de 26%, et couvre la bande de fréquence exemptée de licence allant de 5.25 GHz à 5.85 GHz pour le WiMAX. Comparés à d'autres filtres à micro-ruban, les filtres proposés ont les avantages d'être planaire, de présenter une bonne immunité aux interférences et couplages et d'être facilement réalisables.

### **Décaleur de phase large bande basé sur une structure GIS à fentes**

Un décaleur de phase large bande est proposé dans le chapitre 3. Il est basé sur une structure GIS à fentes non radiative. La structure proposée consiste en deux fentes longitudinales identiques

disposées symétriquement sur les côtés du mur large d'une ligne GIS. Différents types de fentes sur des guides d'onde ont été étudiés dans des travaux précédemment rapportés. Cependant, la plupart des investigations se sont concentrées sur les effets de radiation de ses fentes pour la conception d'antennes. Dans notre travail, une étude en profondeur sur la structure GIS à fentes non radiative est menée. Elle permet de déterminer que la constante de propagation du mode dominant est approximativement linéaire avec la fréquence. Ce mode est supposé quasi-TEM, ce qui est concordant avec une structure coplanaire. Afin de confirmer cette supposition, le mode dominant de notre structure est comparé au mode d'une ligne coplanaire. Il en résulte que la constante de phase de ce mode dominant concorde parfaitement avec le mode d'une ligne coplanaire.

De plus, les caractéristiques de transmission de la ligne GIS à fentes sont examinées et puis appliquées à notre décaleur de phase. Comparé avec les lignes micro-rubans, pour une même largeur, l'atténuation de la ligne GIS à fentes est moindre et même négligeable. Le mode fondamental de la ligne GIS à fentes est quasi-TEM (au lieu du mode  $TE_{10}$  pour une ligne GIS). Ses propriétés de dispersion sont ensuite utilisées pour la conception d'un décaleur de phase à large bande. Pour valider la méthode proposée, un décaleur de phase  $90^\circ$  est implémenté sur une large bande allant de 21 GHz à 28 GHz. L'atténuation en amplitude et la différence de phase mesurée entre les deux chemins du prototype sont de 0.5 dB et  $\pm 4^\circ$  respectivement à travers une très large bande allant de 22 GHz à 28 GHz. La perte d'insertion mesurée est de moins de 1 dB, et la perte d'adaptation meilleure que 14 dB. En fait, les performances obtenues de notre décaleur seraient bien meilleures puisque les résultats présentés sont dégradés par la transition micro-ruban à GIS mise en œuvre en pratique. La qualité principale du décaleur proposé se résume à ce que la dimension est significativement réduite comparé aux autres méthodes précédemment rapportées et peut facilement opérer aux fréquences millimétriques avec de faibles pertes et un bas profil. Aussi, la simple structure résultante monomode est facilement adaptable par les ingénieurs micro-ondes. Avec des caractéristiques très large bande et de faibles pertes, nous pouvons anticiper que le décaleur de phase proposé aura de très nombreuses applications en ondes radiofréquences et millimétriques.



### Mélangeur auto-Oscillant à Seconde-harmonique (MOS)

Une nouvelle structure de mélangeur auto-oscillant à seconde harmonique qui est intégrée avec un filtre passe-bande sélectif GIS est proposée au chapitre 4. Le MOS proposé emploie un transistor FET dans une configuration à source commune. Le signal RF d'entrée passe à travers le filtre passe-bande afin de filtrer le bruit avant d'entrer dans le MOS. L'isolation entre l'entrée RF et l'oscillateur local est un paramètre très important lorsque l'on conçoit un circuit MOS. En ce qui concerne cette mise en œuvre, un filtre GIS à bande étroite est nécessaire afin d'obtenir une bonne isolation entre les fréquences RF et LO qui sont proche l'une de l'autre. Typiquement, les filtres passe-bande de type micro-ruban peuvent difficilement atteindre une bande étroite de moins de 5% avec des performances raisonnables dans et en dehors de la bande d'intérêt. C'est la raison pour laquelle le filtre passe-bande n'a pas été intégré dans les conceptions reportées dans la littérature jusqu'à présent. Dans notre travail, la propriété de haut facteur Q des cavités GIS est utilisée pour la mise en œuvre d'un filtre passe-bande étroit. Le concept est basé sur les caractéristiques de transmission de deux différents modes dans une cavité GIS. À savoir que le mode fondamental et les modes d'ordre supérieur peuvent coexister dans une même cavité et ce, sans interférer.

Notre filtre passe-bande consiste en quatre cavités GIS. Pour les trois premiers ordres du filtre, le mode fondamentale  $H_{101}$  de la cavité GIS est utilisé à la fréquence RF. La quatrième cavité est conçue de sorte que le mode  $H_{202}$  opère à la fréquence RF et que pour générer une résistance négative, le mode fondamental crée les conditions d'oscillation à la fréquence d'oscillation LO désirée. D'un point de vue système, notre approche permet une intégration directe avec une antenne afin de faire un frontal de réceptions millimétrique compacte.

Pour démontrer la méthodologie de conception, un prototype en bande  $K_a$  du MOS proposé est présenté. La bande  $K_a$  a été choisie pour l'implémentation à cause de la limitation due à notre procédé de fabrication de circuit imprimé et au fait que le transistor soit de type monté en surface. Le nouveau concept est validé par la simulation et la mesure qui permettent de suggérer une puissance d'environ 8.5 dBm et -3 dBm respectivement pour la première et la seconde harmonique de l'oscillateur local. Le mélangeur, implémenté en transposition vers la fréquence intermédiaire, permet d'obtenir une perte de conversion de 12 dB et un bruit de phase de -81 dBc/Hz à 100 kHz de la fréquence centrale avec un signal d'entrée à 34 GHz. Il convient de mentionner que la conception proposée présente plus d'avantages pour les hautes fréquences millimétriques.

## Systèmes de réception millimétriques GIS

Dans les chapitres 1 à 4, la technologie GIS a été appliquée pour la conception de circuits et composants millimétriques. Cependant, notre travail était principalement consacré au niveau composant. D'un point de vue système, il est plus intéressant d'implémenter la technique GIS en ondes millimétriques afin que ses avantages soit exploités pour améliorer les performances.

Dans le chapitre 5, les architectures classiques et les paramètres des systèmes de réceptions sont introduits afin de permettre la démonstration de systèmes de communication dans les chapitres suivants. Basés sur les propriétés de différentes architectures de récepteurs, nos systèmes de communication emploient une topologie hétérodyne bistatique mettant en œuvre deux antennes au lieu d'un circulateur ou d'un interrupteur avec une seule antenne qui présenterait beaucoup trop de pertes aux fréquences millimétriques. Dans notre prototype expérimental, la modulation I/Q est réalisée par un générateur de signaux vectoriel, et un démodulateur AD8347 d'*Analog Device* est utilisé. La sortie du démodulateur est enregistrée pour différentes puissances RF d'entrée et différents taux de symbole  $R_s$  de la modulation QPSK. Finalement, l'analyse du récepteur est menée et les paramètres du système incluant le plancher de bruit, la sensibilité et le taux d'erreurs bit à bit sont étudiés. L'importance d'une source stable et pure dans le système de réception est notamment démontrée.

Basés sur l'étude menée au chapitre 5, trois différents circuits de réceptions en ondes millimétriques sont conçus dans les chapitres 6 à 8. Le premier est mis en œuvre à partir d'un mélangeur large bande millimétrique basé sur une diode et qui utilise un circuit hybride  $180^\circ$  innovant. Cet hybride  $180^\circ$  consiste en un coupleur 3 dB en plan H et un déphaseur  $90^\circ$  à large bande introduits dans le chapitre 3. Un prototype expérimental en bande K du mélangeur est mis en œuvre. Les résultats de mesure démontrent que les pertes de conversion sont meilleures que 10 dB sur toute la bande de fréquences allant de 20 à 26 GHz, pour une transposition en haute et en basse fréquence. La fréquence intermédiaire IF mesurée va du DC à 4 GHz. Le mélangeur proposé démontre une excellente linéarité, avec des points de IP3 et  $P_{1dB}$  d'environ 15 dBm et 9 dBm respectivement. De plus, l'isolation port à port est très bonne. Ensuite, un frontal de réceptions est construit en intégrant directement ce mélangeur avec une antenne GIS à fort gain. Également, ce frontal, comme élément d'un système de communication sans fil en bande K utilisant une modulation de type M-QAM, est démontré pour un canal en vision direct. Les résultats mesurés et analytiques montrent que le système proposé est capable de fournir une

communication fiable. Il faut mentionner que la conception proposée présente plus d'avantages pour une application dans les hautes fréquences millimétriques.

Le chapitre 7 présente un nouveau frontal de réceptions basé sur un MOS. Il emploie une technique de verrouillage par injection afin d'améliorer la stabilité en fréquence et le bruit de phase de l'oscillateur. Dans notre frontal de réceptions, un réseau d'antennes GIS à fentes, un filtre passe-bande et un MOS opérant à la seconde harmonique et démontré au chapitre 4, sont intégrés dans un circuit simple couche afin d'obtenir une architecture compacte et faible coût.

Le MOS proposé utilise les caractéristiques de transmission de deux modes opérant dans une cavité GIS. Ainsi, le frontal de réceptions proposé a les avantages d'avoir un faible bruit de phase et une bonne isolation entre l'entrée RF et le signal LO. De plus, un petit signal externe d'injection est appliqué à la fréquence fondamentale d'oscillation comme référence afin d'améliorer le signal d'oscillation. En comparant le fonctionnement avec et sans signal d'injection, on peut observer que le faible signal de verrouillage améliore de beaucoup la stabilité du signal LO et le bruit de phase d'environ -75 dBc/Hz à -100 dBc/Hz à 100 kHz de la fréquence d'oscillation. Un émetteur/récepteur en bande Ka est implémenté pour vérifier l'intérêt de notre frontal de réceptions pour des applications de communication. La mesure du système est réalisée pour une distance de  $d = 30$  cm à 1 m entre l'émetteur et le récepteur ce qui donne une perte d'espace libre allant de 53 à 62 dB. Le signal de sortie est modulé avec une modulation de type QPSK, et la fréquence intermédiaire  $f_{IF}$  est en accord avec le signal RF transposé. Un signal de référence de -30 dBm alimente le port d'injection du MOS. Le spectre mesuré du signal modulé IF transmis et du signal modulé IF reçu sont étudiés. Excepté quelques signaux de bruit non désirés sur le côté des bandes, le spectre du signal IF reçu est très similaire au spectre du signal IF transmis. Ceci indique que notre frontal d'émission/réception transfère correctement le signal modulé. On peut également observer que la constellation du signal est dramatiquement améliorée avec un signal de verrouillage.

Le chapitre 8 se consacre à la bande de fréquence centrée autour de 60 GHz, qui présente une bande libre d'accès de 7 GHz et qui est de plus allouée mondialement (57-64 GHz en Amérique du Nord, 59-66 GHz au Japon et en Europe). Cette bande présente un très fort potentiel pour de très importants taux de transfert de données comparés aux autres fréquences qui présentent une bande très limitée.

La technologie sans fil à 60 GHz présente des caractéristiques incluant une courte distance, un haut débit de donnée, une forte densité et une faible puissance de transmission. Dans ce chapitre, un émetteur/récepteur GIS innovant à 60 GHz présentant une bande d'opérations de 3 GHz est présenté. Les éléments passifs et l'antenne sont totalement intégrés dans le substrat diélectrique. Les autres éléments, qui sont un amplificateur faible bruit (LNA) HMC-ALH382, un amplificateur de puissance (PA) HMC-ABH241 et un mélangeur HMC-MDB169, sont des composants MMICs fournis par *Hittite*. Des lignes de transmission 50 Ohm réalisées sur un substrat d'alumine d'épaisseur 0.254 mm sont utilisées pour router les signaux RF du et vers les MMICs. Les puces MMICs sont collées à un film de 0.150 mm d'épaisseur permettant de dissiper la chaleur, puis connectées à un plan de masse à l'aide d'une colle époxy conductrice en faisant de telles sortes à ce que la surface de la puce soit à la même hauteur que la surface du substrat. Afin de valider l'architecture CIS proposée, un système sans fil de communication à 60 GHz avec des signaux modulés est démontré avec succès pour un canal en vision direct. La technique d'intégration proposée de structure planaire et non-planaire permet la conception de composant passif et actif dans un même boîtier. Les circuits passifs et antennes à fort gain sont intégrés ensemble avec les composants MMICs par le procédé de câblage filaire (ou *wire bonding*). Avec cette technique de conception, notre émetteur/récepteur à 60 GHz démontre des avantages et des propriétés attractives incluant un faible coût, une taille compacte et des performances fiables.

## Conclusion

Bien que des travaux intensifs aient déjà été menés précédemment sur la technologie GIS, la plupart de ces travaux se concentraient exclusivement sur des éléments et peu d'attention avait été apportée à l'incorporation de ses nouvelles propriétés pour les systèmes millimétriques. Cette thèse de doctorat a eu pour objectif d'explorer cette voie. Deux principales contributions en ont résulté

Premièrement, cette thèse présente de multiples projets hautement originaux et innovants qui impliquent l'investigation de structure, la conception de circuits, la mise en œuvre pratique, et enfin la caractérisation par la mesure. Elle a été réalisée dans l'objectif de découvrir des propriétés intéressantes et de nouvelles conceptions avec leurs règles de circuits GISs aux fréquences millimétriques par une recherche théorique et expérimentale détaillée.

Deuxièmement, le travail de recherche décrit dans cette thèse a permis d'appliquer la technologie GIS aux systèmes d'émetteurs/récepteurs en ondes millimétriques. Cette thèse propose de possibles approches afin d'obtenir une forte densité d'intégration tout en préservant les hautes performances requises pour un faible coût.

Pour résumer, notre recherche a permis d'établir les bases afin de promouvoir et d'examiner les concepts GIS pour le développement d'une large gamme de composants et de systèmes en ondes millimétriques. Cette thèse fait une exploration en profondeur dans le développement de futures générations de circuits et de systèmes millimétriques à haute densité d'intégration et dédiés à la production de masse. Elle représente un programme de recherche en ingénierie des ondes millimétriques qui met l'accent sur le développement d'une nouvelle plateforme technologique avancée.

## TABLE OF CONTENTS

<b>ACKNOWLEDGMENT.....</b>	<b>IV</b>
<b>RÉSUMÉ .....</b>	<b>V</b>
<b>ABSTRACT .....</b>	<b>VIII</b>
<b>CONDENSÉ EN FRANÇAIS .....</b>	<b>X</b>
<b>TABLE OF CONTENTS.....</b>	<b>XXI</b>
<b>LIST OF FIGURES .....</b>	<b>XXV</b>
<b>LIST OF TABLES .....</b>	<b>XXXI</b>
<b>LIST OF ACRONYMS AND ABBREVIATIONS .....</b>	<b>XXXII</b>
<b>INTRODUCTION.....</b>	<b>1</b>
<b>CHAPTER 1 DESIGN AND IMPLEMENTATION OF BROADBAND BALUN TRANSFORMERS USING SIW TECHNIQUE .....</b>	<b>13</b>
1.1 Broadband SIW Planar Balun .....	14
1.1.1 Geometry and Design of Broadband SIW Planar Balun Structure .....	14
1.1.2 Simulation and Measurement Results .....	17
1.2 Broadband SIW Microstrip-to-Broadside Parallel Stripline Transition.....	19
1.2.1 Structure Description.....	19
1.2.2 Application to a Broadband Printed Quasi-Yagi Antenna .....	21
1.2.2.1 Antenna Configuration .....	22
1.2.2.2 Simulated and Measured Results .....	23
1.2.2.3 Broadband Quasi-Yagi Array.....	24
1.3 Conclusion.....	27
<b>CHAPTER 2 MINIATURIZATION AND BANDWIDTH ENHANCEMENT OF SIW CIRCUITS .....</b>	<b>28</b>
2.1 Broadband and Compact HMSIW Power Divider .....	30
2.1.1 Structure Description.....	31

2.1.2	Theoretical Analysis and Design of the Proposed HMSIW Wilkinson Power Divider.	33
2.1.3	Simulated and Measurement Results	35
2.1.4	Discussion of Cross-coupling between HMSIWs	38
2.2	5 GHz Bandpass Filter Demonstration Using Quarter-mode SIW Cavity	39
2.2.1	Geometry and Design of QMSIW Filter	41
2.2.2	Result and Discussion	45
2.3	Conclusion	47
<b>CHAPTER 3 DEVELOPMENT OF BROADBAND PHASE SHIFTER USING SLOTTED SIW STRUCTURE</b>		<b>49</b>
3.1	Longitudinal Slotted SIW Transmission Line	51
3.2	Slotted SIW-to-SIW Transition and Parameter Extraction	55
3.3	Theoretical Analysis and Design Technique of Broadband Slotted SIW Phase Shifter	59
3.4	Simulated and Measured Results	64
3.5	Conclusion	66
<b>CHAPTER 4 A MILLIMETER-WAVE SUB-HARMONIC SELF-OSCILLATING MIXER USING DUAL-MODE SIW CAVITY</b>		<b>67</b>
4.1	Structure Description of the Proposed SOM	67
4.2	Dual-Mode SIW Band-Pass Filter	68
4.2.1	RF Mode	69
4.2.2	LO Mode	74
4.3	Second Harmonic SOM	76
4.4	Experimental Results and Discussions	80
4.5	Conclusion	86
<b>CHAPTER 5 GENERIC ARCHITECTURES AND PARAMETERS OF RECEIVER SYSTEMS</b>		<b>88</b>
5.1	Receiver architectures	88
5.2	Experimental Setup of Our Communication Systems	90
5.3	Receiver Analysis	95
5.3.1	Noise in Receiver Systems	96

5.3.2	Receiver Noise Floor.....	97
5.3.3	Receiver Sensitivity.....	98
5.3.4	Bit-error rate (BER) .....	101
5.3.5	Effects of RF Impairments on BER Performance .....	102
5.4	Conclusion.....	105
<b>CHAPTER 6 BROADBAND MILLIMETER-WAVE SINGLE BALANCED MIXER AND ITS APPLICATION TO SUBSTRATE INTEGRATED WIRELESS SYSTEMS....</b>		<b>106</b>
6.1	180-degree Hybrid Implemented with Broadband Slotted SIW Phase Shifter .....	108
6.2	Broadband Single Balanced Mixer .....	110
6.3	Our Proposed K-band Receiver Front-end.....	116
6.4	Experimental Measurement of K-band Wireless Communication System.....	121
6.4.1	System Test Setup for Line-of-sight Channels .....	121
6.4.2	Constellation Diagram and EVM.....	125
6.5	Conclusion.....	130
<b>CHAPTER 7 MILLIMETER-WAVE RECEIVER FRONT-END USING INJECTION-LOCKED SUB-HARMONIC SELF-OSCILLATING MIXER.....</b>		<b>131</b>
7.1	Our Proposed Receiver Front-end System .....	131
7.1.1	Quality Factor of the SIW Cavity .....	132
7.1.2	Dual-Mode SIW BPF .....	134
7.1.3	Injection Locking Technique in the Proposed SOM.....	135
7.1.4	SIW Slot Array.....	137
7.2	Test Setup of Our K <sub>a</sub> -band Wireless Communication System.....	139
7.3	Measurement Results .....	141
7.4	Conclusion.....	145
<b>CHAPTER 8 60 GHZ TRANSCEIVER ARCHITECTURES DEPLOYING SICS TECHNIQUE .....</b>		<b>146</b>
8.1	60 GHz Transceiver and Receiver Front-ends .....	148
8.2	Test setup of 60 GHz Communication Systems.....	152
8.3	Measurement Results .....	154
8.4	Conclusion.....	158



<b>CONCLUSIONS AND FUTURE WORK .....</b>	<b>159</b>
Conclusions .....	159
Future Work .....	160
<b>BIBLIOGRAPHY .....</b>	<b>162</b>
<b>LIST OF PUBLICATIONS.....</b>	<b>171</b>

## LIST OF FIGURES

Figure 1: Topologies of different SIC structures and their dielectric waveguide counterparts. ....	3
Figure 2: SIW structure synthesized with arrays of metalized vias .....	5
Figure 3: Integrated transitions from planar circuits to SIW (a) microstrip line, (b) conductor backed CPW line .....	6
Figure 1.1: Proposed broadband SIW planar balun .....	15
Figure 1.2: Electrical field plots on the A plane .....	15
Figure 1.3: Physical dimensions of the experimental prototype of the proposed SIW planar balun. ....	17
Figure 1.4: S-parameters of the proposed balun: (a) amplitude responses (b) phase responses ...	18
Figure 1.5: (a) Top view and (b) Cross-sectional view of the proposed microstrip-to-broadside parallel stripline transition.....	20
Figure 1.6: Structure of two back-to-back SIW-to-broadside parallel stripline transitions .....	20
Figure 1.7: Simulated return loss and insertion loss of the proposed back-to-back transitions.....	21
Figure 1.8: Geometry of the proposed quasi-Yagi antenna .....	22
Figure 1.9: Input return loss of the proposed quasi-Yagi antenna .....	23
Figure 1.10 Measured E-plane radiation patterns ( $\theta = 90^\circ$ ) of the antenna at 25.5 GHz .....	24
Figure 1.11: SIW quasi-Yagi antenna array .....	25
Figure 1.12: Input return loss of the SIW quasi-Yagi antenna array .....	26
Figure 1.13: Measured E-plane radiation patterns ( $\theta = 90^\circ$ ) of the antenna array at 26.5 GHz.....	26
Figure 2.1: (a) Top view and (b) Cross-sectional view of the conventional H-plane SIW power divider and the proposed HMSIW power divider .....	32
Figure 2.2: Simulated S-parameter performance of an HMSIW power divider. ....	33
Figure 2.3: Physical dimensions of the experimental prototype of the proposed HMSIW power divider.....	33
Figure 2.4: Odd-mode decomposition of the proposed HMSIW Wilkinson power divider .....	34
Figure 2.5: E field distribution of the proposed HMSIW power divider (a) Even-mode and (b) odd-mode.....	36
Figure 2.6: S-parameters of the proposed power divider: (a) input return loss and insertion loss responses (b) output return loss and output isolation responses. ....	37
Figure 2.7: HMSIW model for cross-coupling investigation.....	38

Figure 2.8: Simulated cross-coupling versus gap between HMSIWs with different thickness RO6002 substrate at 24 GHz.....	39
Figure 2.9: Top view of the conventional SIW and the proposed QMSIW cavities.....	40
Figure 2.10: External quality factor of a QMSIW cavity and the coupling coefficient between QMSIW cavities.....	41
Figure 2.11: Physical dimensions of two experimental prototypes of the proposed QMSIW BPFs..	44
Figure 2.12: Photograph of the fabricated QMSIW filter prototypes .....	45
Figure 2.13: S-parameters of the proposed QMSIW filters. ....	46
Figure 2.14: Group delay of the proposed QMSIW filters .....	47
Figure 3.1: Propagation constants of different modes.....	50
Figure 3.2: Longitudinal slotted SIW transmission line .....	51
Figure 3.3: Simulated propagation constant of the dominant mode of the proposed slotted SIW line.....	51
Figure 3.4: Phase constants of the normal modes in the slotted SIW structure and of the isolated CPW and SIW modes.....	52
Figure 3.5: Transverse electric field of the first normal mode at various frequencies.....	53
Figure 3.6: Transverse electric field of the second normal mode at 40 GHz.....	53
Figure 3.7: Comparison of the attenuation between the slotted SIW lines and microstrip lines. ..	54
Figure 3.8: Comparison of wave impedances between the slotted SIW lines with different widths and the SIW line.....	54
Figure 3.9: Slotted SIW-to-SIW transition and its equivalent circuit. ....	56
Figure 3.10: De-embedded S-parameters of the transition .....	57
Figure 3.11: Extracted values of $X_1$ , $X_3$ and $X_2$ . ....	57
Figure 3.12: Lumped-element equivalent circuit and the composed line model of the proposed transition.....	58
Figure 3.13: Comparison of the simulated phase delay and the phase delay of the composed line model.....	58
Figure 3.14: The proposed slotted SIW and the conventional SIW .....	59
Figure 3.15: Phase difference $\phi_{diff}$ versus frequency .....	60
Figure 3.16: Relationship between effective dielectric constant $\epsilon_{eff}$ and the slot line width $W_{Line}$ .....	61

Figure 3.17: Comparison of the phase delays by using different approaches .....	63
Figure 3.18: Physical dimensions of the proposed 90 degree SIW phase shifter .....	64
Figure 3.19: Measured and simulated S-parameters of the 90 degree prototype .....	65
Figure 4.1: Basic design configuration of the proposed SIW SOM.....	68
Figure 4.2: Two orthogonal transmission modes in the proposed BPF circuit .....	69
Figure 4.3: Physical dimensions of the experimental prototype of the proposed dual-mode SIW band-pass filter .....	71
Figure 4.4: Equivalent circuit of the impedance inverter.....	71
Figure 4.5: Simulated S-parameter results of the experimental prototype of the proposed dual- mode SIW band-pass filter .....	73
Figure 4.6: Equivalent circuit of the LO-mode SIW BPF.....	74
Figure 4.7: Comparison of the modeled equivalent circuit response and the simulated S- parameters of the LO-mode SIW BPF .....	75
Figure 4.8: Layout of the proposed SIW second harmonic SOM .....	76
Figure 4.9: Two-port network configuration of our circuit.....	77
Figure 4.10: Simulated stub length versus negative resistance and oscillating frequency .....	79
Figure 4.11: Load plane stability circle of the unstabilized HJFET.....	80
Figure 4.12: Photograph of the K <sub>a</sub> -band experimental prototype .....	81
Figure 4.13: Mixing spectrum of the proposed second harmonic SOM .....	82
Figure 4.14: Measured RF port input return loss .....	82
Figure 4.15: Spectrum of (a) self oscillation and (b) second harmonic .....	84
Figure 4.16: Phase noise measurement of IF signal.....	84
Figure 4.17: Measured LO-RF isolation .....	85
Figure 4.18: Intermediate frequency (IF) shift and conversion loss variation with respect to drain bias ( $V_{GS} = -0.5$ V) .....	85
Figure 5.1: Architecture of a super-heterodyne receiver.....	88
Figure 5.2: Architecture of a homodyne receiver .....	89
Figure 5.3: Test bench of our proposed communication systems .....	91
Figure 5.4: Photograph of the (a) I/Q demodulator and (b) differential amplifier with common- mode output.....	92
Figure 5.5: Schematic of the baseband elliptic LPF in the demodulation board .....	92

Figure 5.6: Frequency response of 20 MHz baseband LPF .....	93
Figure 5.7: Test setup of the demodulation board with common-mode output .....	93
Figure 5.8: Demodulated I/Q waveform output (left) and I/Q diagram (right).....	95
Figure 5.9: Demodulated waveform I-output (left) and I/Q diagram (right), with (a) $SNR = -5$ dB, (b) $SNR = 0$ dB, (c) $SNR = 5$ dB, and (d) $SNR = 10$ dB .....	100
Figure 5.10: BER curves for different modulation schemes for AWGN channel .....	101
Figure 5.11: Simulink model of RF impairments in receiver systems.....	103
Figure 5.12: BER for QPSK with different phase noise effect .....	104
Figure 5.13: BER for QPSK with different frequency drifting effect under the condition that phase noise is -80 dBc/Hz at 100 kHz offset .....	104
Figure 6.1: Simplified illustration of a broadband millimeter-wave system.....	106
Figure 6.2: Circuit diagram of conventional single balanced diode mixer .....	107
Figure 6.3: Physical dimensions of the experimental prototype of the proposed 180-degree hybrid. .....	108
Figure 6.4: Simulated and measured S-parameters of the experimental prototype of the proposed 180-degree hybrid. ....	109
Figure 6.5: Currents and voltages in the diodes of a 180-degree balanced mixer. ....	110
Figure 6.6: Photograph of the proposed broadband single balanced diode mixer .....	112
Figure 6.7: Measured conversion gain/loss of the proposed mixer performed as up-converter and down-converter.....	113
Figure 6.8: Measured conversion gain/loss versus IF bandwidth .....	113
Figure 6.9: Mixing spectrum of the proposed single balanced mixer.....	114
Figure 6.10: Measured LO-RF isolation .....	114
Figure 6.11: Two-tone inter-modulation test of the proposed single balanced mixer .....	115
Figure 6.12: Measured Input IP3 and $P_{1dB}$ points of the proposed mixer performed as down- converter.....	116
Figure 6.13: Layout of our proposed K-band receiver front-end.....	116
Figure 6.14: Longitudinal slot in the broad wall of an SIW .....	117
Figure 6.15: Equivalent circuit of a linear SIW array .....	118
Figure 6.16: Measured input return loss of the SIW slot array .....	119
Figure 6.17: Measured radiation patterns of the SIW slot array at 24 GHz.....	120

Figure 6.18: System test setup for the $K$ -band receiver front-end .....	121
Figure 6.19: Photograph of our test setup .....	122
Figure 6.20: Measured and calculated $PL$ at 24 GHz .....	123
Figure 6.21: Measured spectra for QPSK at transmitter and receiver IF output.....	124
Figure 6.22: Graphical representation of error vector.....	125
Figure 6.23: BER versus EVM for M-ary modulations .....	126
Figure 6.24: Measured constellation diagrams at receiver IF output.....	127
Figure 6.25: Measured constellation diagrams of QPSK.....	127
Figure 6.26: Measured and calculated RMS EVM versus SNR .....	129
Figure 6.27: Measured RMS EVM at various IF frequencies for QPSK.....	129
Figure 7.1: Layout of our proposed receiver front-end.....	132
Figure 7.2: Measured reflection response of the SIW cavity .....	133
Figure 7.3: Simulated and measured S-parameters of the proposed dual-mode SIW BPF .....	134
Figure 7.4: Measured LO spectra at the IF port (a) free-running and (b) with an external injection of -30 dBm. ....	135
Figure 7.5: Locking range versus injected power .....	136
Figure 7.6: Measured phase noise for various injected power.....	137
Figure 7.7: Simulated and measured return losses of the $2 \times 8$ SIW slot array antenna.....	138
Figure 7.8: Measured radiation patterns of the receive antenna at 30 GHz .....	138
Figure 7.9: Photograph of the proposed transceiver front-end.....	139
Figure 7.10: Block diagram of the proposed communication system.....	140
Figure 7.11: Measured and calculated $PL$ at 30 GHz .....	141
Figure 7.12: Photograph of our test setup .....	141
Figure 7.13: Comparison of IF spectra of (a) the transmitted modulated signal, and (b) the received modulated signal for QPSK with $R_b = 40$ Mbps, $d = 30$ cm. ....	143
Figure 7.14: Measured QPSK constellation diagrams at the receiver IF output for $d = 30$ cm and $R_b = 40$ Mbps (a) without injected signal and (b) with -30 dBm injected signal.....	144
Figure 7.15: Measured and calculated RMS EVM versus SNR for QPSK, with $R_s = 40$ Mbps and $d = 30$ cm.....	144
Figure 8.1: 60 GHz available spectrum.....	146

Figure 8.2: a) 60 GHz system scenario in office environment; b) 60 GHz system scenario in home environment.....	147
Figure 8.3: Photographs of our demonstrated 60 GHz transmitter and receiver front-ends .....	148
Figure 8.4: Physical dimensions of the 60 GHz SIW-based $2 \times 8$ slot array antenna. ....	149
Figure 8.5: Simulated return loss of the 60 GHz $2 \times 8$ slot array antenna.....	149
Figure 8.6: Simulated radiation pattern of the 60 GHz $2 \times 8$ slot array antenna .....	150
Figure 8.7: Photographs of the wire bonding techniques.....	152
Figure 8.8: Block diagram of the 60 GHz system test setup.....	153
Figure 8.9: Measured and calculated $PL$ at 60 GHz .....	153
Figure 8.10: Photograph of our system test setup .....	155
Figure 8.11: Spectra of the (a) transmitted and (b) received modulated IF signal for QPSK, $R_b = 100$ Mbps.....	156
Figure 8.12: Comparison of the received and transmitted I/Q signals.....	157
Figure 8.13: Comparison of the transmitted and received I/Q diagrams .....	157

## LIST OF TABLES

Table 2.1: Design parameters of two experimental prototypes.....	44
Table 3.1: Physical dimensions of 24 GHz 90° phase shifters designed by two different methods .....	62
Table 4.1 Measured S-parameter of the unstablized HJFET .....	79
Table 5.1: Comparison between heterodyne and homodyne receivers .....	90
Table 5.2: Typical bandwidths for various digital modulation methods.....	98
Table 5.3: Thermal noise power ( $N_0 = kTB$ ) for QPSK with different data rate.....	98
Table 5.4: Minimum acceptable $SNR$ at the demodulator input for QPSK with data symbol rate $R_s$ = 2 Msps .....	101



## LIST OF ACRONYMS AND ABBREVIATIONS

ADC	Analog-to-Digital Converter,
ADS	Advanced Design System
AWGN	Additive White Gaussian Noise
BER	Bit Error Rate
BPF	Band Pass Filter
BPSK	Binary Phase Shift Keying
CMOS	Complementary Metal-Oxide-Semiconductor
CPS	Co-Planar Stripline
CPW	Co-Planar Waveguide
CST	Computer Simulation Technology
DBPSK	Differential Binary Phase Shift Keying
DC	Direct Current
DQPSK	Differential Quadrature Phase Shift Keying
DSP	Digital Signal Processor
EBG	Electromagnetic Band Gap
EMI	Electromagnetic Interference
EVM	Error Vector Magnitude
FET	Field-Effect Transistor
FSS	Frequency Selective Surface
HFSS	High Frequency Structure Simulator
HJFET	Hetero-Junction Field Effect Transistor
HMSIW	Half Mode Substrate Integrated Waveguide
HTCC	High Temperature Co-fired Ceramic
IC	Integrated Circuit
IF	Intermediate Frequency
IMPATT	IMPact ionization Avalanche Transit-Time
IP3	Third-order Intercept Point
I/Q	In-phase and Quadrature
LNA	Low Noise Amplifier
LO	Local Oscillator

LOS	Line of Sight
LPF	Low Pass Filter
LTCC	Low Temperature Co-fired Ceramic
MCM	Multi-Chip Module
MICs	Microwave Integrated Circuits
MMICs	Monolithic Microwave Integrated Circuits
M-QAM	M-ary Quadrature Amplitude Modulation
MSK	Minimum-Shift Keying
NF	Noise Figure
OFSK	Optical Frequency-Shift-keying
PA	Power Amplifier
PCB	Printed Circuit Board
PL	Path Loss
PR	Pseudorandom
PPG	Programmable Pulse Generator
PSD	Power Spectral Density
QMSIW	Quarter-Mode Substrate Integrated Waveguide
QPSK	Quadrature Phase Shift Keying
RF	Radio Frequency
RMS	Root-Mean Square
SIC	Substrate Integrated Circuit
SIIDG	Substrate Integrated Image Dielectric Guide
SIINDG	Substrate Integrated Inset Dielectric Guide
SINRD	Substrate Integrated Non-Radiative Dielectric Guide
SIIG	Substrate Integrated Image Guide
SISW	Substrate Integrated Slab Waveguide
SiP	System in Package
SIW	Substrate Integrated Waveguide
SNR	Signal to Noise Ratio
SOM	Self-Oscillating Mixer
SSB	Single Side-Band

SRRC	Square Root Raised Cosine
TCXO	Temperature Compensated Crystal Oscillator
TE	Transverse Electric
TEM	Transverse Electromagnetic
TM	Transverse Magnetic
TRL	Through-Reflect-Line
VCO	Voltage Controlled Oscillator
VNA	Vector Network Analyzer
VSA	Vector Signal Analyzer
VSG	Vector Signal Generator
VSWR	Voltage Standing Wave Ratio
WiMAX	Worldwide Interoperability for Microwave Access
WLAN	Wireless Local Area Network

## INTRODUCTION

Compared with most of well-developed applications at lower frequency bands, millimeter-wave frequencies take the advantages associated with the increased operating frequency, namely increased available bandwidth, improved resolution, and enhanced security. Meanwhile, owing to smaller component size, entire millimeter-wave systems may be more compact and lightweight. Due to these reasons, millimeter-wave spectrum is expectedly useful for future high-speed wireless services and radar applications. Potential commercial wireless applications at millimeter-wave or sub-millimeter-wave frequencies include wireless point-to-multipoint services, chip-to-chip high-speed links, satellite communications, automotive radars, radiolocation, and imaging and security systems for weapon and hazardous material detections [1]-[4].

On the other hand, there are plenty of technological and technical challenges in designing millimeter-wave circuits and systems, such as cost pressure, smaller size, increased system density, and lower system power dissipation. Classical waveguides have been predominating in the millimeter-wave system design by offering low loss and extremely high power handling capability [5]-[6]. However, this matured scheme is not suitable for low-cost mass-production since tedious and expensive post fabrication tuning and assembling presents a bottleneck problem for manufacturers. In addition, the waveguide components are normally bulky and hardly applied to reduce the weight and volume, judging from a system point of view. Although a number of design techniques of integrating rectangular waveguides with planar circuits have been reported for developing low-cost, high-performance and mass-producible millimeter-wave systems, none of them has been proven attractive for widespread applications. Meanwhile, it is difficult and even impossible for achieving a wideband impedance matching between low-impedance active elements (IMPATT diodes, for example) and high-impedance waveguide circuits.

As an attractive solution for making high-density integration, system in package (SiP), which is characterized by incorporating multiple active and/or passive components into a single package to provide functions associated with a system or sub-system, is still a mainstream in millimeter-wave domain [7]-[8]. Compared with discrete packages, SiP can provide a better solution for power saving, electromagnetic interference (EMI) reduction, and complexity reduction of overall designs. On the negative side, it also leads to low production yield, poor quality control, and more complicated manufacturing process. Especially, the cost advantage of deploying SiP

technology in millimeter-wave system design is not quite appealing as most of SiP applications are created in an expensive integrated circuit (IC) environment. Consequently, an alternative low-cost manufacturing platform is highly demanded.

A promising candidate for developing this platform is the concept of a new generation of high-frequency integrated circuits called substrate integrated circuits (SICs) [9]. The fundamental of the SICs concept is to synthesize non-planar structure with a planar dielectric substrate and integrate them in a single platform with other planar structures. This can usually be achieved by creating artificial waveguiding channels. SICs can greatly facilitate interconnects and integrations between planar and non-planar circuits, which can be made within a patch fabrication process. As a matter of fact, it provides unprecedented advantages for developing microwave and millimeter-wave components, systems and wireless photonic applications, considering its contributions in offering a potentially cost-effective and performance-promising solution for mass commercial applications.

The SICs concept can be used to synthesize a variety of dielectric and/or metallic-based waveguide structures by using metallised and/or air-filled via holes in the conventional low-cost single and multilayer printed circuit board (PCB) environment. Certainly, this technology is also compatible with many other fabrication processes such as thin film, high temperature co-fired ceramic (HTCC), low temperature co-fired ceramic (LTCC) and possibly semiconductor-based microwave monolithic integrated circuit (MMIC) as well as CMOS, and therefore successfully stirs the growing interest of the scientific and technological community. There are several popular SIC structures [10]-[13] which include substrate integrated waveguide (SIW), substrate integrated slab waveguide (SISW), substrate integrated non-radiating dielectric (SINRD) guide, substrate integrated image dielectric guide (SIIDG), substrate integrated inset dielectric guide (SIINDG), and substrate integrated insular guide (SIIG). Figure 1 shows the topologies of these different SIC structures.

As shown in Figure 1, SIWs are integrated waveguide-like structures fabricated with a dielectric substrate sandwiched in between two ground planes and using two periodic rows of metalized vias or slots or even trenches to connect the top and bottom ground planes. Compared with other SICs technologies, the SIW is the most developed platform as it is quite easy to map the existing and matured modeling and design techniques of rectangular waveguide components into the SIW.

Research on conventional waveguides has paved the way for exploiting the SIW in designing high performance (high Q) passive circuits such as resonators, filters, couplers, power dividers, circulators and antennas [14]-[19].

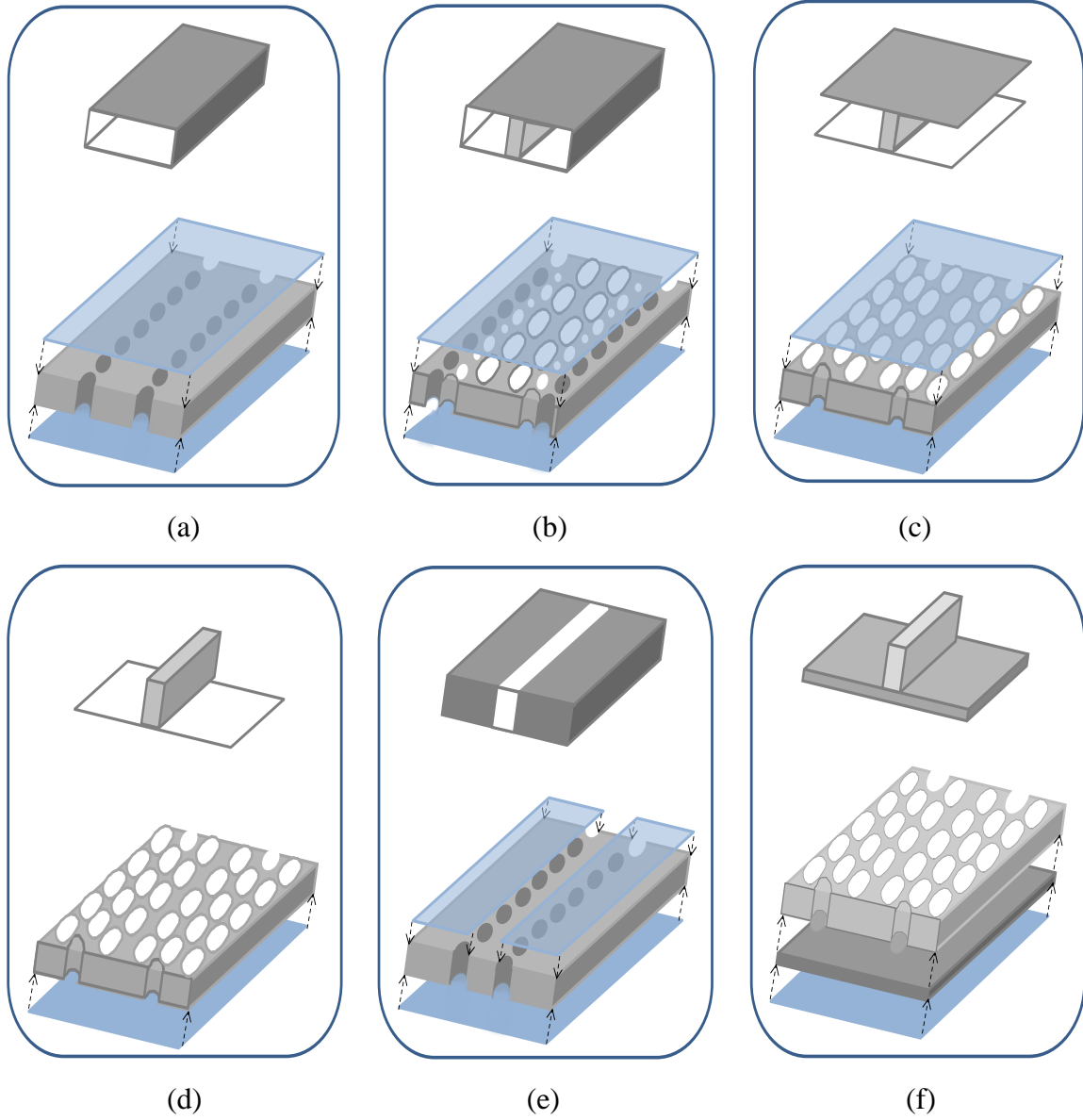


Figure 1: Topologies of different SIC structures and their dielectric waveguide counterparts (reprint according to [9]) (a) Substrate Integrated Waveguide (SIW), (b) Substrate Integrated Slab Waveguide (SISW), (c) Substrate Integrated Non-Radiating Dielectric (SINRD) guide, (d) Substrate Integrated Image Dielectric Guide (SIIDG), (e) Substrate Integrated Inset Dielectric

Guide (SIINDG), and (f) Substrate Integrated Insular Guide (SIIG). Note that white circle stands for air hole and dark circle for metallised via. Dielectric material is coloured as light grey.

#### A) SIW design rules

For the convenience of fabrication process, the rectangular waveguides are typically synthesized by placing two rows of periodic metallic posts in the substrate, as shown in Figure 2, where  $d$  is the diameter of the metallic posts,  $s$  is the spacing between the centers of two posts,  $w$  and  $w_{eff}$  stand for the physical and effective widths of the SIW, respectively. In fact, this periodic structure is more complicated for analysis than the conventional waveguide as the edge of the fictitious electrical side wall is subject to several parameters, especially the post diameter  $d$ . There are several methods to find out the effective width of the SIWs,  $w_{eff}$ , either by using simulation tools or empirical equations. As introduced in [20], the effective width can be obtained with the aid of commercial or self-coded simulation software through three simple steps:

1. Two straight SIW sections of different length ( $L_1 > L_2$ ) are simulated.
2. Phase difference between these two transmission coefficients for the  $TE_{10}$  mode is used to calculate its propagation constant with (1).

$$\beta_{SIW} = \frac{\angle S_{21}^{L_2} - \angle S_{21}^{L_1}}{L_1 - L_2} \quad (1)$$

3. Effective width of the SIW can be obtained using (2).

$$w_{eff} = \frac{\pi}{\sqrt{\omega^2 \mu_0 \epsilon_0 \epsilon_r - \beta_{SIW}^2}} \quad (2)$$

There is also an empirical equation which can be used to estimate the effective width of the SIWs [21]:

$$w_{eff} = w - 1.08 \frac{d^2}{s} + 0.1 \frac{d^2}{w} \quad (3)$$

The transmission loss is another important concern in designing SIW structures. Due to the dielectric substrate and reduced volume, the SIWs normally have a degraded Q factor compared with the rectangular waveguide counterparts. Power leakage needs to be carefully avoided to preserve the advantages of SIW circuits. In fact, the side wall radiation of SIWs can be

determined by the geometries of SIW structures as well as the properties of substrate. For example, the higher the dielectric constant and the thinner the substrate is, the smaller the radiation between the metallic posts will be, because the energy will be much more confined within the waveguide region. On the other hand, the leakage power will be a product of  $d$  and  $s$  once the substrate is specified. Design rules have been concluded in a previously reported work to ensure that the radiation loss be kept at a negligible level [20].

$$\begin{aligned} d &< \lambda_g / 5 \\ s &\leq 2d \end{aligned} \quad (4)$$

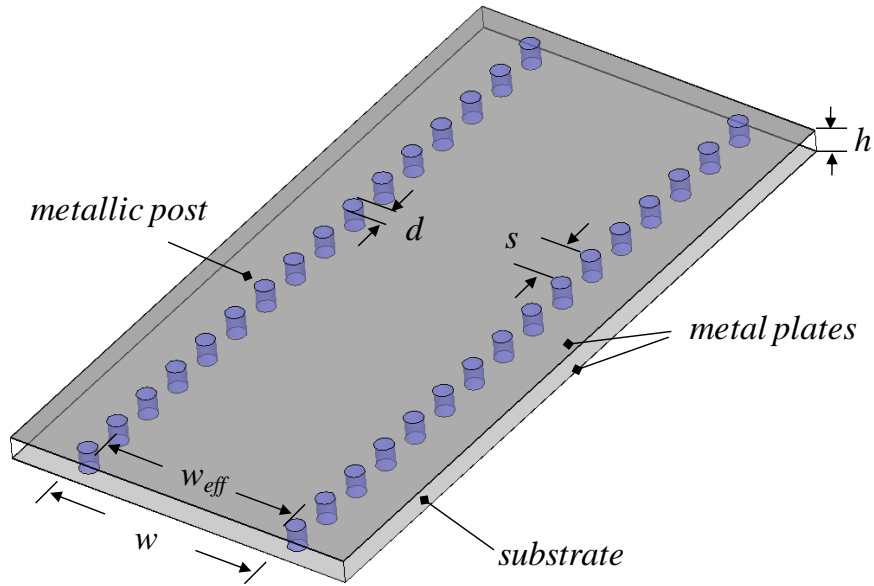
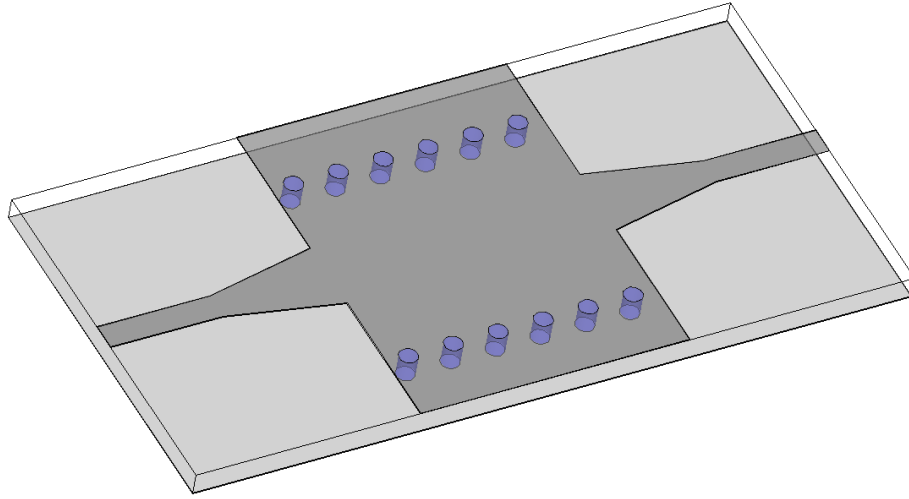


Figure 2: SIW structure synthesized with arrays of metalized vias

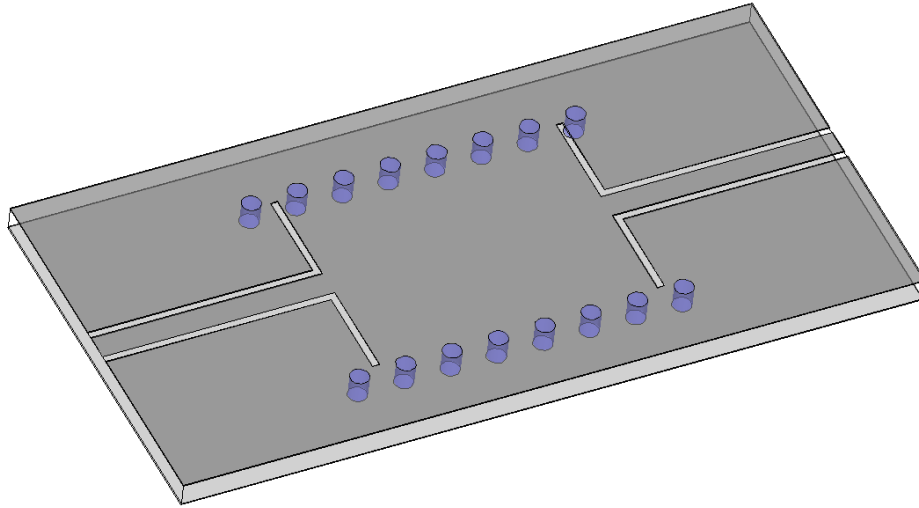
## B) SIW transitions

In order to integrate SIWs and other planar circuits, various SIW-planar structure transitions are developed. The first transition was proposed for SIW-microstrip line connection [22]. The design of the SIW-microstrip transition is straightforward, which simply makes use of a tapered microstrip line to excite the waveguide mode, as shown in Figure 3(a). It has excellent performance over a very broad bandwidth that can cover the entire SIW bandwidth.





(a)



(b)

Figure 3: Integrated transitions from planar circuits to SIW (a) microstrip line, (b) conductor backed CPW line

In the millimeter-wave range, coplanar waveguide (CPW) is a preferred transmission line because the microstrip line may cause a severe surface wave loss in many designs if a thick substrate is used. Shown in Figure 3(b), a low-loss and broadband SIW-conductor backed CPW transition was presented in [23], which consists of a CPW section with  $90^\circ$  bend at the end of each slot. Of course, better performance can be expected by using an inclined bend to build a smoother transition, but this will also result in a larger size.

### C) Passive SIW components

Since SIWs can be perceived as dielectric substrate based waveguides in planar form, most of classical waveguide components can be transplanted into SIWs without significant changes in their structures. Compared to microstrip devices, there are mainly two reasons of choosing SIWs:

- 1) Their losses are lower than in the corresponding microstrip devices, especially in the millimeter-wave frequency range.
- 2) There are no radiation and packaging problems.

Up to date, a great number of applications using the SIW technology have been reported. Among them, low cost filters received particular attention. There are a variety of SIW filter topologies: The first SIW filter was proposed by Deslandes and Wu in 2003 [15], which made use of inductive posts to design a three-pole Chebyshev band-pass filter (BPF) operating at 28 GHz. In the same year, the authors presented a dual mode BPF by using an oversized cavity [24]. The  $TE_{102}$  and  $TE_{201}$  modes are the operating modes and a transmission zero appears when these two modes are used to cancel out with each other. Subsequently, a cavity filter with irises operating at 60 GHz [25] was designed and fabricated. The filter is composed of three half-wavelength SIW resonators together with microstrip line to waveguide transitions at both ends of the SIW cavity. In addition, SIW filters with an electromagnetic band-gap (EBG) or defected structure in the ground plane were presented to achieve specific performance like super-wide bandwidth or better stopband rejection [26]-[27]. A number of techniques of designing SIW elliptic filters were also developed and examined to improve the selectivity by introducing transmission zeros [28]-[29]. While most of these filters were demonstrated to operate in the microwave range, it was also demonstrated that SIW filters could easily be realized up to 180 GHz using a thick film ceramic fabrication technique [30].

Besides filters, many other passive components have also been developed in SIW technology. For example, planar SIW phase shifters [31], power dividers [17], circulators [18], directional couplers [16], six-port circuits [32] and magic Tees [33] all have been implemented and demonstrated since 2003.

#### D) SIW antennas

Based on the SIW technology, many kinds of integrated antennas have been proposed. In 2004, a  $4 \times 4$  SIW slot array antenna at X-band was realized for the first time by etching longitudinal slots on the top metallic surface of the SIW [34]. Another SIW antenna topology was the leaky-wave antenna firstly proposed by Deslandes and Wu, which made use of one of the fundamental characteristics of this synthetic waveguide, namely, its property to generate leakage loss when the longitudinal spacing of metallic vias is sufficiently large [35]. Furthermore, folded SIW structures were applied in order to reduce the antenna size [36]. Besides these antenna topologies, filtering antennas (filtennas), a module providing combined functions of a bandpass filter and a horn antenna, have been realized by covering SIW cavity frequency selective surface (FSS) at the aperture of a horn antenna [37]. Other antenna structures, which utilized the SIW as a feeding network scheme, have also been presented and investigated [38].

#### E) Active SIW components

SIW technology was also used in the design of active components, thanks to the advantage of its easy integration with surface mounted or embedded diodes, transistors or MMIC chips. For example, a 12 GHz feedback oscillator was proposed in [39]. This oscillator was stabilized by using an injection-locking scheme. Another K<sub>a</sub>-band Gunn diode oscillator was developed as an effort to build up a stable and low-phase-noise signal source for synchronized communications [40]. In addition, a four-way K<sub>a</sub>-band spatial power combiner was proposed, where the SIW architecture exhibited a good power combining efficiency along with a good heat sink [41]. Iris-type inductive discontinuities in SIWs have also been used in designing the input and output networks of an X-band amplifier to pursue a maximally flat gain and high input and output return losses in the entire frequency band [42].

Although extensive studies of SIW technology have been carried out, some of them simply maps rectangular waveguide structures into SIWs. In fact, one of the significant advantages of SIW over traditional waveguide lies in the fact that it provides a low cost and low profile platform to

integrate non-planar waveguide concepts with planar transmission lines like microstrip or CPW. As such, the unique features of waveguides (For example, high Q factor) and conventional transmission lines (For example, planar circuit) can be united to achieve a complementary and unprecedented combination which is particularly useful at millimeter-wave bands since insertion loss and manufacturing cost are always major concerns associated with increased frequencies. Our first task in this thesis is to explore interesting features of this combined technique through intensive theoretical and experimental research. In Chapters 1 to 4, a number of original concepts and innovative structures are proposed and demonstrated, which emphasize on exploiting the advantages of SIWs, such as broadband balanced structures, miniaturization techniques, and inherent high pass property.

On the other hand, most of previously reported work solely focused on a single element, and little attention has been paid to incorporate advantageous features of SIW to millimeter-wave system performance. In order to fill up this under exploited field, the second major topic of this thesis is on the development of SIW circuits and investigations for wireless communication systems. From Chapter 5 on, sub-millimeter/millimeter wave systems are focused. Several different SIW based receiver architectures are demonstrated.

The organization of this doctoral dissertation is as follows:

The main topic of Chapter 1 is on the development of broadband SIW balun transformers. First of all, a broadband SIW planar balun implemented on a single layer PCB is proposed and presented. The balun structure consists of a 3 dB SIW power divider for equal power splitting and microstrip lines which are placed on different sides of the PCB substrate at balanced ports to obtain an  $180^\circ$  phase shift. Technical merits of this balun are concluded by the fact that it can easily operate at millimeter-wave frequencies and does not require any tight coupling sections as usually used in many MMIC balun structures. In addition, the balun can be integrated with other planar circuits including nonplanar and multilayered structures for achieving high circuit efficiency. Another newly proposed broadband microstrip-to-broadside parallel stripline transition is also demonstrated in this chapter. The proposed transition is constructed with the SIW scheme which can achieve broadband performance and offer several advantages over other counterparts such as low insertion loss, good design tolerance and compact circuit size in the millimeter-wave range. With the proposed transition as the feeding network, a novel broadband

printed quasi-Yagi antenna is developed. A two-way SIW quasi-Yagi antenna array is then designed and measured to further demonstrate the performance of the proposed quasi-Yagi antenna within an array environment.

Chapter 2 focuses on the miniaturization and bandwidth enhancement of SIW circuits. First of all, a broadband half-mode substrate integrated waveguide (HMSIW) Wilkinson power divider is proposed and presented. This broadband H-plane power divider utilizes the half-mode structure of SIWs such that the overall size is largely reduced. In addition, the lossy network or resistor branch is successfully integrated with the SIW structure to guarantee good output matching and isolation. This is critical for the development of a power combining or non-equal power dividing with potentially poor output port matching. A simple design theory is presented by using the even-odd mode analysis technique. Secondly, a so-called quarter-mode substrate integrated waveguide (QMSIW) technique is introduced, in bid to achieve a next step of size reduction. The QMSIW structure is generated by bisecting the HMSIW with another fictitious magnetic wall. To demonstrate the design concepts in details, two C-band four-pole Chebychev filters are designed and fabricated for different bandwidth applications.

Chapter 3 presents a broadband phase shifter that makes use of non-radiating longitudinal slots in the broad wall of an SIW. The proposed broadband phase shifter is developed on the basis of a dispersive phenomenon of SIW and slotted SIW lines. The design concept is developed on different propagation constants of  $TE_{10}$  mode and quasi-TEM mode, which are the fundamental modes of SIWs and our proposed slotted SIWs, respectively. The proposed method is then validated by both theory and experiments. It is shown that the proposed phase shifters have features of wideband, low insertion loss, and easy to fabricate.

In Chapter 4, a novel sub-harmonic self-oscillating mixer (SOM) topology that makes use of the transmission characteristics of two operating modes in an SIW cavity is proposed. The SOM circuit consists of a dual-mode SIW band-pass filter, a common source hetero-junction FET and a low-pass filter. The fundamental mode ( $H_{101}$ ) of the SIW cavity is used for RF mode operation while the  $H_{202}$  mode is used for local oscillation. A  $K_a$ -band experimental prototype is designed and fabricated to demonstrate and validate our proposed circuit concept. The measured power levels of the self and second harmonic LO signals are about 8.5 dBm and -3 dBm, respectively.

The mixer, implemented as a down-converter, achieves 12 dB conversion loss and IF phase noise of -81 dBc/Hz at 100 kHz offset with 34 GHz RF input.

In Chapter 5, generic architectures and parameters of receiver system are discussed as a guideline for our communication systems to be demonstrated in the following chapters. Based on the features of different receiver architectures, our communication systems of interest employ a traditional heterodyne topology, and a dual-antenna scheme is used instead of using a circulator or switch platform for single-antenna solution which may be too lossy at millimeter-wave frequencies. In our experimental setup, the I/Q modulation is performed by using vector signal generator and, a direct quadrature demodulator, AD8347 from Analog Device, is used for demodulation. The output of the demodulation board is measured with different RF input power levels  $P_{in}$  and different symbol rates  $R_s$  for QPSK scheme. Finally, receiver analysis is carried out and system parameters, such as receiver noise floor, receiver sensitivity and RF impairments that may affect the bit error rate (BER), are studied. It is found that a pure and stable source plays a crucial role in receiver systems.

Chapter 6 presents a broadband millimeter-wave single balanced diode mixer that makes use of an innovative SIW based 180-degree hybrid, fabricated with conventional PCB technique. It has low conversion loss of less than 10 dB, excellent linearity and high port-to-port isolations over a wide frequency range of 20 to 26 GHz. The proposed mixer has advantages over previously reported millimeter-wave mixer structures judging from a series of aspects such as cost, ease of fabrication, planar construction and broadband performance. Furthermore, a receiver front-end that integrates a high-performance SIW slot array antenna and our proposed mixer is presented. With the proposed receiver front-end, a K-band wireless communication system with M-ary quadrature amplitude modulation (M-QAM) is developed and demonstrated for line-of-sight (LOS) channels. Excellent overall error vector magnitude (EVM) performance is obtained.

Chapter 7 presents a novel SOM-based receiver front-end which deploys an injection locking scheme in order to improve the frequency stability and phase noise of the oscillating signal. In our receiver front-end, an SIW-based slot array antenna, a band-pass filter and a second-harmonic SOM which has been demonstrated in Chapter 4 are integrated into a single layer substrate as an effort to establish a compact, low-cost and low profile architecture for millimeter-wave wireless systems. The proposed SOM makes use of the transmission characteristics of two operating

modes in an SIW cavity. As such, the proposed receiver front-end has the advantages of low phase noise and decent isolation between radio frequency (RF) and local oscillator (LO) signals. In addition, a small externally injected signal is applied at the fundamental frequency as a reference to improve the LO signal. Comparing the free running mode and injection locking mode of the proposed SOM, it can be observed that the small reference signal successfully stabilizes the LO signal and improves the phase noise from around -75 dBc/Hz to -100 dBc/Hz at the 100 KHz offset. This chapter further presents a K<sub>a</sub>-band transceiver system to verify the feasibility of our receiver front-end for practical wireless communication applications. Excellent results are obtained.

Finally in Chapter 8, an innovative 60 GHz substrate integrated transceiver system with a broad bandwidth up to 3 GHz is presented. To validate the proposed SICs scheme, a 60 GHz wireless communication system with modulated signals is successfully demonstrated for LOS channels. The proposed integration technique of planar and non-planar structures allows the design of passive components and active devices within a single package. The passive circuits and high-gain antennas are integrated together with monolithic microwave integrated circuits (MMICs) by simple wire-bonding process. With this design and implementation technique, our 60 GHz transceiver system can demonstrate attractive advantages and features such as low-cost, compact size, low profile and reliable performance.

## **CHAPTER 1      DESIGN AND IMPLEMENTATION OF BROADBAND BALUN TRANSFORMERS USING SIW TECHNIQUE**

A balun is a device or circuit that converts signals between an unbalanced circuit structure and a balanced counterpart. A large number of analog RF and microwave circuits require balanced inputs and outputs in order to reduce noise and high order harmonics as well as improve dynamic range of circuits. With the inherent features of generating balanced signals, baluns are widely used in many wireless communication systems for realizing critical building blocks such as balanced mixer, push-pull amplifier and antenna feed networks.

Based on the above mentioned definition of the term “balun”, two categories of planar-form baluns with respect to their applications can be defined. The first category of balun can be referred to as the microstrip-to-microstrip balun, which means that the interface of unbalanced and balanced ports is microstrip line. The second category of balun can be referred to as a transition between an unbalanced line (microstrip or CPW) and a balanced line such as broadside parallel strip and coplanar stripline (CPS).

This chapter focuses on the design of broadband SIW balun transformers. Two different types of balun structures are proposed and presented.

The first proposed balun consists of a 3 dB SIW power divider [43] for equal power splitting and microstrip lines which are placed on different sides of a dielectric substrate at balanced ports to obtain  $180^\circ$  phase shift. Since the SIW power divider presents broadband characteristics, the proposed balun structure can provide a broadband frequency response, which is a critical feature of many wireless communication systems.

In the second part of this chapter, we propose a new microstrip-to-broadside parallel stripline transition constructed with the SIW scheme which can achieve a broadband performance and offer several advantages over other counterparts such as low insertion loss, good design tolerance and circuit size compactness at the millimeter-wave range. One major characteristic of the proposed transition is that the balanced line is created by geometric features, not by frequency sensitive structures. Therefore, it can provide good performance over a fairly wide bandwidth.



To demonstrate the design methodology and structural features, experimental prototypes of the proposed baluns are presented in this chapter. The designs are made through the use of a commercial software package (Ansoft HFSS v10.1) and validated by experiments.

## 1.1 Broadband SIW Planar Balun

Although various types of baluns have been reported for applications in connection with microstrip circuits in the form of MICs and MMICs, a planar balun structure with favourable performance has been a challenging research topic over the past several decades [43]-[46]. Among them, the 180 degree hybrids and multi-section half-wave baluns are frequently used in microwave circuits as they can easily be realized in many design procedures and fabrication processes, and also they provide satisfactory performance, namely, low VSWR, small insertion loss and good amplitude/phase imbalance between balanced ports. However, they fail to maintain those advantageous features over a wide frequency range. Furthermore, they are hardly employable when the operating frequency goes into millimeter-wave frequency band. The Marchand balun is a known broadband solution but its performance largely depends on a tight coupling of the coupled line sections. In addition, it is difficult to design with the conventional PCB process at frequencies beyond 20 GHz. Due to those challenging issues in the design of planar baluns, non-planar baluns are usually used instead [47]-[48]. However, the use of a non-planar topology may prevent itself from its seamless integration with planar circuits, especially with respect to surface mounted chip structures.

### 1.1.1 Geometry and Design of Broadband SIW Planar Balun Structure

The SIW structure is known to have broadband monomode characteristics compared to its conventional waveguide counterpart as the SIW usually supports only  $TE_{n0}$  modes. This is because the synthesis of bilateral metallic walls is made with discontinued metallised via or slot arrays in the thin dielectric substrate, which does not allow the guidance of the TM modes. Therefore, the monomode bandwidth is guaranteed with  $TE_{10}$  mode related to  $TE_{20}$  mode.

Figure 1.1 shows the structure of the proposed broadband SIW planar balun. The dark area stands for the metallization parts on the bottom plane of the double-sided PCB substrate and the gray area stands for the metallization on the top plane. The proposed balun consists of a 3 dB SIW power divider for equal power splitting and microstrip line sections which are placed on different

sides of the PCB substrate at balanced ports so as to obtain an  $180^\circ$  phase shift. To further demonstrate this idea with a better explanation, an intersection plane A is chosen, which is marked in Figure 1.1. Figure 1.2 illustrates the electrical fields on plane A, from which it can be found that the E-field orientations of balanced ports are different from each other, which means an  $180^\circ$  phase difference.

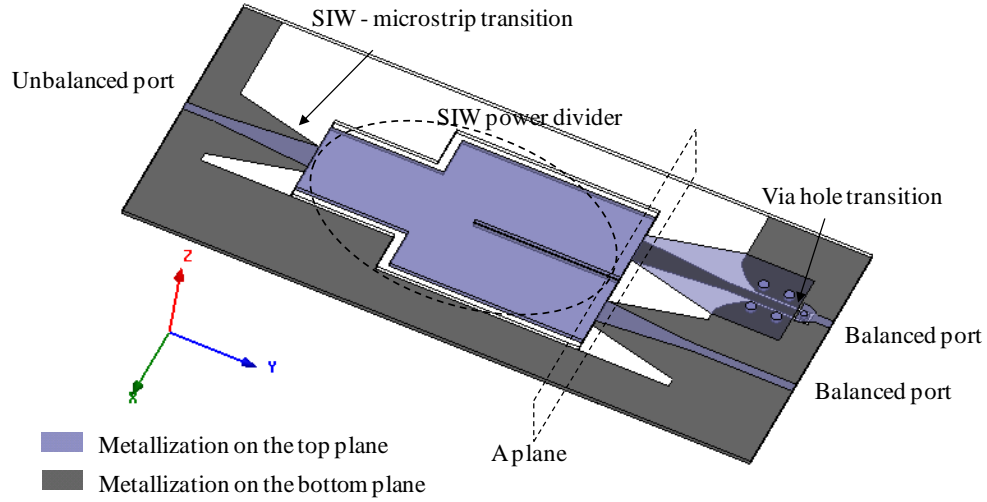


Figure 1.1: Proposed broadband SIW planar balun



Figure 1.2: Electrical field plots on the A plane

The transition between the SIW and microstrip line is referred to a well-described tapered line structure given in [22]. The only difference is that the ground plane of the transitions is also modified in the form of a tapered section so that the transitions can provide better performance. The planarity of balanced ports is further achieved using a metallic via hole transition to conduct one of the differential signals from one side to the other. As such, the new balun can easily be

designed and fabricated on a double-sided PCB substrate. As shown in Figure 1.3, the via-hole transition and the tapered ground plane are carefully designed to ensure that the RF signal can be smoothly transferred to the output port with very low insertion loss and little discontinuity. All the interconnections that generate the discontinuities are made into tapered shape so that the discontinuity and inductance effects are minimized. The optimization is done with the aid of Ansoft HFSS v10.1. Compared to previously reported structures, the proposed balun can easily be used at millimeter-wave frequencies and also the structure does not require tight coupling sections as usually made in many MMIC balun structures. Of course, the proposed topology can be integrated with other planar structures including non-planar circuits within the same substrate for achieving high efficiency at low cost.

To demonstrate the design methodology and electrical performance, an experimental prototype of the proposed balun is designed and fabricated at 24 GHz. The substrate used in our work is RO6002 with a thickness of 10 mil and a dielectric constant  $\epsilon_r = 2.94$ . Figure 1.3 shows the physical dimensions of the designed broadband SIW planar balun. The via hole transition part is enlarged to provide a clear illustration. The gray area in this case stands for the metallization on the top plane of the substrate while the dashed-line area stands for the metallization on the bottom plane of the substrate. The SIW is realized by using metallic slots. The balanced ports are extended to different directions just for the measurement consideration.

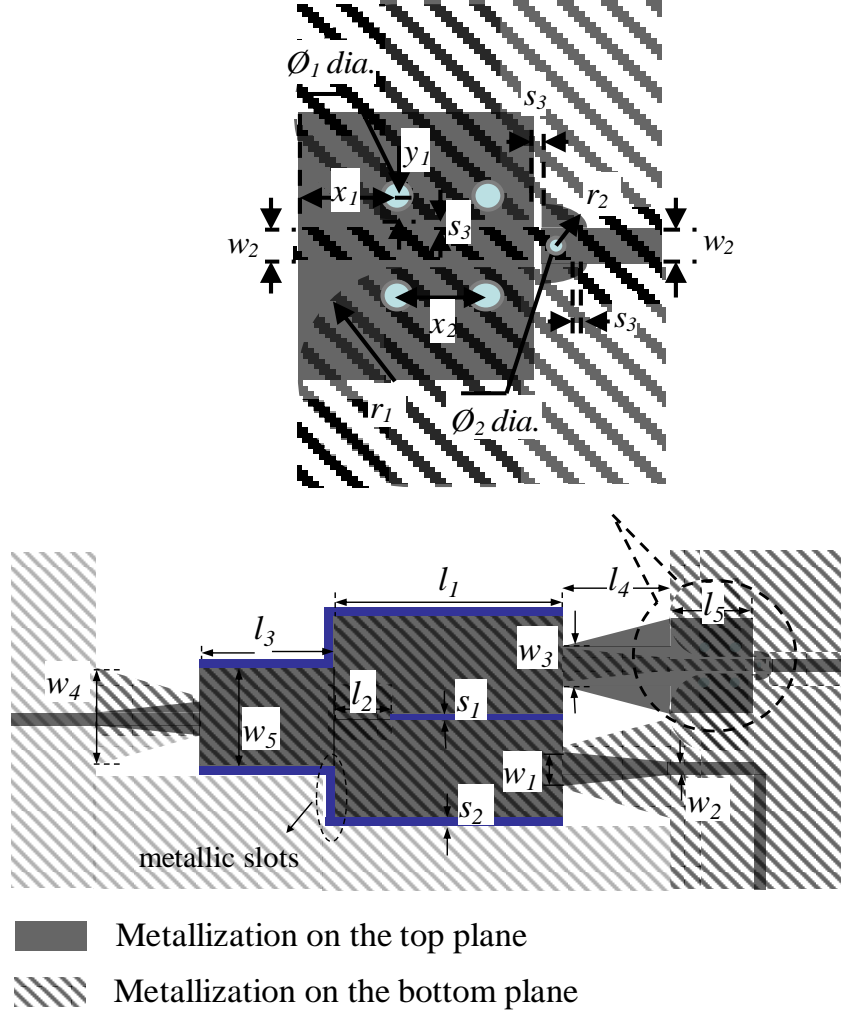
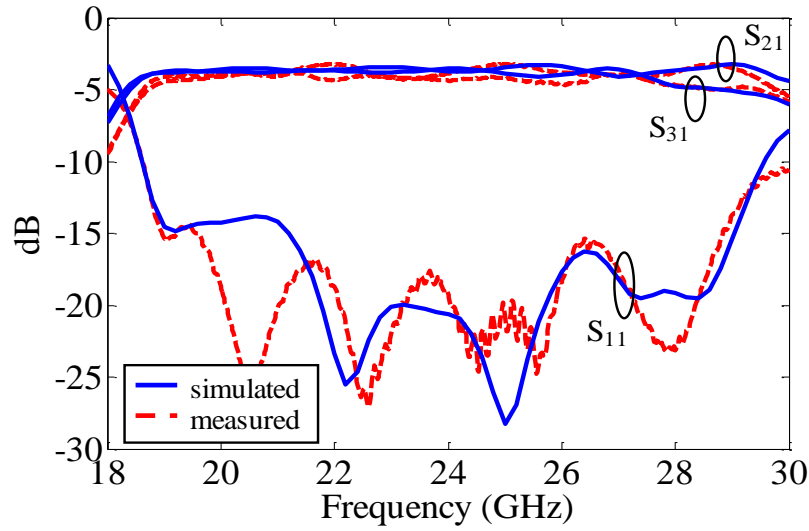


Figure 1.3: Physical dimensions of the experimental prototype of the proposed SIW planar balun ( $w_1 = 1.74$  mm,  $w_2 = 0.6$  mm,  $w_3 = 2.14$  mm,  $w_4 = 5.2$  mm,  $w_5 = 5.2$  mm,  $l_1 = 12$  mm,  $l_2 = 3$  mm,  $l_3 = 7$  mm,  $l_4 = 5.6$  mm,  $l_5 = 4.25$  mm,  $s_1 = 0.3$  mm,  $s_2 = 0.6$  mm,  $s_3 = 0.15$  mm,  $x_1 = 1.8$  mm,  $x_2 = 1.6$  mm,  $y_1 = 0.4$  mm,  $r_1 = 1.6$  mm,  $r_2 = 0.75$  mm,  $\phi_1 = 0.6$  mm and  $\phi_2 = 0.25$  mm).

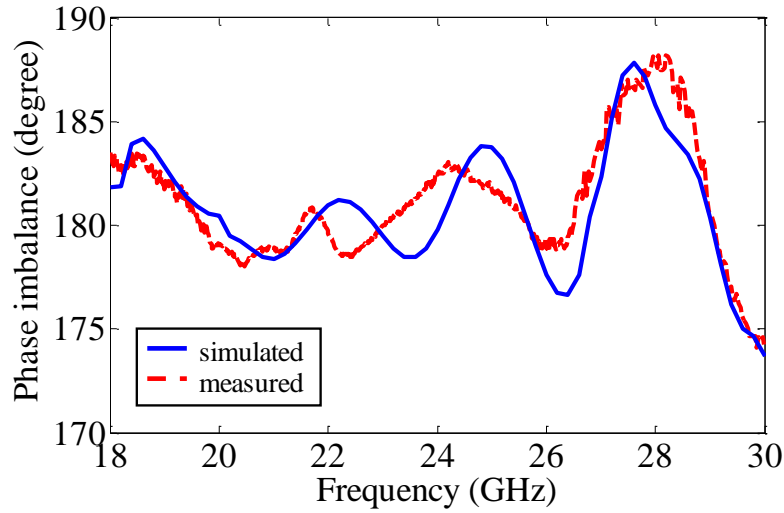
### 1.1.2 Simulation and Measurement Results

Figures 1.4(a)-1.4(b) display the simulated and measured results for the amplitude response and phase balance of the proposed planar balun, in which the solid line stands for the simulated results and the dashed line stands for the measured results. This balun is simulated by using Ansoft HFSS v10.1. The measurements are carried out by using an Anritsu test fixture model 3680K with the maximum frequency up to 40 GHz and an HP8510C vector network analyzer.

The calibration work is done by using a set of TRL calibration standards. It is observed that a good agreement is achieved between the measurement and the simulation. Measured results show that better than 10 dB return loss of the unbalanced port is well achieved across the whole bandwidth of interest from around 19 GHz to 29 GHz, or 42% of bandwidth. Within the bandwidth of operation, the measured amplitude and phase imbalance between the two balanced ports are respectively within 1 dB and  $\pm 5^\circ$ , except that the phase imbalance reaches  $8^\circ$  at around 28 GHz.



(a)



(b)

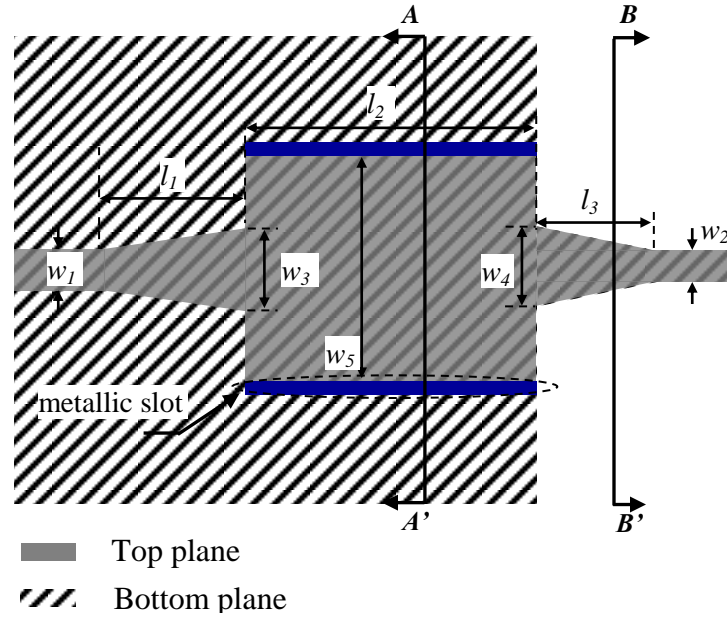
Figure 1.4: S-parameters of the proposed balun: (a) amplitude responses (b) phase responses

## 1.2 Broadband SIW Microstrip-to-Broadside Parallel Stripline Transition

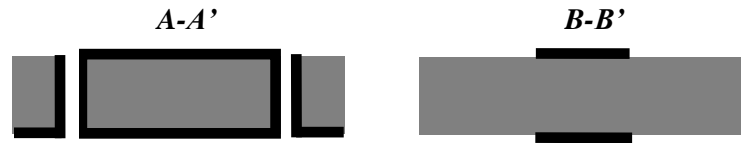
Broadside parallel stripline and CPS line are balanced lines which have widely been used in the design of feeding networks of printed dipole antennas, balanced mixers and optoelectronic circuits. One of the most popular microstrip-to-broadside parallel stripline transition configurations is derived from Duncan's works in 1960 [48]. Although this tapered coupled line transition can achieve an ultra-broad bandwidth, it is hard to be adapted to millimeter-wave operation. In this section, we intend to develop a broadband and planar-form microstrip/SIW-to-broadside parallel stripline transition favorable to millimeter-wave applications.

### 1.2.1 Structure Description

Figure 1.5 shows the top and cross-sectional views of our proposed microstrip-to-broadside parallel stripline transition, in which the SIW is realized by using metallic slots. The gray area stands for the metallization of the front side of substrate while dashed line area stands for the back side. As can be seen, the SIW-to-broadside parallel stripline transition is achieved by a section of tapered broadside coupled line. The experimental prototype is designed for a center operating frequency at around 24 GHz. The microstrip line at the input port is assumed to have  $50\ \Omega$  and the characteristic impedance of the broadside parallel stripline is  $70\ \Omega$ . The dielectric substrate used in this work is RO6002 with  $\epsilon_r = 2.94$  and 10 mil in thickness. The geometrical parameters of the structure are given by (unit: mm):  $w_1 = 0.6$ ,  $w_2 = 0.6$ ,  $w_3 = 1.66$ ,  $w_4 = 1.4$ ,  $w_5 = 5$ ,  $l_1 = 4$ ,  $l_2 = 7$ , and  $l_3 = 2.1$ .



(a)



(b)

Figure 1.5: (a) Top view and (b) Cross-sectional view of the proposed microstrip-to-broadside parallel stripline transition

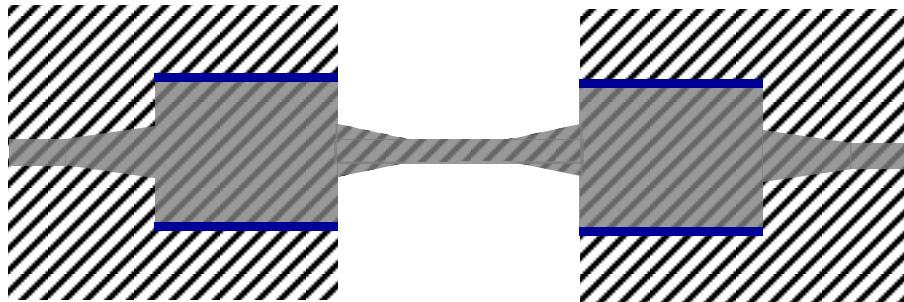


Figure 1.6: Structure of two back-to-back SIW-to-broadside parallel stripline transitions

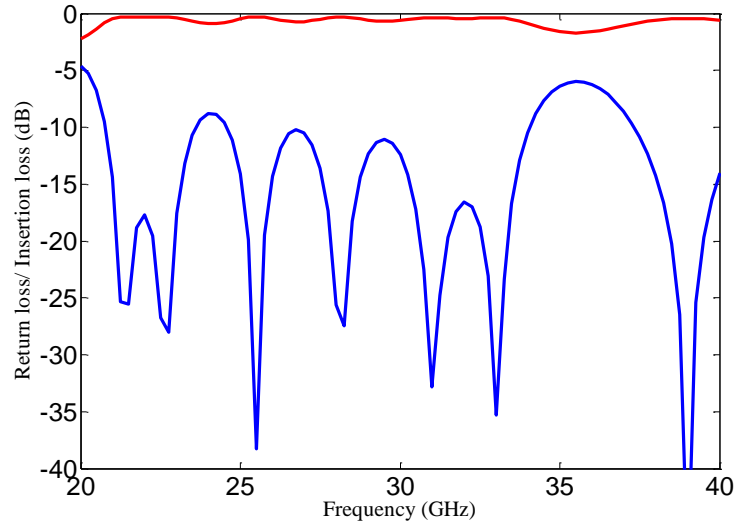


Figure 1.7: Simulated return loss and insertion loss of the proposed back-to-back transitions

To evaluate performance of the microstrip-to-broadside parallel stripline transition, a back-to-back transition configuration is developed, as shown in Figure 1.6. A section of 4.5 mm long broadside parallel stripline is used to connect these two back-to-back transitions. Figure 1.7 displays the simulated results of the back-to-back transitions. The transitions are simulated by using commercial software Ansoft HFSS v10.1. It can be observed that the return loss is around or better than -10 dB over the frequency band from 20.5 GHz to 34 GHz, or 49.5% bandwidth.

### 1.2.2 Application to a Broadband Printed Quasi-Yagi Antenna

Yagi-Uda antenna is one of the most popular antenna configurations to achieve the end-fire beam formation. However, its applications have been restricted at relatively low frequencies for a long time and usually mentioned as home television antennas. Recently, several interesting works have drawn attention of researchers back to this old antenna scheme [49]-[50]. Among them, Kaneda *et al.* proposed a new approach to realize a Yagi-Uda dipole array fed by a microstrip-to-CPS transition on a single layer PCB substrate. Within this antenna configuration, the transition feeding network plays an important role in the overall antenna performance. This microstrip-to-CPS transition was realized by using a half-wave microstrip balun structure [51]. The designers need to ensure an  $180^\circ$  phase difference between two output branches of the transition, which means a half wavelength difference. At millimeter wave frequencies, the wavelength is very



small and the inductance of any interconnection becomes significant. Therefore, this transition configuration is no longer suitable for conventional PCB fabrication process.

### 1.2.2.1 Antenna Configuration

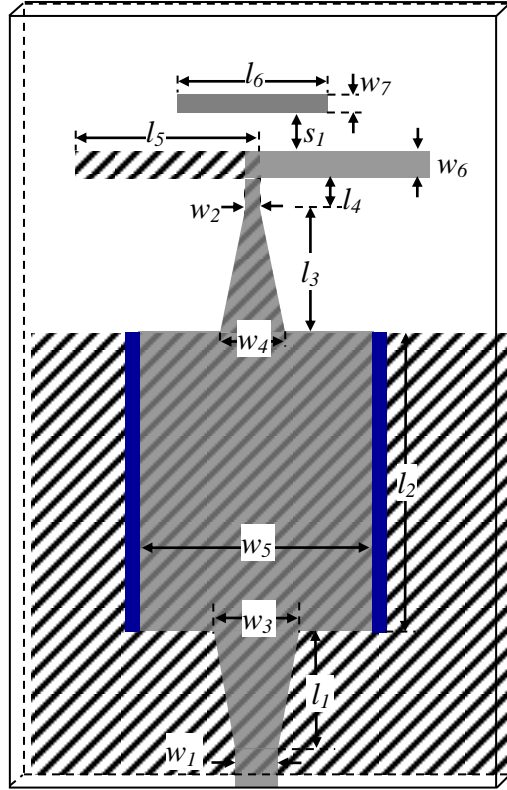


Figure 1.8: Geometry of the proposed quasi-Yagi antenna

The geometry of the proposed broadband printed quasi-Yagi antenna fed by the microstrip-to-broadside parallel stripline transition is described in Figure 1.8. As discussed in [49], the metallization on the top and bottom planes serves as the reflector element for the antenna while the director element on the top plane directs the antenna propagation toward the end-fire direction. The impedance matching is mostly determined by the width of the driver element ( $w_6$ ) and the spacing between the director and driver elements ( $s_1$ ). The circuit optimization is made with the aid of Ansoft HFSS v10.1. The antenna is designed for K-band operation. The whole antenna structure is built on a  $10 \times 19 \text{ mm}^2$  RO6002 substrate with  $\epsilon_r = 2.94$  and 10 mil in thickness. The

optimized dimensions of the antenna are the following (unit: mm):  $w_1 = 0.6$ ,  $w_2 = 0.2$ ,  $w_3 = 1.66$ ,  $w_4 = 1.4$ ,  $w_5 = 5$ ,  $w_6 = 0.6$ ,  $w_7 = 0.4$ ,  $l_1 = 3$ ,  $l_2 = 7$ ,  $l_3 = 2.95$ ,  $l_4 = 0.55$ ,  $l_5 = 3.5$ ,  $l_6 = 3$ , and  $s_1 = 0.7$ .

### 1.2.2.2 Simulated and Measured Results

Figure 1.9 illustrates the simulated and measured return losses of the proposed antenna. The input return loss measurement was carried out by using an Anritsu one port test fixture on a HP8510C vector network analyzer. It is observed that a good agreement is achieved between the measurement and the simulation. The measured input return loss of the quasi-Yagi antenna is under -10 dB with an impedance bandwidth as wide as 14 GHz (~20 GHz to 34 GHz), or 51%. The radiation patterns were also measured across the entire -10 dB return loss bandwidth with our compact-range anechoic chamber. Figure 1.10 shows the measured E-plane radiation pattern of the antenna at 25.5 GHz across the entire angle  $\phi$  from  $-180^\circ$  to  $180^\circ$ . The red dashed line stands for the co-polarization radiation pattern and the blue solid line stands for the cross-polarization pattern. In Figure 1.10, the maximum gain is shown around 4 dBi at  $\phi \approx 0^\circ$  and the minimum points of the gain show up at around  $\phi \approx \pm 90^\circ$ , which means that a good end-fire beam form is achieved. In addition, the front-to-back ratio is found to be better than 10 dB and the cross-polarization level is better than -10 dB across the entire bandwidth.

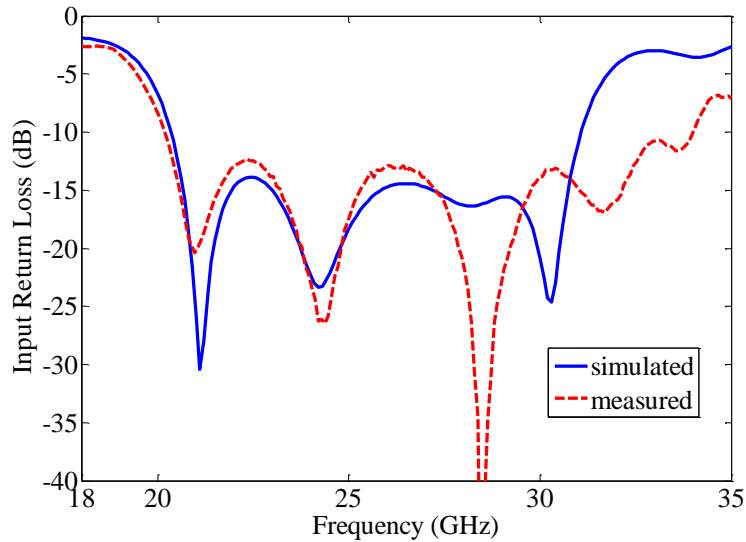


Figure 1.9: Input return loss of the proposed quasi-Yagi antenna

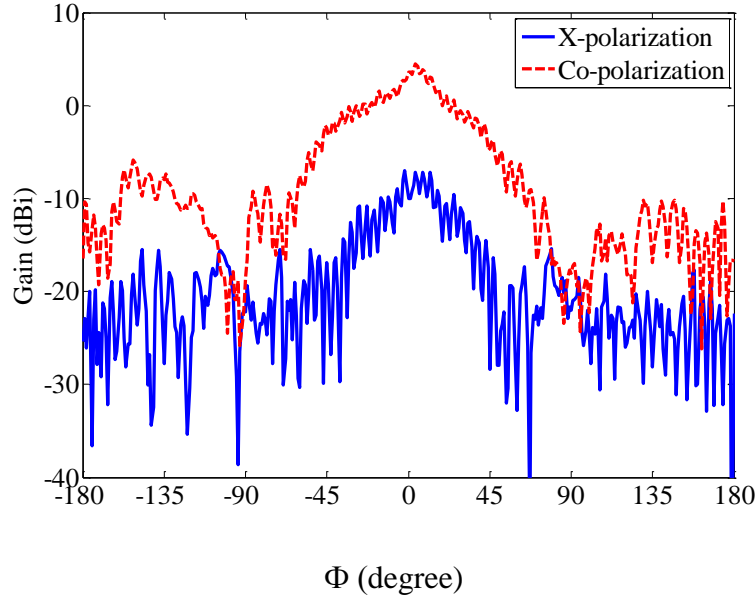


Figure 1.10 Measured E-plane radiation patterns ( $\theta = 90^\circ$ ) of the antenna at 25.5 GHz

### 1.2.2.3 Broadband Quasi-Yagi Array

To further demonstrate the performance of the proposed quasi-Yagi antenna within an array environment, a two-way SIW quasi-Yagi antenna array is designed, as shown in Figure 1.11. The enclosed area in Figure 1.11 is an SIW H-plane power divider designed to provide an equal power distribution to the antenna elements. As well known, the mutual coupling between elements is particularly important in the design of small arrays of printed antennas. The quasi-Yagi structure has very small mutual coupling characteristics in both coplanar and stacked configurations [49], and herein it is a good option for the array applications. The whole antenna array was built on a  $17 \times 26 \text{ mm}^2$  RO6002 substrate with  $\epsilon_r = 2.94$  and 10 mil in thickness. The space between two quasi-Yagi elements is a half wavelength. Referring to Figure 1.8, the optimized dimensions of the antenna element are the following (unit: mm):  $w_4 = 1.4$ ,  $w_5 = 4.65$ ,  $w_6 = 0.6$ ,  $w_7 = 0.4$ ,  $l_3 = 3$ ,  $l_4 = 0$ ,  $l_5 = 2.3$ ,  $l_6 = 2$ , and  $s_I = 0.7$ . The second director is 1 mm long and 0.3 mm wide. The spacing between two directors is 0.6 mm.

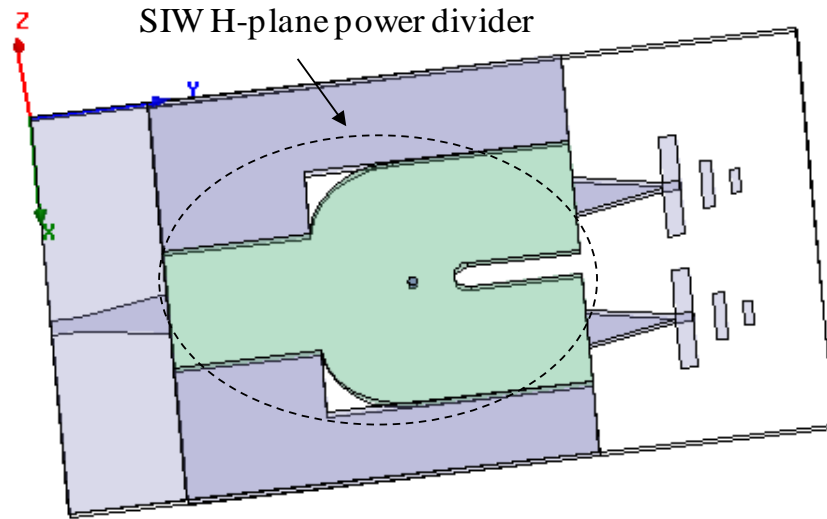


Figure 1.11: SIW quasi-Yagi antenna array

Figure 1.12 illustrates the simulated and measured return losses of the proposed quasi-Yagi array. It is observed that a good agreement is achieved between the measurement and the simulation. The measured input return loss of the quasi-Yagi antenna is around or under -10 dB with an impedance bandwidth as wide as 11 GHz (~22 GHz to 33 GHz), or 40%. It can be found that the input return loss of the quasi-Yagi array deteriorates a little bit compared to the previous single antenna unit. This is attributed to the well-known fact that a lossless reciprocal three-port network such as the H-plane SIW power divider cannot achieve good output isolation. Figure 1.13 shows the measured E-plane radiation pattern of the antenna at 26.5 GHz across the entire angle  $\phi$  from  $-180^\circ$  to  $180^\circ$ . It can be observed that a good Quasi-Yagi antenna array performance is achieved. The gain was measured as 5.1-5.6 dB across the entire -10 dB return loss bandwidth with our compact-range anechoic chamber. In addition, the front-to-back ratio is found to be better than 15 dB and the cross-polarization level is better than -14 dB across the entire bandwidth.

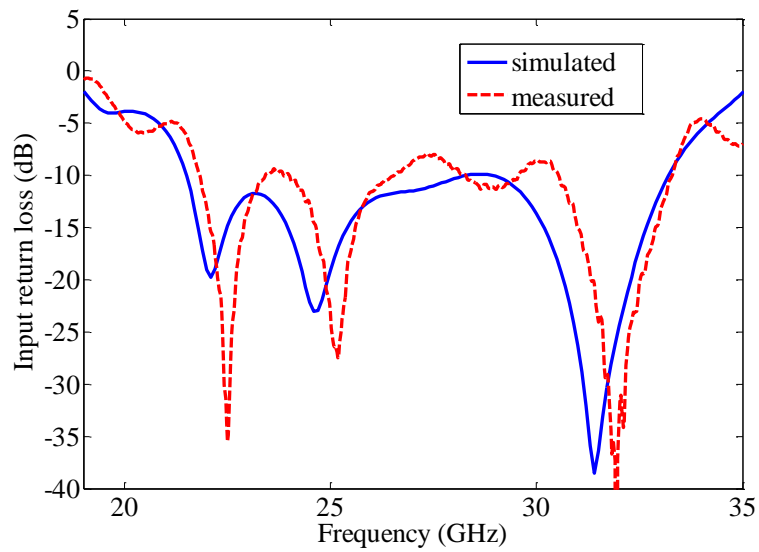


Figure 1.12: Input return loss of the SIW quasi-Yagi antenna array

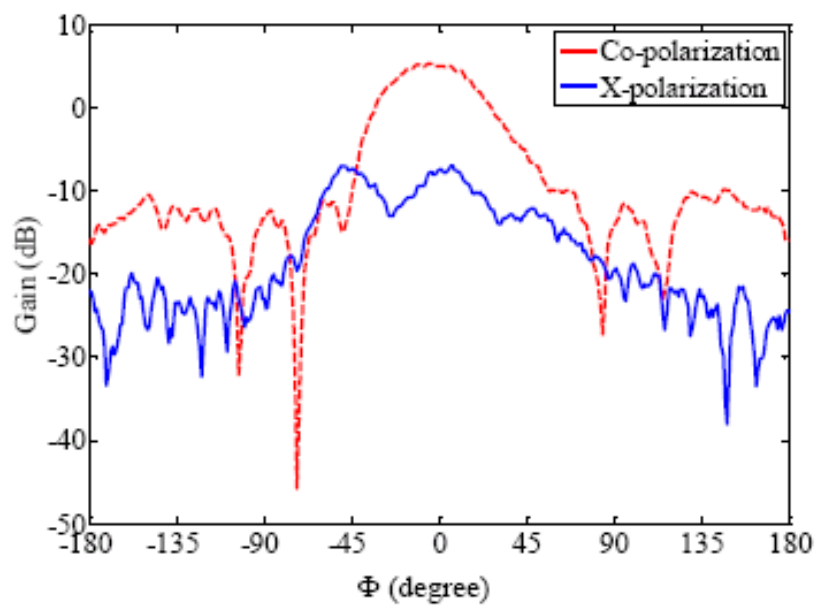


Figure 1.13: Measured E-plane radiation patterns ( $\theta = 90^\circ$ ) of the antenna array at 26.5 GHz

### 1.3 Conclusion

In this chapter, SIW balun transformers are studied and novel structures are developed for broadband sub-millimeter or millimeter wave applications. First of all, a broadband SIW planar balun is proposed. The balun structure consists of a 3 dB SIW power divider for equal power splitting and microstrip lines which are placed on different sides of the PCB substrate at balanced ports to obtain an  $180^\circ$  phase shift. The merits of this balun are concluded by the fact that it can easily operate at millimeter wave frequencies and does not require any tight coupling sections as usually used in many MMIC balun structures. In addition, the balun can be integrated with other planar circuits including nonplanar and multilayered structures for achieving high circuit efficiency. Subsequently, a broadband microstrip-to-broadside parallel stripline transition is proposed and it is further implemented as the feeding network of a printed quasi-Yagi antenna. The proposed transition is constructed with the SIW scheme which can achieve a broadband performance and offer several advantages over other counterparts such as low insertion loss, good design tolerance and compact circuit size at the millimeter wave range. The design concept is validated by a design example for K-band operation. The measured input return loss of the quasi-Yagi antenna is under -10 dB with an impedance bandwidth as wide as 14 GHz (~20 GHz to 34 GHz), or 51%. The measured front-to-back ratio is found to be better than 10 dB and the cross-polarization level is better than -10 dB across the entire bandwidth. Finally, to further demonstrate the performance of the proposed quasi-Yagi antenna within an array environment, a two-way SIW quasi-Yagi antenna array is also designed and measured.

## CHAPTER 2      MINIATURIZATION AND BANDWIDTH ENHANCEMENT OF SIW CIRCUITS

Due to the increasing demand of wireless communications in the past decades, unremitting efforts have been made to bring down the size and cost of microwave circuits. Usually, the size of SIW circuits is quite larger than their microstrip or CPW counterparts. This could be advantageous for millimeter-wave applications since the fabrication tolerance of PCB process will be much more relaxed with respect to circuit size and processing parameters. However, a large size of SIW components also poses a problem for their applications at low frequencies. In order to reduce the inherent size of SIW circuits, novel techniques have been proposed and demonstrated such as folded SIW [52]-[53]. Recently, half-mode structure of SIWs, a very recently reported concept that the SIW can be bisected with a fictitious magnetic wall and each half of the SIW becomes an HMSIW structure and the new structure can almost preserve the original field distribution [54]-[55], is proposed.

In [56], the properties of HMSIW have been studied systematically. It was mentioned that the field components of dominant mode inside the HMSIW can be calculated as follows:

$$E_{y,(0.5,0)} = Ak_x \sin k_x (w-x) e^{-jk_z z} \quad (2.1a)$$

$$H_{x,(0.5,0)} = \frac{-Ak_x k_z}{\omega\mu} \sin k_x (w-x) e^{-jk_z z} \quad (2.1b)$$

$$H_{z,(0.5,0)} = \frac{A(\epsilon_r k_0^2 - k_z^2)}{j\omega\mu} \cos k_x (w-x) e^{-jk_z z} \quad (2.1c)$$

with

$$\begin{aligned} k_x &= \frac{\pi}{2(w-a)} \\ k_y &= 0 \\ k_z &= \sqrt{k_0^2 \epsilon_r - \frac{\pi^2}{4(w-a)^2}} \end{aligned}$$

where  $0 \leq x \leq w$ , the subscript (0.5, 0) stands for the half mode,  $\omega$  is the phase frequency,  $\mu$  is the substrate permeability,  $k_0$  is the free-space wave number and  $a$  is the x-coordinate of the position of the maximum electric field along the cross section of the HMSIW.

It should be noted that in equations (2.1), the origin of coordinates is set right in the middle of the open edge of the HMSIW (referring to Fig. 1 in [56]). Keeping the same coordinates, the field components of  $TE_{mn}$  mode in a conventional SIW (assuming that the width of the conventional SIW is  $2w$ ) are given by:

$$E_x = A_{mn} \frac{\beta_y}{\varepsilon} \cos[\beta_x(w-x)] \sin\left[\beta_y\left(y - \frac{h}{2}\right)\right] e^{-j\beta_z z} \quad (2.2a)$$

$$E_y = -A_{mn} \frac{\beta_x}{\varepsilon} \sin[\beta_x(w-x)] \cos\left[\beta_y\left(y - \frac{h}{2}\right)\right] e^{-j\beta_z z} \quad (2.2b)$$

$$E_z = 0 \quad (2.2c)$$

$$H_x = A_{mn} \frac{\beta_x \beta_z}{\omega \mu \varepsilon} \sin[\beta_x(w-x)] \cos\left[\beta_y\left(y - \frac{h}{2}\right)\right] e^{-j\beta_z z} \quad (2.2d)$$

$$H_y = A_{mn} \frac{\beta_y \beta_z}{\omega \mu \varepsilon} \cos[\beta_x(w-x)] \sin\left[\beta_y\left(y - \frac{h}{2}\right)\right] e^{-j\beta_z z} \quad (2.2e)$$

$$H_z = -jA_{mn} \frac{\beta_c^2}{\omega \mu \varepsilon} \cos[\beta_x(w-x)] \cos\left[\beta_y\left(y - \frac{h}{2}\right)\right] e^{-j\beta_z z} \quad (2.2f)$$

with

$$\begin{aligned} \beta_x &= \frac{m\pi}{2w} \\ \beta_y &= \frac{n\pi}{h} \\ \beta_z &= \beta^2 - \left[ \left( \frac{m\pi}{2w} \right)^2 + \left( \frac{n\pi}{h} \right)^2 \right] \end{aligned}$$

where  $-w \leq x \leq w$ ,  $-\frac{h}{2} \leq y \leq \frac{h}{2}$ .



Comparing equations (2.1) and (2.2), we can find that the major difference lies in the fact that the term of  $y - \frac{h}{2}$  is close to 0 since the substrate is very thin, which leads to  $\sin\left[\beta_y(y - \frac{h}{2})\right] \approx 0$  and  $\cos\left[\beta_y(y - \frac{h}{2})\right] \approx 1$ .

In addition, the cutoff frequency and phase constant of the dominant mode in an HMSIW can be calculated by [56]:

$$f_{c,TE_{0.5,0}} = \frac{c}{4\sqrt{\epsilon_r} w_{eff,HMSIW}} \quad (2.3)$$

$$k_{z,TE_{0.5,0}} = \sqrt{k_0^2 \epsilon_r - \left(\frac{\pi}{2w_{eff,HMSIW}}\right)^2} \quad (2.4)$$

in which, the effective width of HMSIW  $w_{eff,HMSIW}$  is given by:

$$w_{eff,HMSIW} = \frac{w_{eff,SIW}}{2} + \Delta w \quad (2.5)$$

where the effective width of a conventional SIW  $w_{eff,SIW}$  was discussed before in (3), additional width  $\Delta w$  due to the fringe effect at the open edge of an HMSIW can be estimated by

$$\begin{aligned} \Delta w = & (0.05 + \frac{0.30}{\epsilon_r})h \\ & \times \ln(0.79 \frac{w_{eff,HMSIW}'^2}{h^3} + \frac{104w_{eff,HMSIW}' - 261}{h^2} + \frac{38}{h} + 2.77) \end{aligned} \quad (2.6)$$

where  $w_{eff,HMSIW}' = w_{eff,SIW}/2$ .

In this chapter, techniques on miniaturizing SIW circuits will be examined and several innovative designs are proposed.

## 2.1 Broadband and Compact HMSIW Power Divider

Power dividers and combiners are passive devices that allow a microwave signal to be split equally or non-equally between two or more branches, depending on the design requirement. In

most cases, the equally-divided powers are needed in practical design. These devices then allow signals to be distributed and processed as needed. In the microwave engineering, the T-junction H-plane waveguide power divider is a simple and widely used three-port network. However, the conventional H-plane power divider suffers from the problem of not being matched at all ports and, in addition, does not have a good isolation between the output ports. In many applications, output matching and isolation of power divider should be considered, which can enhance circuit performance. For example, in antenna array applications, the outputs of a power divider are usually directly connected to the antenna elements. Good output isolation can effectively avoid interference between antenna elements.

On the other hand, the Wilkinson power divider is a lossy network judging from the resistor branch that is used for the isolation of output ports. Such a divider is especially useful because the output ports can be simultaneously isolated and matched [57]. This scheme, which was implemented in the design of microstrip T-junction long time ago, has never been addressed so far in the design of waveguide T-junctions. This may be attributed to the difficulty on how to design a lossy network and also to integrate it with the waveguide structure. In this section, a broadband SIW H-plane Wilkinson power divider is proposed and presented for the first time, which is made in a single layer PCB.

### 2.1.1 Structure Description

The proposed broadband SIW-based Wilkinson power divider employs the half-mode structure of SIWs. In our newly proposed power divider structure, the HMSIW is utilized not only to achieve size reduction but also to make the E-field a maximum value at one vertical edge plane along the propagation direction for the integration of a lossy network.

Figure 2.1 shows the top and cross-sectional views of the conventional H-plane SIW power divider as well as the proposed HMSIW power divider, inside which the SIW structures are realized by using metallic slots. For measurement purpose, the transitions between the SIW and microstrip line are designed. As can be seen from the figure, the size of the HMSIW power divider can be miniaturized as compared with its conventional counterparts. Another significant benefit of this HMSIW structure relies on the suppression of the dominant higher-order mode  $TE_{20}$ . Figure 2.2 presents simulated S-parameter performance of an HMSIW power divider without looking into any optimized structure. The circuit simulation was made with the aid of

Ansoft HFSS software package v10.1. It can be observed that  $TE_{20}$  mode cannot propagate in such an HMSIW structure so that the bandwidth performance of the proposed power divider can greatly be enhanced. Figure 2.2 shows that a broad bandwidth from 18 GHz to 45 GHz (or 86%) is easily achieved for our proposed HMSIW power divider.

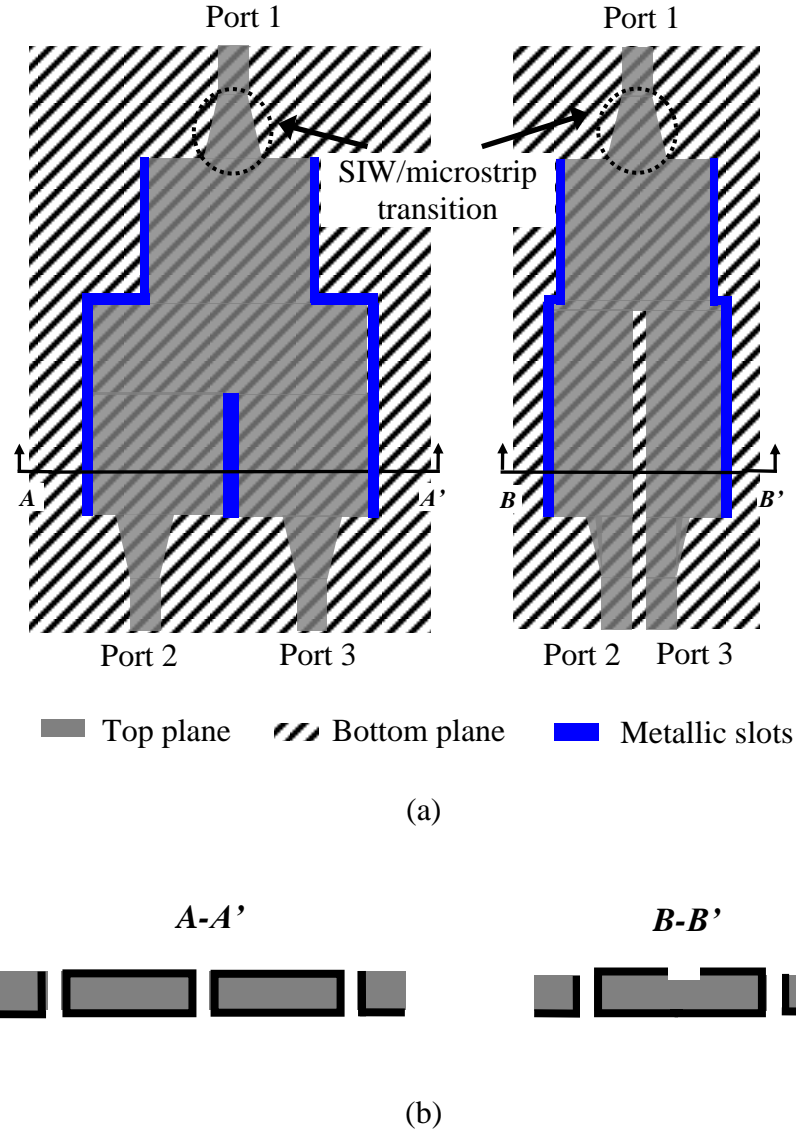


Figure 2.1: (a) Top view and (b) Cross-sectional view of the conventional H-plane SIW power divider and the proposed HMSIW power divider

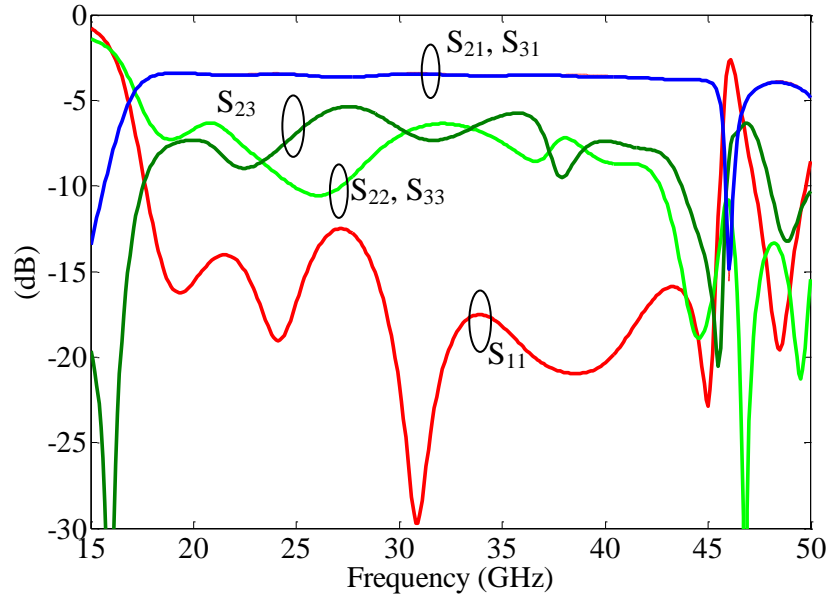


Figure 2.2: Simulated S-parameter performance of an HMSIW power divider.

### 2.1.2 Theoretical Analysis and Design of the Proposed HMSIW Wilkinson Power Divider

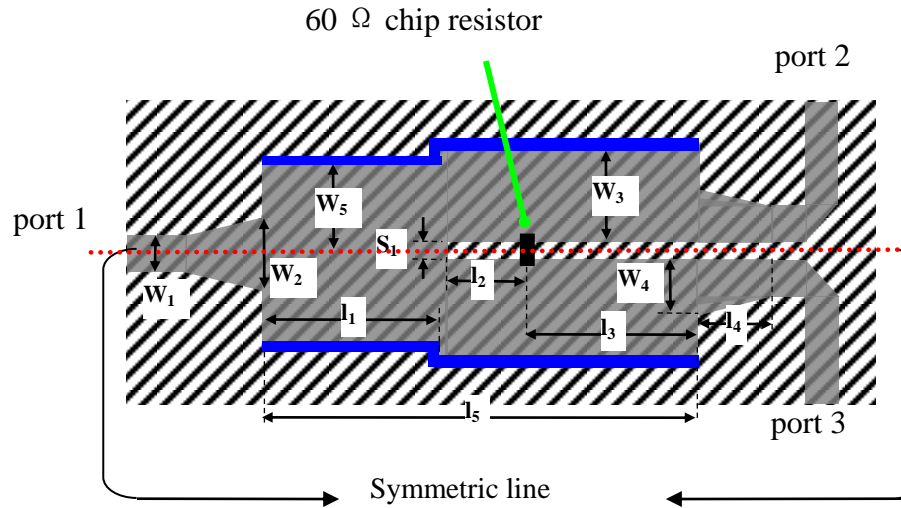


Figure 2.3: Physical dimensions of the experimental prototype of the proposed HMSIW power divider ( $w_1 = 0.6$  mm,  $w_2 = 1.4$  mm,  $w_3 = 2.8$  mm,  $w_4 = 1.13$  mm,  $w_5 = 2.7$  mm,  $l_1 = 5$  mm,  $l_2 = 2.1$  mm,  $l_3 = 3.1$  mm,  $l_4 = 2.4$  mm,  $l_5 = 10.5$  mm,  $s_1 = 0.5$  mm).

From Figure 2.2 it can also be found that the output matching and isolation of the HMSIW power divider are still not improved or even not good enough for practical application since no lossy element (or resistor branch) is introduced. This is in particular important when the structure is used as a power combiner or the power division is not equally made with a potentially poor matching condition at output ports. In order to solve this problem, we propose an HMSIW Wilkinson power divider circuit that is described in Figure 2.3. In our proposed HMSIW power divider, a chip resistor is added between the HMSIWs with a quarter guided wavelength distance from the splitting point of the power divider on the basis of the well-described theory.

The analysis of the proposed power divider can be simplified by using the well-described even-odd mode technique. Using the even-odd mode analysis technique, the power divider circuit can be decomposed into a superposition of two simpler ones which are considerably easy for analysis. In the even-mode case, the voltage condition on the symmetric line shown in Figure 2.3 becomes open circuit. As such, the proposed power divider is simplified into basic HMSIW power divider circuit as shown in Figure 2.1. For the odd-mode case, the voltage condition on the symmetric line becomes short circuit and the corresponding odd-mode decomposition is shown in Figure 2.4. With the aid of Ansoft HFSS v10.1, it can be found that the HMSIW  $TE_{10}$  mode impedance in our case is around  $30\ \Omega$ . From Figure 2.4, it can also be verified that the output port are well matched by using the chip resistor since the proper arrangement of the location of the resistor will make  $Z_{in}$  equal to  $30\ \Omega$ .

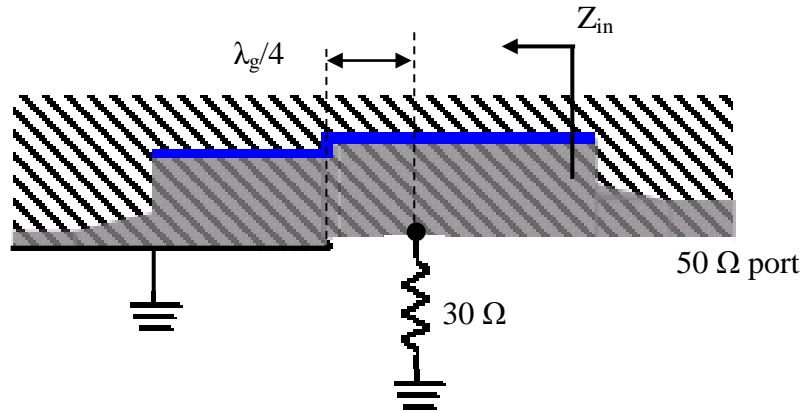
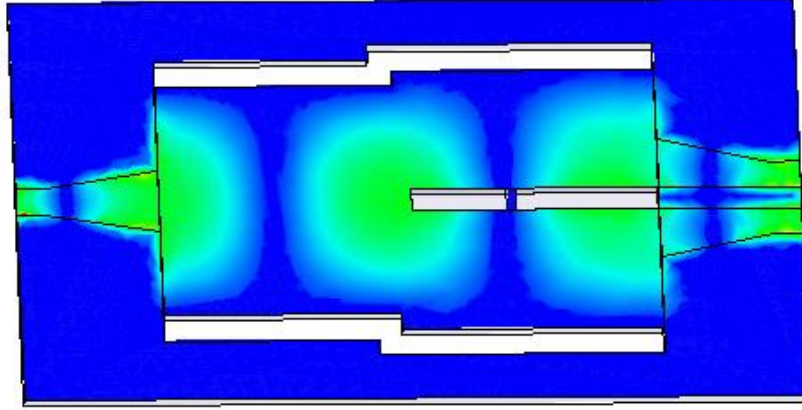


Figure 2.4: Odd-mode decomposition of the proposed HMSIW Wilkinson power divider

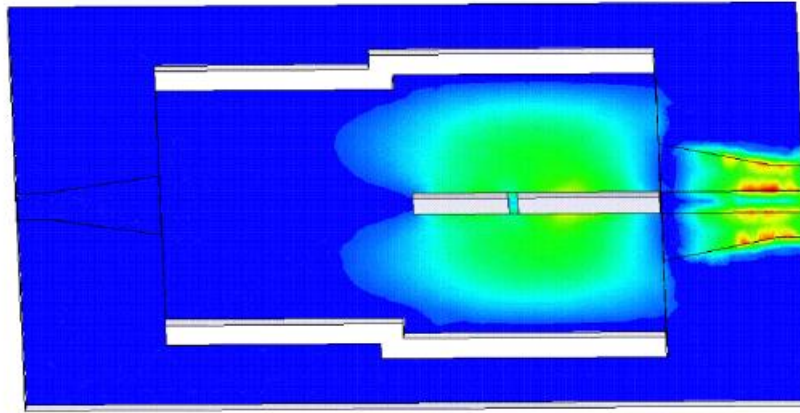
To demonstrate the design methodology and also expected electrical performance, an experimental prototype of the proposed power divider is then designed and fabricated over K-band. The substrate used in our work is RO6002 with a thickness of 10mil and a dielectric constant  $\epsilon_r = 2.94$ . Figure 2.3 gives the physical dimensions of the designed broadband HMSIW Wilkinson power divider. 0402 chip resistor is used in our design. The SIW is made of metalized slot arrays in the dielectric substrate and the width of those slots is 0.6 mm. For measurement purpose, the output ports are extended to the opposite direction. The overall size of the K-band prototype is  $17 \times 12 \text{ mm}^2$ .

### 2.1.3 Simulated and Measurement Results

Figures 2.5(a)-2.5(b) exhibit both even and odd mode E field distributions of the proposed HMSIW Wilkinson power divider. The figures can further verify the aforementioned analysis process. Even- and odd- mode excitations are applied on the ports 2 and 3, respectively so that the proposed circuit is analyzed as a power combiner. For the even-mode case, the resistor branch does not affect the original field distribution. While for the odd-mode case, the resistor branch will deplete the energy from the excitation ports. Figures 2.6(a)-2.6(b) display the simulated and measured S-parameter results. The circuit simulation was made with the aid of Ansoft HFSS v10.1. The measurements were carried out by using an Anritsu test fixture model 3680K with the maximum frequency up to 40 GHz and an HP8510C vector network analyzer. The calibration work was done by using a set of single band TRL calibration standards for central frequency at 24 GHz. It can be found that a good agreement between the measured and simulated S-parameter responses is achieved. Measured results suggest that good input return loss ( $S_{11}$ ) and insertion loss ( $S_{21}$ ,  $S_{31}$ ) performance can be achieved across a very broad bandwidth from 18 GHz up to above 30 GHz. In the meanwhile, the output return loss ( $S_{22}$ ,  $S_{33}$ ) and isolation ( $S_{23}$ ) better than -10 dB are also ensured across a 40% bandwidth from 18 GHz to 27 GHz. It should be noted that the bandwidth of output parameters is markedly narrower than that of the input ones. This is because the resistor is inserted at a specific fraction of wavelength thus causing a frequency sensitive reaction. However, the input parameters do not get affected since it has been mentioned earlier that the resistor is open for input signals. According to the measurements, this power divider is well suitable for most of the millimeter wave broadband applications.



(a)

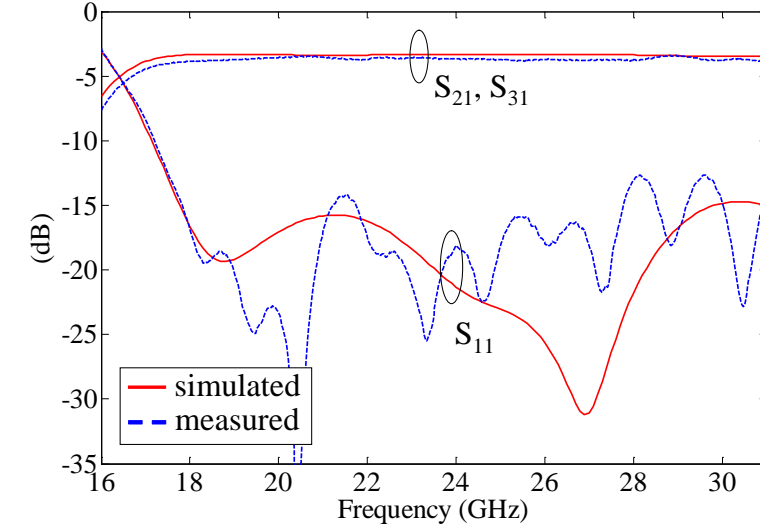


(b)

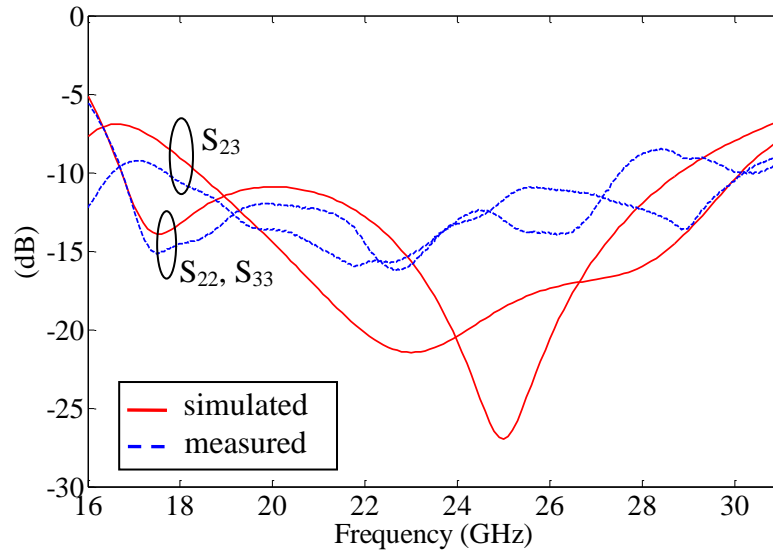
Figure 2.5: E field distribution of the proposed HMSIW power divider (a) Even-mode and (b) odd-mode.

Compared to the previously reported structures, the primary features of the proposed power divider present good output matching and isolation across a very broad bandwidth. In addition, this design takes the advantages of SIWs such as low profile, low insertion loss and low interference but the resulting structure becomes smaller in size. It is also worth mentioning that the half-mode configuration does not support the higher order mode  $TE_{20}$  as in the case of SIWs. Therefore, a broader bandwidth is another side product of the proposed power divider in contrast

with its counterparts. The proposed HMSIW Wilkinson power divider can easily be used at millimetre wave frequencies and also this structure is favourable for the microwave integrated circuit applications.



(a)



(b)

Figure 2.6: S-parameters of the proposed power divider: (a) input return loss and insertion loss responses (b) output return loss and output isolation responses.



### 2.1.4 Discussion of Cross-coupling between HMSIWs

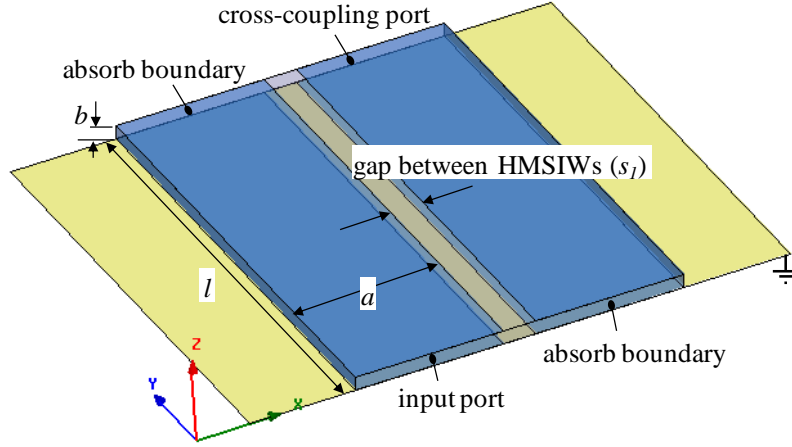


Figure 2.7: HMSIW model for cross-coupling investigation.

Cross-coupling between HMSIWs should be considered in the proposed structure. A close gap between the HMSIWs can result in a big interference between HMSIWs such that the circuit performance will be deteriorated. The relationship between the cross-coupling and the gap between HMSIWs is investigated by using HFSS. Figure 2.7 shows the model built in HFSS. Two HMSIWs are placed in parallel with a gap ( $s_l$ ) between them. The cross-coupling is simulated with the other two ports assigned absorbing boundary, which means no reflection occur. The substrate used in this model is RO6002 with different thickness. The length and width of the HMSIW are 9 mm and 2.8 mm, respectively. Figure 2.8 shows the simulated cross-coupling at 24 GHz. It can be observed that the cross-coupling gets stronger with a thicker substrate because of more leakage from the open edge of the HMSIW. For our design condition that substrate thickness  $b = 0.254$  mm, the cross-coupling does not vary sharply with the gap between the HMSIWs since the energy is largely confined inside the HMSIW structure. It can also be found that the 0.5 mm gap can guarantee a cross-coupling around -20 dB in our proposed power divider structure.

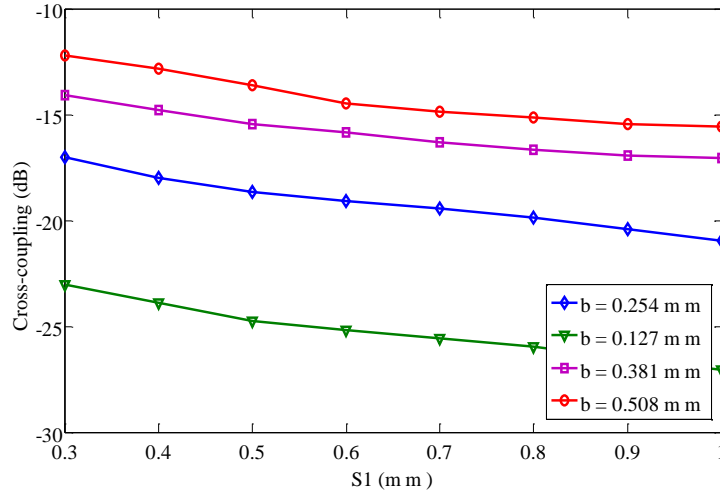


Figure 2.8: Simulated cross-coupling versus gap between HMSIWs with different thickness RO6002 substrate at 24 GHz ( $a = 2.8$  mm,  $l = 9$  mm).

## 2.2 5 GHz Bandpass Filter Demonstration Using Quarter-mode SIW Cavity

The SIW cavity filter is one of the most popular applications of the SIW technology in microwave circuits. Compared with other planar filters using microstrip or CPW schemes, SIW filters have shown excellent performance such as high Q-factor and low insertion loss [58]. However, the size of SIW filters is usually much larger than their microstrip or CPW counterparts, which poses a significant challenge for compact system designs, especially at low frequency bands. In fact, the most challenging integrated filter design is related to few GHz as there are no outstanding techniques available out there. Current SAW filter techniques and other proposed schemes are limited either by loss and performance or by structure size.

In order to yield a much compact size, a new concept, named quarter-mode substrate integrated waveguide (QMSIW), is proposed and applied to our filter design in this section. Figure 2.9 illustrates the QMSIW structure, which is generated by bisecting the HMSIW with another fictitious magnetic wall. From this figure, it can be observed that the maximum E field of the dominant  $TE_{101}$  mode locates at the corner of a QMSIW cavity. The overall size of a QMSIW

$TE_{101}$  mode cavity is around a quarter of its original SIW counterpart. Therefore, the proposed QMSIW shows an excellent potential for low frequency (less than few GHz) applications.

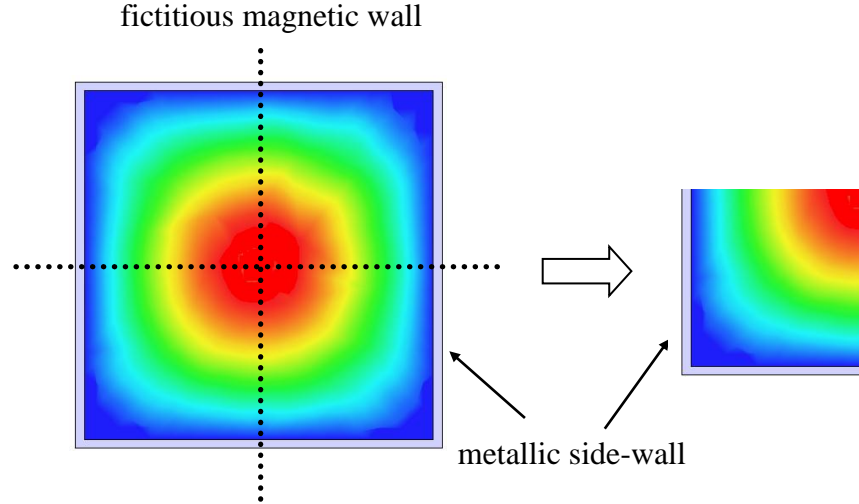
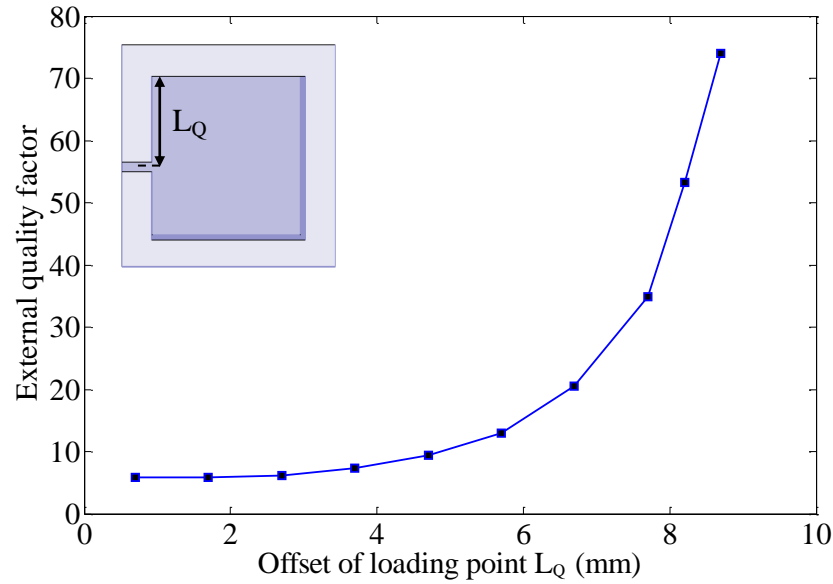


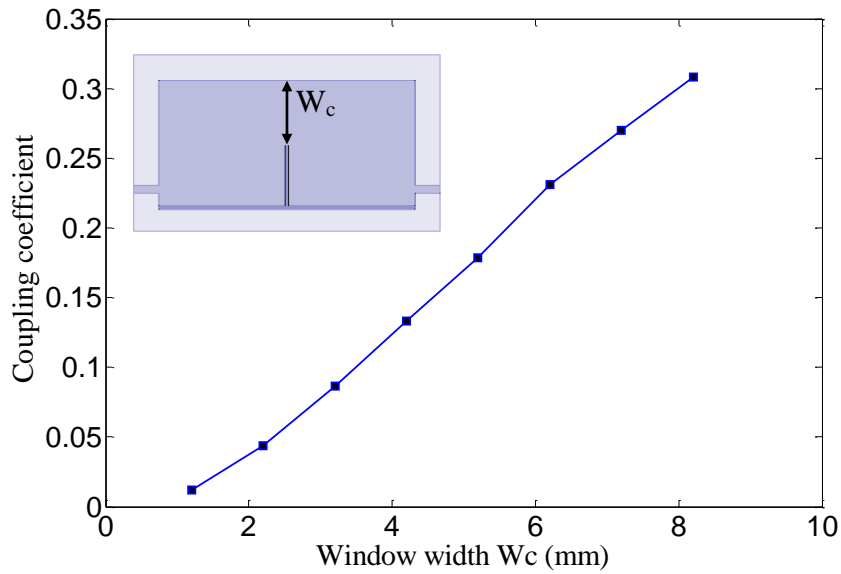
Figure 2.9: Top view of the conventional SIW and the proposed QMSIW cavities.

The  $Q$  value of our proposed QMSIW structure is usually about half lower than their conventional SIW counterparts since the two open edges are not perfect magnetic walls and some amount of radiation may happen. Due to the decreasing of the  $Q$  value, the proposed QMSIW filter cannot be adopted for high  $Q$  BPF with very narrow bandwidth performance (less than 5%) as SIW filters have already demonstrated. However, the proposed QMSIW can obtain a much stronger coupling coefficient between two neighbourhood sections. Therefore, it can be used for achieving broadband BPF performance for which conventional SIW filters cannot easily make. To demonstrate the design concept in details, two C-band four-pole Chebychev filters are designed and fabricated for different bandwidth applications. One filter works at the center frequency of 5.85 GHz with a fractional bandwidth of around 14%. The other operates at the center frequency of 5.5 GHz with a fractional bandwidth of around 26%, which covers the license-exempt frequency band 5.25 GHz to 5.85 GHz for the interest of WiMAX. Compared with other filters in the form of microstrip, the proposed filter takes the advantages of being planar structure, low electromagnetic interference or cross-talk, no coupled line structure and easy fabrication.

### 2.2.1 Geometry and Design of QMSIW Filter



(a)



(b)

Figure 2.10: External quality factor of a QMSIW cavity and the coupling coefficient between QMSIW cavities. (a) External quality factor versus offset of loading point  $L_Q$ . (b) Coupling coefficient versus coupling window width  $W_c$  between QMSIW cavities.

The design procedure of SIW BPFs has been well documented in previous reported work. From the circuit elements of the low-pass prototype filter, design parameters, namely, the external quality factor and coupling coefficients for the  $n$ -pole QMSIW band pass filters can be determined [59]

$$(Q_e)_A = \frac{g_0 g_1}{FBW}, \quad (Q_e)_B = \frac{g_n g_{n+1}}{FBW}$$

$$k_{j,j+1} \big|_{j=1 \text{ to } n-1} = \frac{FBW}{\sqrt{g_j g_{j+1}}} \quad (2.7)$$

where  $g_i (i=1 \text{ to } n+1)$  stand for the normalized element values for the low-pass filter prototypes;  $(Q_e)_A$  and  $(Q_e)_B$  are the external  $Q$ 's for the input and output ports;  $k_{j,j+1} (j=1 \text{ to } n-1)$  are the coupling coefficients of the adjacent cavities;  $FBW$  stands for the fractional bandwidth.

From (2.7), it can be found that the bandwidth of our proposed QMSIW BPF is determined by the external quality factor and coupling coefficients. As shown in Figure 2.10, a single QMSIW cavity is modeled to determine the external  $Q$ -factor, and two coupled QMSIW cavities are modeled to determine the internal coupling. Both models are built up in Ansoft HFSS v10.1 and the external  $Q$ -factor and coupling coefficients are obtained from the simulated  $S$ -parameters. The dimension of the simulated QMSIW cavity is  $10 \times 10 \text{ mm}^2$  on the substrate RO6002 with thickness of 10 mil and dielectric constant of  $\epsilon_r = 2.94$ .

The central resonant frequency separates into two discrete ones as two SIW cavities are coupled with each other [26]. The coupling coefficient can be extracted by

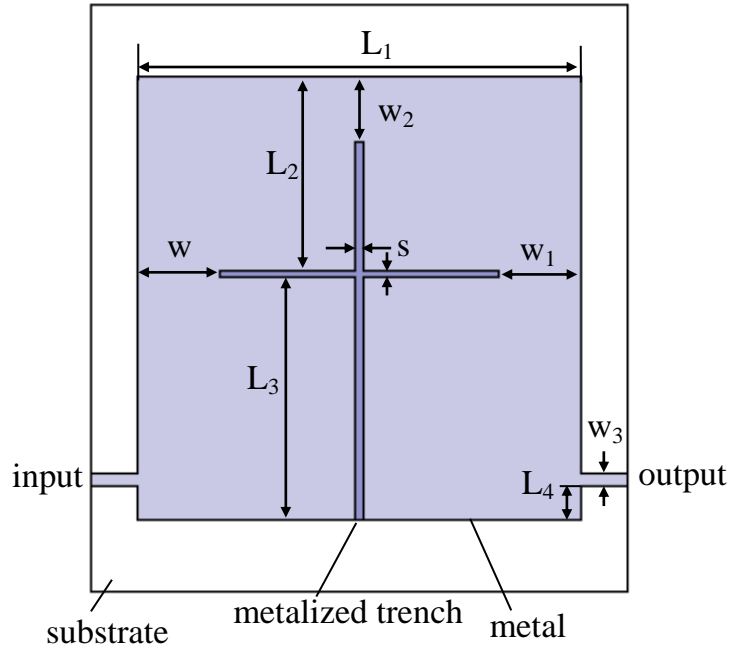
$$k = \frac{f_U^2 - f_L^2}{f_U^2 + f_L^2} \quad (2.8)$$

where  $f_U$  and  $f_L$  stand for the upper and lower resonant frequencies, respectively. In fact, a stronger coupling results in a wider separation of the two resonant peaks and a deeper trough in the middle.

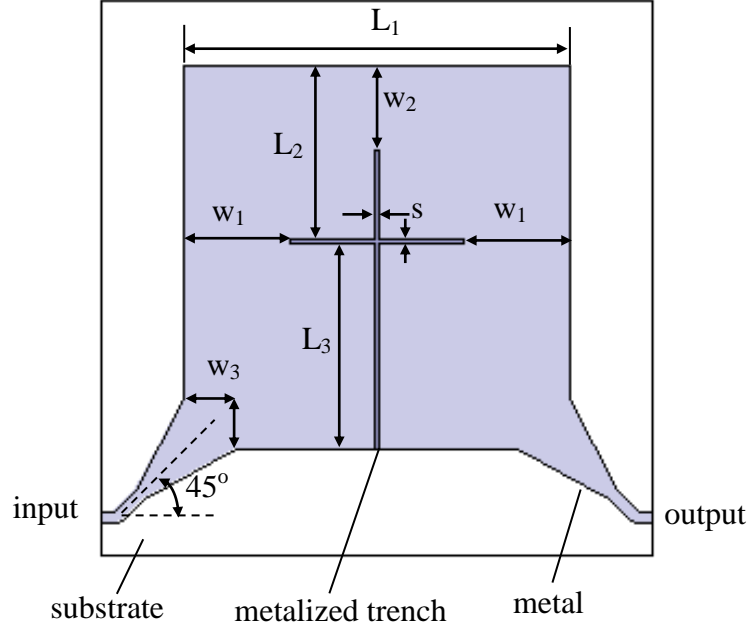
On the other hand, this external coupling factor  $Q_e$  can be extracted using simulated values of a single SIW cavity, that is

$$Q_e = \frac{2f_0}{\Delta f_{-3dB}} \quad (2.9)$$

Compared with the reported design parameters of SIWs [58], it can be found that the external quality factor of the proposed QMSIW structure is not as good as the original SIWs since the two open edges are subject to some amount of radiation. However, the internal coupling coefficient in our proposed QMSIW structure is much stronger than the conventional SIW. To demonstrate the design methodology and electrical performance, two experimental prototypes of the proposed QMSIW BPF are designed and fabricated over C band. The substrate used in our work is RO6002 with thickness of 10 mil and dielectric constant  $\epsilon_r = 2.94$ . Figure 2.11 shows the physical dimensions of the designed QMSIW planar BPFs. Both filters in Figure 2.11 follow the Chebyshev low pass filter (LPF) prototype design procedure with 0.1 dB passband ripple. The prototype I in Figure 2.11(a) is designed at center frequency of 5.85 GHz with a fractional bandwidth of around 14%. The prototype II in Figure 2.11(b) is designed at center frequency of 5.5 GHz with a fractional bandwidth of around 26%, which covers the license-exempt frequency band 5.25 GHz to 5.85 GHz for the interest of WiMAX. Table 2.1 gives the design parameters of these two experimental prototypes. The photograph of the fabricated experimental prototypes is shown in Figure 2.12.



(a)



(b)

Figure 2.11: Physical dimensions of two experimental prototypes of the proposed QMSIW BPFs. (a) Prototype I with 14% fractional bandwidth.  $w_1 = 3.57$  mm,  $w_2 = 2.86$  mm,  $w_3 = 0.6$  mm,  $L_1 = 19.22$  mm,  $L_2 = 8.4$  mm,  $L_3 = 10.5$  mm,  $L_4 = 1.42$  mm,  $s = 0.3$  mm. (b) Prototype II with 26% fractional bandwidth.  $w_1 = 5.09$  mm,  $w_2 = 4.15$  mm,  $w_3 = 2.47$  mm,  $L_1 = 18.64$  mm,  $L_2 = 8.4$  mm,  $L_3 = 9.93$  mm,  $s = 0.3$  mm.

Table 2.1: Design parameters of two experimental prototypes

Parameters No.	$FBW$	External $Q$ ( $Q_A$ , $Q_B$ )	$K_{12}$	$K_{23}$	$K_{34}$
Prototype I	14%	7.92	0.116	0.092	0.116
Prototype II	26%	4.265	0.216	0.171	0.216

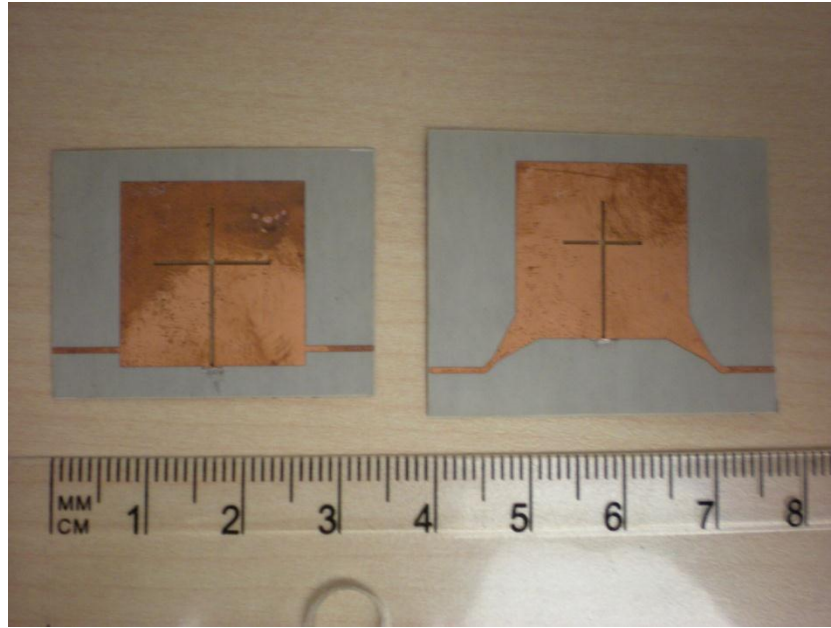
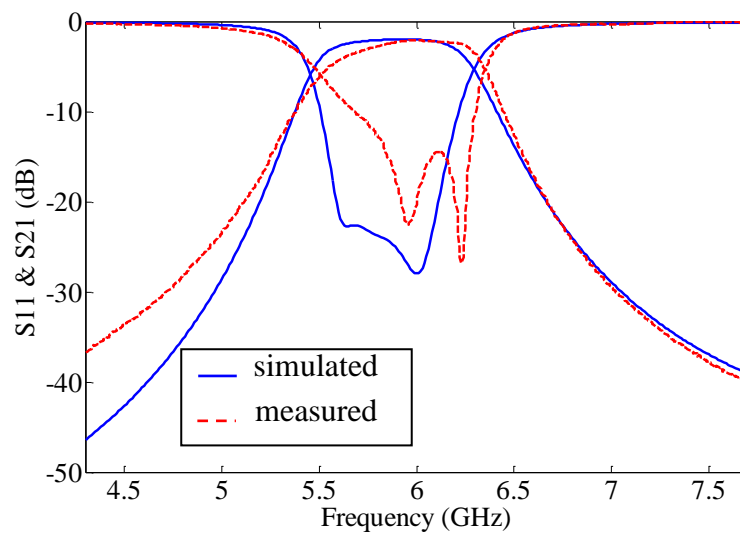


Figure 2.12: Photograph of the fabricated QMSIW filter prototypes

### 2.2.2 Result and Discussion



(a)



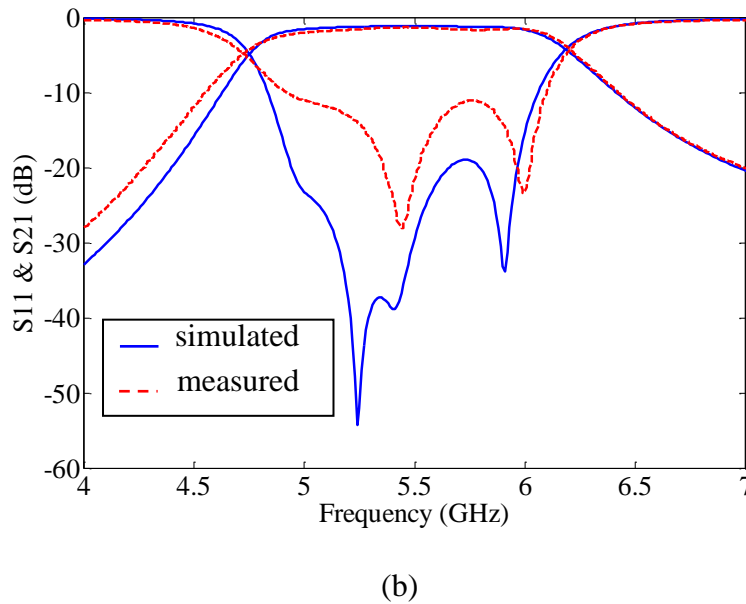


Figure 2.13: S-parameters of the proposed QMSIW filters: (a) Prototype I (b) Prototype II.

Figures 2.13(a)-2.13(b) display simulated and measured results for the S-parameter response of the proposed filters, in which the solid line stands for the simulated results and the dashed line stands for the measured results. The filters are simulated by using Ansoft HFSS v10.1. The measurements were carried out by using an Anritsu test fixture model 3680K and an HP8510C vector network analyzer. The calibration work was done by using a set of TRL calibration standards. It is observed that a reasonably good agreement is achieved between the measurements and the simulations. Discrepancy may mainly come from simulation errors of the numerical tool and/or fabrication tolerances. Measured results show that the insertion losses of the prototype I and prototype II filters are 2.0 dB and 1.2 dB, respectively. The measured input return losses of both cases are better than -13 dB across the band of interest. Figure 2.14 shows the group delay of the proposed filter prototypes. For both cases, the variation of the group time delay of the transmission path is smaller than 10% over 50% of the pass band around the central frequency.

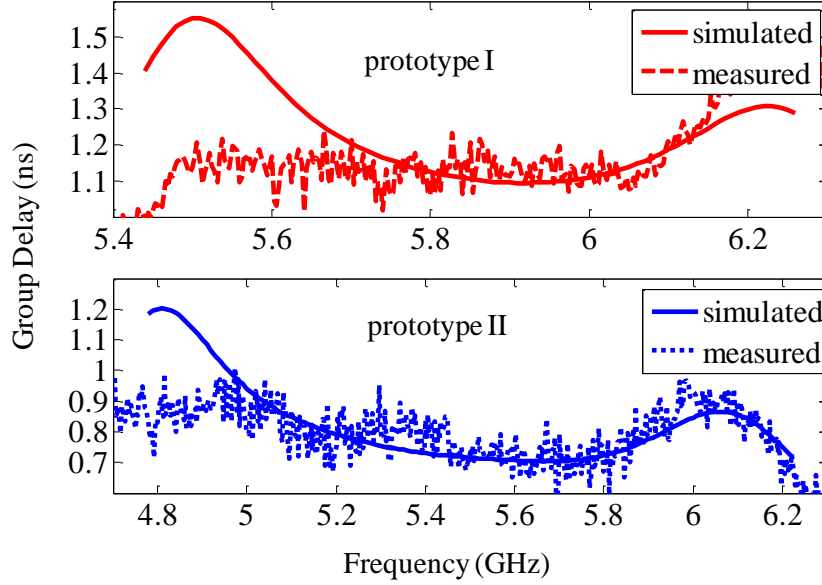


Figure 2.14: Group delay of the proposed QMSIW filters

The unloaded quality factor of our proposed QMSIW cavity is also extracted by using full-wave simulation software Ansoft HFSS v10.1. A  $10 \times 10 \text{ mm}^2$  QMSIW cavity on the substrate RO6002 with thickness of 0.254mm and dielectric constant of  $\epsilon_r = 2.94$ , which works at around 5.85 GHz, gives an unloaded  $Q_u$  value of 172.8. Here, the unloaded  $Q_u$  is extracted by using the formula:

$$Q_u = \frac{Q_L}{1 - |S_{21}|} \quad (2.10)$$

Under the same conditions, the  $Q_u$  of a  $14.8 \times 10.6 \text{ mm}^2$  half-wavelength microstrip line resonator is around 166.2. On the other hand, the size of our proposed prototypes is roughly  $0.5 \lambda_g \times 0.5 \lambda_g$ , while a fourth-order band-pass filter in microstrip line version almost occupies a double sized surface.

## 2.3 Conclusion

In this chapter, half and quarter mode techniques have been studied and applied in the SIW circuit designs to achieve smaller size occupation.

First of all, a broadband HMSIW Wilkinson power divider is proposed. This broadband H-plane power divider utilizes the half-mode structure of SIWs such that the overall size is largely reduced. In addition, the lossy network or resistor branch is successfully integrated with the SIW structure to guarantee good output matching and isolation. This is critical for power combining or non-equal power dividing with potentially poor output port matching. A simple design theory is presented by using the even-odd mode analysis technique. To demonstrate the design concept, an experimental prototype is designed and fabricated. The power divider structure is validated by both simulated and measured results.

Besides this, two QMSIW planar filters are also proposed and presented in this chapter. The filter is composed of cascading QMSIW cavities, which are magnetically coupled with the neighbourhood sections. The quarter-mode structure of SIWs makes the overall size largely reduced such that the proposed filter can be used in many wireless applications at low frequencies. To demonstrate the design concept, two experimental prototypes are fabricated. The merits of this type of filter are concluded by the fact that it has a very compact size for low frequency applications. In addition, the coupling coefficient between QMSIW cavities is much stronger than the original SIW counterparts. Therefore, the proposed filter can be used to design broadband bandpass filters. Also compared with other filters in the microstrip form, the proposed filter takes the advantages of planar structure form, low electromagnetic interference and cross-talk, no coupled line structures and easy fabrication.

### CHAPTER 3      DEVELOPMENT OF BROADBAND PHASE SHIFTER USING SLOTTED SIW STRUCTURE

Phase shifters are used to alter the transmission phase angle of a circuit or network [60]-[61]. They are key components extensively deployed in phased array antennas, electronic scanning radars, power amplifier phase-controlled compensation circuits and so on [62]-[63]. To achieve decent broadband performance, various microwave phase shifter structures that utilize the dispersive feature of rectangular waveguides, have already been proposed in [62]-[66]. Usually, there are two types of waveguide phase shifters depending on their structures: (a) waveguides partially filled with dielectric or ferrite slabs [62]-[64]; and (b) waveguides with inductive posts inserted inside [65]-[66]. For type (a), designers have to consider multimode propagation inside the waveguide. In this case, the design methodologies are very much more involved. Furthermore, those design concepts are hard to implement in the planar integrated circuits. This may prohibit their applications from many wireless communication systems. On the other hand, phase shifters of type (b) can easily be analyzed using circuit models and they are suitable for various fabrication processes. However, such structures fail to yield satisfactory broadband performance, e.g., over 20% fractional bandwidth.

Recently, Chen *et al.* [67] has introduced a new type of broadband phase shifter which is based on the SIW technique. In [67], the broadband SIW phase shifter is designed based on the dispersive nature of waveguides with different widths that result in different propagation constants. Unlike the TEM mode, the propagation constant of the  $TE_{10}$  mode is a nonlinear variable with frequency, as illustrated in Figure 3.1. Compared the  $TE_{10}$  modes of two SIWs with different widths (i.e.,  $SIW_1$  and  $SIW_2$  in Figure 3.1), it can be observed that the difference in their propagation constants does not change sharply with frequency. This perspective broadband feature can be exploited in the design of a broadband phase shifter.

In this chapter, a broadband phase shifter is proposed, which is based on a non-radiating slot structure in an SIW, namely slotted SIW for simplicity [68]. Various types of slots in waveguides have been well studied in previous work [69]-[71]. Nevertheless, most of those investigations focused on the radiation effects of these slots for the purpose of antenna designs. This chapter carries out an in-depth study on the non-radiating slotted SIW structure. Its transmission characteristics is examined and is further applied to our broadband phase shifter of interest. The

proposed structure consists of two identical longitudinal slots which are placed symmetrically on different sides along the midline on the broad wall of an SIW. Compared with microstrip lines with the same widths, the attenuation of the proposed structure is smaller and in fact negligible. The fundamental mode of the proposed slotted SIW line is a quasi-TEM mode instead of  $TE_{10}$  and its dispersive properties are then used to design a broadband phase shifter (see Figure 3.1).

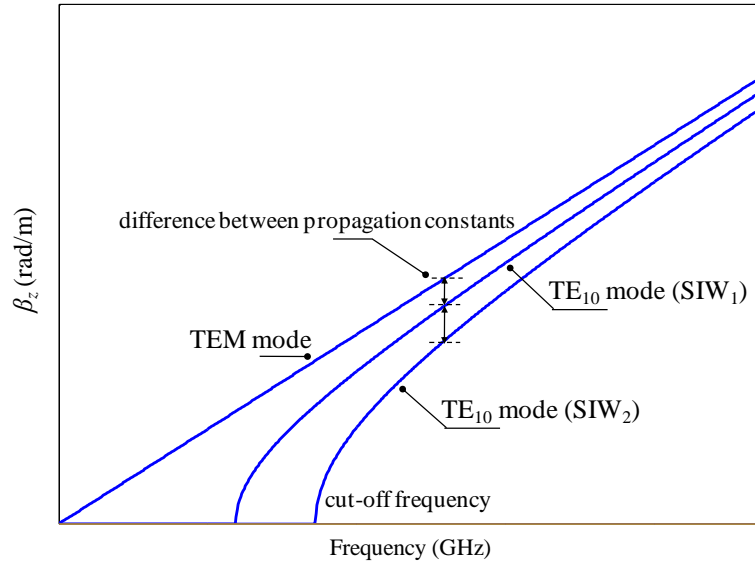


Figure 3.1: Propagation constants of different modes

Compared to the previously reported structures [60]-[67], our proposed phase shifter shows its great advantages of broader bandwidth, smaller insertion loss, lower profile and easier integration in SIW circuits. Therefore, it can easily be used at millimeter-wave frequencies, and also its structure is favourable to the microwave integrated circuit applications. To demonstrate the design methodology and structural features, the design theory and procedure are studied and discussed in detail. In particular, a K-band experimental prototype of the proposed phase shifter is shown. This new design is validated by both theoretical analysis and experimental results.

### 3.1 Longitudinal Slotted SIW Transmission Line

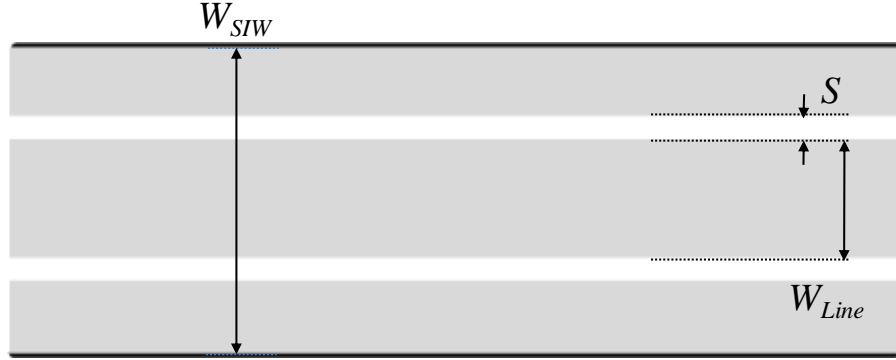


Figure 3.2: Longitudinal slotted SIW transmission line

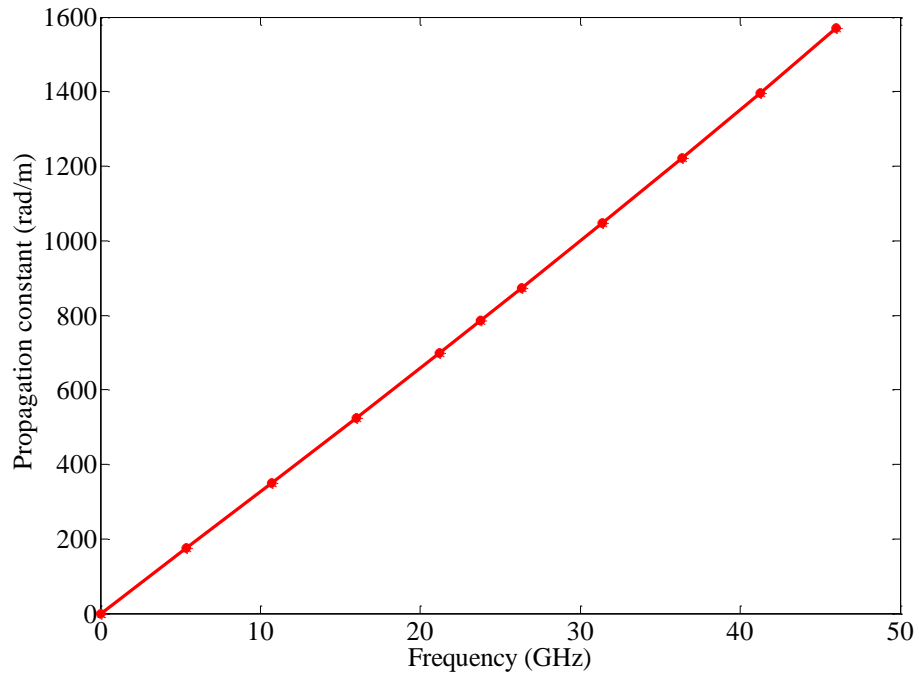


Figure 3.3: Simulated propagation constant of the dominant mode of the proposed slotted SIW line ( $W_{SIW} = 4.8$  mm,  $W_{Line} = 1.2$  mm and  $S = 0.24$  mm).

The so-called longitudinal slotted SIW transmission line, as shown in Figure 3.2, is somewhat similar to a grounded CPW structure. With the aid of commercial full-wave simulation software

Ansoft HFSS v11.1 and CST Microwave Studio 2009, the transmission modes of the longitudinal slotted SIW are investigated. The substrate used in this work is RT6002 from Rogers with thickness of 0.254 mm. The geometry of the proposed slotted SIW line is characterized by  $W_{SIW} = 4.8$  mm,  $W_{Line} = 1.2$  mm and  $S = 0.24$  mm. Figure 3.3 shows simulated propagation constant curve of the dominant mode. It can be found that the propagation constant of the dominant mode is approximately linear with frequency. Of course, this mode can be assumed as a quasi-TEM mode, which is consistent with the grounded CPW structure. To confirm this assumption, the dominant mode of our proposed structure is compared with the grounded CPW mode, which is analyzed by moving the SIW's sidewalls close enough together so that the second higher mode cannot be supported. In Figure 3.4, it can be found that the phase constant of this dominant mode (normal mode 1) makes an excellent agreement with that of the isolated grounded CPW mode.

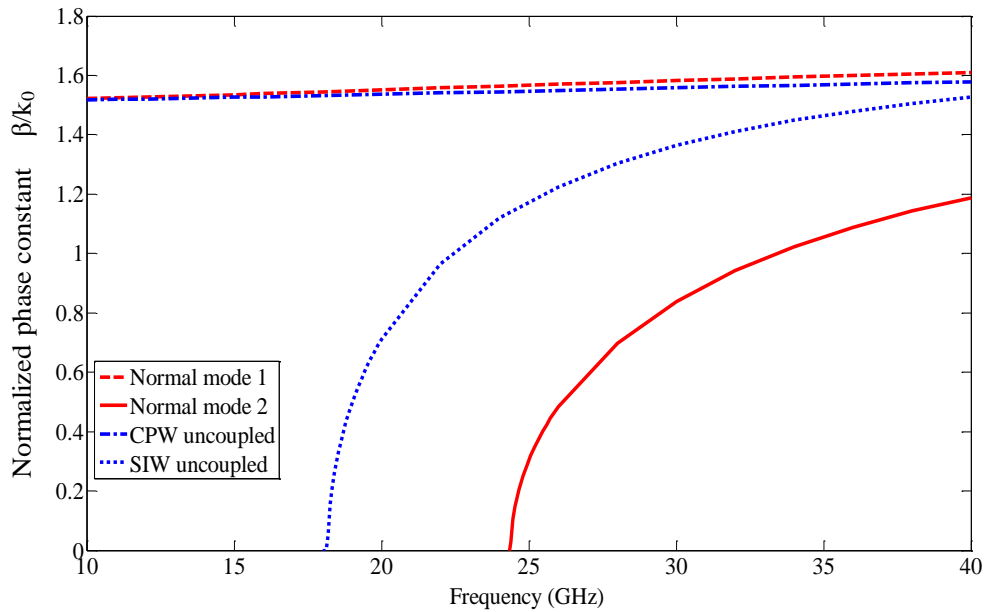


Figure 3.4: Phase constants of the normal modes in the slotted SIW structure and of the isolated CPW and SIW modes

The transverse electric field of the dominant mode is displayed at various frequencies in Figure 3.5 and the examined range is sufficiently broad to cover our frequency of interest. Once again, the electric field reveals that the dominant mode is essentially a grounded CPW mode.

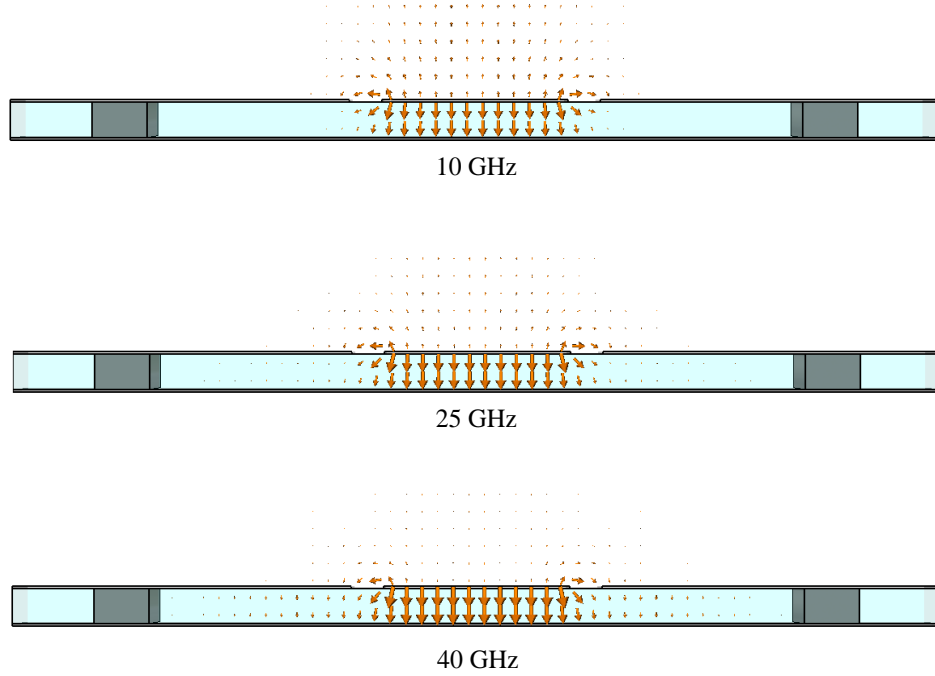


Figure 3.5: Transverse electric field of the first normal mode at various frequencies

It was mentioned in [68] that this slotted SIW transmission line can also support waveguide modes. As a matter of fact, the second mode in this structure is observed as a half-mode SIW since its cutoff frequency increases when  $W_{Line}$  (see Figure 3.2) increases. As shown in Figure 3.4, the cutoff frequency of the second mode is clearly distinct from the SIW mode, which is analyzed by removing the slots in our structure. The transverse electric field of the second mode in Figure 3.6 can further verify our statement. It should also be noted that this second mode can be avoided by the excitation approach in our case since the excited energy is along the central line.

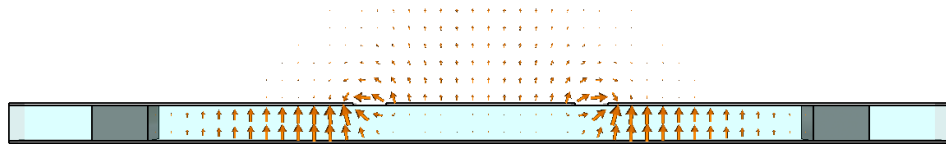


Figure 3.6: Transverse electric field of the second normal mode at 40 GHz



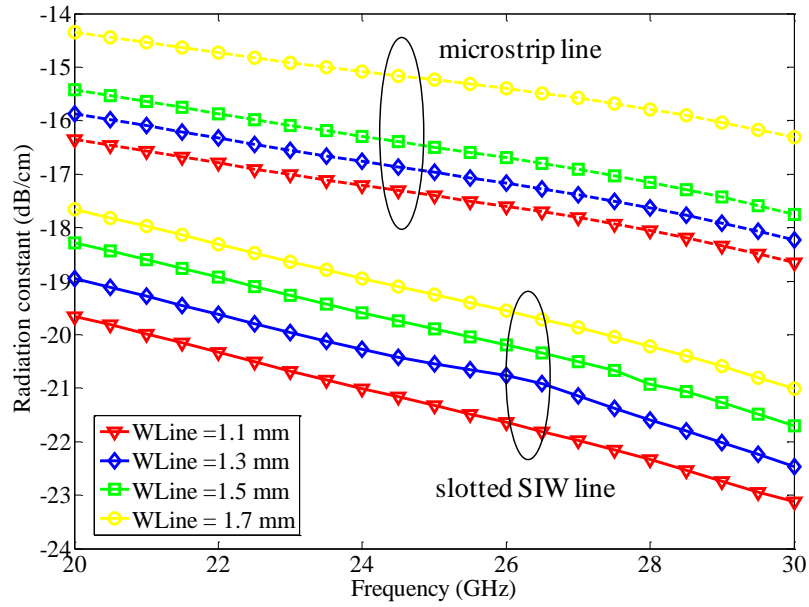


Figure 3.7: Comparison of the attenuation between the slotted SIW lines and microstrip lines.

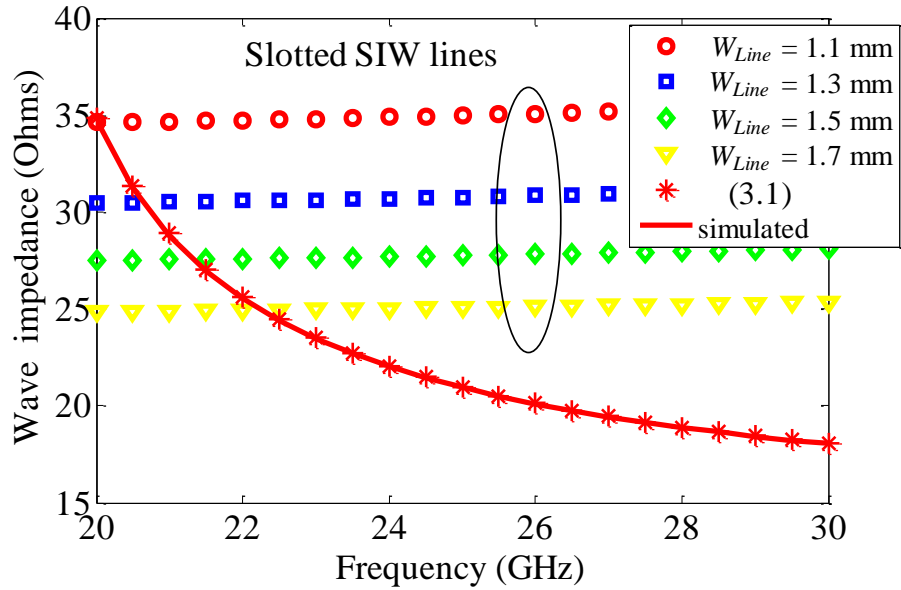


Figure 3.8: Comparison of wave impedances between the slotted SIW lines with different widths  $W_{Line}$  (see Figure 3.2) and the SIW line.

Another important factor, the attenuation of the transmission line, which includes conductor loss, dielectric loss and radiation loss, is also examined. The attenuation of the transmission line can be defined as  $1-|S_{11}|^2-|S_{21}|^2$  and it can be extracted with the aid of HFSS. Figure 3.7 compares the attenuation between the slotted SIW lines and microstrip lines with respect to different line widths  $W_{Line}$  (see Figure 3.2). It can be seen that the proposed slotted SIW line is superior to the typical microstrip line for millimeter-wave applications.

The wave impedance of the SIW follows the power-current definition of impedance for TE<sub>10</sub> wave in a rectangular waveguide [72], which is given by,

$$Z_g = \frac{465 \frac{b}{a} \sqrt{\frac{\mu_R}{\epsilon_R}}}{\sqrt{1 - \left(\frac{f_c}{f}\right)^2}} \quad (3.1)$$

where  $a$  and  $b$  are the interior dimensions of the SIW, and  $f_c$  stands for the cutoff frequency. As shown in Figure 3.8, simulated wave impedances agree well with values calculated by (3.1). In addition, it can be found that the impedance of a wider slotted SIW line  $W_{Line}$  (see Figure 3.2) better fits with the wave impedance of the TE<sub>10</sub> mode in the SIW. For this reason, the slotted SIW-to-SIW transition is designed in a tapered form as shown in Figure 3.9.

### 3.2 Slotted SIW-to-SIW Transition and Parameter Extraction

Figure 3.9 also illustrates the equivalent circuit of the transition between the SIW and slotted SIW sections. The tapered line is simply made in the form of a 90 degree arc. The transition can be represented by a T-type network. The real parts of the series and shunt impedances can be ignored since the very small-sectioned network is assumed to be lossless.

The values of the series and shunt reactance, i.e.,  $X_1$ ,  $X_2$  and  $X_3$ , can be acquired with the aid of HFSS. The substrate considered here is RT6002 with thickness of 0.254 mm and dielectric constant  $\epsilon_r = 2.94$ . The procedures are given as follows: First, the overall structure of the slotted SIW-to-SIW transition (see Figure 3.9) is simulated. Second, S-parameters of the transition can be extracted after numerically de-embedding the transmission lines between the reference ports and the transition. To do this, S-parameters can be converted to T-parameters for the purpose of

handy matrix calculations [72]. Finally, the equivalent circuit parameters (i.e.,  $X_1$ ,  $X_2$  and  $X_3$ ) can easily be obtained from the de-embedded Z-parameters of the transition based on (3.2).

$$\mathbf{Z} = \begin{bmatrix} j(X_2 + X_1) & jX_2 \\ jX_2 & j(X_2 + X_3) \end{bmatrix} \quad (3.2)$$

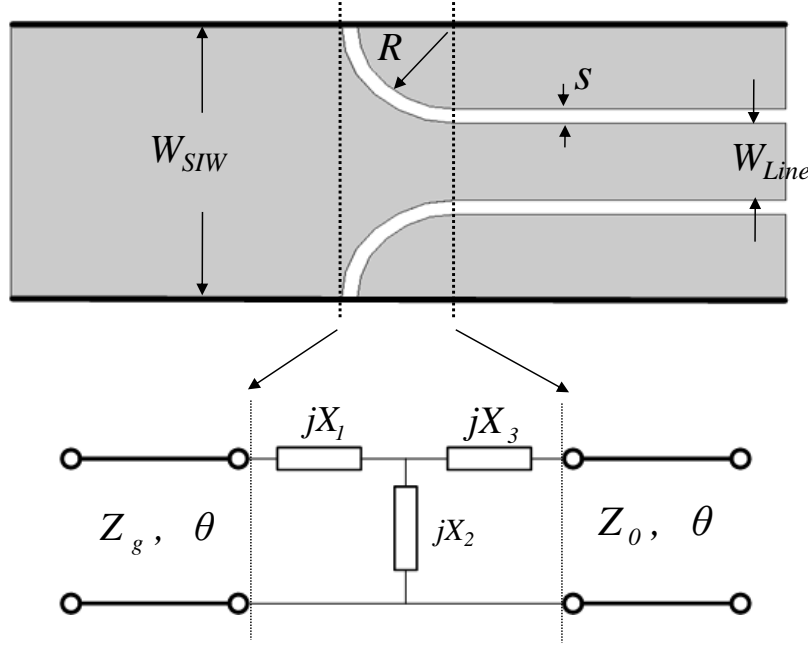


Figure 3.9: Slotted SIW-to-SIW transition and its equivalent circuit.

Figure 3.10 plots the de-embedded S-parameters of the transition obtained from the above procedures. Referring to Figure 3.9, the geometry of the proposed transition is characterized by  $W_{SIW} = 4.8$  mm,  $W_{Line} = 1.2$  mm,  $R = 1.56$  mm and  $S = 0.24$  mm. It can be observed that the proposed transition has fairly good insertion loss and return loss. The dips of the S-parameters at around 28 GHz are mainly attributed to the discontinuities of the proposed transition. Moreover, Figure 3.11 shows the extracted values of the series and shunt reactance. According to the values of  $X_1$ ,  $X_2$  and  $X_3$ , the lumped-element equivalent circuit of the proposed transition is similar to the T-network model of a typical transmission line.

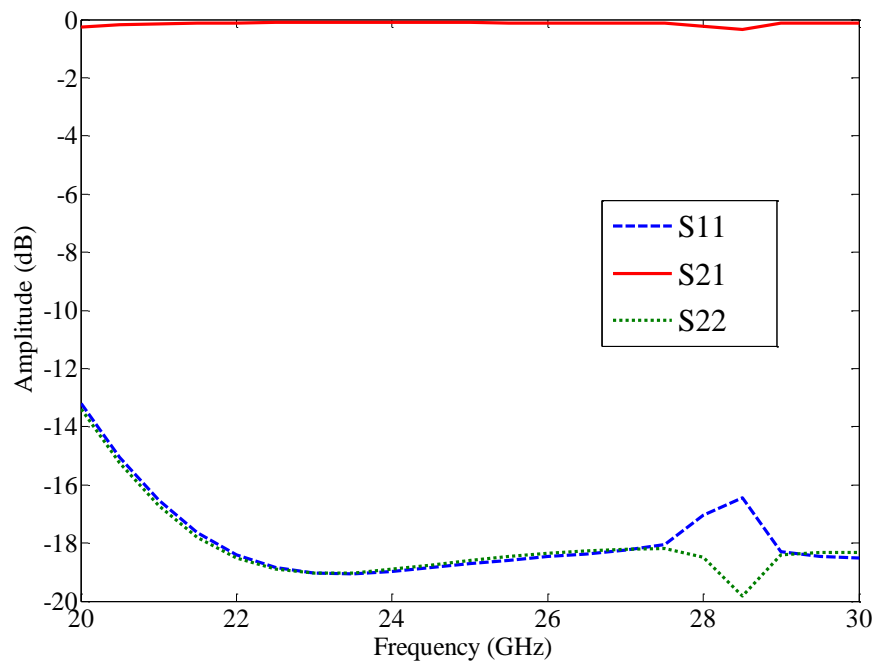


Figure 3.10: De-embedded S-parameters of the transition ( $W_{SIW} = 4.8$  mm,  $W_{Line} = 1.36$  mm,  $R = 1.48$  mm and  $S = 0.24$  mm).

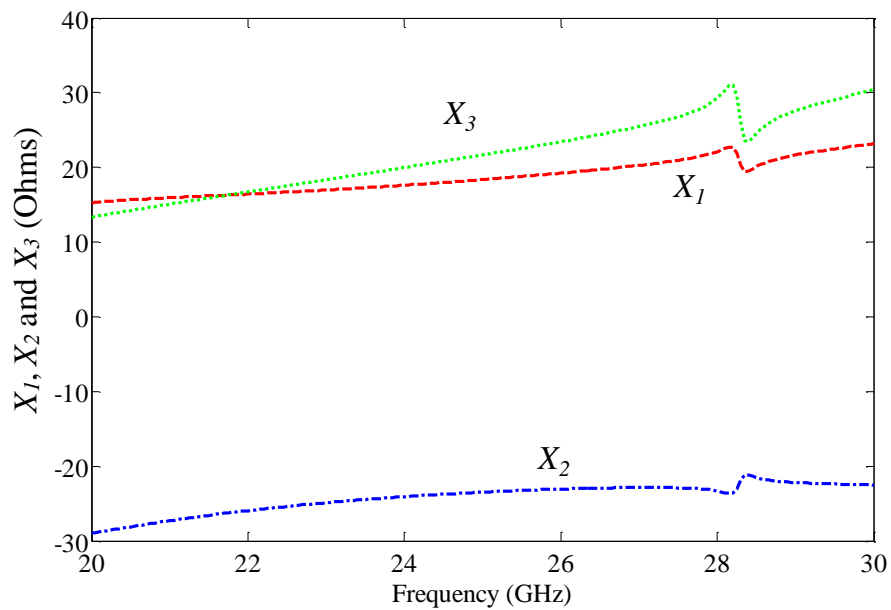


Figure 3.11: Extracted values of  $X_1$ ,  $X_3$  and  $X_2$ .

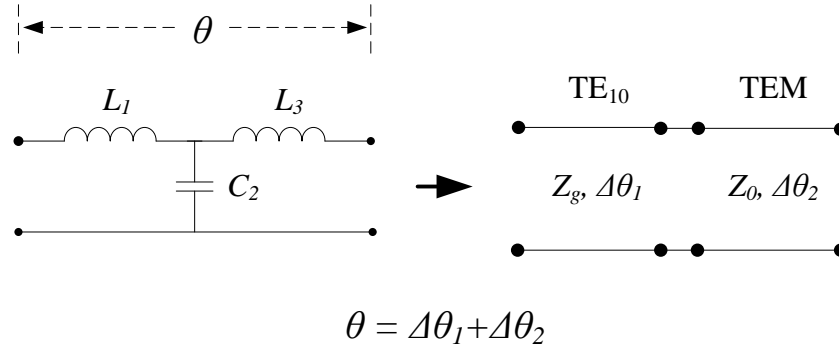


Figure 3.12: Lumped-element equivalent circuit and the composed line model of the proposed transition.

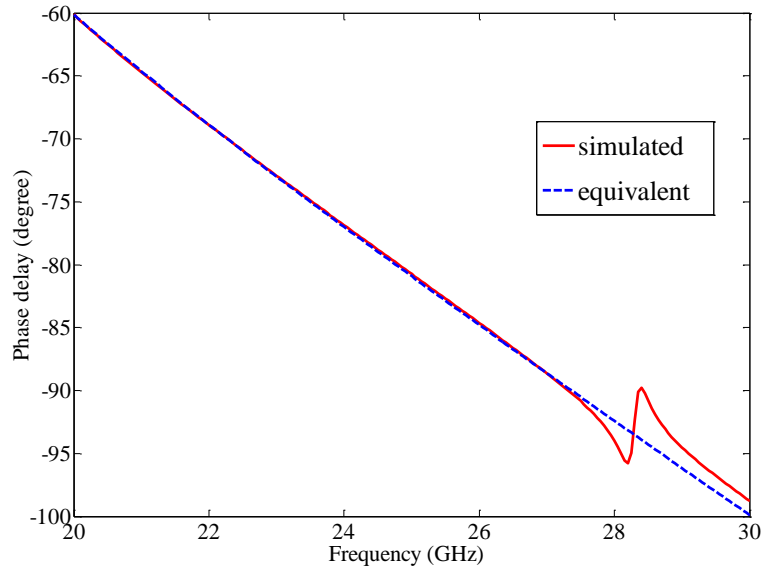


Figure 3.13: Comparison of the simulated phase delay and the phase delay of the composed line model.

In order to model the phase delay, the transition can further be considered as a small section of rectangular waveguide line cascaded with another small section of quasi-TEM line, as shown in Figure 3.12. It is well known that the propagation constants of waveguide  $TE_{10}$  mode and quasi-

TEM mode are  $\beta_{TE_{10}} = \sqrt{\omega^2 \mu \epsilon - (\frac{\pi}{a})^2}$  and  $\beta_{TEM} = \sqrt{\omega^2 \mu \epsilon}$ , respectively. Figure 3.13 compares the simulated phase delay and phase delay of the composed line model. In this figure, the solid line stands for the phase delay of the transition simulated by HFSS, and the dash line stands for the phase delay calculated from a model which consists of a section of  $TE_{10}$  mode waveguide transmission line and a section of TEM mode transmission line. It is shown that these two curves are well matched.

### 3.3 Theoretical Analysis and Design Technique of Broadband Slotted SIW Phase Shifter

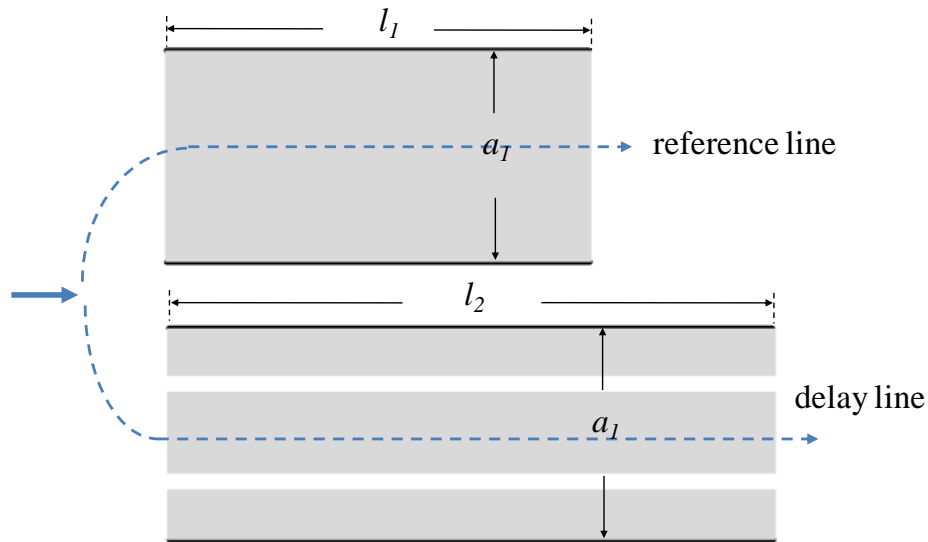


Figure 3.14: The proposed slotted SIW and the conventional SIW

Figure 3.14 shows a section of the proposed slotted SIW and the conventional SIW. The conventional SIW works as a reference line and the phase difference between these two lines is given by

$$\Phi_{diff} = \sqrt{\omega^2 \mu \epsilon_{eff}} \cdot l_2 - \sqrt{\omega^2 \mu \epsilon - (\frac{\pi}{a_1})^2} \cdot l_1 \quad (3.3)$$

where  $a_1$  denotes the width of the SIW sections,  $\epsilon_{eff}$  and  $\epsilon$  are the effective dielectric constant of the slotted SIW line and the dielectric constant of the SIW, respectively. A curve of  $\phi_{diff}$  versus

frequency is plotted in Figure 3.15, from which it can be found that there is a minimum value that occurs at the frequency point:

$$f_c = \frac{1}{2} \sqrt{\frac{l_2^2 \cdot \epsilon_{eff}}{\mu \epsilon (l_2^2 \cdot \epsilon_{eff} - l_1^2 \cdot \epsilon) a_1^2}} \quad (3.4a)$$

Since the slope of phase difference  $\phi_{fc}$  changes very slowly near frequency  $f_c$ , a broadband phase shifter can be designed by setting  $f_c$  as the operation frequency of interest. At this special frequency point  $f_c$ , the phase difference between the two different paths can be further obtained by

$$\Phi_{fc} = \pi \sqrt{\frac{\epsilon_{eff} \cdot l_2^2 - \epsilon \cdot l_1^2}{\epsilon \cdot a_1^2}} \quad (3.4b)$$

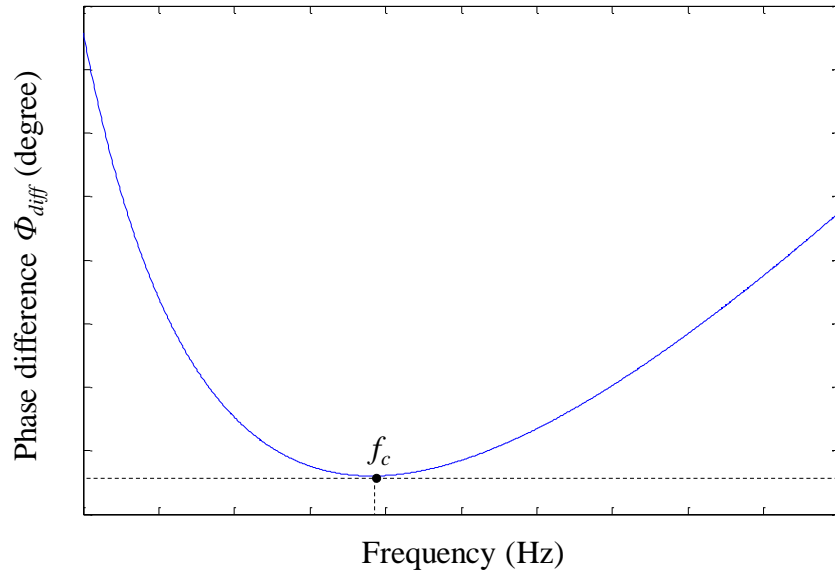


Figure 3.15: Phase difference  $\phi_{diff}$  versus frequency according to (3.3)

Effective dielectric constant  $\epsilon_{eff}$  is determined by the dielectric constant of the substrate and the geometries of the slotted SIW line. Figure 3.16 shows a relationship between effective dielectric constant  $\epsilon_{eff}$  and slot line width  $W_{Line}$ , when the width of SIW  $W_{SIW} = 4.8$  mm and slot gap  $s = 0.24$  mm.

Our proposed broadband phase shifter is designed based on (3.4a) and (3.4b). Given desired phase difference  $\phi_{fc}$ , operation frequency  $f_c$  and SIW line width  $a_1$ , the length of reference line  $l_1$  and the length of delay line  $l_2$  can be calculated. In [67], two design equations, (3.5a) and (3.5b), can easily be derived from the method proposed in this chapter, where  $a_1$  and  $a_2$  represent different widths of two SIWs.

$$f_c = \frac{1}{2} \sqrt{\frac{(l_2^2 \cdot a_2^2 - l_1^2 \cdot a_1^2)}{\mu\epsilon \cdot (l_2^2 - l_1^2) \cdot a_1^2 \cdot a_2^2}} \quad (3.5a)$$

$$\Phi_{fc} = \sqrt{\frac{\pi^2 (a_2^2 - a_1^2) \cdot (l_2^2 - l_1^2)}{a_1^2 \cdot a_2^2}} \quad (3.5b)$$

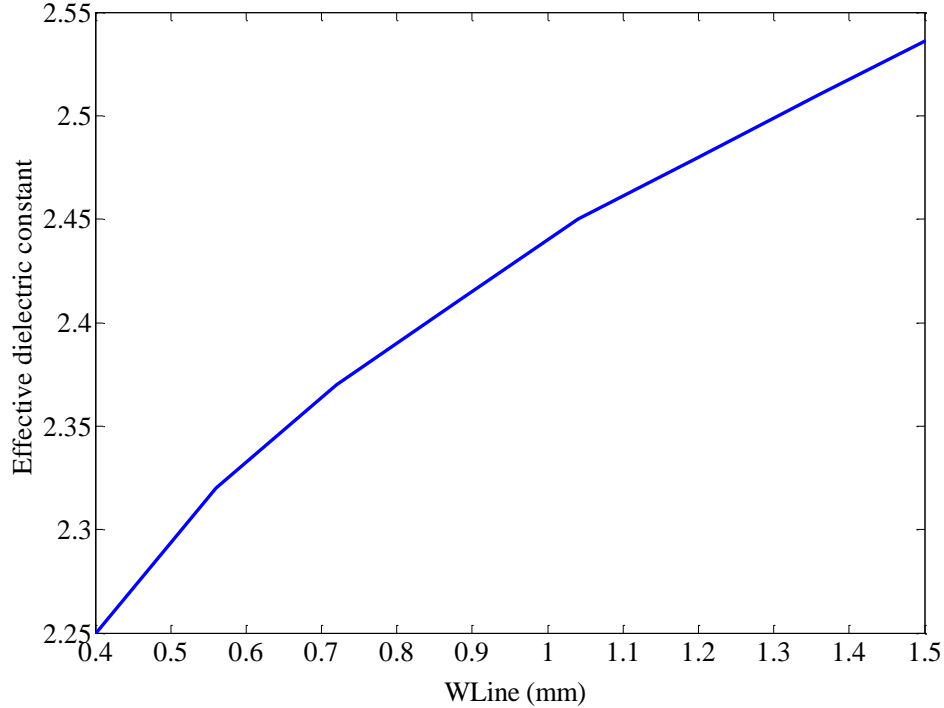


Figure 3.16: Relationship between effective dielectric constant  $\epsilon_{eff}$  and the slot line width  $W_{Line}$ .

Compared to [67], our proposed method has two significant advantages: 1) the overall size of the reference and delay lines is greatly reduced to achieve a certain degree of phase shift. Table 3.1 compares the physical dimensions of 24 GHz 90° phase shifters designed by these two methods. Both designs make use of the same PCB substrate of RT6002 with thickness of 0.254 mm and  $\epsilon_r$



$= 2.94$ . Our proposed broadband phase shifter is designed with the slot gap  $s = 0.24$  mm and the slot line width  $W_{Line} = 1.36$  mm. The effective dielectric constant is found to be 2.51. It is obvious that the length of our proposed circuit is much shorter than that presented in [67]; 2) our proposed method makes use of the SIWs with the same width. Since the phase shifter in [67] has to use two SIWs with different widths, discontinuities may pose a problem when the phase shifter is connected with other parts of SIW circuits.

Table 3.1: Physical dimensions of 24 GHz 90° phase shifters designed by two different methods

90-degree phase shifter	$a_1$ (mm)	$a_2$ (mm)	$l_1$ (mm)	$l_2$ (mm)
proposed	4.8	4.8	2.06	3.423
[67]	4.8	5.8	6.536	7.81

Furthermore, to make an investigation of the bandwidth performance, our proposed phase shifter is theoretically compared with some of the well-known approaches including a 90-degree meandered microstrip line, a 90-degree SIW line and the 90-degree phase shifter based on [67]. The bandwidth performance largely depends on the properties of the substrate. Therefore, all the counterparts are designed on the same PCB substrate of RT6002 with thickness of 0.254 mm and  $\epsilon_r = 2.94$  and at the central frequency of 24 GHz. As has been mentioned above, the phase delay of our proposed phase shifter can be obtained from (3.3). For the 90-degree meandered microstrip line, the 90-degree SIW line and the phase shifter proposed in [67], the phase delays can be expressed with the following equations.

$$\Phi_{diff\_ustrip} = \sqrt{\omega^2 \mu \epsilon_{eff}} \cdot l_{ustrip} (\lambda/4) \quad (3.6)$$

$$\Phi_{diff\_SIW} = \sqrt{\omega^2 \mu \epsilon - \left(\frac{\pi}{a_1}\right)^2} \cdot l_{SIW} (\lambda/4) \quad (3.7)$$

$$\Phi_{diff\_ [67]} = \sqrt{\omega^2 \mu \epsilon - \left(\frac{\pi}{a_2}\right)^2} \cdot l_2 - \sqrt{\omega^2 \mu \epsilon - \left(\frac{\pi}{a_1}\right)^2} \cdot l_1 \quad (3.8)$$

The width of 50 Ohm microstrip line on the specified substrate is about 0.6 mm. The corresponding effective dielectric constant  $\epsilon_{eff}$  is found to be around 2.34. The quarter wavelength

of the microstrip line is 2.04 mm. For the 90-degree SIW delay line, the width is set to be 4.8 mm for the operation frequency of 24 GHz. The quarter guide wavelength is about 2.8 mm. The geometries of our proposed phase shifter and that based on [67] is the same as given in Table 3.1. The comparison of the phase delays by using the different approaches mentioned above is plotted in Figure 3.17. It can be found that our proposed approach is able to provide the broadest bandwidth with a specified phase tolerance ( $5^\circ$  in Figure 3.17).

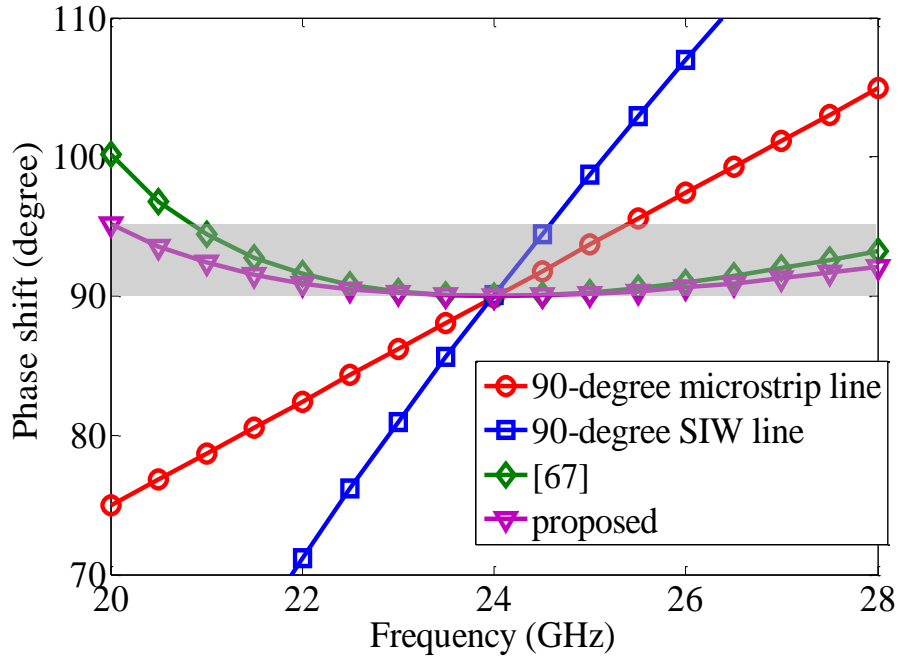
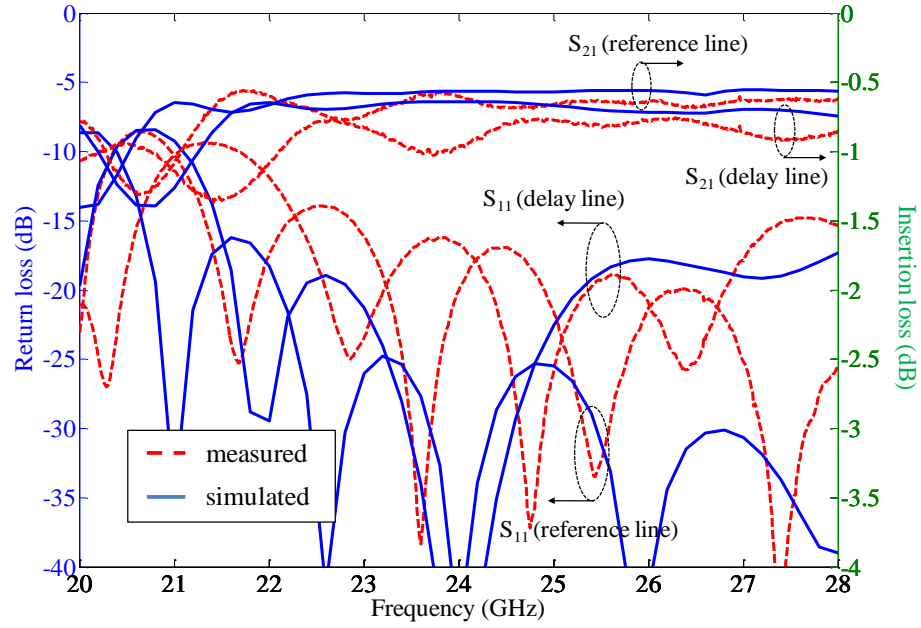


Figure 3.17: Comparison of the phase delays by using different approaches

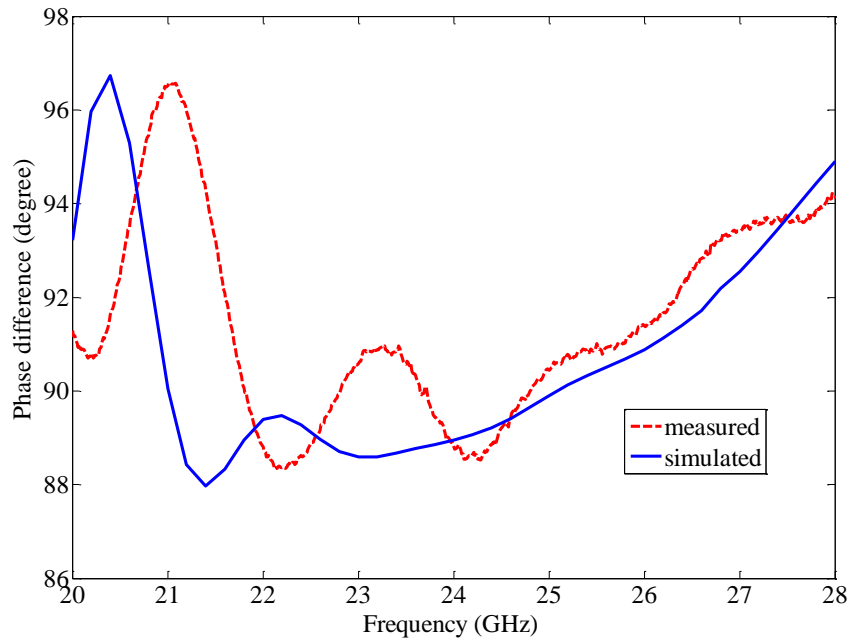
A 90 degree phase shifter is designed to verify the design methodology and electrical performance. Again, the experimental prototype is fabricated on the substrate RT6002 with thickness of 0.254 mm and  $\epsilon_r = 2.94$ . Figure 3.18 illustrates the physical dimensions of the designed broadband 90 degree phase shifter. A microstrip line feeder is used in our design for the convenience of measurements. In Figure 3.18, the phase shifter is embedded in the SIW structure, and both of the sections are 4.8 mm in width. The delay line section is shaped into a meandered form to make the lengths of the two lines equal.



performance of our proposed phase shifters would be better than the present measured results since the microstrip-to-SIW transitions used in our test slightly degrade the performance.



(a)



(b)

Figure 3.19: Measured and simulated S-parameters of the 90 degree prototype: (a) amplitude responses (b) phase responses

### 3.5 Conclusion

A novel broadband slotted SIW phase shifter has been presented and demonstrated in this chapter. The proposed SIW based phase shifter makes use of non-radiating longitudinal slots in the broad wall of SIW structures. Our design is based on the specific dispersive nature of the  $TE_{10}$  mode and quasi-TEM mode. The phase shifter structure has been verified by both theoretical analysis and experimental results. The principal merits of the proposed phase shifter can be concluded that the circuit size is significantly reduced compared with the previously reported method and it can easily operate at millimetre wave frequencies with a low profile and low loss structure. Furthermore, the resulting simple structure and monomode propagation inside the proposed slotted SIW are straightforward to microwave engineers for their design. With very broadband and low loss features, it can be anticipated that the proposed phase shifter will have a wide range of RF and millimeter-wave applications.

## CHAPTER 4      A MILLIMETER-WAVE SUB-HARMONIC SELF-OSCILLATING MIXER USING DUAL-MODE SIW CAVITY

The development of compact and low-cost millimeter-wave modules is critical for millimeter-wave wireless systems. With the consideration of the effectiveness and cost of generating a high frequency signal, the self-oscillating mixer (SOM) architecture presents an outstanding choice, which has been popularly used in designing wireless systems such as radio, radar and imaging applications. An SOM circuit simultaneously provides both oscillating and mixing functions within a single block [73]–[77]. In addition, a harmonic of the LO frequency can be used to lower the LO frequency requirement.

This chapter presents a novel structure of the second harmonic SOM which is integrated with a narrow bandwidth BPF by using SIW technique. The proposed sub-harmonic SOM employs a single FET transistor of common source configuration. The input RF signal passes through the BPF to filter out the noise before entering the SOM module. In our circuit design consideration, a narrowband SIW BPF is required to achieve a good RF-LO isolation between closely spaced frequencies. Typically, BPFs in the microstrip form can hardly achieve a narrow bandwidth less than 5% with reasonably good in- and out-band performances. In our work, the high-Q property of SIW cavities is utilized to design narrow bandwidth BPFs. The design concept is based on the transmission characteristics of two different transmission modes in an SIW cavity. That is, the fundamental mode and higher-order modes can co-exist in a single SIW cavity without interference. The SOM circuit utilizes the fundamental mode ( $H_{101}$ ) of the SIW cavity for RF mode and the  $H_{202}$  mode for LO mode.

### 4.1 Structure Description of the Proposed SOM

Figure 4.1 illustrates the basic design configuration of our proposed SOM circuitry. In our design, the input RF signal first passes through a BPF module which consists of four SIW cavities. For the first three orders of the BPF, the fundamental mode ( $H_{101}$ ) of the SIW cavity is used at RF frequency. The fourth SIW cavity is designed so to choose  $H_{202}$  mode for RF mode while the fundamental mode of this cavity is used to generate a negative resistance for oscillation conditions at the oscillating frequency. From a system point of view, our proposed design can be

integrated directly with an antenna to build up a very compact receiver front-end of a millimeter-wave system.

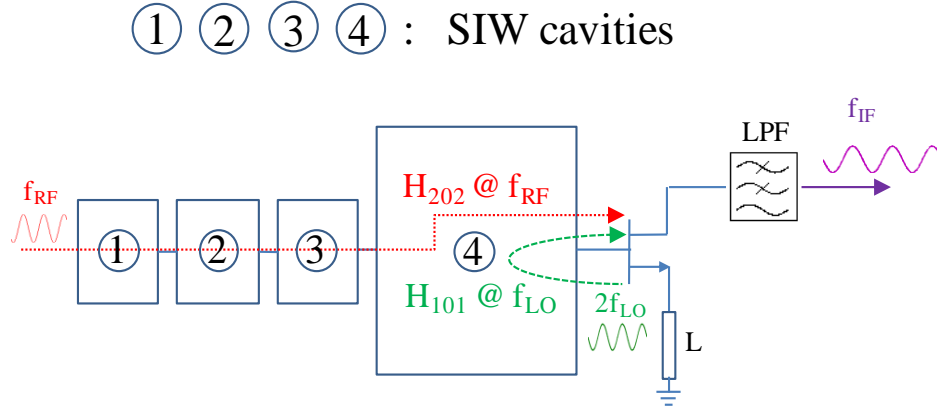
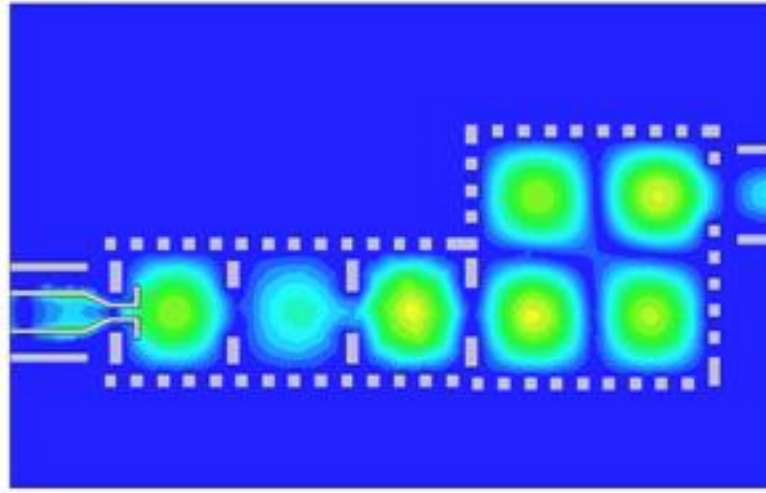


Figure 4.1: Basic design configuration of the proposed SIW SOM

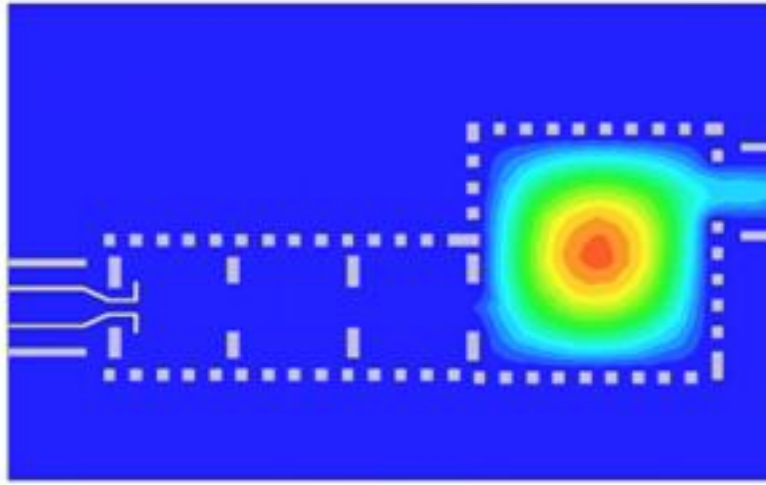
To demonstrate the design methodology and structural features, a K<sub>a</sub>-band prototype of the proposed SOM circuit concept is presented due to the limitations of our PCB fabrication process and the surface mounted FET transistor. It is well known that in an amplifier circuit, as the operation frequency of transistors increases, the available effective gain per transistor decreases. The proposed new design is then validated by simulated and measured results. It is worthwhile mentioning that the proposed design concept exhibits more advantageous features over higher millimeter-wave bands.

## 4.2 Dual-Mode SIW Band-Pass Filter

It has been known that the SIW narrow-band band-pass filters take the advantages of low insertion loss, sharp selectivity, compact size and low cost, which are extremely useful for millimeter-wave applications [24]–[30]. In this part, a dual-mode SIW BPF is designed to accommodate two operating functions in a simultaneous way. The LO mode employs the  $H_{101}$  mode of the fourth SIW cavity, while the RF mode utilizes the  $H_{202}$  mode, as shown in Figure 4.2.



(a) RF mode



(b) LO mode

Figure 4.2: Two orthogonal transmission modes in the proposed BPF circuit

#### 4.2.1 RF Mode

As mentioned above, the RF mode of our circuit is used for the narrow band BPF design. The design procedure of SIW BPFs based on the external quality factor and coupling coefficients for  $n$ -pole SIW band-pass filters was discussed earlier in Chapter 2.



To demonstrate our design concept, an experimental prototype of the proposed dual-mode SIW BPF is designed. The center RF frequency of the experimental prototype is around 34 GHz and the bandwidth is about 700 MHz. The designed SIW BPF follows a typical Chebyshev LPF prototype design procedure with 0.1 dB passband ripple. Figure 4.3 shows the physical dimensions of our circuit. A broadside coupled microstrip capacitor which is used as a DC-block is included in Figure 4.3. Both RF and LO signals need to pass through this capacitor. In this design, the synthesis of bilateral metallic walls is made with periodic metallised trenches in the dielectric substrate, which does not allow the guidance of TM modes. The substrate used is RT6002 with dielectric constant of 2.94 and thickness of 0.508 mm. For the design and fabrication considerations, the width of each metallised trench is set to be 0.4 mm which is smaller than a tenth of the wavelength of the maximum frequency of operation and also it can guarantee a good metallization of these trenches during the prototype processing. In the meanwhile, the spacing between metallised trenches is also set to be 0.4 mm to avoid any potential leakage [20]. The design procedures of our proposed SIW band-pass filter can be described as follows:

First of all, the size of each SIW cavity needs to be determined. Just like a traditional rectangular cavity, the size of an SIW cavity is estimated by using the following well known equation:

$$(f_r)_{mnp}^{TE} = \frac{1}{2\sqrt{\mu\epsilon}} \sqrt{\left(\frac{m}{w_e}\right)^2 + \left(\frac{n}{t_e}\right)^2 + \left(\frac{p}{l_e}\right)^2} \quad (4.1)$$

where  $w_e$ ,  $t_e$  and  $l_e$  stand for the effective width, thickness and length of the SIW cavity, respectively. Once the resonant frequency is chosen, the dimension of each SIW cavity,  $w_e$  and  $l_e$ , can be determined.

Second, based on the coupling coefficients calculated from (2.7), the width of the window between two neighbourhood sections can be determined. The bigger the window is, the stronger the coupling between two SIW cavities will be and vice versa.

Third, the external quality factors are mainly determined by the geometries and forms of the loads. As can be found in Figure 4.3, two different loading methods are used in our design as our circuit structure is not symmetric at input and output ports.



The design procedure can be summarized as follows:

1) Calculate the impedance inverter values by using

$$\begin{aligned} \frac{K_{01}}{Z_0} &= \sqrt{\frac{\pi}{2} \frac{\omega_\lambda}{g_0 g_1 \omega_1'}} \\ \frac{K_{j,j+1}}{Z_0} \bigg|_{j=1 \text{ to } n-1} &= \frac{\pi \omega_\lambda}{2 \omega_1'} \frac{1}{\sqrt{g_j g_{j+1}}} \\ \frac{K_{n,n+1}}{Z_0} &= \sqrt{\frac{\pi}{2} \frac{\omega_\lambda}{g_n g_{n+1} \omega_1'}} \end{aligned} \quad (4.2)$$

where

$$\omega_\lambda = \frac{\lambda_{g1} - \lambda_{g2}}{\lambda_{g0}}$$

and  $\lambda_{g0}$ ,  $\lambda_{g1}$ ,  $\lambda_{g2}$  stand for the guided wavelength at  $\omega_0$  and at lower and upper passband edge frequencies, respectively.

2) Determine the geometry of the coupling sections. Using the equivalent circuit of the impedance inverter as shown in Figure 4.4, there is

$$K_{j-1,j} = \left| \tan\left(\frac{1}{2}\phi_j + \tan^{-1} X_{sj}\right) \right| \quad (4.3)$$

$$\phi_j = -\tan^{-1}(2X_{pj} + X_{sj}) - \tan^{-1} X_{sj} \quad (4.4)$$

$X_s$  and  $X_p$  can be extracted from the scattering matrix of the inductive iris window. The equations are given by

$$jX_s = \frac{1 - S_{12} + S_{11}}{1 - S_{11} + S_{12}} \quad (4.5)$$

$$jX_p = \frac{2S_{12}}{(1 - S_{11})^2 - S_{12}^2} \quad (4.6)$$

In order to get the physical lengths of the iris windows, the computation of the S parameters must be repeated until the required impedance inverter values are obtained.

3) Finally the lengths of the resonators can be obtained by using

$$L_j \Big|_{j=1 \text{ to } n} = \frac{\lambda_{g0}}{2\pi} \left[ \pi - \frac{1}{2}(\phi_j + \phi_{j+1}) \right] \quad (4.7)$$

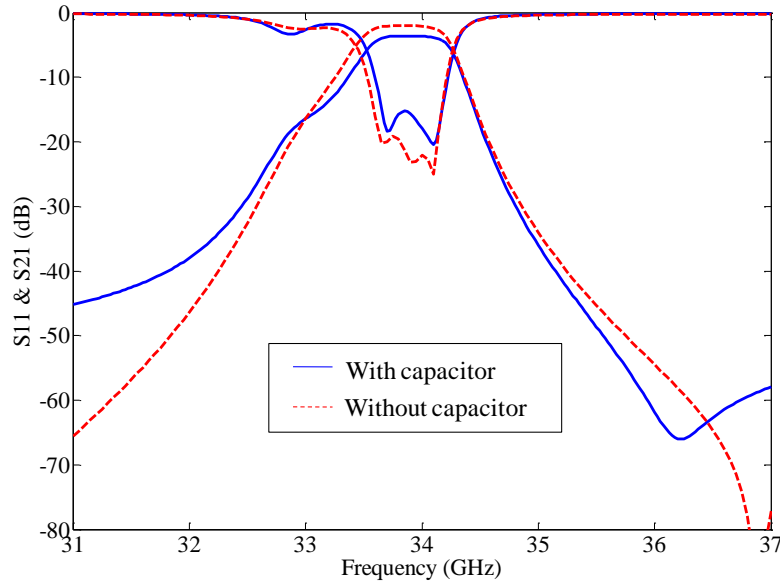


Figure 4.5: Simulated S-parameter results of the experimental prototype of the proposed dual-mode SIW band-pass filter

Simulated S-parameters of the proposed dual-mode SIW BPF are shown in Figure 4.5. The dashed lines stand for the performance of the SIW BPF by itself and the solid lines stand for the performance of the SIW BPF under the influence of the DC-block capacitor. It can be found that the insertion loss of the dual-mode SIW BPF is about 2 dB which can be attributed to several factors, namely, dielectric loss, metal loss and loss generated by the external loads. The DC-block capacitor is found to introduce an additional 1.6 dB insertion loss at the RF frequency band. The simulated results show a good selectivity of our proposed dual-mode BPF which has a pass band

of 33.55 - 34.25 GHz. The narrow bandwidth can guarantee a good RF isolation from undesired signals like the self and higher order LO signals and other mixing products.

#### 4.2.2 LO Mode

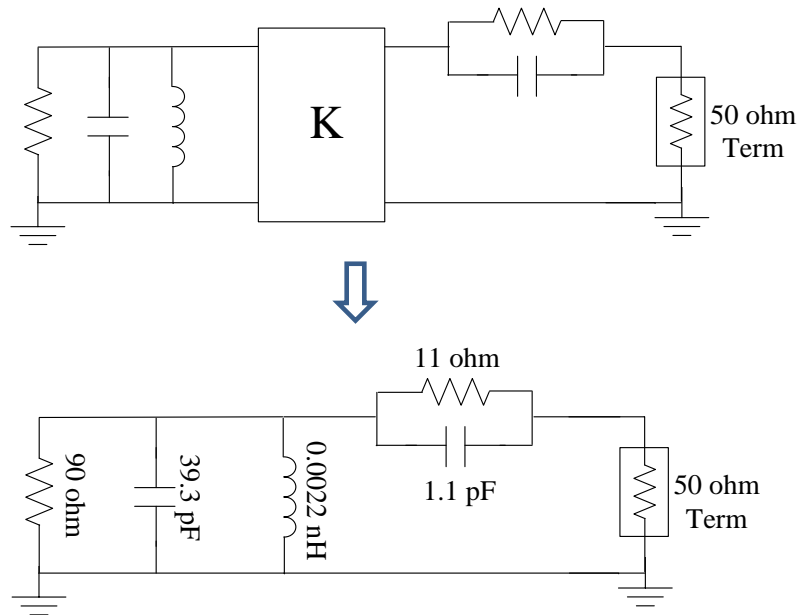
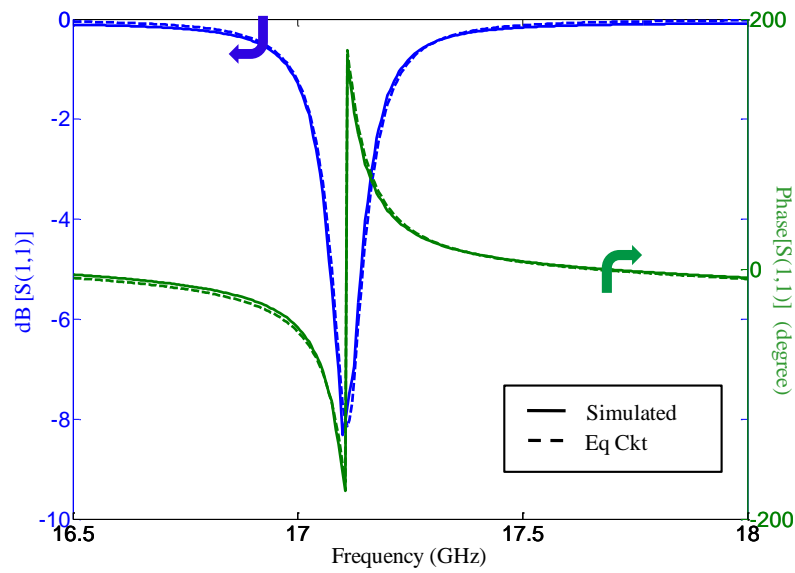
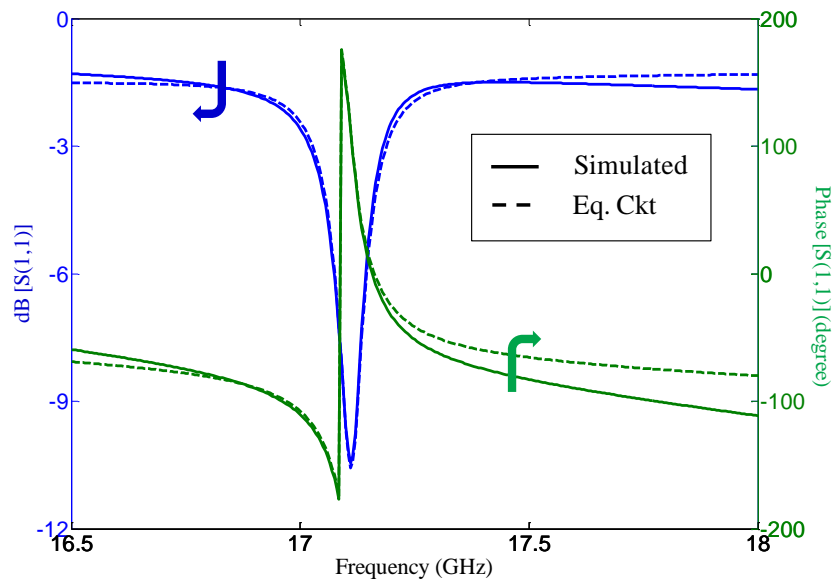


Figure 4.6: Equivalent circuit of the LO-mode SIW BPF

Since the first three SIW cavities effectively cutoff the oscillating frequency, the dual-mode SIW BPF circuit can be deemed as a one-port network for the LO mode. Figure 4.6 displays the equivalent circuit of the LO-mode SIW BPF with a 50 ohm terminal. The values of all the elements are marked out, which are extracted with the aid of commercial software Zeland IE3D v14.0. The  $H_{101}$  mode cavity is modeled as a shunt capacitor and inductor together with a shunt resistor. The DC-block capacitor is modeled as a series capacitor and a series resistor that are configured in parallel. Figures 4.7(a)-(b) compare the frequency response of the modeled equivalent circuit and the full-wave simulated S-parameters of the LO-mode SIW BPF. The circuit modeling fits with the simulated results quite well. In Figure 4.7(b), the discrepancy at the upper band is mainly attributed to the fact that the broadside coupled capacitor is a frequency dependent component.



(a) without capacitor



(b) with capacitor

Figure 4.7: Comparison of the modeled equivalent circuit response and the simulated S-parameters of the LO-mode SIW BPF

Figure 4.6 indicates that the unloaded and loaded Q-factors of the  $H_{101}$  mode SIW cavity are about 380 and 155, respectively. There is a significant improvement of the quality factor by employing the SIW cavities since it has been proven that the maximum achievable unloaded quality factor  $Q_0$  of half-wavelength microstrip resonators is between 150-200 [78]–[79]. The oscillation performance largely depends on the LO mode. The high-Q factor of our SIW cavity can improve the phase noise of the oscillating signal. It should also be mentioned that the oscillation occurs at a specific frequency such that [80]

$$Z_L = -\frac{R_d}{3} - jX_d \quad (4.8)$$

which is close to but different from the resonant frequency of the  $H_{101}$  mode. In (4.8),  $Z_L$  is the load impedance;  $R_d$  and  $X_d$  are the negative resistance and the reactance at the drain, respectively.

### 4.3 Second Harmonic SOM

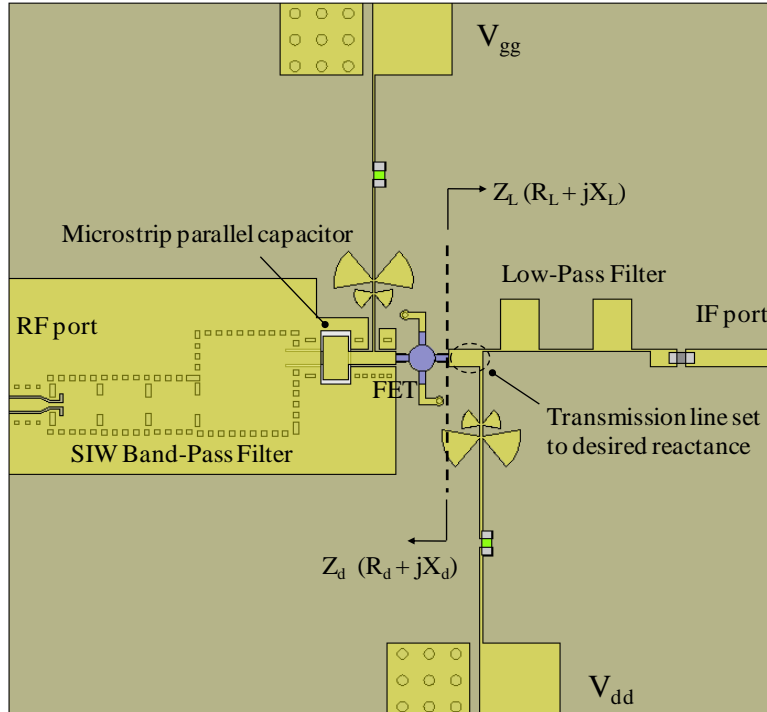


Figure 4.8: Layout of the proposed SIW second harmonic SOM

Figure 4.8 shows the layout of our proposed SIW second harmonic SOM. The transistor used in our circuit is the pseudomorphic hetero-junction FET (HJFET) NE3210S01 from NEC. DC biases are carefully designed and applied to the gate and drain of the HJFET. Two butterfly stubs are used to prevent the LO and RF signals from leaking into DC supplies. At the IF port, a microstrip low-pass filter is used to suppress the signals other than IF frequency. Shorting stubs are connected with the source of the FET to make it working in an unstable region. The design of the stubs is based on the small signal S-parameters of the transistor.

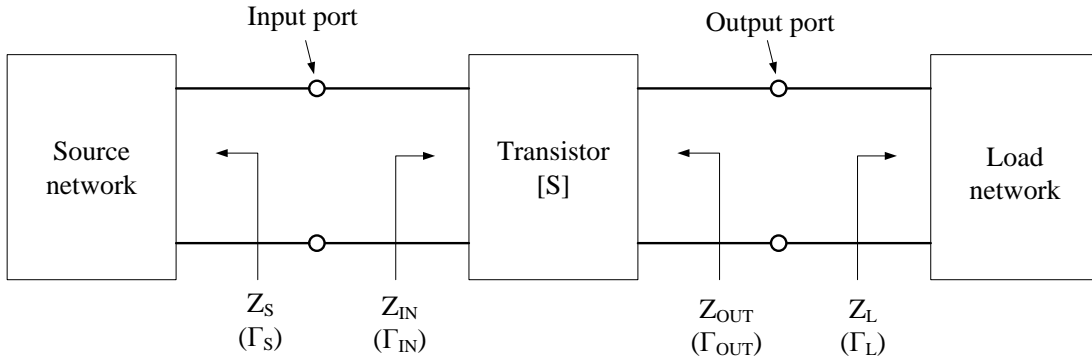


Figure 4.9: Two-port network configuration of our circuit

A two port network configuration of our circuit is shown in Figure 4.9. It is characterized by the S parameter of our unstabilized HJFET, the source impedance  $Z_S$ , and the load impedance  $Z_L$ . It can be obtained that:

$$\Gamma_{IN} = S_{11} + \frac{S_{12}S_{21}\Gamma_L}{1 - S_{22}\Gamma_L} \quad (4.9)$$

$$\Gamma_{OUT} = S_{22} + \frac{S_{12}S_{21}\Gamma_S}{1 - S_{11}\Gamma_S} \quad (4.10)$$

In addition, the radii and centers of the input and output stability circles are given by

Output stability circle in the  $\Gamma_L$  plane:



$$r_L = \left| \frac{S_{12}S_{21}}{|S_{22}|^2 - |\Delta|^2} \right| \quad (\text{radius}) \quad (4.11)$$

$$C_L = \frac{(S_{22} - \Delta S_{11}^*)^*}{|S_{22}|^2 - |\Delta|^2} \quad (\text{center}) \quad (4.12)$$

Input stability circle in the  $\Gamma_S$  plane:

$$r_s = \left| \frac{S_{12}S_{21}}{|S_{11}|^2 - |\Delta|^2} \right| \quad (\text{radius}) \quad (4.13)$$

$$C_s = \frac{(S_{11} - \Delta S_{22}^*)^*}{|S_{11}|^2 - |\Delta|^2} \quad (\text{center}) \quad (4.14)$$

where

$$\Delta = S_{11}S_{22} - S_{12}S_{21}$$

It can be proved that the necessary and sufficient conditions for unconditional stability are:

$$K = \frac{1 - |S_{11}|^2 - |S_{22}|^2 + |\Delta|^2}{2|S_{12}S_{21}|} > 1 \quad (4.15)$$

and

$$|\Delta| < 1 \quad (4.16)$$

The length of the shorting stub ( $L$ ) affects the oscillating frequency and the negative resistance at the drain. Agilent's Advanced Design System (ADS) (2008 version) is used to simulate their relationship, which is shown in Figure 4.10. For our design, the length of the short stub is set to be 2.5 mm which makes the HJFET unstabilized and the corresponding oscillating frequency is around 15.2 GHz. Since the datasheet from NEC only provides the S-parameters of the HJFET transistor up to 26 GHz, the measurement of the HJFET is carried out under the recommended bias conditions ( $V_{DS} = 2$  V,  $I_D = 10$  mA) in order to precisely extract the S-parameters in our frequency bands of interest. The TRL calibration is applied to eliminate calibration errors

including the bias circuits. The measured S-parameters of the unstabilized HJFET are tabulated in Table 4.1 for both the LO and RF frequencies, respectively.

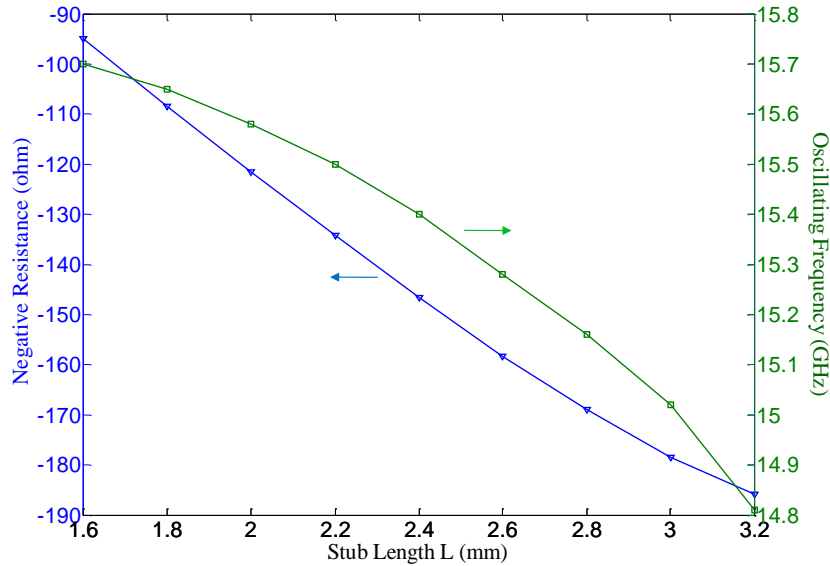


Figure 4.10: Simulated stub length versus negative resistance and oscillating frequency

Table 4.1 Measured S-parameter of the unstabilized HJFET

freq. (GHz)	$S_{11}$	$S_{21}$	$S_{12}$	$S_{22}$
15.2	3.520 /-8.75°	0.884 /-104.40°	0.808 /-125.71°	0.577 /-8.24°
34	0.946 /-144.13°	0.139 /22.59°	0.143 /174.24°	0.539 /-83.90°

Based on our measured results, the unstable region of the HJFET at the LO frequency nearly covers the whole smith chart, as shown in Figure 4.11. While it should be noted that the length of the short stub is almost a half-wavelength at the RF frequency which makes the transistor operate in the stable region for the RF signal. As for the RF input, the RF port sees a nonlinear load at the gate of the FET and the input impedance varies with the DC operation point of the FET and LO power level. From our simulations, this value is normally not very far away from the 50 Ohm load when the FET is operating at this point ( $V_{DS} = 2$  V,  $I_{DS} = 10$  mA) and saturated. This

impedance level seems appropriate for most of the FET mixers. Due to this reason, no specific RF input matching network is designed in our circuit. In the meanwhile, it can be observed that the designed negative resistance at the drain of the HJFET is around  $-150 \Omega$ . As such, without using an additional output matching circuit, a 50 ohm output port connected directly with FET drain can fulfill the oscillation condition (4.8). It is also noted that when the LPF is applied, the load impedance will not be 50 ohm any more. To make the circuit still oscillate at the same frequency, the load impedance  $Z_L = 0$  is required, which is obtained by carefully designing the transmission line in front of the IF LPF to tune the imaginary part of the  $Z_L$  to zero (Referring to Figure 4.8). As such, the circuit remains oscillating with the condition  $R_L + R_d < 0$  and  $X_L + X_d = 0$  (Because  $R_d$  will become less negative as the oscillator power builds up, it is necessary to choose  $R_L$  so that  $R_L + R_d < 0$ ).

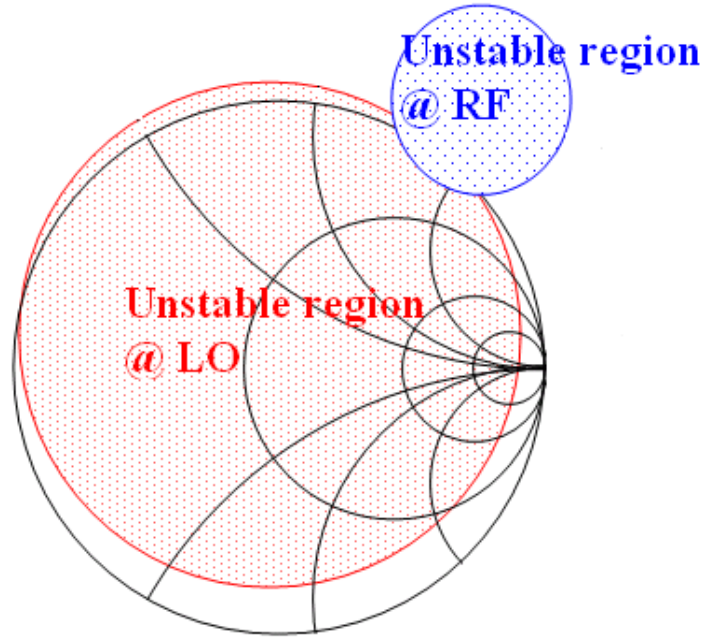


Figure 4.11: Load plane stability circle of the unstabilized HJFET

#### 4.4 Experimental Results and Discussions

Our proposed  $K_a$ -band SIW second harmonic SOM is measured using a test fixture Aritsu SC5226 and a spectrum analyzer Agilent E4446A. The photograph of the circuit under test is

shown in Figure 4.12. The RF signal is at 34 GHz and generated by using a microwave generator Anritsu MG3694A. Figure 4.13 shows the measured mixing spectrum of our proposed SOM circuit with a RF input of -2 dBm. Considering a 1-2 dB transmission loss in the connection cables and test fixture probes, the conversion loss is about -12 dB. Here it should be noted that the conversion loss is also determined by the amplifying ability of the transistor we used at RF frequency. The maximum transducer power gain, under simultaneous conjugate match conditions, is given by

$$G_{T,\max} = \frac{|S_{21}|}{|S_{12}|} (K - \sqrt{K^2 - 1}) \quad (4.17)$$

In our case, the maximum transducer power gain at RF frequency (34 GHz) is calculated to be about -5 dB, which indicates that a high performance transistor may be necessary to improve the conversion loss.

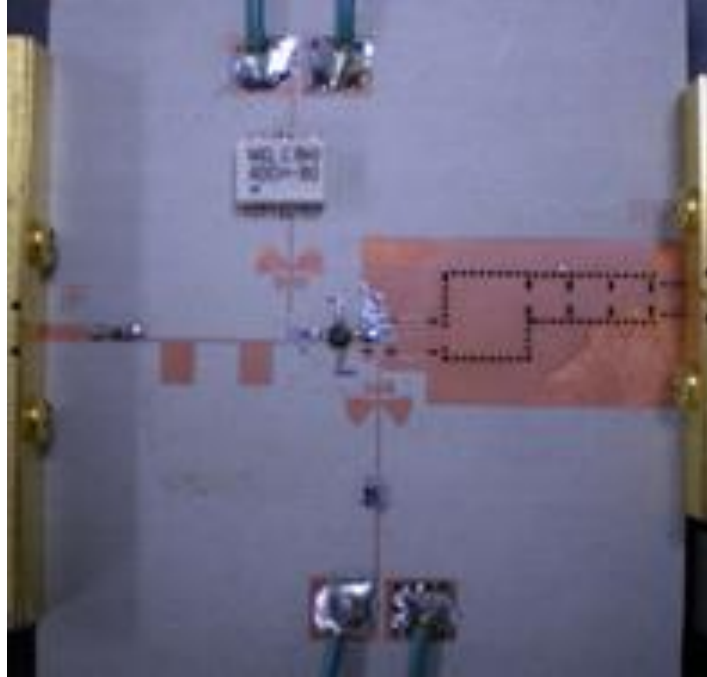


Figure 4.12: Photograph of the K<sub>a</sub>-band experimental prototype

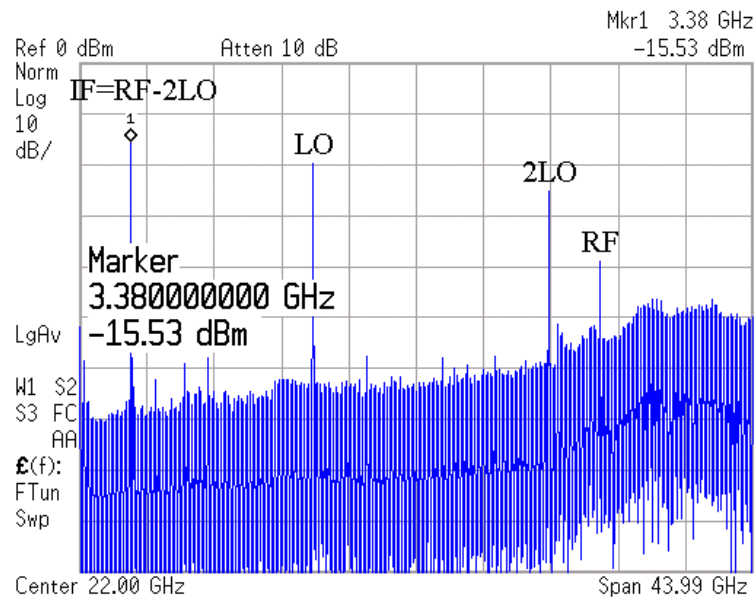


Figure 4.13: Mixing spectrum of the proposed second harmonic SOM

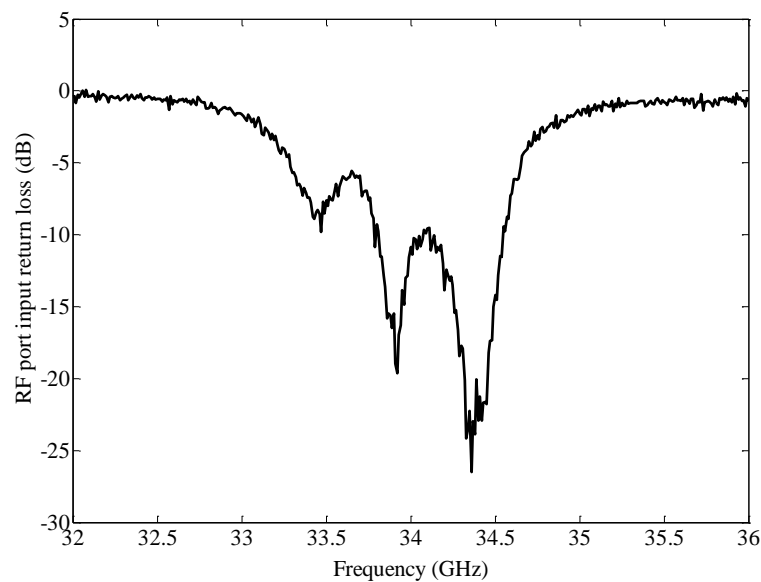


Figure 4.14: Measured RF port input return loss

The RF input return loss is also measured and plotted in Figure 4.14. The result shows a fairly good matching for the RF input signal. At the same time, the LO signal can be measured with the RF signal and the LPF excluded. Figure 4.15 shows the spectrum of the self and second harmonics of the LO signal. It is measured with the LPF removed and all the bias conditions are

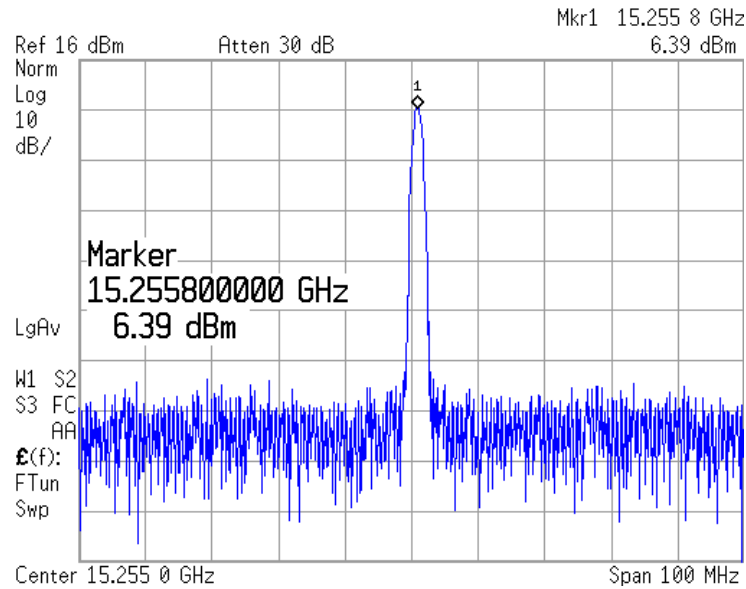
kept the same. Removing the 2 dB calibration loss, the self and second harmonic LO signals are found to exhibit about 8.5 dBm and -3 dBm, respectively. The phase noise of the IF signal is also measured with the resolution bandwidth of our spectrum analyzer was set to be 10 KHz. Figure 4.16 shows that a -81 dBc/Hz phase noise at 100 KHz offset is obtained.

Phase noise can be expressed using the Leeson equation as given below:

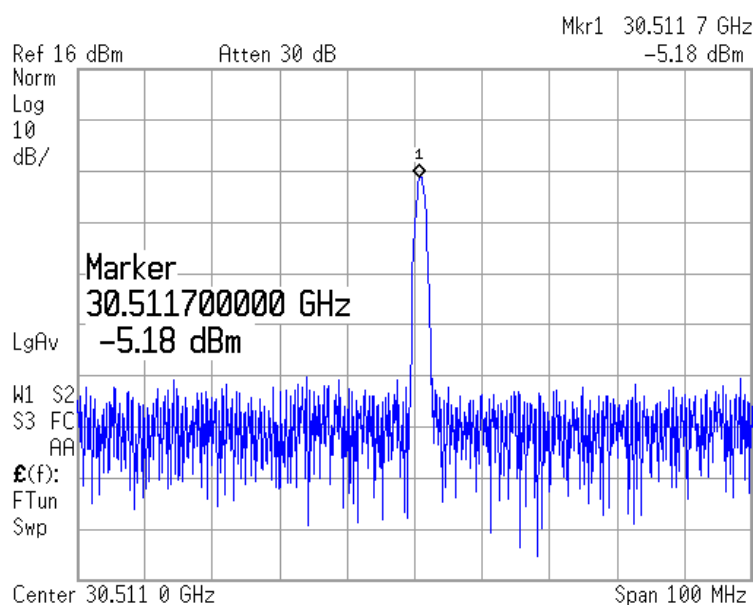
$$L(f_m) = 10 \log_{10} \left\{ \frac{FkT}{2P_{avs}} \left[ 1 + \frac{f_c}{f_m} + \left( \frac{f_0}{2f_m Q_L} \right)^2 \left( 1 + \frac{f_c}{f_m} \right) \right] \right\} \quad (4.18)$$

where  $L(f_m)$  = Phase noise (dBc/Hz);  $Q_L$  = loaded Q;  $f_m$  = carrier offset frequency (Hz);  $f_0$  = carrier centre frequency (Hz);  $f_c$  = flicker corner frequency of the active device (Hz);  $T$  = temperature ( $^{\circ}$ K);  $P_{avs}$  = Average power through the resonator (W);  $F$  = Noise factor of the active device;  $k$  = Boltzman constant.

From Equation (4.18), it can be found that in addition to loaded Q, the phase noise is related to several other factors. The performance of the active transistor and the transmission power loss all have big influences on the phase noise. The biasing circuit may also degrade the phase noise. In our design, the phase noise and conversion loss are affected by the broadside coupled DC-block capacitor (see Figure 4.8) since it generates some amount of radiation. To avoid this effect, a high performance microwave chip capacitor is recommended.



(a)



(b)

Figure 4.15: Spectrum of (a) self oscillation and (b) second harmonic

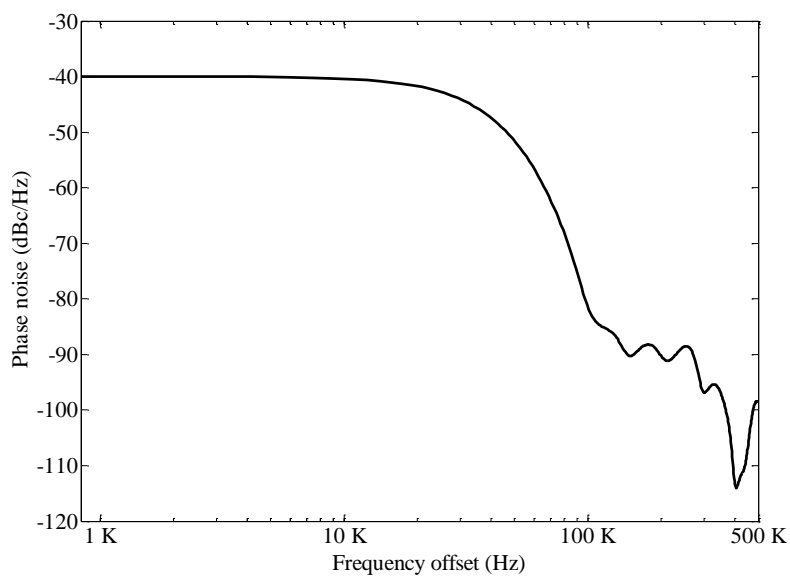


Figure 4.16: Phase noise measurement of IF signal

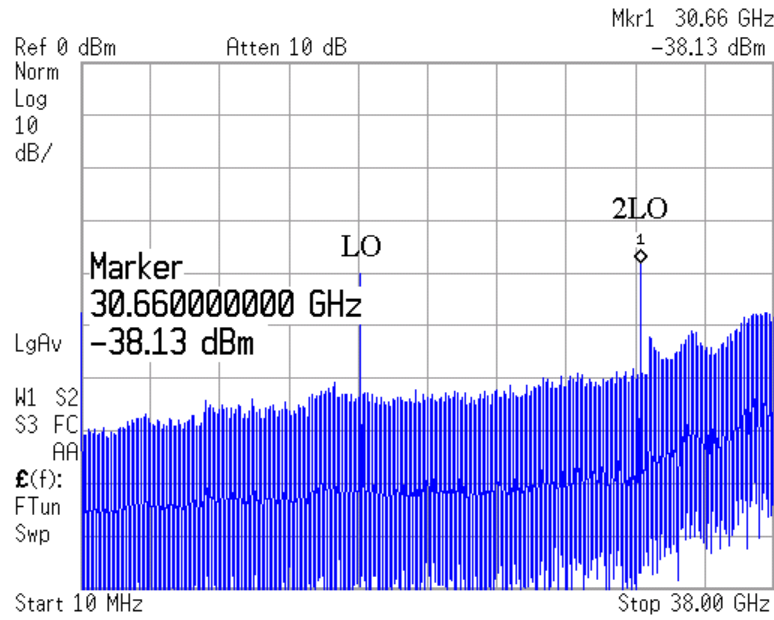


Figure 4.17: Measured LO-RF isolation

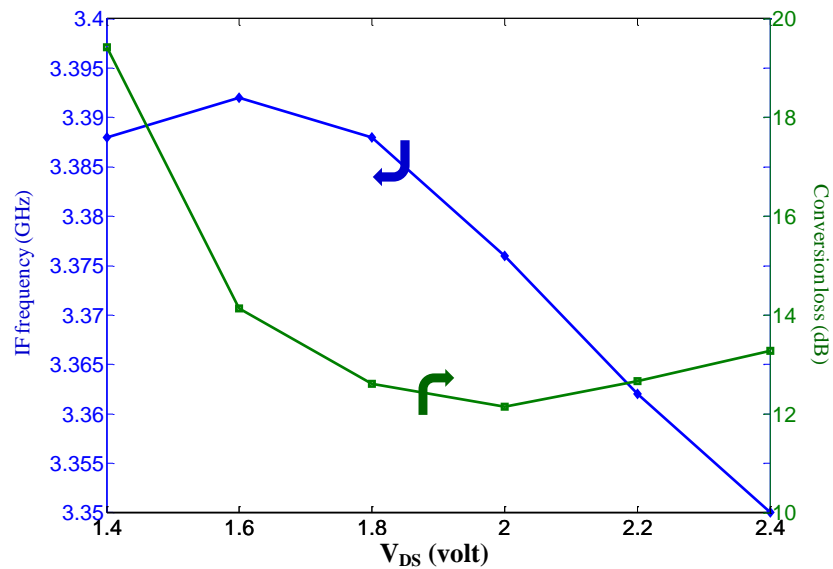


Figure 4.18: Intermediate frequency (IF) shift and conversion loss variation with respect to drain bias ( $V_{GS} = -0.5$  V)

For our circuit design and implementation, a good LO-RF isolation can be guaranteed since the LO signal is under the cutoff frequency of the RF cavities. In addition, a high-selectivity of the



dual-mode SIW BPF yields a good performance of the second harmonic LO-RF isolation. Figure 4.17 displays the measured results, which indicate that the self and second harmonic LO-RF isolations are about -50 dB and -33 dB, respectively. It is noted that the second harmonic LO-RF isolation is slightly lower than the value ( $< -40$  dB) which is expected from the out-of-band performance of the BPF as shown in Figure 4.4. This may be due to the fact that the input impedance at the gate of the FET is not exactly 50 Ohm.

In addition, the IF frequency shift with respect to the drain bias is investigated, as can be seen in Figure 4.18. It can be found that the IF frequency is relatively stable when the drain bias changes. The IF frequency shift is within 60 MHz when  $V_{GS} = -0.5$  V, and  $V_{DS}$  varies from 1.4 V to 2.4 V. The optimal conversion loss happens when  $V_{DS}$  is around 2 V. The measured drain current for the optimal conversion loss is about 11 mA.

Compared with [75], our proposed circuit presents a new way of implementing the SOM and this is the first time that a dual-mode SIW resonator/filter is used for such applications, according to our knowledge. In addition, [75] mainly focused on an oscillator design with an SIW cavity, and made use of microstrip line and microstrip antenna which may introduce higher loss at millimeter-frequencies. From a system point of view, our proposed SOM receiver can be seamlessly integrated with an SIW slot antenna array which provides a good option for millimeter-wave applications since microstrip patch array antenna is no longer suitable at such high frequencies. No SIW-microstrip line transition is required and this could be a significant advantage for millimeter-wave applications.

## 4.5 Conclusion

A sub-harmonic SOM that makes use of transmission characteristics of two operating modes in an SIW cavity is proposed and presented in this chapter for the first time. The SOM circuit utilizes the fundamental mode ( $H_{101}$ ) of the SIW cavity for RF mode and the  $H_{202}$  mode for LO mode. A  $K_a$ -band experimental prototype is designed and measured. The measured results show that the conversion loss of our experimental prototype is about 12 dB at 34 GHz. The measured phase noise of the IF signal is around -81 dBc/Hz at 100 KHz offset. The conversion loss and phase noise can be further improved by carefully considering and reducing the loss of the broadside coupled DC block capacitor. The proposed mixer circuit exhibits good frequency selectivity. The self and second harmonic LO-RF isolations are found to be about -50 dB and -33

dB, respectively. Our proposed design can be integrated directly with antenna to build up a very compact receiver front-end of a millimeter-wave system.

## CHAPTER 5      GENERIC ARCHITECTURES AND PARAMETERS OF RECEIVER SYSTEMS

In the previous chapters, SIW technique has been applied and explored in the development of millimeter-wave circuits and devices. However, most of them aforementioned were investigated as single elements. From the system point of view, it will be more meaningful to implement SIW technique in millimeter-wave systems so that its advanced features can be used to improve the system performance.

In this chapter, generic architectures and parameters of receiver systems are discussed and used as a guideline for our millimeter-wave system design. From this chapter on, sub-millimeter/millimeter wave systems based on SIW technique will be demonstrated.

### 5.1 Receiver architectures

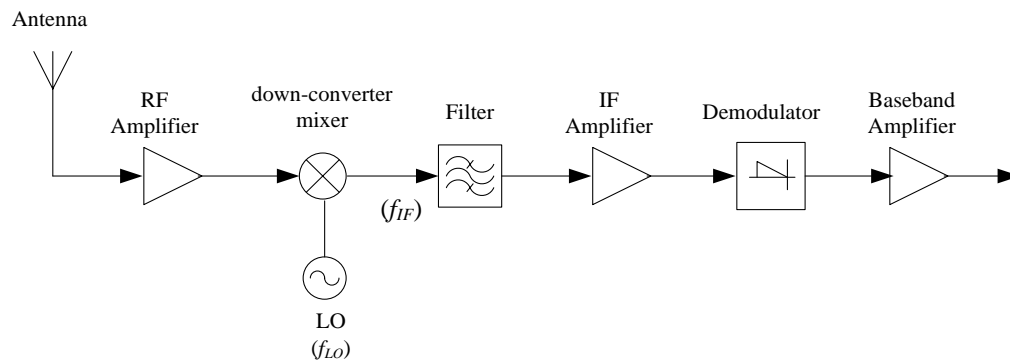


Figure 5.1: Architecture of a super-heterodyne receiver

Standard wireless receivers typically make use of two architectures: "heterodyne" and "homodyne". The (super-)heterodyne receiver is widely used. A heterodyne receiver has a local oscillator (LO), which produces a signal that is adjusted to be close in frequency to the RF signal being received. The mixing products of RF and LO signals include two new frequencies, namely sum term  $(f_{RF} + f_{LO})$  and difference term  $(f_{RF} - f_{LO})$  of the original frequencies. One of these two new frequencies is discarded, usually the higher one  $(f_{RF} + f_{LO})$ , by filtering it out of the mixer output. The remaining difference frequency is called the IF, and it is subject to signal processing

that eventually extracts the desired modulated information. It should be mentioned that the main difference between a super-heterodyne and a heterodyne receiver is the use of a high gain IF amplifier which can improve the selectivity and sensitivity of the receiver.

Homodyne receiver is also called as "direct-conversion" or "zero-IF" receiver. The principle is illustrated in Figure 5.2. The RF signal is first amplified at a low noise stage and then down converted with an LO signal to base-band directly. When the frequencies of the RF and the LO signals are equal, this scheme works as a phase detector. In some literature, only when the local oscillator is synchronized in phase with the incoming carrier frequency, the receiver is called homodyne.

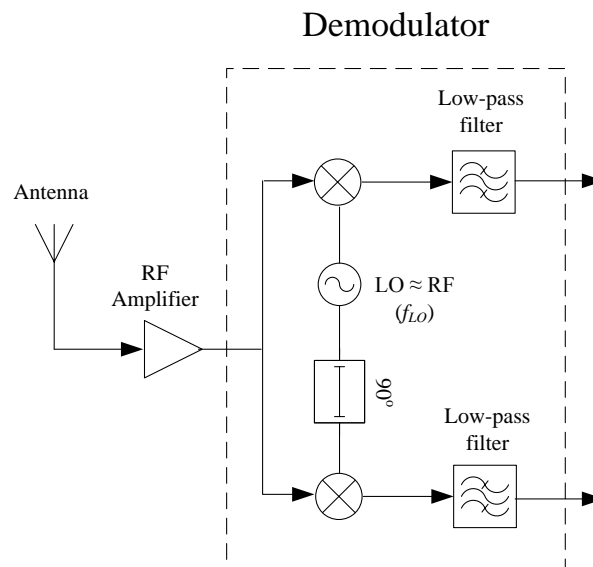


Figure 5.2: Architecture of a homodyne receiver

In summary, a homodyne (direct-conversion) receiver requires only a single stage of detection and filtering, as opposed to the more common super-heterodyne receiver design, which converts the carrier frequency to an IF frequency first before extracting the modulation, and thus requires at least two stages of detection and filtering.

The benefits and drawbacks of heterodyne and homodyne receivers can be concluded as below:

Table 5.1: Comparison between heterodyne and homodyne receivers

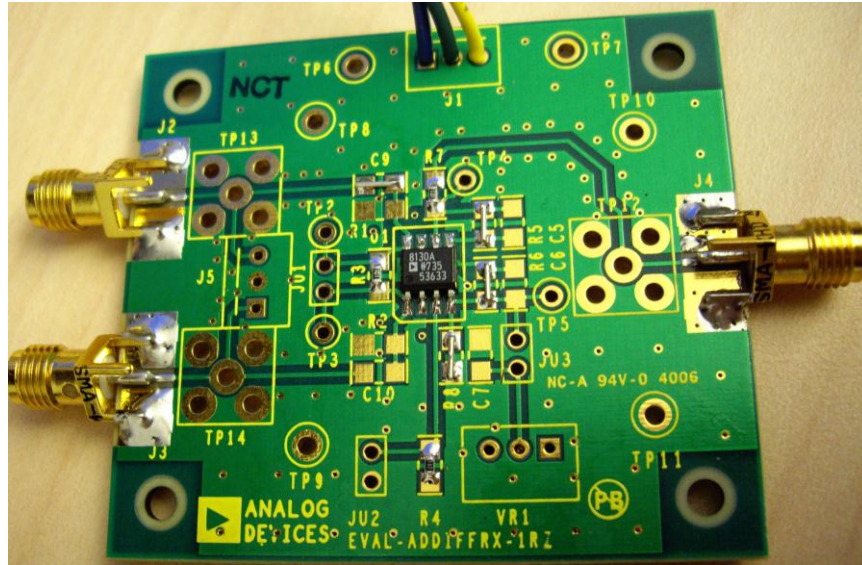
	Heterodyne receiver	Homodyne receiver
Benefits	A broad dynamic range A higher selectivity and sensitivity Little interference with the I/Q signal imbalance	High integration, small volume and low cost Low power consumption No need of image reject filter
Drawbacks	Complex in structure and low integration Many discrete filters are used which makes the systems bulky High power consumption	Design of active LPF at baseband is challenging to achieve a good dynamic range, low noise and good linearity Unwanted DC offset may corrupt the signal and, more importantly, saturate the following stages Carrier recovery is difficult as the carrier frequency is at RF frequency Very sensitive to the I/Q imbalance

## 5.2 Experimental Setup of Our Communication Systems

Our communication systems are based on a basic block diagram as depicted in Figure 5.3. It can be found that our proposed systems employ a traditional heterodyne architecture and a dual-antenna scheme is applied. The digital number in red color is used to represent the signals in the system flow chart. In the following chapters, slight changes may be made according to different applications. Further details about the system hardware will be discussed later. This section focuses on describing the demodulation techniques.

In order to obtain common-mode baseband demodulated I/Q output signals for the baseband ADC/DSP board, one AD8347 direct I/Q demodulator (0.8 GHz to 2.7 GHz) and two differential amplifiers AD8130 (see Figure 5.4) are used. In addition, Figure 5.5 presents the schematic diagram of a baseband elliptic LPF assembled in the AD8347 evaluation board. The LPF is allocated between the I/Q mixer outputs and the input of the baseband amplifiers to reduce the signal distortion. The simulated frequency response of the elliptic LPF is shown in Figure 5.6. It can be observed that the 3 dB cutoff frequency is about 20 MHz, which indicates that the upper





(b)

Figure 5.4: Photograph of the (a) I/Q demodulator and (b) differential amplifier with common-mode output

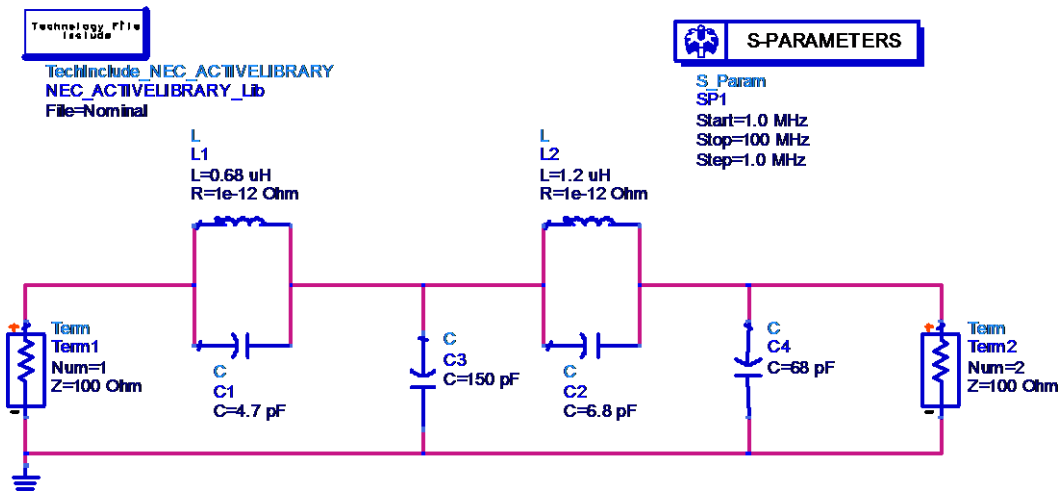


Figure 5.5: Schematic of the baseband elliptic LPF in the demodulation board

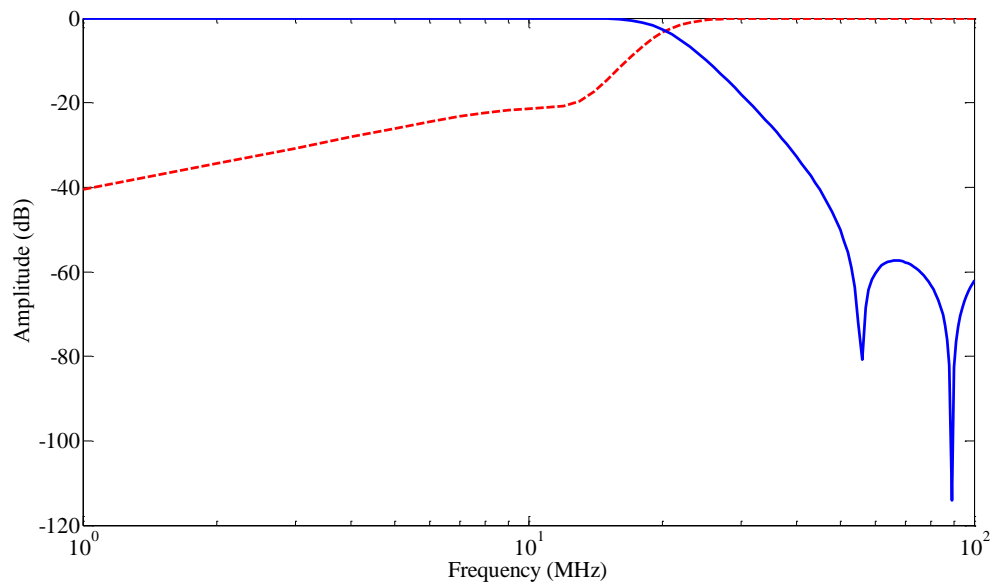


Figure 5.6: Frequency response of 20 MHz baseband LPF

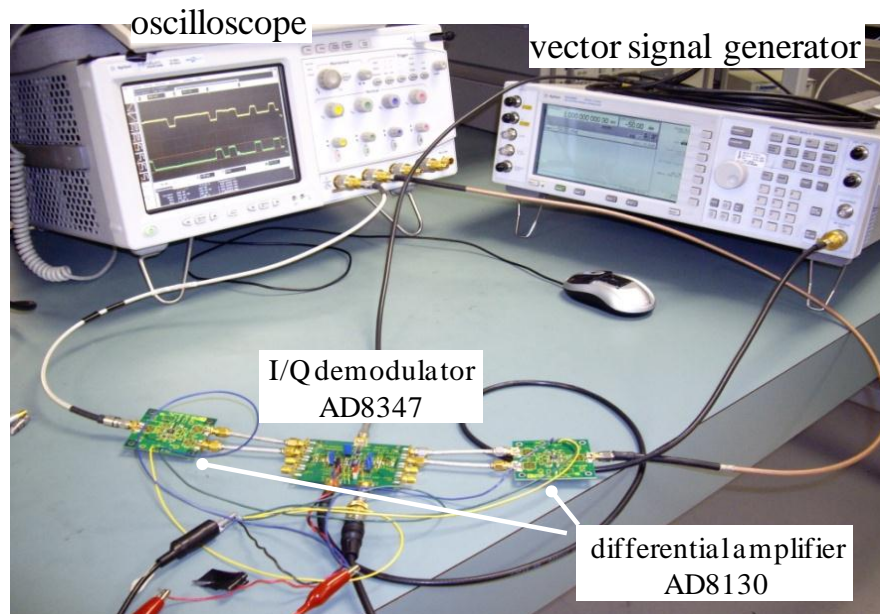
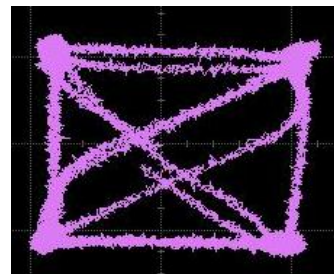
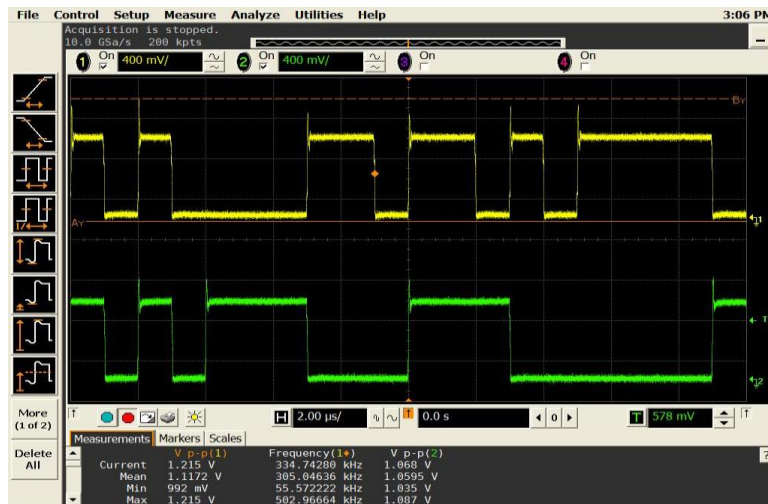


Figure 5.7: Test setup of the demodulation board with common-mode output

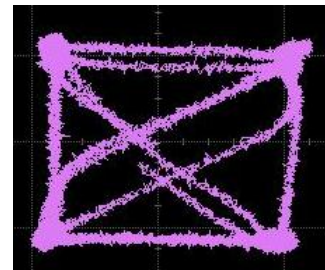
The output of the demodulation board is measured with different RF input power levels  $P_{in}$  and different symbol rates  $R_s$  for QPSK scheme. It can be found that 1 GHz IF modulated signal is



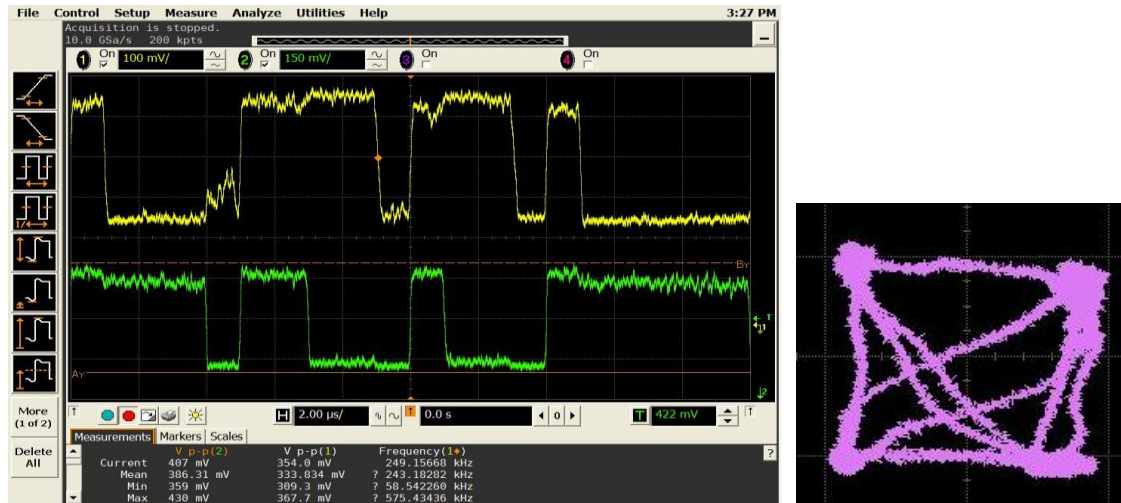
correctly demodulated with the symbol data rates  $R_s$  of 1-10 Msps, and the signal distortion becomes more severe when the symbol rate increases and the input power level decreases. Figures 5.8a-5.8c plot the measured demodulated output I/Q waveform and I/Q diagram.



(a)  $P_{in} = -10$  dBm,  $R_s = 2$  Msps



(b)  $P_{in} = -50$  dBm,  $R_s = 2$  Msps



(c)  $P_{in} = -60$  dBm,  $R_s = 1$  Msps

Figure 5.8: Demodulated I/Q waveform output (left) and I/Q diagram (right)

### 5.3 Receiver Analysis

In a receiver, the signal detected by the antenna is usually a weak carrier modulated with the desired digital data signal. The demodulator is able to recover the desired signal only if the power of the signal exceeds a conceivable level, which depends on signal strength, incoming noise power, type of demodulation, and so on. However, in most of cases, if the noise power is higher than the signal power, (i.e., the ratio of carrier to noise ratio at the demodulator input is lower than a threshold value), the signal cannot be demodulated and separated from the carrier.

Moreover, in order to ensure the fidelity of power transportation and manipulation, distortion of the desired signal must be reduced as much as possible. The source of the distortion is mainly attributed to the non-linearity of the devices and the interferences inside the circuit block. An active device has linear and non-linear regions. Its non-linear terms produce harmonics and spurious products which contribute to the distortion of the signal. The effects of noise and spurious products on a receiver are different. Noise is directly related to the sensitivity of the receiver. The sensitivity of a receiver is high if its noise figure is low and vice versa. The

spurious products cause distortion of the signal, but they are not directly related to the sensitivity of a receiver.

### 5.3.1 Noise in Receiver Systems

Noise is any unwanted input that may limit systems ability to process weak signals. It can be attributed to different sources: 1) random noise in resistors and transistors, 2) mixer noise, 3) undesired cross-coupling noise, and 4) power supply noise. On the other hand, noise figure ( $NF$ ) is a measure of degradation of the signal-to-noise ratio ( $SNR$ ), caused by passive or active components in a system. The noise figure is defined as the ratio of the output noise power of a device to the portion thereof attributable to thermal noise in the input termination at standard noise temperature  $T_0$  (usually 290 K). The noise figure is thus the ratio of actual output noise to that which would remain if the device itself did not introduce noise. It is a number by which the performance of a radio receiver can be specified.

The noise factor of a system is defined as:

$$F = \frac{SNR_{in}}{SNR_{out}} \quad (5.1)$$

where  $SNR_{in}$  and  $SNR_{out}$  are the input and output power signal-to-noise ratios, respectively. The noise figure is defined as:

$$NF = 10 \log F = 10 \log \left( \frac{SNR_{in}}{SNR_{out}} \right) = SNR_{in,dB} - SNR_{out,dB} \quad (5.2)$$

where  $SNR_{in,dB}$  and  $SNR_{out,dB}$  are in decibels (dB).

In general, the noise figure of a noisy block can be expressed by

$$NF = NF_{min} + \frac{R_n}{G_s} [(G_s - G_{s,opt})^2 + (B_s - B_{s,opt})^2] \quad (5.3)$$

where

$NF$  = noise figure of noisy block.

$NF_{min}$  = minimum of noise figure of noisy block.

$R_n$  = equivalent noise resistance.

$Y_s$  = admittance of input source.

$G_s$  = conductance of input source.

$B_s$  = susceptance of input source.

$Y_{s, opt}$  = optimum admittance of input source.

$G_{s, opt}$  = optimum conductance of input source.

$B_{s, opt}$  = optimum susceptance of input source.

The noisy two port block can reach a minimum of noise figure

$$NF = NF_{\min} \quad (5.4)$$

when

$$Y_s = Y_{s, opt}$$

For a multistage (cascaded) system, the total noise factor can be found with Friis' Formula:

$$F = F_1 + \frac{F_2 - 1}{G_1} + \frac{F_3 - 1}{G_1 G_2} + \frac{F_4 - 1}{G_1 G_2 G_3} + \dots + \frac{F_n - 1}{G_1 G_2 G_3 \dots G_{n-1}} \quad (5.5)$$

where  $F_n$  is the noise factor for the  $n$ -th device and  $G_n$  is the power gain (dimensionless) of the  $n$ -th device. In a well designed receive chain, the noise factor of the first amplifier should be the most significant.

### 5.3.2 Receiver Noise Floor

A real receiver noise floor includes thermal noise ( $N_0 = kTB$ ) and noise figure in the receiver itself.  $N_0 = kTB$  is the noise power, where  $k$  is Boltzman's constant ( $1.38 \times 10^{-23}$  J/K),  $T$  is system temperature, usually 290 K, and  $B$  is system bandwidth (Hz). Table 5.2 displays typical bandwidths for various digital modulation methods. It should be noted that the values in Table 5.2 is higher than the theoretical minimum system bandwidth calculated with the Nyquist formula. This is because the separation of two frequencies has to be considered in practice.

Table 5.2: Typical bandwidths for various digital modulation methods

Modulation method	Typical bandwidth (null-to-null)
QPSK, DQPSK	$1.0 \times \text{bit rate}$
MSK	$1.5 \times \text{bit rate}$
BPSK, DBPSK, OFSK	$2.0 \times \text{bit rate}$

Based on Table 5.2, the noise power  $N_0$  for QPSK modulation with different data bit rate  $R_b$  and symbol rate  $R_s$  is calculated and tabulated in Table 5.3.

Table 5.3: Thermal noise power ( $N_0 = kTB$ ) for QPSK with different data rate

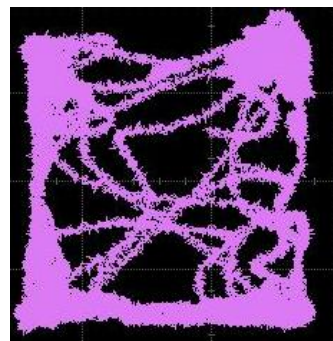
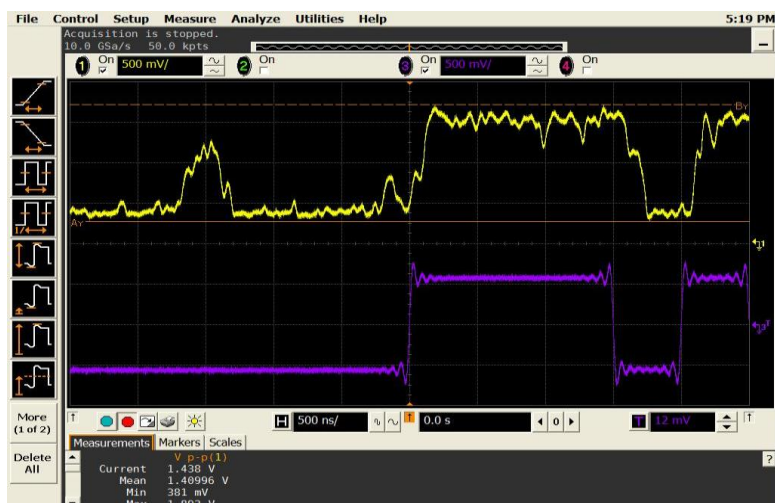
$R_b$ (Mbps)	$R_s$ (Msps)	$B$ (Hz)	Noise Power $N_0$ (dBm)
2	1	$2 \times 10^6$	-111
4	2	$4 \times 10^6$	-108
10	5	$1 \times 10^7$	-104
20	10	$2 \times 10^7$	-101

The noise floor limits the smallest measurement that can be taken with certainty since any measured amplitude can on average be no less than the noise floor. In our receiver prototype, the noise floor =  $N_0 + NF$ .

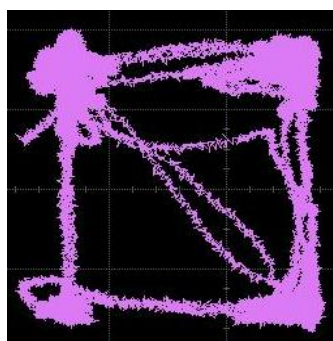
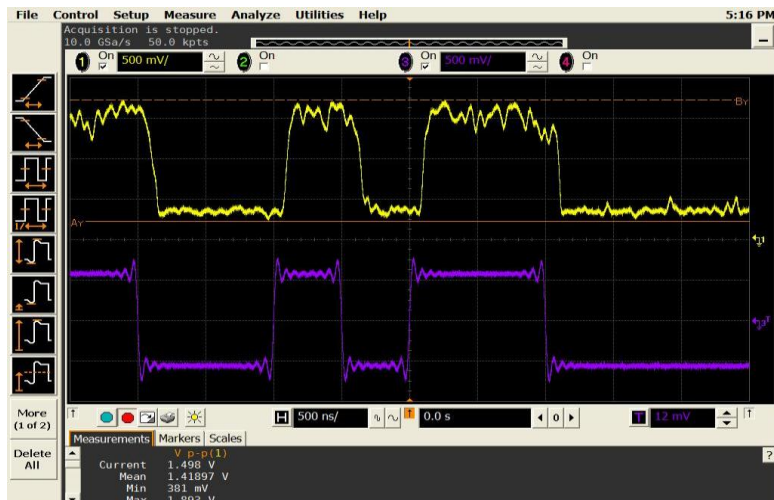
### 5.3.3 Receiver Sensitivity

The quality of the output waveform is definitely related to the signal to noise ratio ( $SNR$ ) level. Our demodulator is able to detect the desired signal only if the power of the weak carrier exceeds a conceivable level. The measured demodulated I-channel output waveforms and I/Q diagrams are plotted in Figures 5.9(a)-(d), with different signal power  $P_s$  and noise power level  $P_n$  for data symbol rate  $R_s = 2$  Msps. In our measurement, the  $SNR$  value is controlled with the use of a signal and noise combiner which combines the noise generated from the noise source with the modulated signal at the IF output (before demodulation). The signal and noise combiner employs a traditional Wilkinson power combiner scheme, with a signal branch and a noise branch. The signal input port is connected to the IF output of the down converter mixer, and the noise path

consists of a noise source, a Gali39 amplifier (16.8 dB gain @ 1 GHz), and an adjustable attenuator (0 ~ -60 dB).

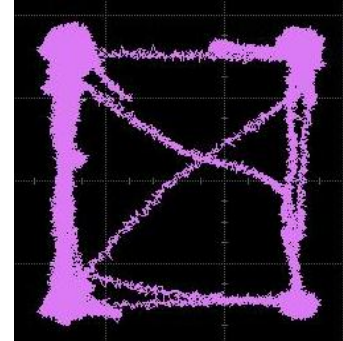
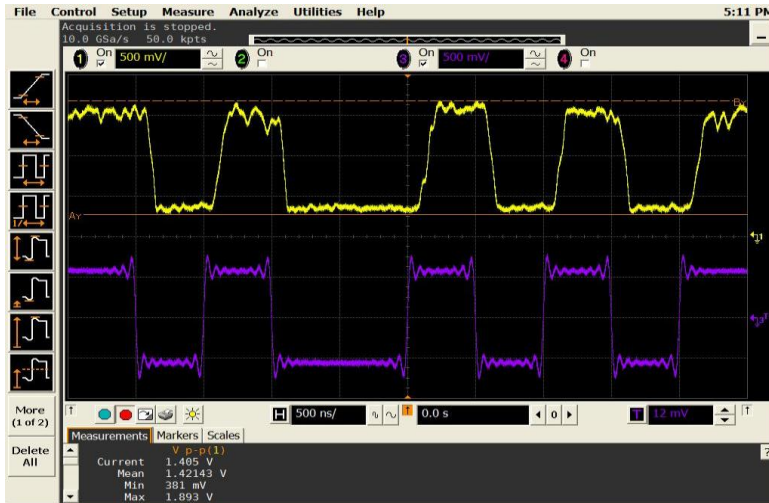


(a)

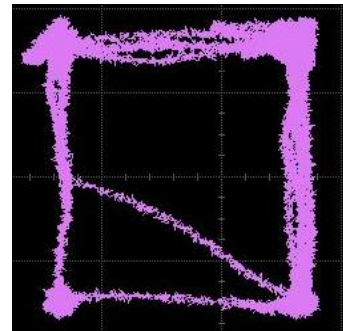
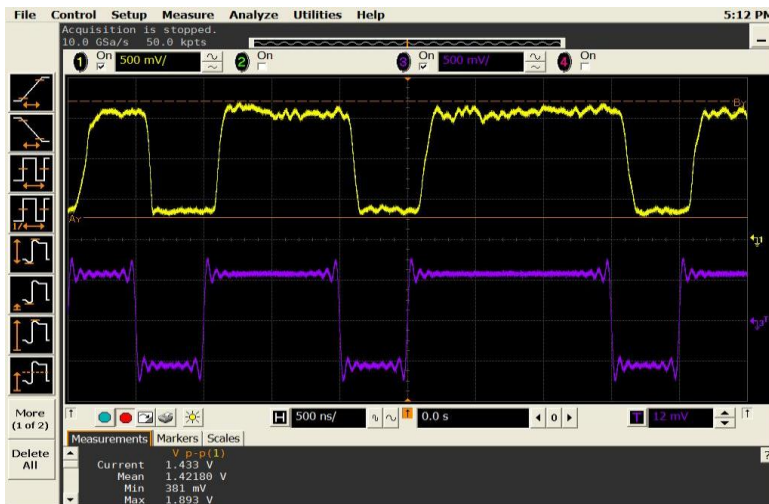


(b)





(c)



(d)

Figure 5.9: Demodulated waveform I-output (left) and I/Q diagram (right), with (a)  $SNR = -5$  dB, (b)  $SNR = 0$  dB, (c)  $SNR = 5$  dB, and (d)  $SNR = 10$  dB

Based on the figures above, the minimum acceptable  $SNR$  ( $P_s/P_n$ ) at the demodulator input for QPSK demodulation with data symbol rate  $R_s = 2$  Msps is evaluated and summarized in Table 5.4. It can be observed that the minimum  $SNR$  ( $P_s/P_n$ ) should be around or better than 5 dB in order to obtain satisfactory demodulated I/Q output signals.

Table 5.4: Minimum acceptable  $SNR$  at the demodulator input for QPSK with data symbol rate  $R_s = 2$  Msps

Signal $P_s$ (dBm)	Noise $P_n$ (dBm)	$SNR$ (dB)	Quality of Demodulation
-70	-75	-5	Bad
-70	-70	0	fair
-70	-75	+5	Satisfactory
-70	-80	+10	Good

Thus, in this case, the receiver sensitivity ( $P_{RX}$ ) is given by:

$$P_{RX} = \text{Receiver Noise Floor} + SNR_{min} = N_0 + NF + SNR_{min} \quad (5.6)$$

### 5.3.4 Bit-error rate (BER)

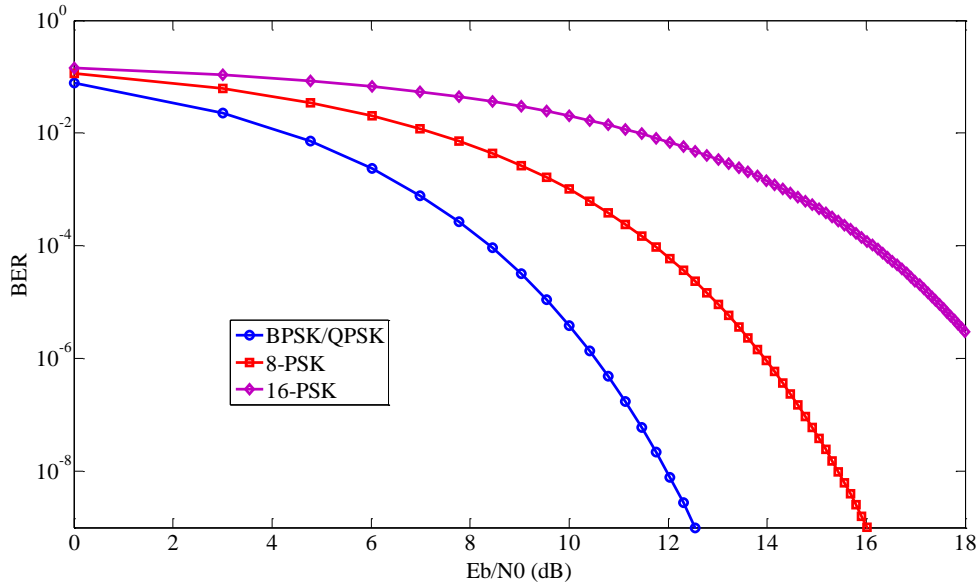


Figure 5.10:  $BER$  curves for different modulation schemes for AWGN channel

Selection of modulation method determines system bandwidth, power efficiency, and sensitivity. A given modulation technique affects the  $SNR$  necessary for a receiver to achieve a specified level of reliability in terms of BER. For BPSK/QPSK modulation,  $SNR = E_b/N_0$ , and the BER in additive white Gaussian noise (AWGN) channel is given by [81]:



$$P_e = \frac{1}{2} \operatorname{erfc}\left(\sqrt{\frac{E_b}{N_0}}\right) \quad (5.7)$$

where  $\operatorname{erfc}(x) = \frac{2}{\sqrt{\pi}} \int_x^\infty \exp(-t^2) dt$ .

Figure 5.10 compares the *BER* curves for BPSK, QPSK, 8-PSK and 16-PSK for AWGN channel. It can be found that higher order modulations exhibit higher *BER*, however in exchange they deliver a higher data rate.

### 5.3.5 Effects of RF Impairments on BER Performance

The effects of RF impairments (i.e. phase noise and phase/frequency shift) on the overall *BER* performance of receiver systems are investigated with the aid of Matlab/Simulink. The Simulink model is shown in Figure 5.11.

Figure 5.12 plots the *BER* with different phase noise values for QPSK scheme. It can be observed that the phase noise of the oscillating signal has a significant impact on receiver systems. When the phase noise is below a certain level, increasing the  $E_b/N_0$  makes little improvement on *BER* performance. For example, when phase noise is -70 dBc/Hz at 100 kHz offset for QPSK, as shown in Figure 5.12, the *BER* curve is becoming saturated at the upper bound even if the  $E_b/N_0$  increases. In addition, the effects of frequency stability of the oscillating signal on *BER* are also investigated with the phase noise -80 dBc/Hz at 100 KHz offset. Figure 5.13 shows that the *BER* performance is very sensitive to the frequency instability. Frequency drifting of a few tens of Hertz may totally ruin our system performance. It can be claimed that a pure and stable source is the “heart” of wireless systems.

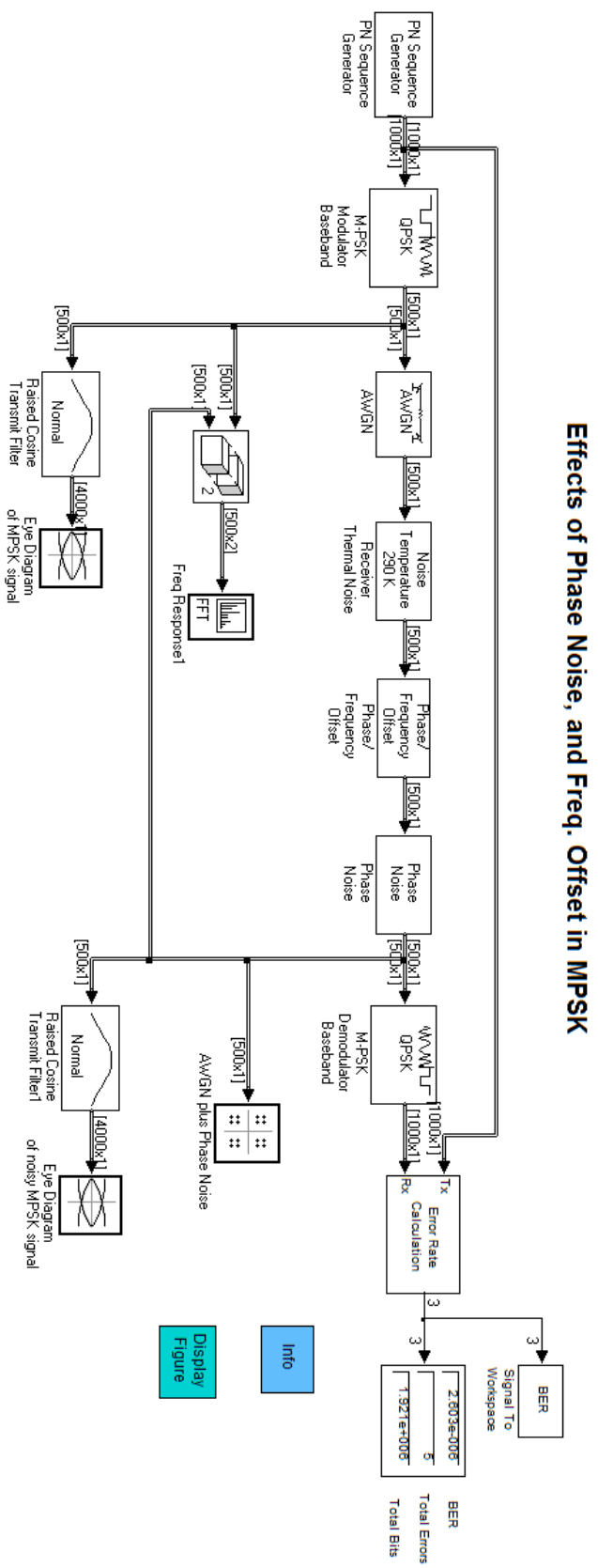


Figure 5.11: Simulink model of RF impairments in receiver systems

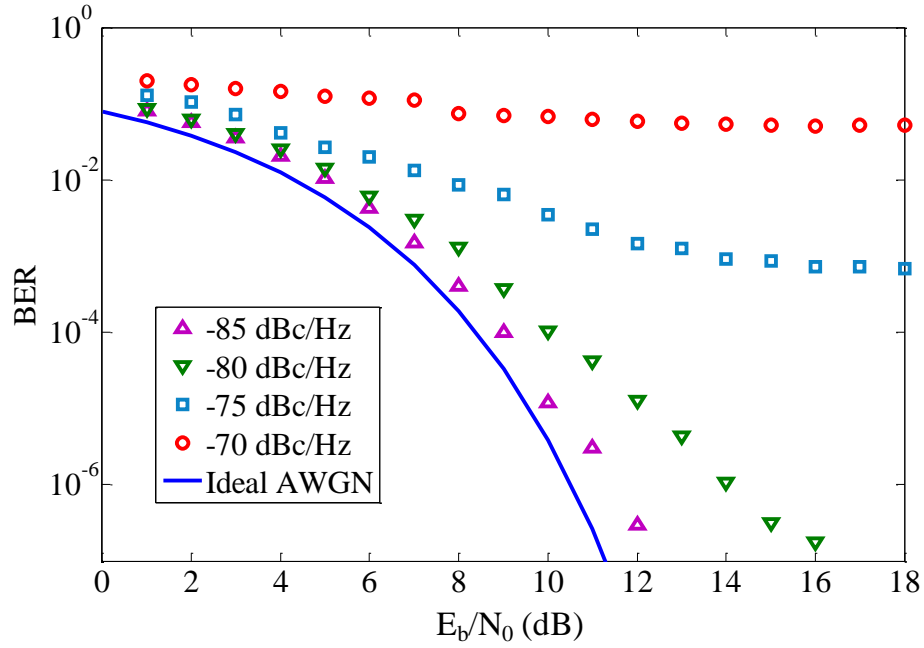


Figure 5.12: BER for QPSK with different phase noise effect

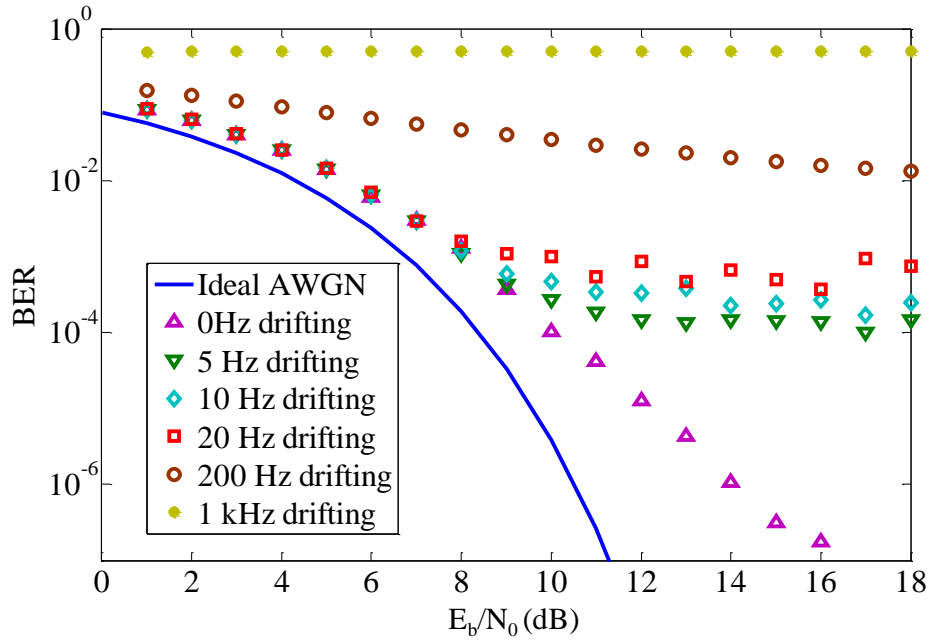


Figure 5.13: BER for QPSK with different frequency drifting effect under the condition that phase noise is -80 dBc/Hz at 100 kHz offset

## 5.4 Conclusion

In this chapter, generic architectures and parameters of receiver systems are discussed as a guideline for the development of our communication systems to be demonstrated in the following chapters. Based on the features of different receiver architectures, our communication systems employ a traditional heterodyne topology, and a dual-antenna scheme is used instead of using circulator or switch platforms for single-antenna solution which may be too lossy at millimeter-wave frequencies. In our experimental setup, the I/Q modulation is performed by using vector signal generator and a direct quadrature demodulator, AD8347 from Analog Device, is used for demodulation. The output of the demodulation board is measured with different RF input power levels  $P_{in}$  and different symbol rates  $R_s$  for QPSK scheme. Finally, receiver analysis is carried out and system parameters such as receiver noise floor, receiver sensitivity and RF impairments that may affect the BER are studied. It is found that a pure and stable source plays a crucial role in receiver systems.

## CHAPTER 6      BROADBAND MILLIMETER-WAVE SINGLE BALANCED MIXER AND ITS APPLICATION TO SUBSTRATE INTEGRATED WIRELESS SYSTEMS

Recently, millimeter-wave techniques have become prevalent in the request of high speed communication applications [82]–[84]. Meanwhile, with the increase of operation frequency in millimeter-wave region, wideband transmitters or receivers are essentially required to cope with the system design. Multi-antenna architecture thanks to short wavelength at millimeter-wave frequencies, as shown in Figure 6.1, may be used in such a broadband system without sacrificing the required antenna performance and transmitter-receiver isolation.

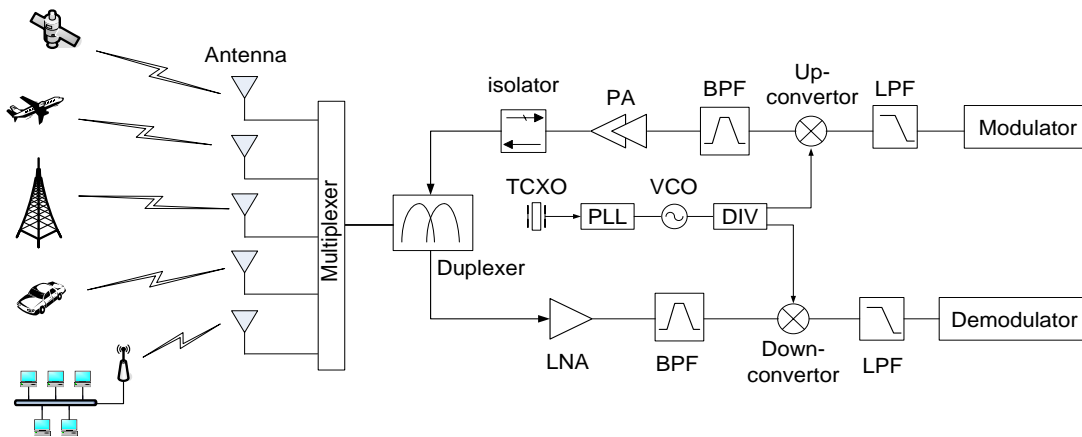


Figure 6.1: Simplified illustration of a broadband millimeter-wave system

As one basic building block of communication systems, millimeter-wave mixers have widely been studied, especially with regards to the aspects of port isolation and spurious rejection. As has been well known, balanced-type mixers have advantages of good isolation and undesired signal suppression, higher power-handling capabilities and so on. Typically, balanced mixers consist of nonlinear devices interconnected by single or multiple hybrids, transformers, or baluns. In particular, the fundamental types of single balanced mixer usually involve 180-degree or 90-degree hybrids. Compared with the 90-degree hybrid mixers, the 180-degree circuits exhibit superior electrical performance such as better RF-to-LO isolation and less spurious products [85].

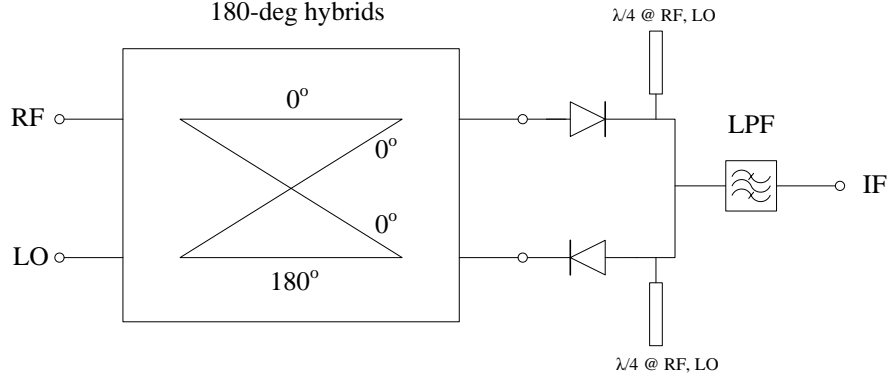


Figure 6.2: Circuit diagram of conventional single balanced diode mixer

In this chapter, we present a broadband millimeter-wave single balanced mixer according to the circuit diagram as described in Figure 6.2. Our proposed 180-degree hybrid consists of a standard H-plane 3-dB coupler and the 90-degree broadband SIW phase shifter proposed in Chapter 3. Compared to the previously reported structures [86]–[88], our proposed mixer shows its advantages of broad bandwidth, excellent port-to-port isolation, small insertion loss, low profile and easy integration in SIW circuits. Therefore, it can easily be used at millimeter-wave frequencies, and also its structure is favourable for the microwave integrated circuit applications. To demonstrate the design methodology and structural features, a K-band prototype of the proposed broadband millimeter-wave single balanced mixer is designed and implemented with our PCB fabrication process and surface mounted diodes. The proposed design methodology is validated by simulated and measured results.

Moreover, a receiver front-end, which integrates an SIW slot array antenna and our proposed mixer in a single layer substrate, is developed as a particular effort to establish a geometry-compact, low-cost and low-profile architecture. Experimental validation of a K-band wireless communication system integrated with our receiver front-end is then presented. EVM and signal to noise ratio (SNR) are investigated for M-QAM schemes. EVM is commonly used to measure the departure of signal constellation from its ideal reference in wireless communication standards such as wireless local area network (WLAN) where a maximum level of EVM is specified [89]–[90]. In fact, the proposed mixer can also be employed in radar systems.

## 6.1 180-degree Hybrid Implemented with Broadband Slotted SIW Phase Shifter

Figure 6.3 illustrates our proposed 180-degree hybrid that consists of an H-plane 3-dB coupler and the aforementioned broadband 90-degree slotted SIW phase shifter. Herein, the design procedure of the 90-degree phase shifter is omitted since it has been well demonstrated in Chapter 3. To comply with the fabrication condition based on our in-house PCB processing technique, a K-band 180-degree hybrid is designed to verify the proposed design methodology and the above-discussed electrical performance. An experimental prototype is fabricated on substrate RT6002 with thickness of 0.254 mm and dielectric constant  $\epsilon_r = 2.94$ . Physical dimensions of the designed broadband 180-degree hybrid are given in Figure 6.3. Microstrip line feeders are used in the sum and difference input ports and they are designed for 50 Ohm condition.

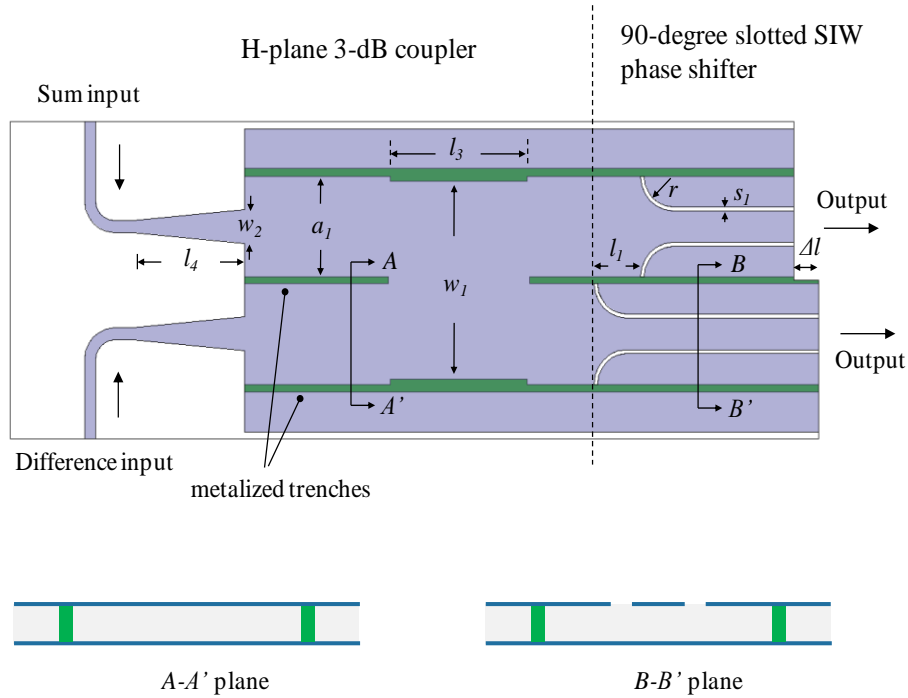


Figure 6.3: Physical dimensions of the experimental prototype of the proposed 180-degree hybrid ( $w_1 = 10.03$  mm,  $w_2 = 1.7$  mm,  $l_1 = 2.5$  mm,  $\Delta l = l_2 - l_1 = 1.34$  mm,  $l_3 = 7.36$  mm,  $l_4 = 6$  mm,  $r = 1.55$  mm,  $s_1 = 0.2$  mm, and  $a_1 = 5.1$  mm).

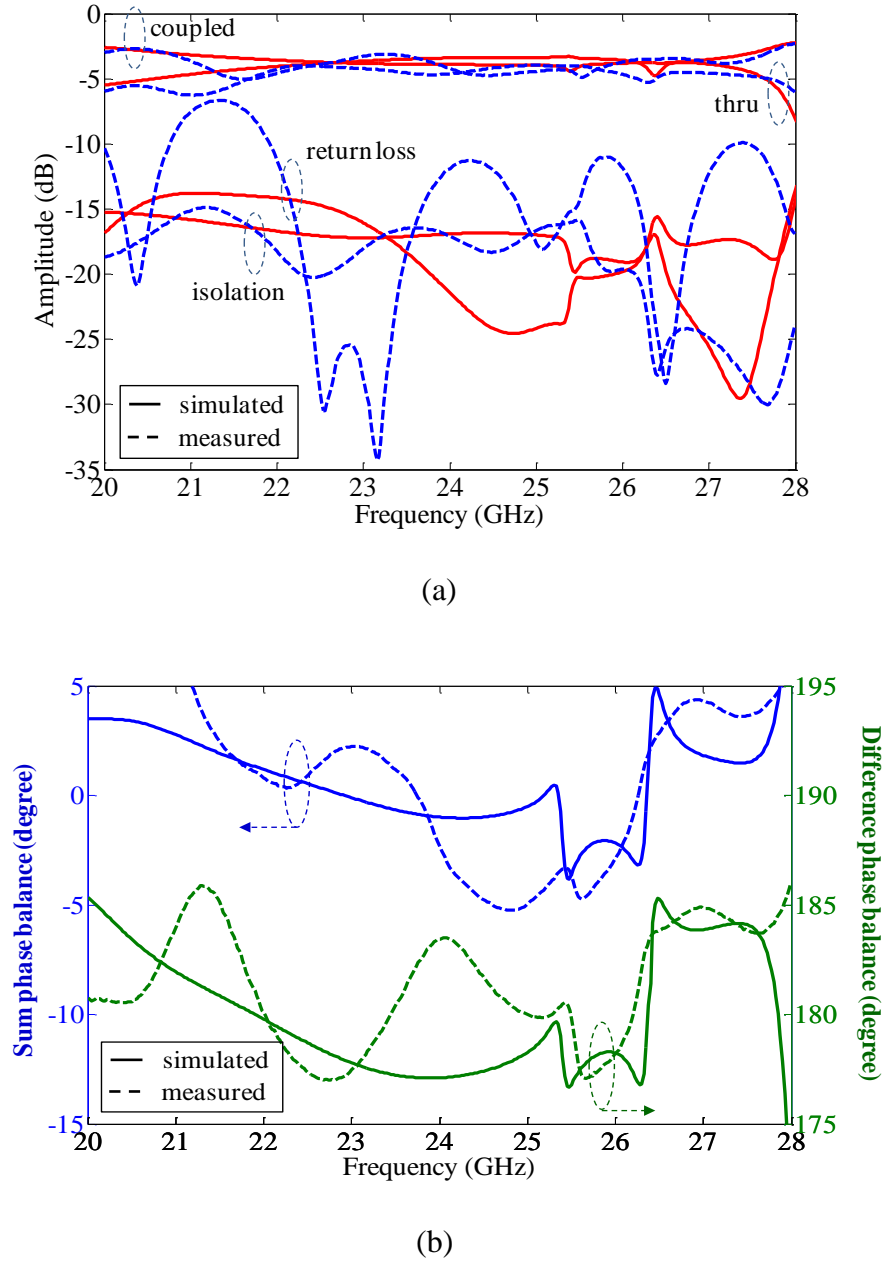


Figure 6.4: Simulated and measured S-parameters of the experimental prototype of the proposed 180-degree hybrid (a) amplitude responses and (b) phase balances.

Figures 6.4(a) and 6.4(b) show simulated and measured amplitude responses and phase balances of the K-band 180-degree hybrid prototype, respectively. The circuit simulation is made with the aid of Ansoft HFSS v12.0.1. The measurements are carried out by using an Anristu 37397 vector network analyzer. From Figure 6.3, it should be noted that the output port impedance is not 50



Ohm. For the convenience of experimental measurements, a quarter-wave microstrip impedance transformer is used at the output ports to convert the grounded CPW line to 50 Ohm microstrip line. Of course, the circuit performance degrades by doing this because of the discontinuities and limited bandwidth of the quarter-wave impedance transformer.

It can be observed that the measured amplitude and phase imbalance between output ports of the experimental prototype are within 1.5 dB and  $\pm 5^\circ$ , respectively, across a broad bandwidth from 22 to 27 GHz. In addition, the input port isolation and return loss are both better than -10 dB in the frequency range of interest. The discrepancy between the simulated and measured results is mainly attributed to effects of the impedance transformer.

## 6.2 Broadband Single Balanced Mixer

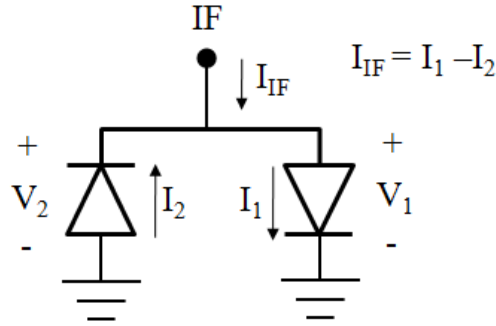


Figure 6.5: Currents and voltages in the diodes of a 180-degree balanced mixer.

When the *RF* signal voltage and *LO* injection are coupled to the anti-parallel diodes, the corresponding currents go through all the *PN* junctions with opposite directions, as shown in Figure 6.5. Owing to the non-linearity of the diodes, these currents interact with each other.

There are two sub-currents,  $I_1$  and  $I_2$ , flowing through the diodes. They are determined by the voltages from the *RF* signal and *LO* injection,  $V_{RF}$  and  $V_{LO}$ :

$$I_1 = a_1 V_1 + a_2 V_1^2 + a_3 V_1^3 + a_4 V_1^4 + \dots \quad (6.1)$$

$$I_2 = -a_1 V_2 + a_2 V_2^2 - a_3 V_2^3 + a_4 V_2^4 + \dots \quad (6.2)$$

where  $a_k = k^{\text{th}}$  order non-linearity coefficient of diode, and

$$V_1 = -V_{LO} \cos(\omega_{LO}t) + V_{RF} \cos(\omega_{RF}t + \varphi) \quad (6.3)$$

$$V_2 = V_{LO} \cos(\omega_{LO}t) + V_{RF} \cos(\omega_{RF}t + \varphi) \quad (6.4)$$

And the IF current is

$$I_{IF} = I_1 - I_2 \quad (6.5)$$

Equations (6.3) and (6.4) are substituted into (6.1) and (6.2). These are, in turn, substituted into (6.5). Trigonometric identities are used to find the current components at the various mixing frequencies. It can be obtained that

$$\begin{aligned} I_{IF} = & -[2a_2V_{RF}V_{LO} + 4a_4V_{RF}V_{LO}(V_{RF}^2 + V_{LO}^2) + \dots]\cos\{\omega_{IF}t + \varphi\} \\ & -[2a_2V_{RF}V_{LO} + 4a_4V_{RF}V_{LO}(V_{RF}^2 + V_{LO}^2) + \dots]\cos\{(\omega_{RF} + \omega_{LO})t + \varphi\} - \dots \end{aligned} \quad (6.6)$$

By filtering out the high frequency items,

$$I_{IF} = -[2a_2V_{RF}V_{LO} + 4a_4V_{RF}V_{LO}(V_{RF}^2 + V_{LO}^2) + \dots]\cos\{\omega_{IF}t + \varphi\} \quad (6.7)$$

Equation (6.7) implies that the odd order non-linearity terms are cancelled with each other. The desired IF signal can be produced only by the even order non-linearity terms.

A K-band single balanced diode mixer is developed by employing the aforementioned 180-degree hybrid. Again, the mixer is fabricated on substrate RT6002 with 0.254 mm thickness and  $\epsilon_r = 2.94$ . Figure 6.6 shows the photograph of our proposed broadband mixer. Diodes used in our circuit are GaAs schottky diode *MGS901* from Aeroflex. Two butterfly stubs are used to prevent the LO and RF signals from leaking into IF port. In addition, a microstrip LPF with a cutoff frequency of 4 GHz is designed at the IF port to suppress the signals other than IF frequency. Since the diode resistance is not 50 Ohm, the output impedance of the 180-degree hybrid is not designed to 50 Ohm. Good matching can be achieved by designing the LPF properly. One of the significant benefits of the proposed structure is that the IF frequency is under the cutoff frequency of the SIW lines. Therefore, no specific design should be considered to prevent the IF signal from leaking into RF/LO port. This results in a significant improvement of conversion efficiency.

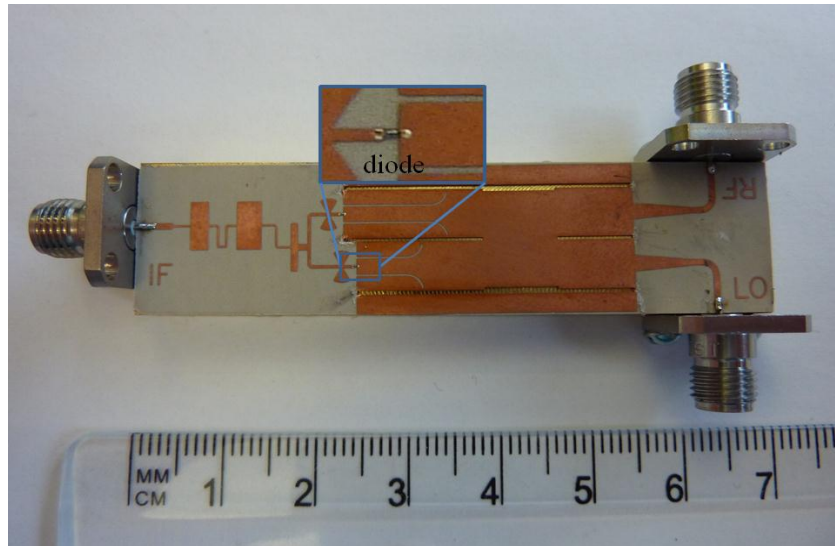


Figure 6.6: Photograph of the proposed broadband single balanced diode mixer

This developed K-band single balanced mixer was measured using spectrum analyzer Rohde & Schwartz FSIQ40. The RF and LO signals are generated by microwave signal generators Anritsu MG3694A. The conversion gain/loss is plotted in Figure 6.7, from which it can be observed that this mixer exhibits a fairly good performance as both down-converter and up-converter. The measurements are performed with LO power  $P_{LO} = 13$  dBm and IF frequency  $f_{IF} = 1.45$  GHz. Meanwhile, Figure 6.8 shows the curve of the measured conversion gain/loss versus IF bandwidth, where the LO input power is 13 dBm at 21 GHz. The measured IF frequency is in the range of DC-4 GHz with a conversion gain/loss better than -10 dB. The IF bandwidth is actually broader considering effects of the LPF.

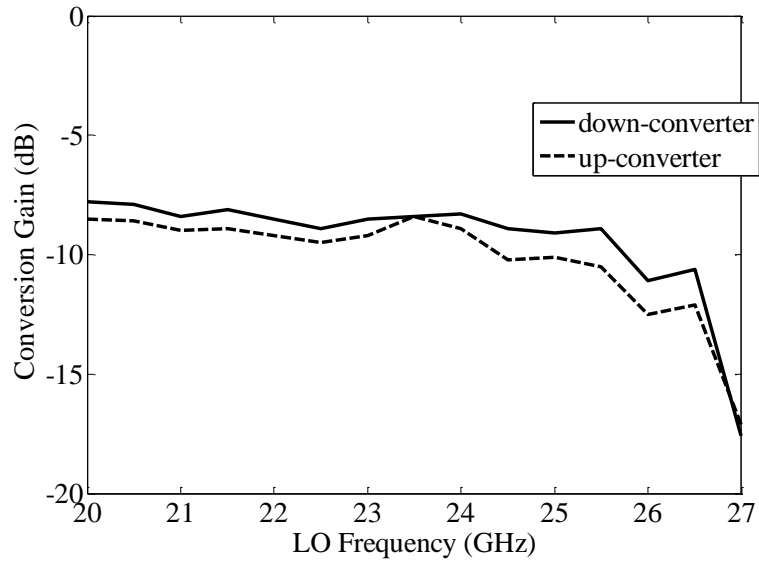


Figure 6.7: Measured conversion gain/loss of the proposed mixer performed as up-converter and down-converter ( $P_{LO} = 13$  dBm and  $f_{IF} = 1.45$  GHz)

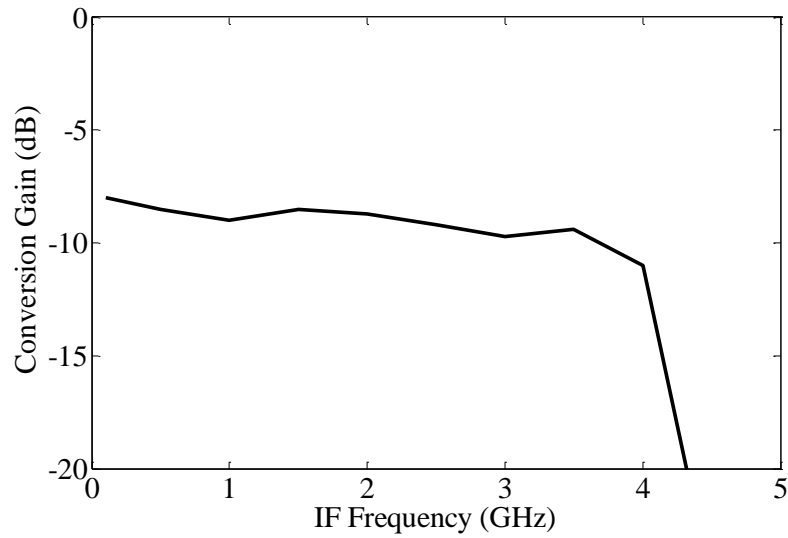


Figure 6.8: Measured conversion gain/loss versus IF bandwidth ( $P_{LO} = 13$  dBm @ 21 GHz)

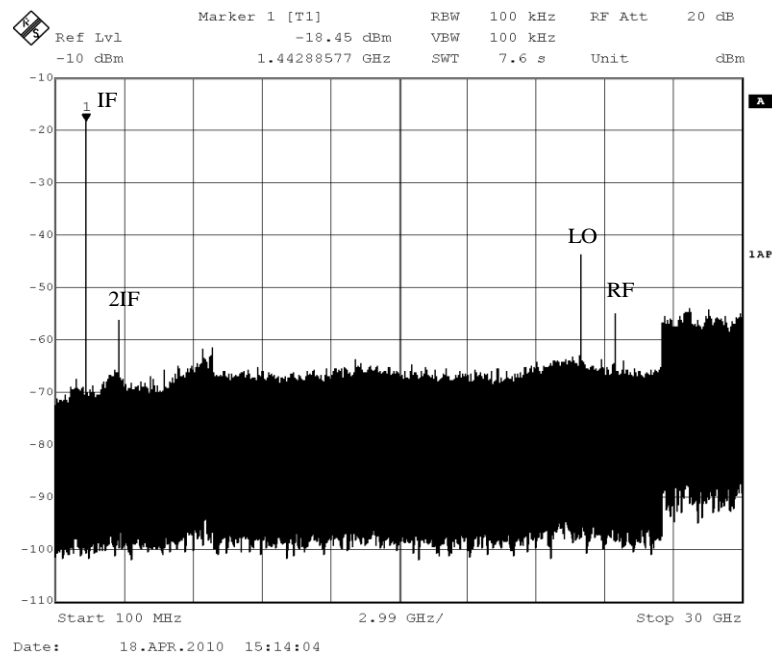


Figure 6.9: Mixing spectrum of the proposed single balanced mixer

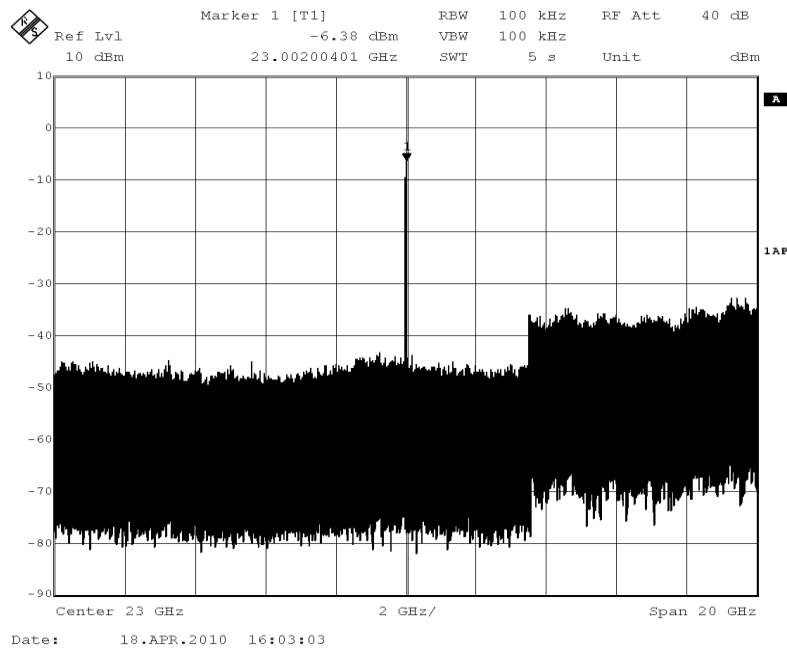


Figure 6.10: Measured LO-RF isolation

For our circuit design, good LO-RF and LO-IF isolations can be guaranteed thanks to the implementation of our 180-degree hybrid. Moreover, a high-selectivity of the LPF yields a good performance of the RF-IF isolation. Figure 6.9 displays the measured IF port spectrum of this mixer performed as a downconverter, with the RF input of -10 dBm and the LO input of 13 dBm, from which it can be found that the LO-IF and RF-IF isolations are about -55 dB and -45 dB, respectively. Measured LO leakage at the RF port is shown in Figure 6.10, suggesting that the LO-RF isolation is about -20 dB.

It is worth mentioning that the proposed mixer circuit also exhibits an excellent property of linearity. As illustrated in Figure 6.11, an input 3rd order intercept (IP3) measurement is carried out by using two tones separated with 2 MHz. Figure 6.12 displays the measured input-IP3 and input compression point  $P_{1dB}$  of the proposed mixer when it is performed as a downconverter, with LO input of 13 dBm. It is observed that the input-IP3 and  $P_{1dB}$  of our mixer is around 15 dBm and 9 dBm, respectively.

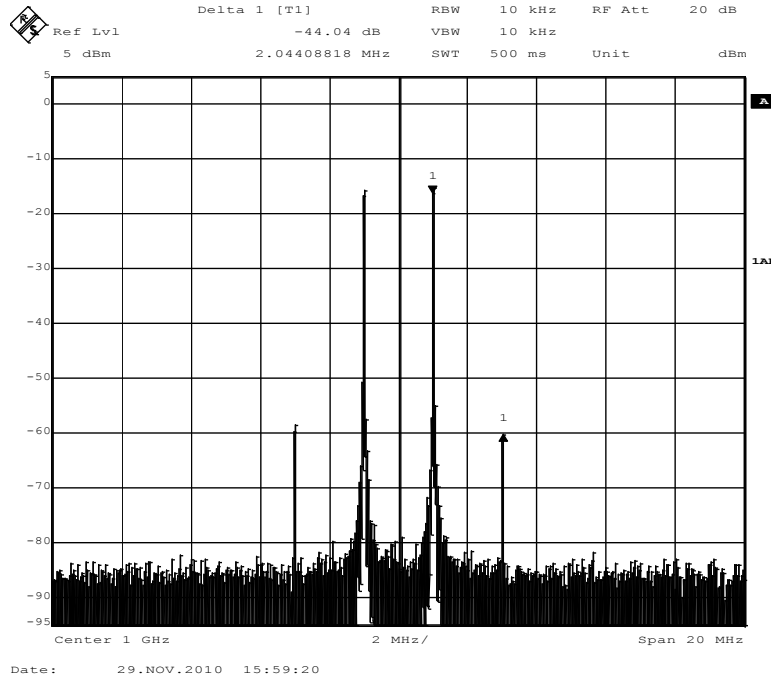


Figure 6.11: Two-tone inter-modulation test of the proposed single balanced mixer ( $P_{LO} = 13$  dBm @ 25 GHz).

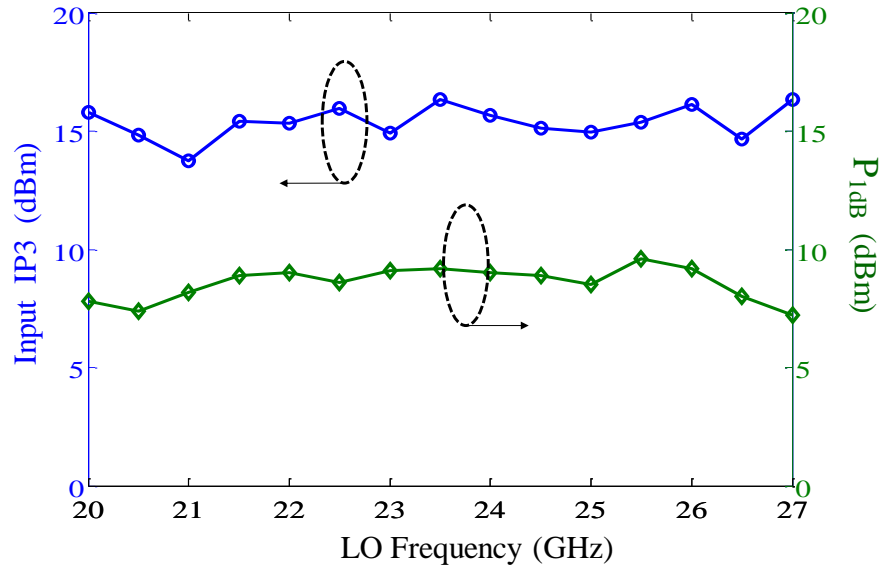


Figure 6.12: Measured Input IP3 and  $P_{1dB}$  points of the proposed mixer performed as down-converter ( $P_{LO} = 13$  dBm and  $f_{IF} = 1.45$  GHz).

### 6.3 Our Proposed K-band Receiver Front-end

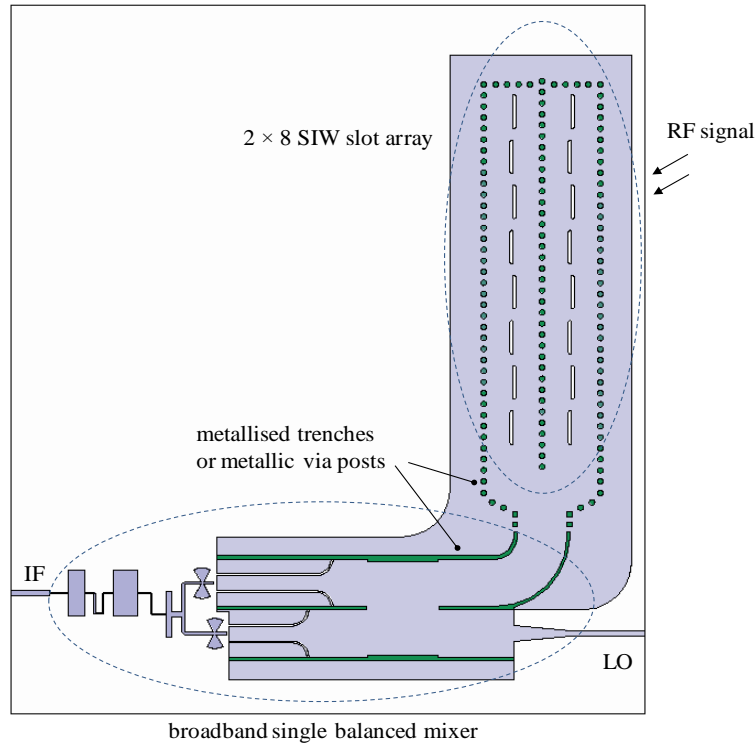


Figure 6.13: Layout of our proposed K-band receiver front-end

In this section, a K-band receiver front-end system is designed and implemented using our proposed broadband mixer. Figure 6.13 shows the layout of the K-band receiver front-end. In this design, the RF signal is first received by an SIW slot array and then fed into our K-band mixer, which functions as a down-converter. The receive antenna in our system is a  $2 \times 8$  slot array in order to achieve a high gain and the center RF frequency is around 24 GHz. The substrate used is again Rogers RT6002 with dielectric constant of 2.94 and thickness of 0.254 mm.

Longitudinal slot in the broad wall of an SIW is the basic building element in the slot antenna structure. Such longitudinal slots are set to interrupt transverse conduction currents which cause the radiation of electromagnetic energy from the waveguide. Stevenson was the first to calculate the impedance of different types of slots in a rectangular waveguide [69]. According to his work, a longitudinal resonant slot (slot length is equal to  $\lambda/2$ ) in the broad wall of a rectangular waveguide can approximately be modelled as a pure normalized admittance, which is given by

$$g = \frac{480}{73\pi} \frac{\lambda_g}{\lambda} \frac{a}{b} \cos^2\left(\frac{\pi\lambda}{2\lambda_g}\right) \sin^2\left(\frac{\pi d}{a}\right) \quad (6.8)$$

where  $a$  and  $b$  are interior dimensions of the rectangular waveguide,  $\lambda$  and  $\lambda_g$  are wavelengths in free space and in the waveguide, respectively.  $d$  is the displacement from the central line of the broad waveguide wall, as shown in Figure 6.14. Although (6.8) is an approximate formula which comes from conventional air-filled waveguide structures, it can provide a sufficient accuracy for the SIW slot array antenna design when low permittivity substrate ( $\epsilon_r < 3$ ) is used.

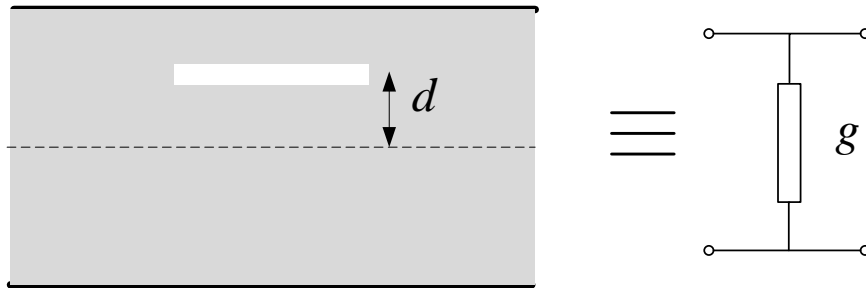


Figure 6.14: Longitudinal slot in the broad wall of an SIW



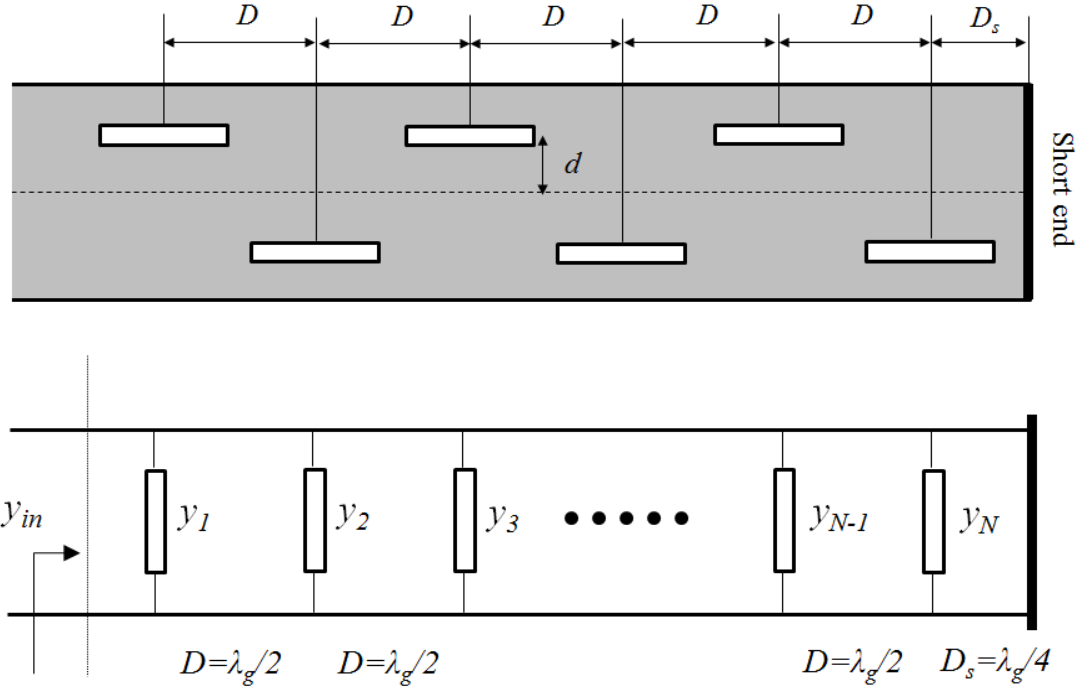


Figure 6.15: Equivalent circuit of a linear SIW array

Figure 6.15 shows the equivalent circuit of a linear SIW array. The input impedance of a length of transmission line with an arbitrary load impedance is given by

$$Z_{in} = Z_0 \frac{Z_L + jZ_0 \tan \beta l}{Z_0 + jZ_L \tan \beta l} \quad (6.9)$$

Based on this equation, it can be found that the space between neighboring slots  $l = D = \lambda_g/2$  gives a zero value for  $\tan(\beta l)$ , which means that the normalized input standing wave admittance can be obtained:

$$y_{in} = \sum_{n=1}^N y_n + y_s \quad (6.10)$$

Setting  $D_s = \lambda_g/4$  and using again equation, it shows that  $y_s = 0$ . Now for the good matching, we need

$$y_{in} = \sum_{n=1}^N y_n = 1 \quad (6.11)$$

For a simplified design with uniform power distribution of the slot array, (6.8) shows that

$$g = \frac{480}{73\pi} \frac{\lambda_g}{\lambda} \frac{a}{b} \cos^2\left(\frac{\pi\lambda}{2\lambda_g}\right) \sin^2\left(\frac{\pi d}{a}\right) = \frac{1}{N} \quad (6.12)$$

Therefore,  $d$  can be calculated according to other known factors  $a$ ,  $b$ ,  $\lambda$  and  $\lambda_g$ .

Furthermore, one can also calculate the array factor using the following relation:

$$F_a(\theta) = \frac{1}{N} \left\{ \left[ \sum_{n=1}^N \cos(\alpha_n \cos \theta) \right]^2 + \left[ \sum_{n=1}^N \sin(\alpha_n \cos \theta) \right]^2 \right\} \quad (6.13)$$

where  $\alpha_n = (n-1)kD = (n-1)\pi \frac{\lambda_g}{\lambda}$

It should be noted that the Stevenson's relations ignore the slot reactances, which may give incorrect results for slot antenna design. Normally, a strong coupling between slot elements due to large slot size and high permittivity material and the large offsets from the central line can cause the slot reactances non-ignorable, and make the Stevenson's relations ineffectual. In these cases, design procedure from Elliot's papers [91] gives much more accurate solution. But of course, it is more complicated and the design has to be finished by using numerical method.

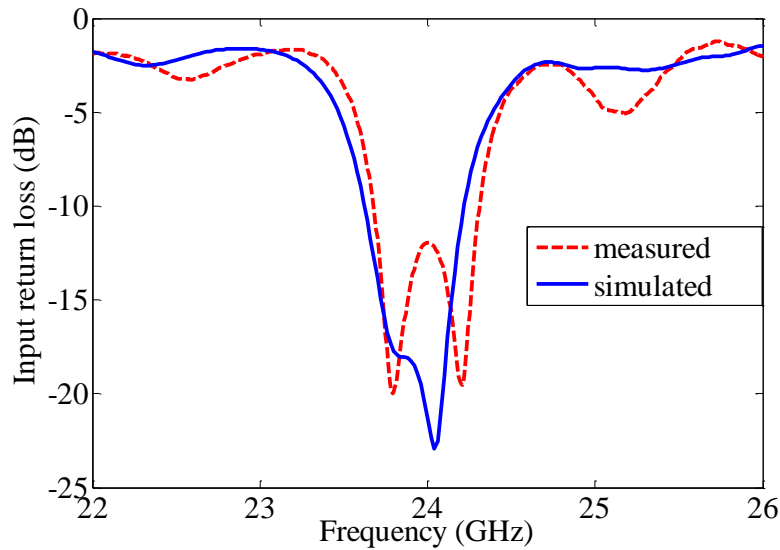


Figure 6.16: Measured input return loss of the SIW slot array

Figure 6.16 shows simulated and measured input return losses of our designed  $2 \times 8$  slot array antenna. It can be seen that the measured operating frequency slightly shifts towards an upper band due to the deviation of the dielectric constant. The -10 dB bandwidth is extended from 23.7 GHz to 24.3 GHz. It should be noted that the ripple in the out-of-band of the antenna is mainly attributed to the microstrip-to-SIW transition that is used for measurement. The radiation patterns of our  $2 \times 8$  slot array at 24 GHz are also plotted in Figure 6.17. It is observed that the measured gain and side-lobe level of our receive antenna are about 13 dBi and 21 dB, respectively.

With the aid of noise figure analyzer Agilent N8975A, the noise figure of the receiver front-end is measured. The measured single-sideband (SSB) noise figure is about 9 dB in the frequency range from 23.7 to 24.3 GHz. Actually, the receiver noise figure can be improved by introducing a low-noise amplifier (LNA) in front of our mixer. The LNA is not applied in our receiver front-end for the consideration of a simplified demonstration.

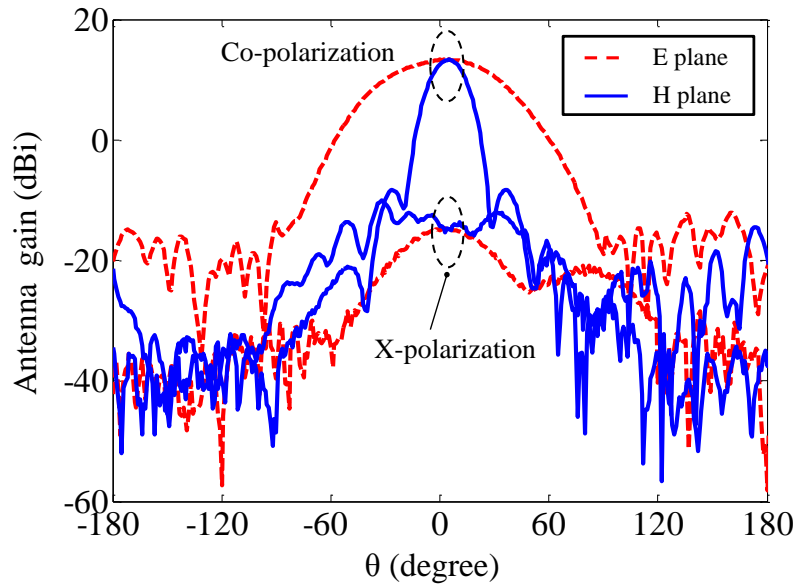


Figure 6.17: Measured radiation patterns of the SIW slot array at 24 GHz

## 6.4 Experimental Measurement of K-band Wireless Communication System

### 6.4.1 System Test Setup for Line-of-sight Channels

To demonstrate the system performance of the proposed receiver front-end, a vector signal wireless communication system is set up. Figure 6.18 depicts the block diagram of the proposed system measurement. At the transmitter end, a pseudorandom (PN) binary sequence is modulated to IF signal  $f_{IF}$  by a vector signal generator (VSG) Agilent E4483C, in M-QAM form. Thereafter, the modulated signal is up-converted to a 24 GHz RF signal by a sub-harmonic mixer HMC264 from Hittite. Anritsu MG3694A provides a -4 dBm, 11.5 GHz carrier signal  $f_{LO}$  for the mixer. The RF signal is then fed into a standard horn antenna SGH (18-26.5 GHz, with a gain of 24 dBi) for transmission. At the receiver side, the received RF signal is down-converted to IF signal using our proposed K-band receiver front-end. A signal generator (Anritsu MG3694A) provides a +13 dBm carrier signal for our proposed single balanced mixer. The IF output signal is then amplified by a two-stage surfaced mounted amplifier cascaded by using GALI-39 from Mini-Circuits. This output signal is sent to a vector signal analyzer (VSA) Agilent 89600 (i.e., an Agilent DSO81204B oscilloscope with VSA software) for analog to digital conversion (ADC), demodulation, and synchronization. The noise generated from a noise source (HP346C) is combined with the modulated signal at the amplifier output (before demodulation) in order to control the SNR conditions.

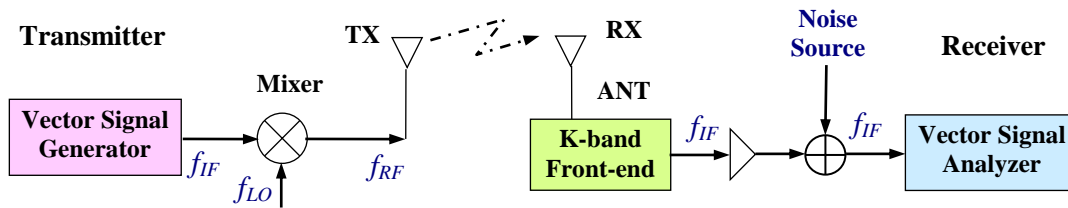


Figure 6.18: System test setup for the K-band receiver front-end

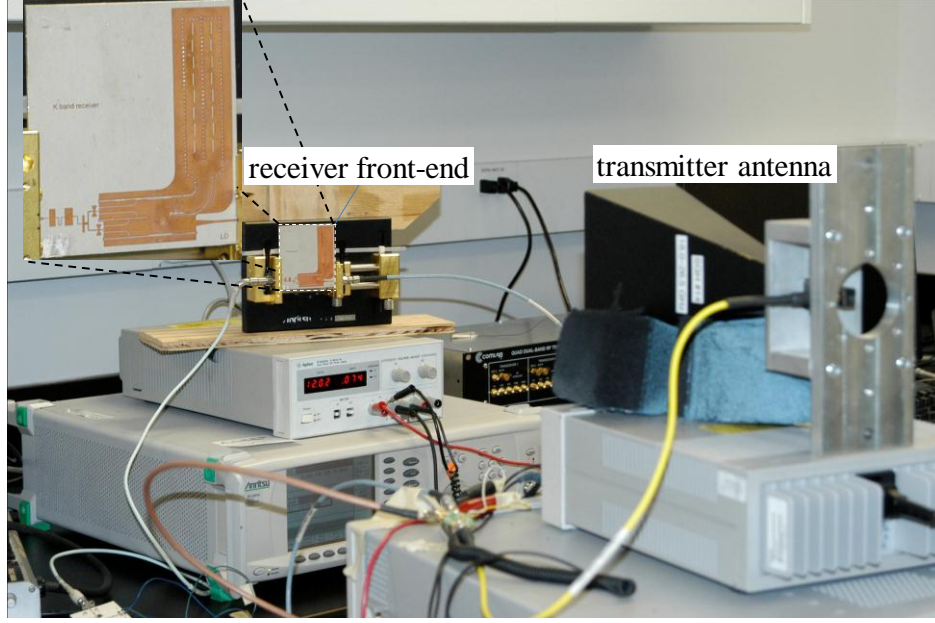


Figure 6.19: Photograph of our test setup

The photograph of our system test setup for LOS channels is shown in Figure 6.19. The characteristic of 24 GHz propagation channel, power analysis, received SNR and EVM are important aspects for wireless communication systems. First of all, the transmitter and receiver front-end modules are tested separately with respect to the RF performance. In the frequency range of interest between 23.7 GHz and 24.3 GHz, the total gains of the transmitter front-end and receiver front-end are around 12 dB and 4 dB, respectively. In addition, the LOS path loss ( $PL$ ) of the 24 GHz wireless channel is measured in our laboratory environment, using two standard horn antennas (SGH 18-26.5 GHz). Theoretically, propagation  $PL$  can be calculated by:

$$PL(dB) = 20 \log\left(\frac{4\pi d}{\lambda}\right) \quad (6.14)$$

where  $d$  is the distance between receiver and transmitter,  $\lambda$  is free space wavelength. As shown in Figure 6.20, it can be seen that the theoretic  $PL$  is the lower bound of the measured  $PL$  and their values are very close.

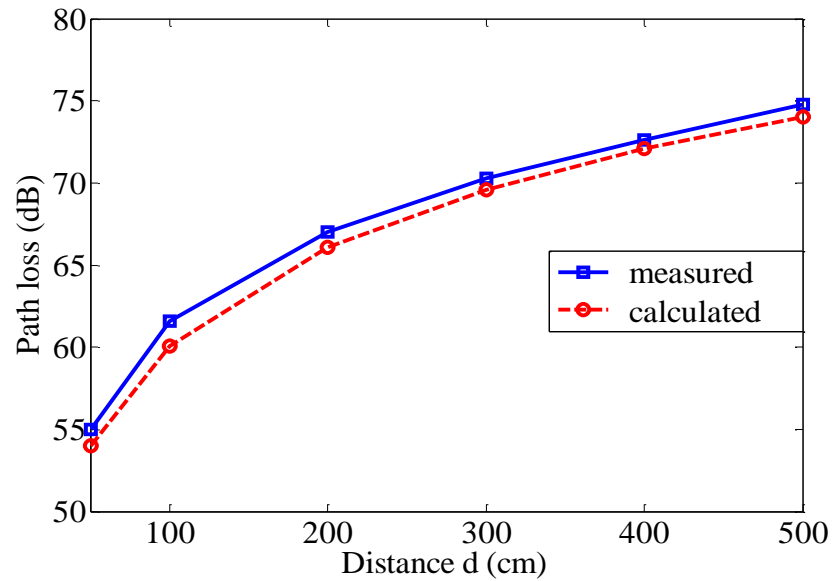
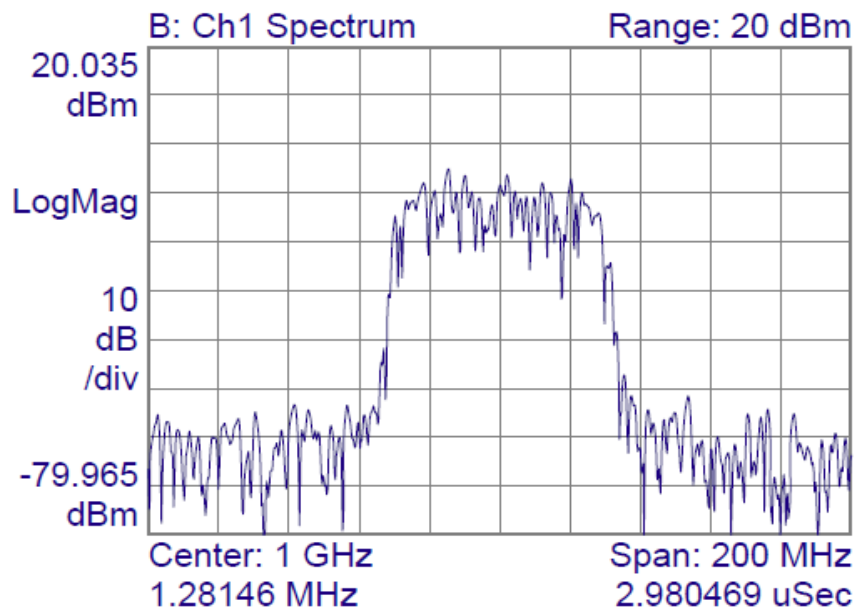
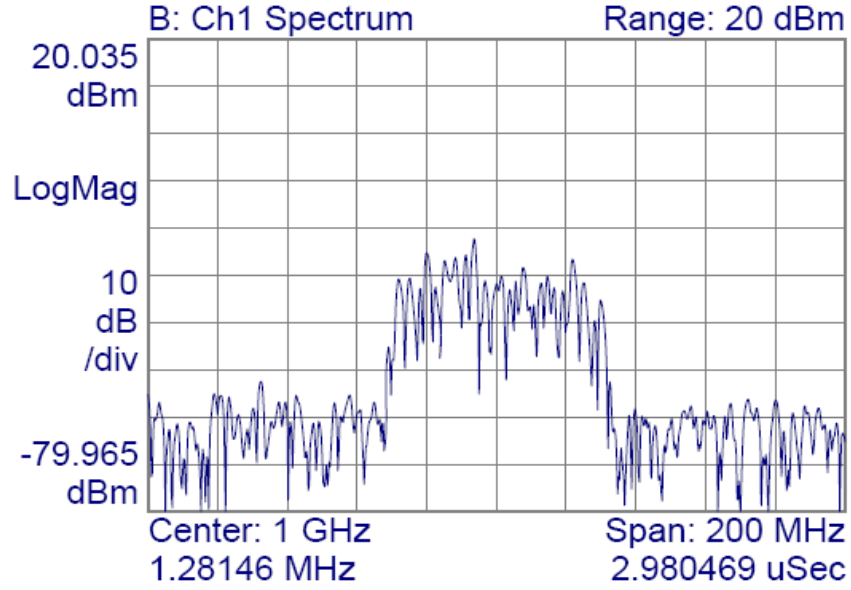


Figure 6.20: Measured and calculated  $PL$  at 24 GHz



(a) Transmitter IF output spectrum



(b) Receiver IF output spectrum

Figure 6.21: Measured spectra for QPSK at transmitter and receiver IF output with  $R_s = 50$  Msps,  $d = 1$  m.

Thereafter, the overall system measurement is carried out with a distance of  $d = 1$  m to 3 m (i.e.,  $PL = 60 \sim 70$  dB) between the transmitter and the receiver. The IF frequency is set to  $f_{IF} = 1$  GHz. Various modulation schemes such as QPSK, 8PSK, 16QAM, and 32 QAM are generated by Agilent E4438C VSG. The baseband modulation filter is set to be a square root raised cosine (SRRC) filter with a roll-off factor of 0.35. At the receiver side, Agilent 89600 VSA is used to measure the transceiver system parameters such as received SNR, EVM, output spectrum and so on. Due to the confined sensitivity of VSA, the received IF output signal is amplified by a two-stage amplifier with a gain of 26 dB. Figures 6.21(a) and 6.21(b) compare the measured spectra of the transmitted and the received modulated IF signals, with  $d = 1$  m,  $f_{IF} = 1$  GHz, transmitted IF power  $P_{IF} = 2$  dBm, and a symbol rate of  $R_s = 50$  Msps. It is observed that the received IF signal spectrum shows its similarity to transmitted IF signal spectrum. The received power spectrum with a bandwidth of 50 MHz is higher than -35 dBm.

### 6.4.2 Constellation Diagram and EVM

The signal constellation and root-mean square (RMS) EVM are extensively used to evaluate the quality of communication systems, particularly when digital modulation is employed. Compared with BER, EVM test is time efficient, and it can directly reveal the underlying impairments that cause degradation.

Figure 6.22 shows the graphical representation of error vector. The EVM is calculated with the ratio of the power of the error vector to the root mean square (RMS) power of the reference. It is defined in percentage as:

$$EVM (\%) = \sqrt{\frac{P_{error}}{P_{reference}}} \times 100\% \quad (6.15)$$

where  $P_{error}$  is the RMS power of the error vector. For single carrier modulations,  $P_{reference}$  is, by convention, the power of the outermost point in the reference signal constellation.

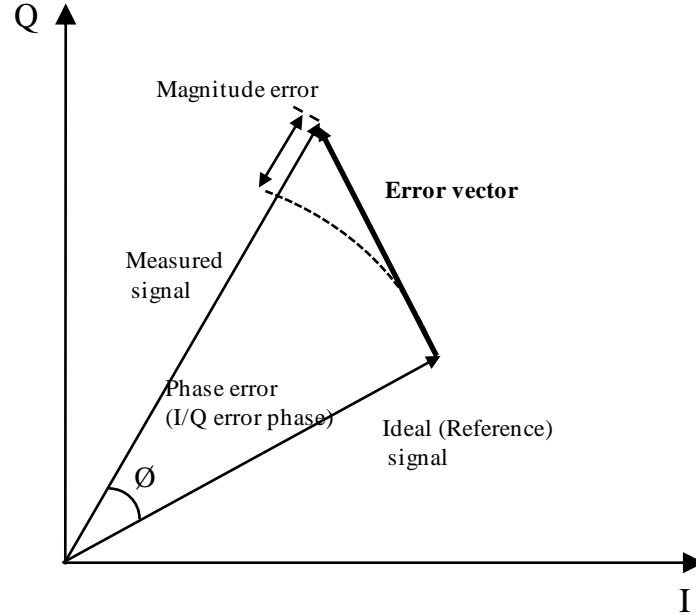


Figure 6.22: Graphical representation of error vector

What's more, for M-ary modulation, the BER can be related with the EVM as follows [92]:



$$P_b \approx \frac{2(1-\frac{1}{L})}{\log_2 L} Q \left[ \sqrt{\left[ \frac{3 \log_2 L}{L^2 - 1} \right] \frac{2}{EVM_{RMS}^2 \log_2 M}} \right] \quad (6.16)$$

where  $L$  is the number of levels in each dimension of the  $M$ -ary modulation system. Based on (6.16), the BER versus EVM curves can be plotted for  $M$ -ary modulations, as shown in Figure 6.23.

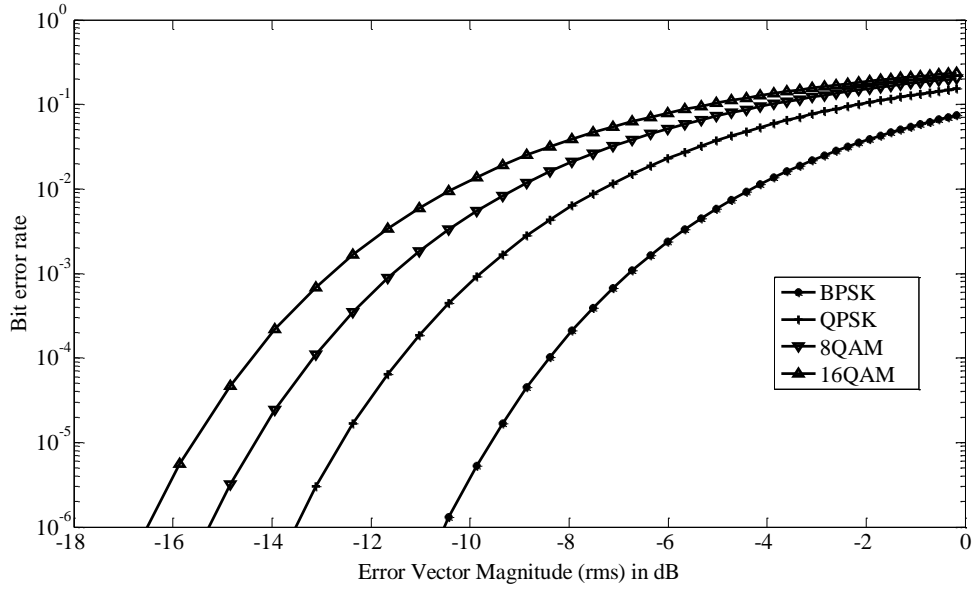
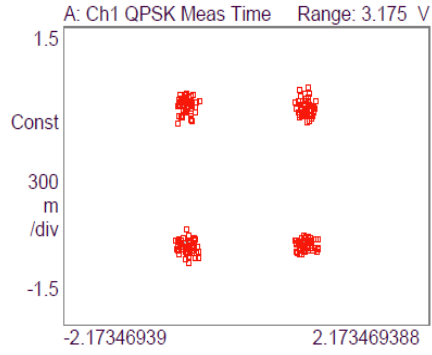
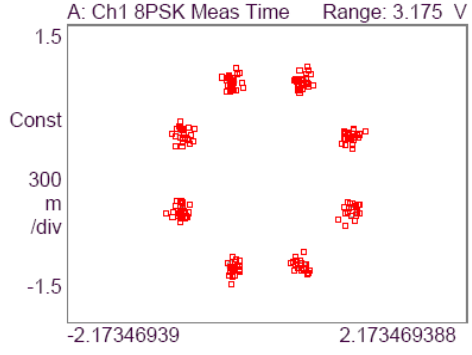


Figure 6.23: BER versus EVM for  $M$ -ary modulations

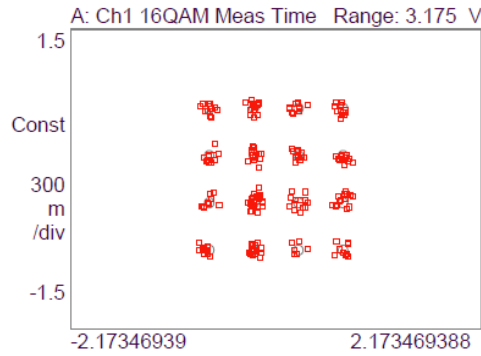
Figures 6.24(a)-(d) show the measured constellation diagrams of QPSK, 8PSK, 16QAM and 32QAM, respectively, under the conditions of the distance  $d = 3$  m,  $SNR = 20$  dB, a symbol rate of  $R_s = 50$  Msps. It can be seen that the output constellations are stable and clear. Moreover, Figure 6.25 presents the measured output constellation diagrams of QPSK at the receiver IF output, with different  $SNRs$ ,  $d = 1$  m and  $R_s = 20$  Msps. It can be observed that the output constellation is stable when the received  $SNR$  is beyond a certain level, e.g.,  $SNR = 15$  dB. The output constellations are definitely clear and the spreading points in the constellations are very close to the reference positions with a high  $SNR$  of 30 dB.



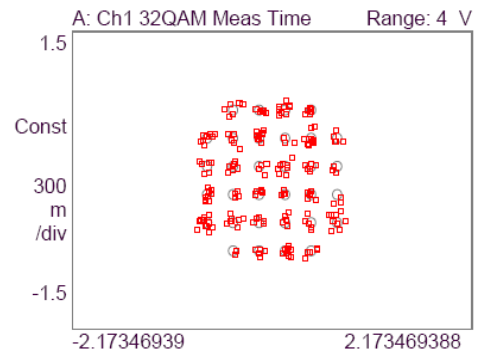
(a) QPSK



(b) 8PSK



(c) 16QAM



(d) 32QAM

Figure 6.24: Measured constellation diagrams at receiver IF output with  $SNR = 20$  dB,  $R_s = 50$  Msps,  $d = 3$  m.

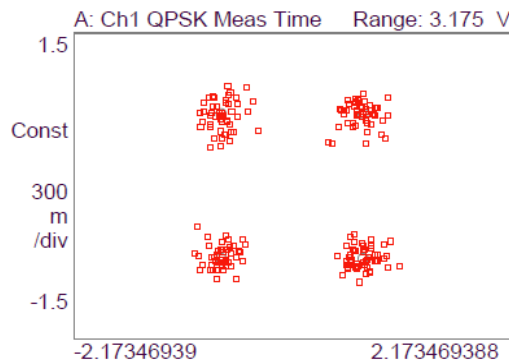
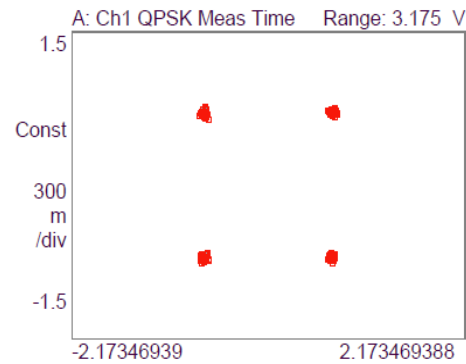
(a)  $SNR = 15$  dB(b)  $SNR = 30$  dB

Figure 6.25: Measured constellation diagrams of QPSK with different SNRs,  $R_s = 20$  Msps,  $f_{IF} = 1$  GHz,  $d = 1$  m.

In [89], Mahmoud *et al.* derived an expression of relating EVM to SNR for QAM signals over AWGN channels, where the signal-to-noise ratio (SNR) is defined as  $SNR = E_s/N_0$ ,  $E_s$  is the average symbol energy,  $N_0/2$  is the noise power spectral density (PSD). Here, the SNR is a function of both the nonlinear distortion and the energy per bit to the noise PSD ratio. The signal degradation sources in our proposed wireless system such as thermal noise, antenna noise, and the noise of transceiver circuits are modeled as Gaussian noise. For a M-QAM signal of order  $M = 2^k$ , a modified EVM expression is obtained by replacing  $SNR$  by  $SNR \times k/2$  for (49) in [89]. Thus, the EVM relation to SNR is calculated by

$$\begin{aligned}
 EVM_{MQAM} = & \left[ \frac{2}{kSNR} - 8\sqrt{\frac{3}{k\pi(M-1)SNR}} \sum_{i=1}^{\sqrt{M}-1} \gamma_i e^{-\frac{3k\beta_i^2 SNR}{4(M-1)}} \right. \\
 & \left. + \frac{12}{(M-1)} \sum_{i=1}^{\sqrt{M}-1} \gamma_i \beta_i \operatorname{erfc} \left( \sqrt{\frac{3k\beta_i^2 SNR}{4(M-1)}} \right) \right]^{1/2}
 \end{aligned} \tag{6.17}$$

where  $\gamma_i = 1 - i/\sqrt{M}$ ,  $\beta_i = 2i - 1$ ,  $k = \log_2(M)$  is the number of bits per symbol for M-QAM,  $\operatorname{erfc}(x)$  is the complementary error function, defined as  $\operatorname{erfc}(x) = \frac{2}{\sqrt{\pi}} \int_x^\infty e^{-t^2} dt$ . EVM is usually expressed as a percentage (%).

Figure 6.26 plots the measured and calculated RMS EVM versus SNR for QPSK, 16QAM and 32 QAM, with  $R_s = 20$  Msps. It can be seen that the measured EVM results are well matched to the EVM values calculated by (6.17), for various modulation orders such as  $M = 4, 16$ , and  $32$ . In general, the RMS EVM of different modulation schemes is within 5% when received SNR is above 25 dB, and EVM is less than 19% when received SNR is more than 15 dB. This indicates that our proposed transceiver system supports reliable communication. It should be noted that the minimum detectable SNR is limited by the dynamic range of measurement instruments such as Agilent DSO81204B. The measured maximum symbol rate is restricted by the baseband test bench such as VSG Agilent E4438C, and the bandwidth of our experimental K-band wireless communication system can reach up to 600 MHz.

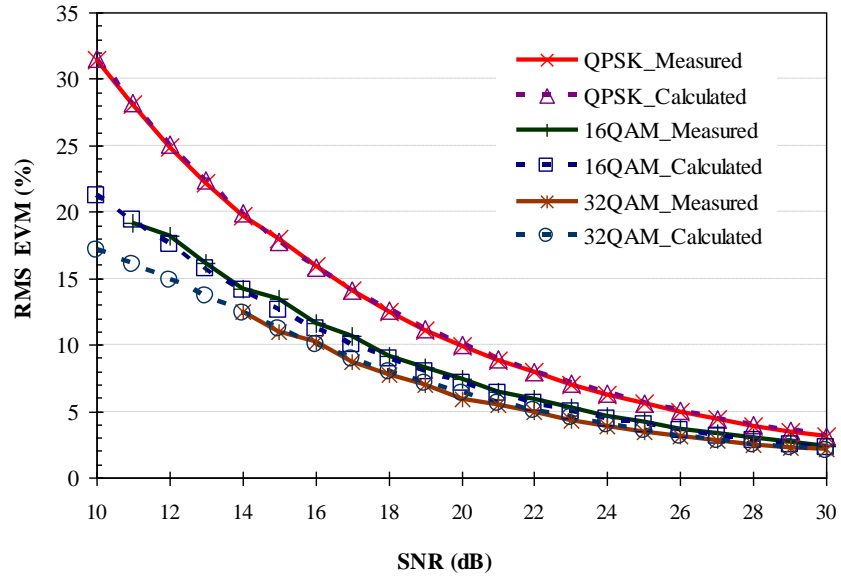


Figure 6.26: Measured and calculated RMS EVM versus SNR for QPSK, 16QAM and 32 QAM,  $R_s = 20$  Msps,  $f_{IF} = 1$  GHz,  $d = 1$  m.

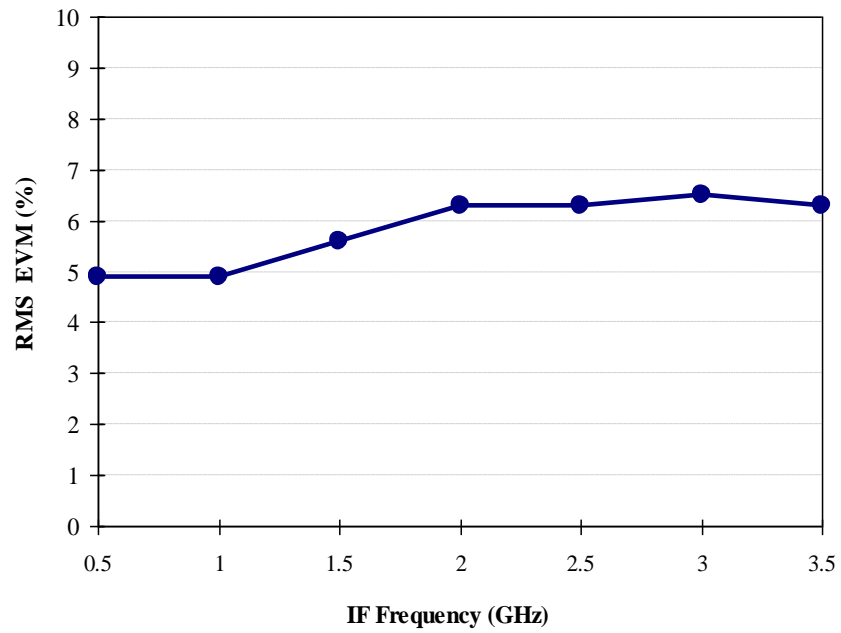


Figure 6.27: Measured RMS EVM at various IF frequencies for QPSK

It has been shown above that the relationship between EVM and SNR can be estimated by (6.17). From the system point of view, the conversion loss and noise figure of a mixer may affect EVM by decreasing SNR. In order to evaluate the broadband performance of the proposed mixer, the RMS EVM of the system is measured by varying the LO frequency over 20-24 GHz. Figure 6.27 shows the measured RMS EVM for QPSK with symbol rate of  $R_s = 20$  Msps, transmitter and receiver distance  $d = 1$  m, transmitted IF power  $P_{IF} = 2$  dBm. It is observed that the measured EVM is quite stable at different IF frequencies. In Figure 6.27, a higher EVM at the upper IF band is caused by the noise figure variation of our proposed mixer.

## 6.5 Conclusion

A broadband millimeter-wave single balanced diode mixer that employs a novel structure of 180-degree SIW hybrid has been proposed and presented in this chapter. This 180-degree hybrid consists of a conventional H-plane 3-dB coupler and a broadband 90-degree phase shifter. A K-band experimental prototype has been designed and measured. Measured results have demonstrated that the conversion loss of our experimental prototype is better than 10 dB across the entire LO/RF frequency range of 20-26 GHz, as up-converter or down-converter. The measured IF frequency is from DC to 4 GHz. The proposed mixer exhibits an excellent linearity property with input IP3 and  $P_{1dB}$  points about 15 dBm and 9 dBm, respectively. In addition, it guarantees good spurious rejection and port-to-port isolations. It is worthwhile mentioning that the proposed design concept would exhibit more advantageous features at higher millimeter-wave frequency bands. In order to evaluate the system performance of this proposed mixer, our design is integrated directly with an SIW high-gain antenna to build up a very compact receiver front-end. Finally, a K-band wireless communication system, using the receiver front-end as a building block, is demonstrated for line-of-sight channels. Measured and analytical results show that the proposed system is able to provide a reliable communication. This chapter has successfully demonstrated a possible application of the proposed mixer in millimeter-wave communication systems.

## CHAPTER 7      MILLIMETER-WAVE RECEIVER FRONT-END USING INJECTION-LOCKED SUB-HARMONIC SELF-OSCILLATING MIXER

This chapter presents a novel SOM based receiver front-end which deploys an injection locking scheme in order to improve the frequency stability and phase noise of the oscillating signal. In our receiver front-end, an SIW slot array antenna, a band-pass filter and a second-harmonic SOM which has been demonstrated in Chapter 4, are integrated into a single layer substrate as an effort to establish a compact, low-cost and low profile architecture for millimeter-wave wireless systems. The SOM makes use of the transmission characteristics of two operating modes in an SIW cavity. As such, the proposed receiver front-end has the advantages of low phase noise and decent isolation between RF and LO signals. In the previous experiments, the frequency drift phenomenon of the self-generated LO signal was still observed. As is well known, any deviation from a pure LO shows up as added phase and amplitude noise in the converted signal, corrupting the original spectral content. Therefore, to generate frequency sources with low phase noise and low spurious signal content for communications and cost effectively is a key design consideration. In this chapter, the injection locking technique is applied to our receiver front-end to improve the quality of the LO signal, and the overall system performance is thus upgraded.

Furthermore, an additional transmitter front-end circuit is introduced to set up a complete  $K_a$ -band transceiver system. Experimental validation of the  $K_a$ -band wireless communication system integrated with our SOM-based receiver front-end is then carried out and presented. EVM and SNR are finally investigated for QPSK modulation scheme.

### 7.1 Our Proposed Receiver Front-end System

Figure 7.1 shows the layout of our proposed receiver front-end system in which a second harmonic SOM is embedded with SIW structures [93]. In our design, the RF signal is first received by an SIW slot array, and then passes through a BPF module that consists of four SIW cavities. As has been illustrated before in Chapter 4, our proposed SOM circuit simultaneously provides both oscillating and mixing functions within a single FET block. For the first three orders of the BPF, the fundamental mode ( $H_{101}$ ) of the SIW cavity is used at RF frequency. The fourth SIW cavity is designed so as to choose  $H_{202}$  mode for RF signal while the fundamental

mode of this cavity is used to generate a negative resistance for oscillation conditions. And the second harmonic of the LO frequency is used for the mixing function. The transistor used in our circuit is the pseudomorphic hetero-junction FET (HJFET) NE3210S01 from NEC. An external LO injection port is included in the proposed circuit in order to stabilize the self generated LO signal and improve its phase noise for communication performance.

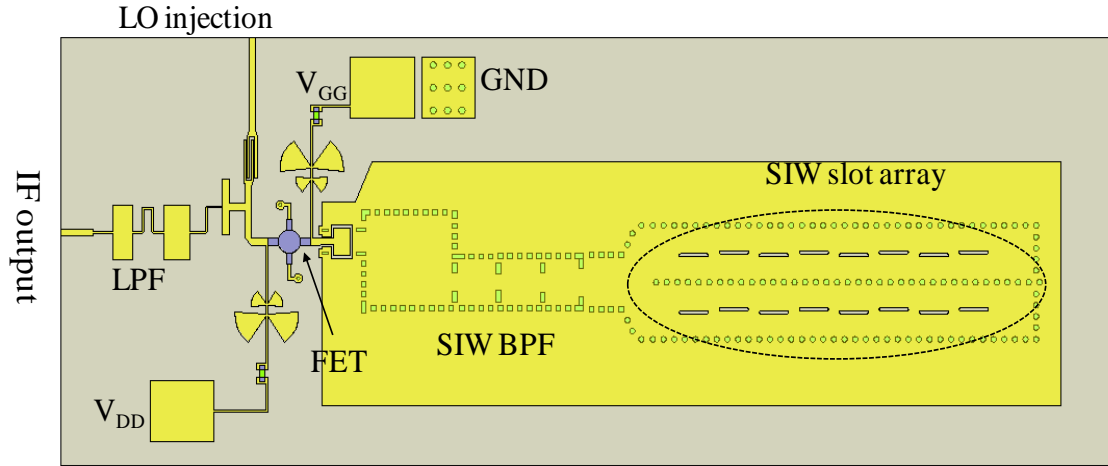


Figure 7.1: Layout of our proposed receiver front-end

To demonstrate features of our proposed receiver front-end, a complete transceiver experimental prototype is designed and implemented. The receive antenna in our system is a  $2 \times 8$  slot array and the transmit antenna is made of a standard microstrip patch for simplicity. The center RF frequency of the prototype is around 30 GHz. The substrate used is Rogers RT6002 with dielectric constant of 2.94 and thickness of 0.254 mm.

### 7.1.1 Quality Factor of the SIW Cavity

As mentioned above, the fundamental mode ( $H_{101}$ ) of the fourth cavity of the proposed dual-mode BPF is used as the resonant mode for the LO signal generation. The quality factors of the cavity, namely loaded  $Q$  ( $Q_L$ ) and unloaded  $Q$  ( $Q_U$ ), can be extracted from the measured one-port reflection parameter of the cavity [94]. Figure 7.2 shows the simulated and measured reflection responses of the SIW cavity around the LO frequency, where  $\rho$  stands for the reflection factor.  $Q_L$  can be obtained from the return loss as

$$Q_L = \frac{\omega_0}{\Delta\omega_{3dB}} \quad (7.1)$$

where  $\omega_0$  is the resonant frequency and  $\Delta\omega_{3dB}$  is the 3 dB bandwidth. It can be obtained that the simulated and measured  $Q_L$  of the SIW cavity are 115.7 and 109.1, respectively.

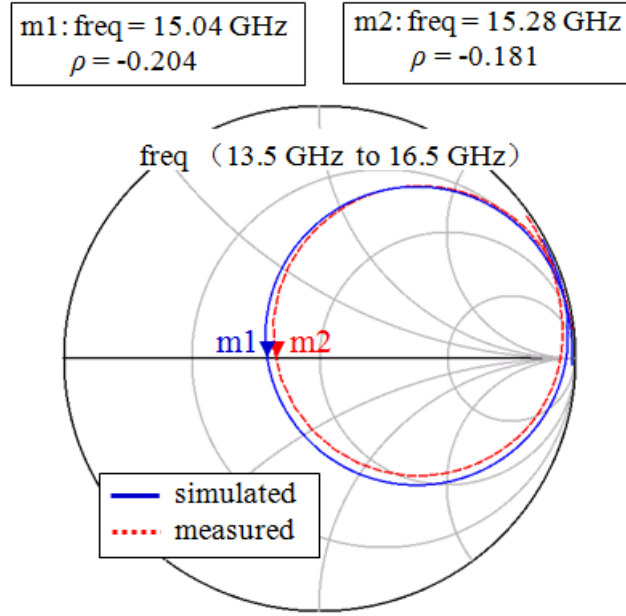


Figure 7.2: Measured reflection response of the SIW cavity

The unloaded quality factor  $Q_U$  can further be obtained from  $Q_L$  and coupling factor  $\beta_c$  as

$$Q_U = Q_L (1 + \beta_c) \quad (7.2)$$

where  $\beta_c$  can be calculated with

$$\beta_c = \frac{1 + \rho}{1 - \rho} \quad (7.3)$$

The coupling factor  $\beta_c$  could be greater or smaller than 1, which indicates the over coupling and under coupling situations, respectively. The simulated and measured  $Q_U$  of our SIW cavity are then calculated as 192.2 and 184.8. Compared with the  $Q_U$  value of 380 in [93], the quality factor in this design degrades because a thinner substrate is used.



### 7.1.2 Dual-Mode SIW BPF

The SIW BPF follows a typical Chebyshev low-pass filter prototype design procedure with 0.1 dB passband ripple, which was described in details in [93]. The simulated and measured S-parameters of the proposed dual-mode SIW BPF are shown in Figure 7.3. The curves with a higher insertion loss stand for the BPF under the influence of the DC block capacitor. It can be seen that the measured operating frequency shifts around 500 MHz towards an upper band due to the deviation of the dielectric constant. The insertion loss of the dual-mode SIW BPF is measured about 3.25 dB which can be attributed to several factors, namely, dielectric loss, metal loss and loss generated by the transitions and external loads. The DC-block capacitor is found to slightly introduce an additional 0.15 dB insertion loss at the RF frequency band. The measured 3 dB bandwidth of the dual-mode SIW BPF is about 900 MHz from 29.85 – 30.75 GHz and within the pass band, the input return loss is better than -20 dB. This highly selective BPF can ensure a good isolation between RF and LO signals. It can be found that the RF-LO isolation is better than -40 dB when LO is spaced 1.3 GHz from RF signal.

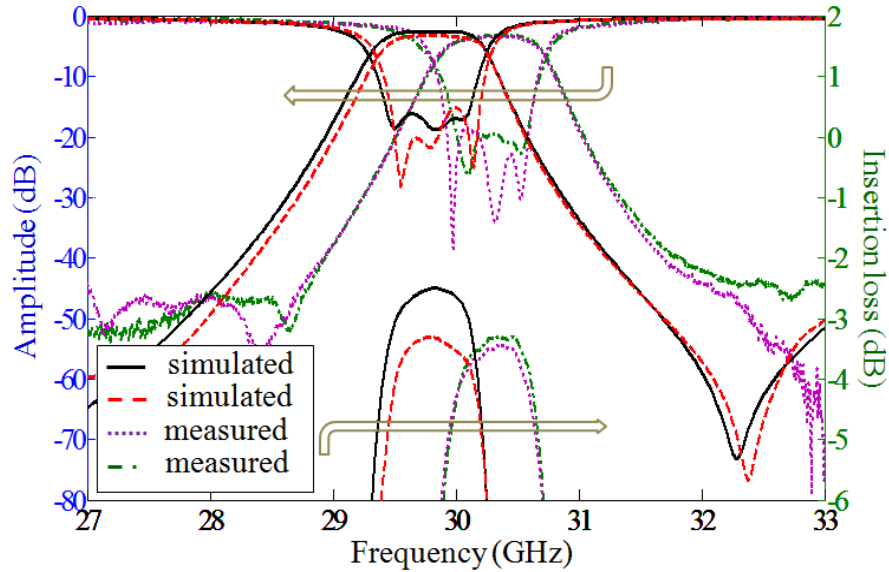
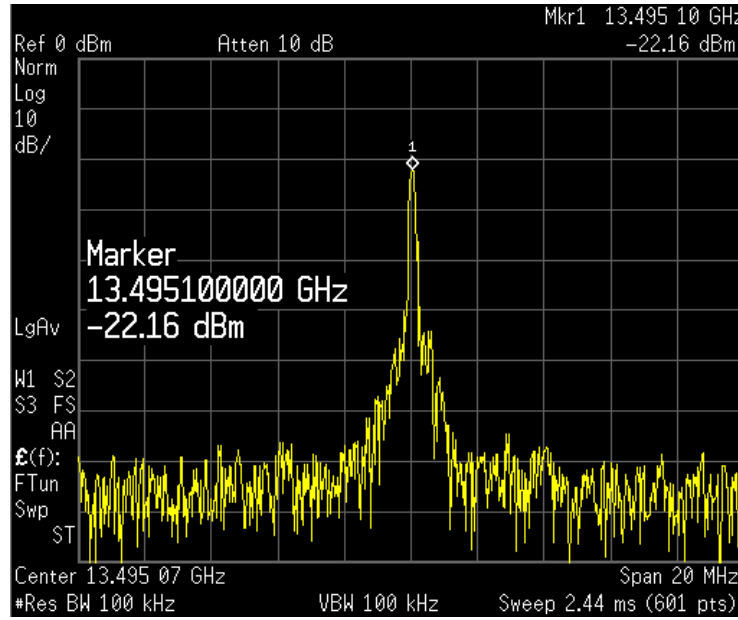
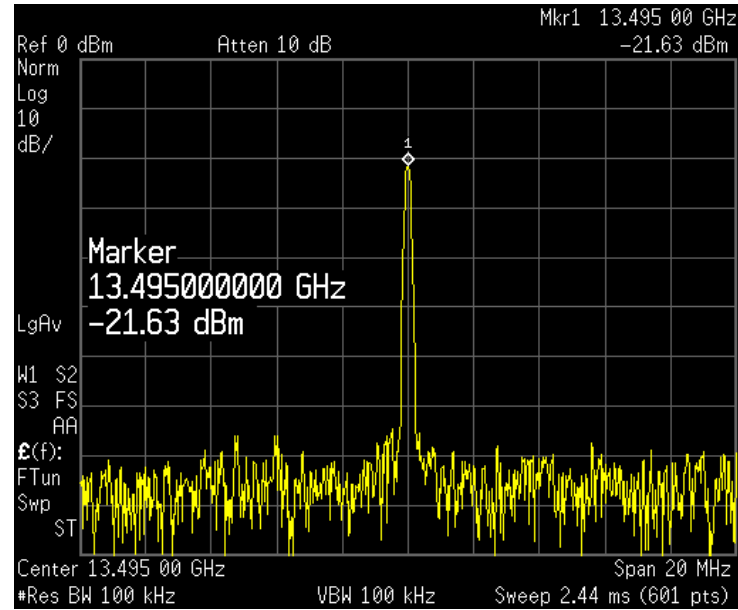


Figure 7.3: Simulated and measured S-parameters of the proposed dual-mode SIW BPF

### 7.1.3 Injection Locking Technique in the Proposed SOM



(a)



(b)

Figure 7.4: Measured LO spectra at the IF port (a) free-running and (b) with an external injection of -30 dBm.

The proposed SOM circuit is measured with embedded in the receiver front-end (see Figure 7.1). Figures 7.4(a) and 7.4(b) show the measured LO spectra at the IF port under the free-running and injection locking conditions, respectively. The injection signal is generated by a microwave signal generator Anritsu MG3694 and the frequency is set at the fundamental frequency of the self oscillating signal which is about 13.5 GHz. As can be seen, the locked signal is much purer and more stable than the free-running self oscillating signal. It should be noted that the output LO power should be about 30 dB higher considering the attenuation of the IF port LPF.

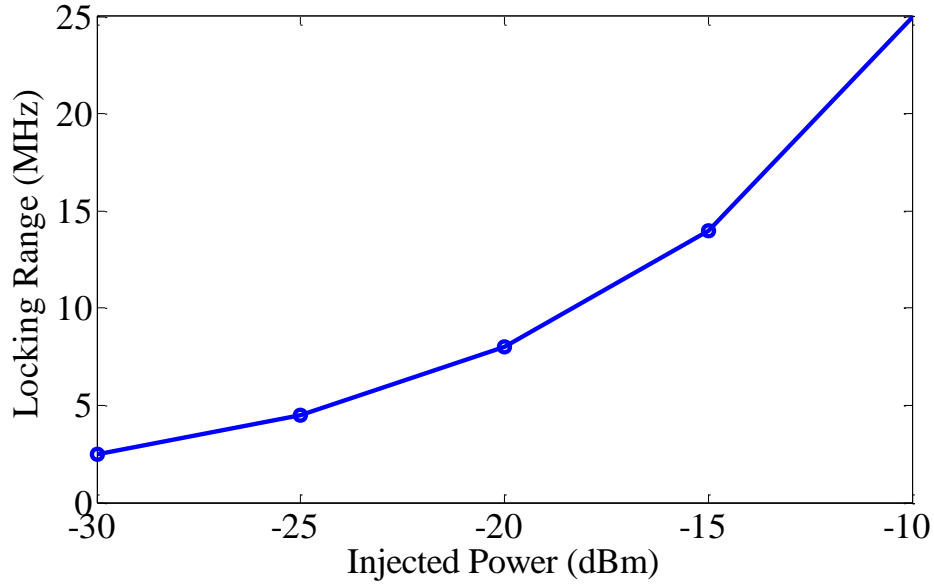


Figure 7.5: Locking range versus injected power

On the basis of the injection locking scheme, the locking range can be approximately expressed as [95]

$$\frac{2\Delta\omega}{\omega_0} \approx \frac{1}{Q_{ext}} \sqrt{\frac{P_{inj}}{P_{out}}} \quad (7.4)$$

where  $2\Delta\omega$  is the locking bandwidth,  $\omega_0$  is the free running frequency,  $Q_{ext}$  is the external quality factor of the circuit,  $P_{out}$  is the output power of the oscillator, and  $P_{inj}$  is the power level of the injected signal. According to (7.4),  $Q_{ext}$  can be estimated by using the measurement results. Figure 7.5 displays the locking range with different injected power levels, based on which the average measured  $Q_{ext}$  can be calculated as about 68. Figure 7.6 illustrates the phase noise of the

designed SOM for different injected power level, compared to the phase noise of the reference signal generator itself. It shows that an injected signal of -30 dBm is sufficient to obtain a phase noise close to the reference source.

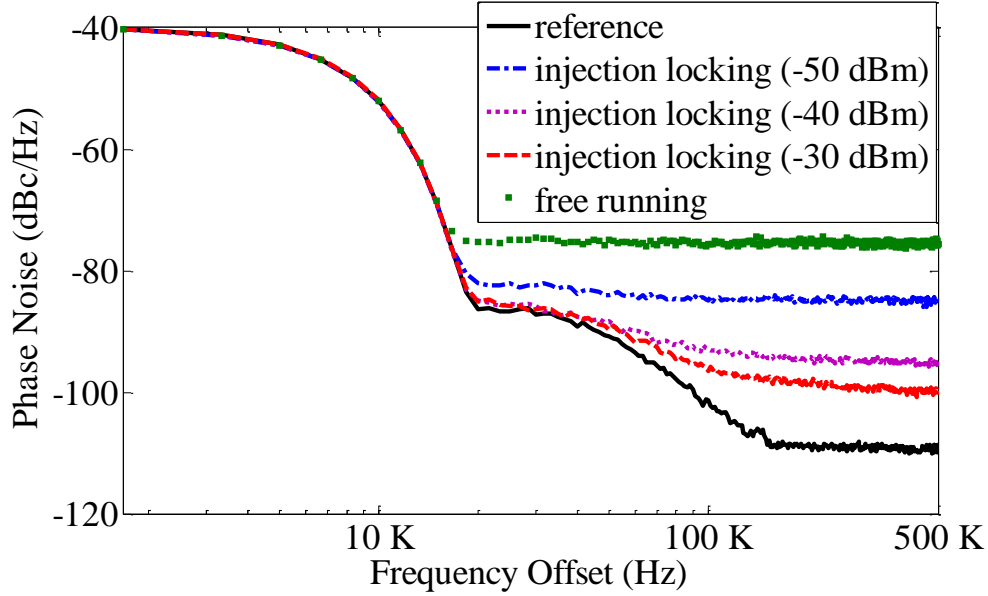


Figure 7.6: Measured phase noise for various injected power

### 7.1.4 SIW Slot Array

The SIW slot array is designed based on the method presented in Section 6.3. Figure 7.7 shows the simulated and measured input return losses of the  $2 \times 8$  SIW slot array antenna. It can be seen that the simulated and measured results fit quite well except that the measured operating frequency shifts around 350 MHz towards an upper band due to the deviation of the dielectric constant, which is consistent with the frequency shift in the dual mode SIW BPF circuit. The measured -10 dB bandwidth is extended from 29.6 GHz to 30.75 GHz. The radiation patterns of our  $2 \times 8$  slot array at 30 GHz are also plotted in Figure 7.8. It is observed that the measured gain and side-lobe level of our receive antenna are about 13 dBi and 18 dB, respectively.

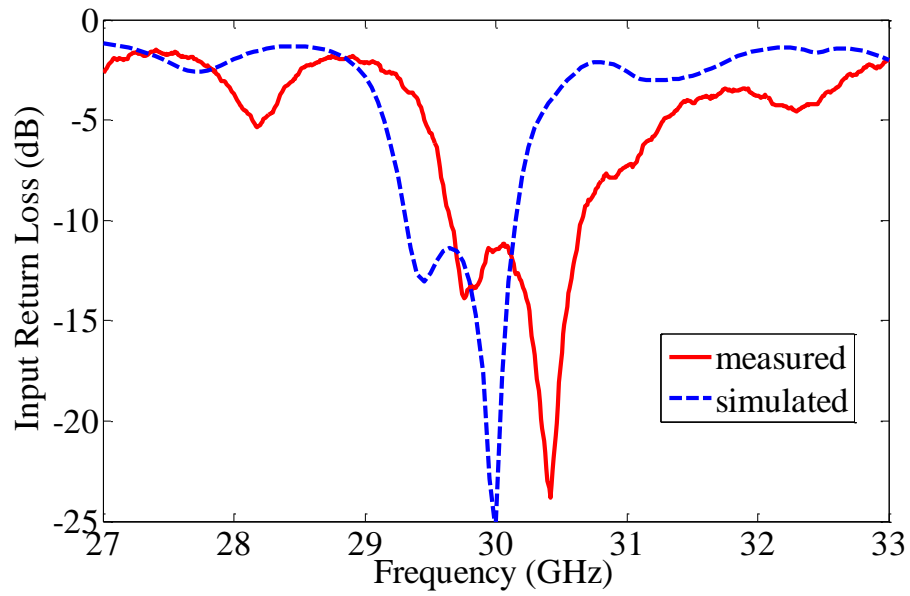


Figure 7.7: Simulated and measured return losses of the  $2 \times 8$  SIW slot array antenna

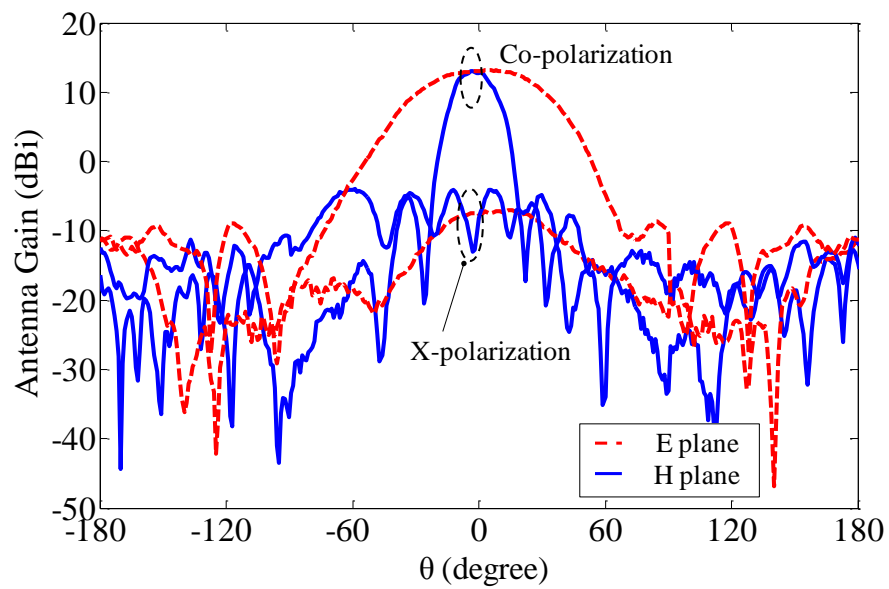


Figure 7.8: Measured radiation patterns of the receive antenna at 30 GHz

## 7.2 Test Setup of Our K<sub>a</sub>-band Wireless Communication System

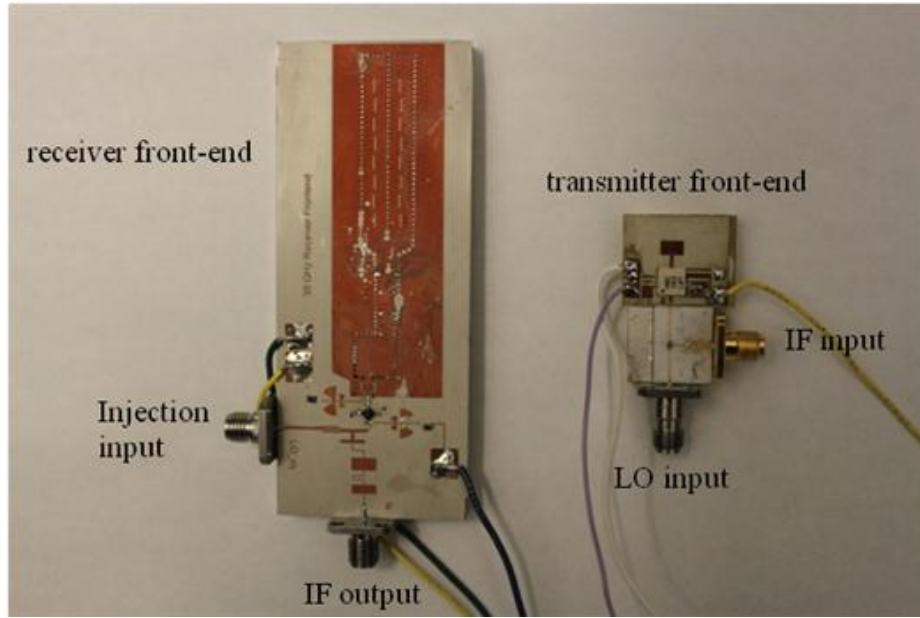


Figure 7.9: Photograph of the proposed transceiver front-end

To demonstrate the system performance of the proposed receiver front-end that was discussed earlier, a K<sub>a</sub>-band transceiver experimental prototype at 30 GHz is implemented. The photograph of our proposed transceiver front-end is shown in Figure 7.9. The transmitter front-end includes a mixer module HMC329, a power amplifier HMC283LM1, both from Hittite, and a microstrip patch antenna with the measured antenna gain of 5.7 dBi. The mixer chip is wire-bonded on a 0.254-mm-thick alumina substrate. The power amplifier HMC283LM1 and the patch antenna are integrated on the same substrate RT6002 with thickness of 0.254 mm and dielectric constant  $\epsilon_r = 2.94$ . The RF output of the mixer is connected to the power amplifier input through wire-bonding. The measured parameters of the commercial K<sub>a</sub>-band mixer HMC329 and PA HMC283LM1 are consistent with the datasheets from Hittite. The total gain of the transmitter front-end is measured about 12 dB.

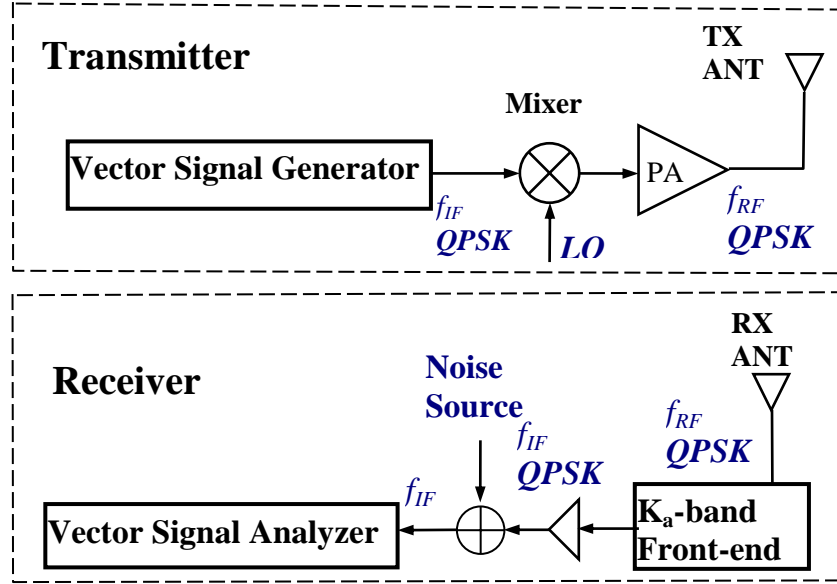


Figure 7.10: Block diagram of the proposed communication system

Figure 7.10 depicts the block diagram of the proposed 30 GHz wireless communication system. At the transmitter end, a PN binary sequence is modulated at an IF signal with QPSK scheme by an Agilent E4483C VSG. Thereafter, the QPSK modulated signal is up-converted to a 30 GHz RF signal by the mixer HMC329. The RF signal is then fed into the power amplifier HMC283LM1 and the transmit antenna for transmission. At the receiver side, the received RF signal is down-converted to IF signal using the proposed receiver front-end. The IF output signal is then amplified by a two-stage amplifier with a total gain of 22 dB at IF frequency. This output signal is sent to a VSA Agilent 89600 (i.e., an Agilent DSO81204B oscilloscope with VSA software) for ADC, demodulation, and synchronization. The noise generated from a noise source (HP346C) is combined with the modulated signal at the amplifier output (before demodulation) in order to control the signal-to-noise ratio (SNR) conditions.

In addition, the *LOS* path loss is measured for a 30 GHz wireless channel in our laboratory environment. It can be observed from Figure 7.11 that the measured *PL* is very close to the theoretical value which is calculated by using (6.14).

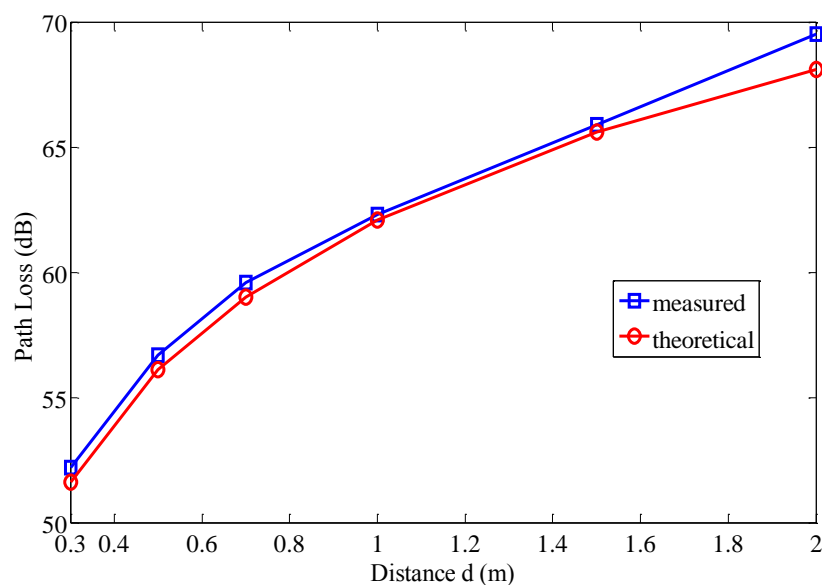


Figure 7.11: Measured and calculated  $PL$  at 30 GHz

### 7.3 Measurement Results

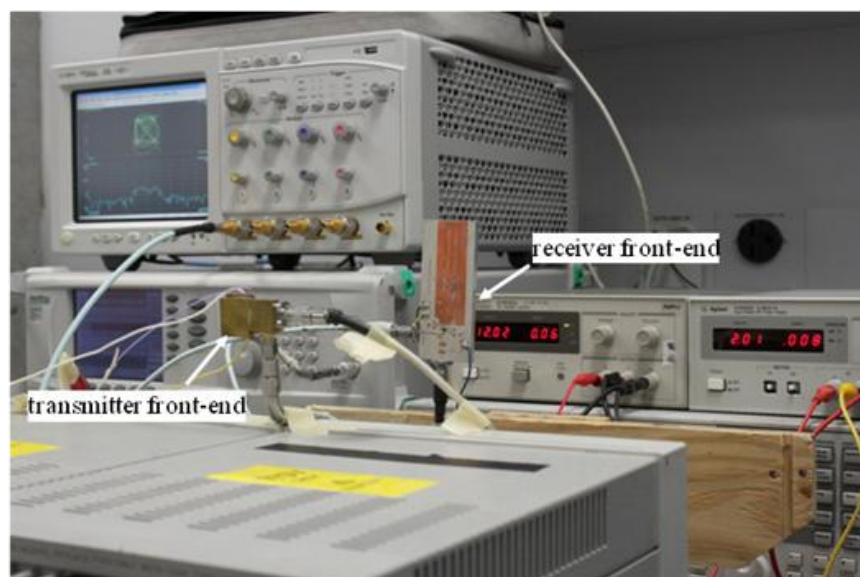


Figure 7.12: Photograph of our test setup

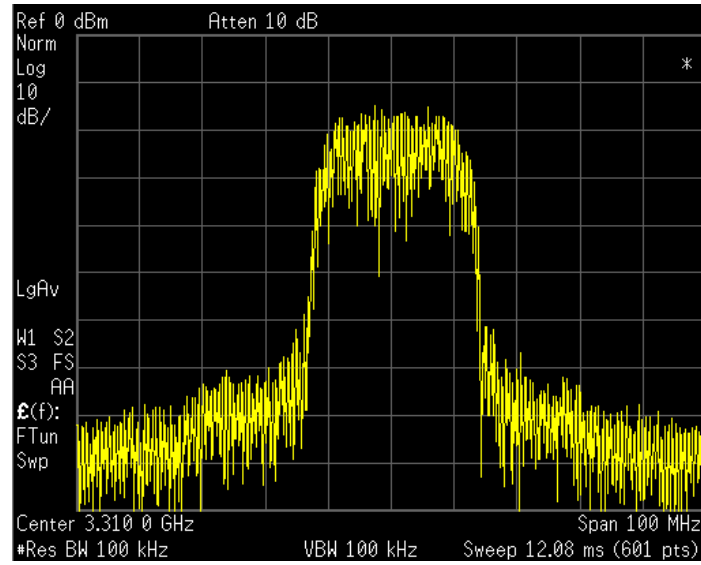
Figure 7.12 shows the photograph of our system test setup as sketched in Figure 7.10. The test equipments include Agilent E4438C VSG, Anritsu MG3694A and 68177C signal generators,



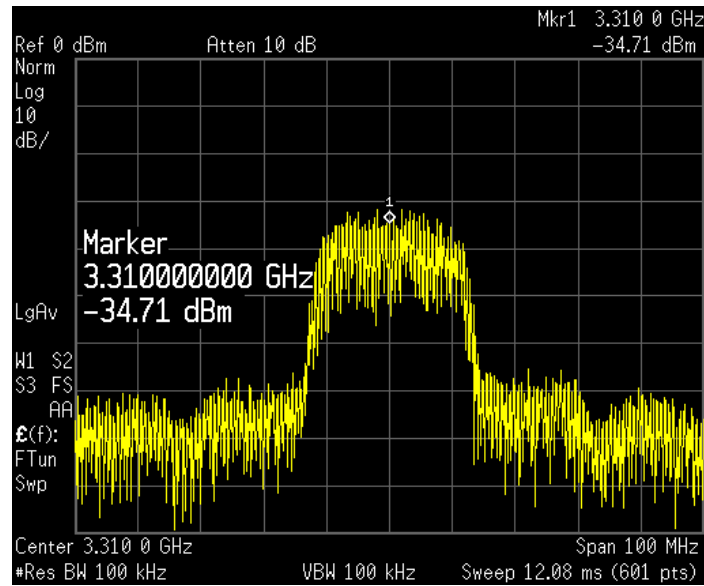
Agilent spectrum analyzer 4446A, Agilent oscilloscope infiniium DSO81204B, several power supplies, and one mobile handcart. At the transmitter side, Agilent E4438C VSG generates QPSK modulated signal. Anritsu MG3694A provides a +13 dBm, K<sub>a</sub>-band carrier signal for the 30 GHz up-converter mixer. At the receiver side, Agilent spectrum analyzer 4446A is used to record the IF and RF signal spectra. In addition, Agilent 89600 VSA is used to measure the transceiver system parameters such as received SNR, EVM, constellation diagrams and so on.

The system measurements are carried out with the distance of  $d = 30$  cm to 1 m between the transmitter and receiver, which determines a  $PL$  in the range of 53~62 dB. The output signal of Agilent E4438C VSG is set to QPSK modulation, and the intermediate frequency  $f_{IF}$  is in accordance with the down-converted IF frequency of the proposed SOM circuit. An external -30 dBm reference signal generated by Anritsu 68177C signal generator is fed into the injection port of the SOM circuit. Comparable to that presented in our early work [93], the measured conversion loss of our 30 GHz SOM circuit is about 12 dB. By setting the transmitted modulated IF signal from VSG at 0 dBm, the expected IF power down-converted by the proposed receiver front-end is about -35 dBm for a distance of  $d = 30$  cm between the transmitter and the receiver. Figures 7.13(a) and 7.13(b) plot the measured spectra of the transmitted modulated IF signal and the received modulated IF signal at the output of the IF amplifier (behind the proposed receiver front-end in Figure 7.10), for QPSK with data bit rate  $R_b = 40$  Mbps,  $d = 30$  cm. It is observed that the IF frequency is about  $f_{IF} = 3.31$  GHz. Except for few additional unwanted noises at the side band, the received IF signal spectrum shows its similarity to the transmitted IF signal spectrum. That is, the input and output signals are well-matched. This indicates that our transceiver frond-end can transfer the modulated signal successfully.

Figure 7.14 presents the measured output constellation diagrams of QPSK at the receiver IF output, without and with the -30 dBm injected signal, for the distance  $d = 30$  cm and data bit rate  $R_b = 40$  Mbps. The measurements are carried out by using Agilent 89600 VSA. Meanwhile, the signal-to-noise ratio ( $SNR$ ) received by the VSA in these two conditions is measured as 15.2 and 25.6 dB, respectively. It is found that the output constellation is dramatically improved with the external injection.

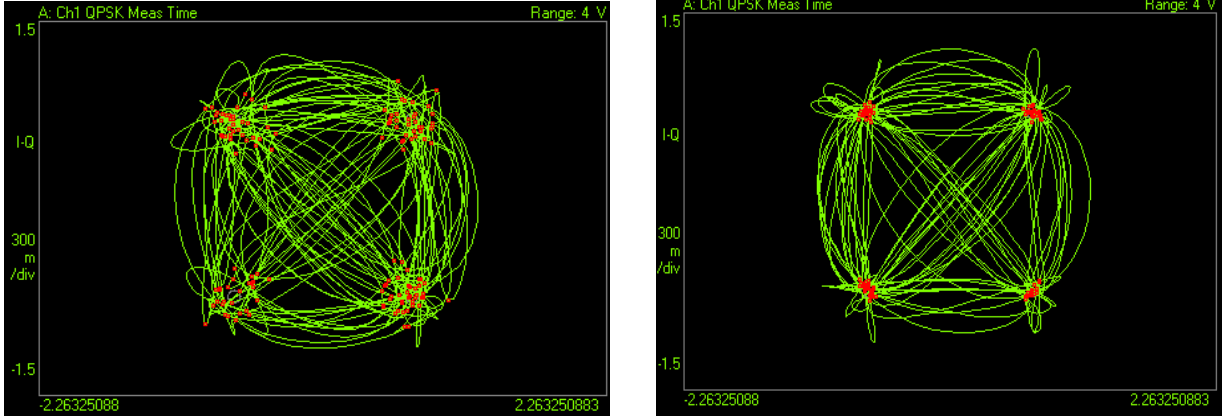


(a)



(b)

Figure 7.13: Comparison of IF spectra of (a) the transmitted modulated signal, and (b) the received modulated signal for QPSK with  $R_b = 40$  Mbps,  $d = 30$  cm.



(a) without injected signal

(b) with -30 dBm injected signal

Figure 7.14: Measured QPSK constellation diagrams at the receiver IF output for  $d = 30$  cm and  $R_b = 40$  Mbps (a) without injected signal and (b) with -30 dBm injected signal.

Figure 7.15 plots the measured and calculated RMS EVM versus SNR for QPSK, with  $R_s = 40$  Mbps and  $d = 30$  cm. It can be seen that the measured EVM results are well matched to the EVM values calculated by (6.17). This indicates that our proposed transceiver system supports reliable communication.

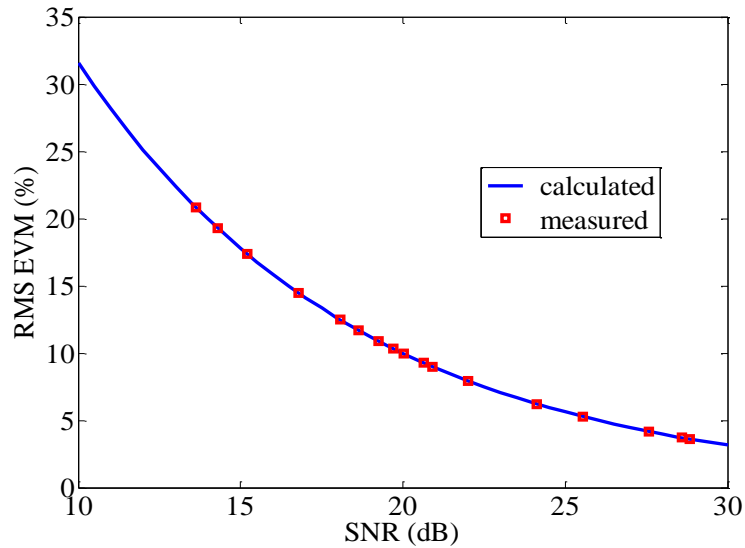


Figure 7.15: Measured and calculated RMS EVM versus SNR for QPSK, with  $R_s = 40$  Mbps and  $d = 30$  cm.

## 7.4 Conclusion

This chapter presents a millimeter-wave wireless communication system with emphasis on  $K_a$ -band operations which employs a novel receiver front-end circuit. Our proposed receiver front-end consists of an SIW-based slot array antenna, a narrow bandwidth BPF and a second-harmonic SOM. In addition, a small externally injected signal is applied at the fundamental frequency to improve the LO signal. It has been evaluated that the proposed receiver front-end has advantages of low phase noise and good isolation between RF and LO signals. A  $K_a$ -band transceiver system is further presented to verify the feasibility of our receiver front-end for practical wireless communication applications. The corresponding transmitter front-end is based on a standard super-heterodyne architecture. QPSK signals are used for system measurements. Measured results have proven the reliable performance of our proposed system.

## CHAPTER 8      60 GHZ TRANSCEIVER ARCHITECTURES

### DEPLOYING SICS TECHNIQUE

During the past decades, communication industry and wireless service providers have witnessed incredible growth in the number of users and diversity of services in connection with wireless applications. In the quest for larger bandwidth, much attention has been paid to the well-advertised 60 GHz band (millimeter-wave) where up to 7 GHz of license free bandwidth has been allocated worldwide (57-64 GHz in North America, 59-66 GHz in Japan and Europe, see Figure 8.1). This unprecedented amount of available spectrum holds the potential for much higher data rate even compared to other currently used bandwidth-limited channels. In general, 60 GHz wireless technologies are characterized by features such as short-range link, high data rate, high density, excellent security, low transmit power and low profile. Figure 8.2 shows the 60 GHz system scenario in office and home environment.

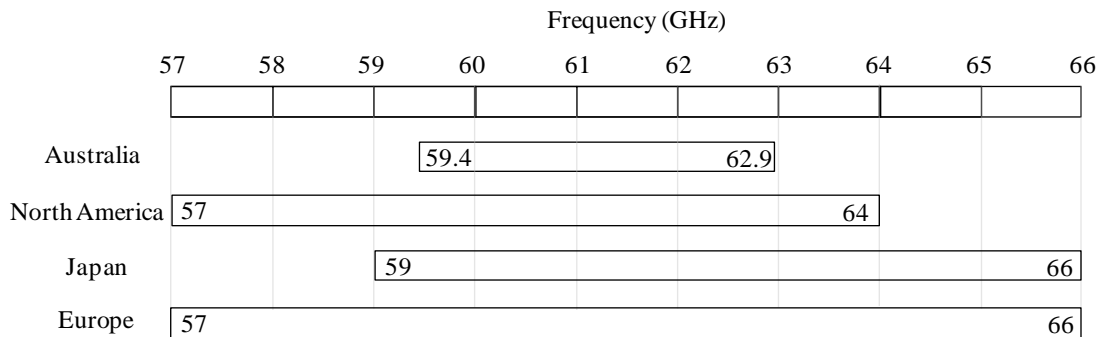
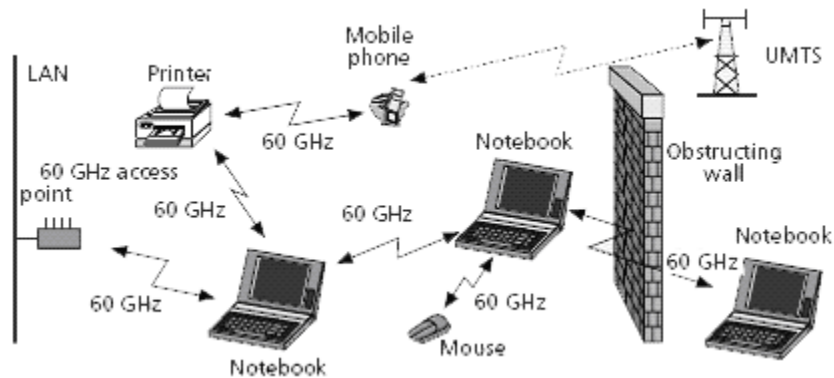
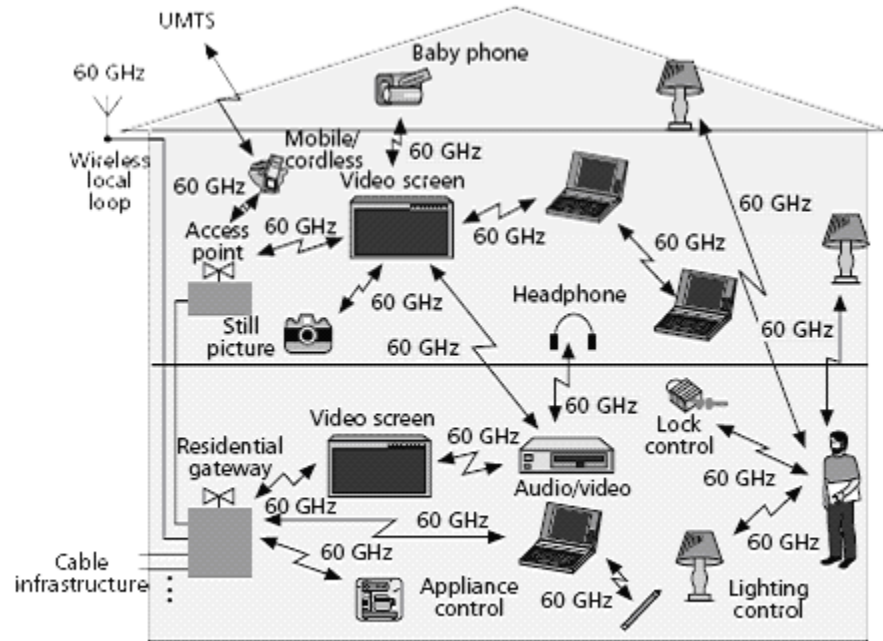


Figure 8.1: 60 GHz available spectrum



(a)



(b)

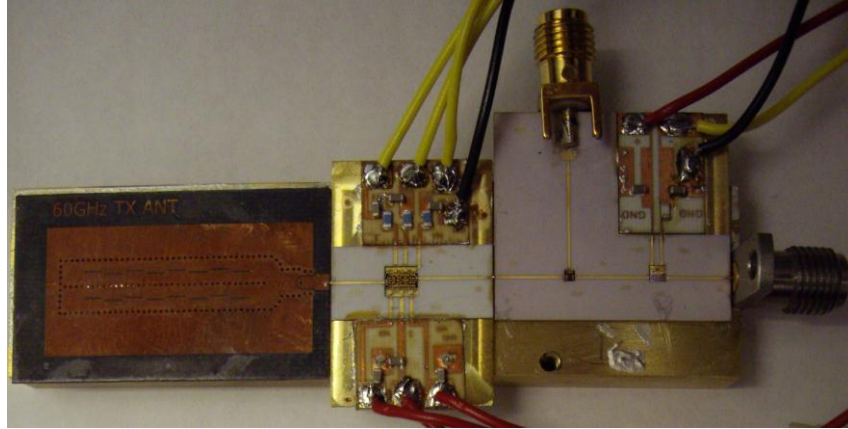
Figure 8.2: a) 60 GHz system scenario in office environment; b) 60 GHz system scenario in home environment (Source: [96])

The development of a low-cost 60 GHz wireless system truly presents a great technological and design challenge although a number of LTCC/RFIC based chip sets as well as MMICs have very recently been demonstrated for the design of 60 GHz transmitters or receivers [97]-[98]. The fundamental bottleneck lies in low-cost development, high-density integration and self-consistent packaging of complete transceivers in which high-gain antenna and high-performance filter as well as other parts should be completely integrated. It has been becoming apparent that the multi-chip module (MCM) with system-in/on package (SiP/SoP) is a reliable solution to this problem [99]. Recently, several researchers have attempted to demonstrate various small-sized transceiver modules at 60 GHz band [100], [101]. However, a complete low-cost substrate integrated transceiver still remains unexploited.

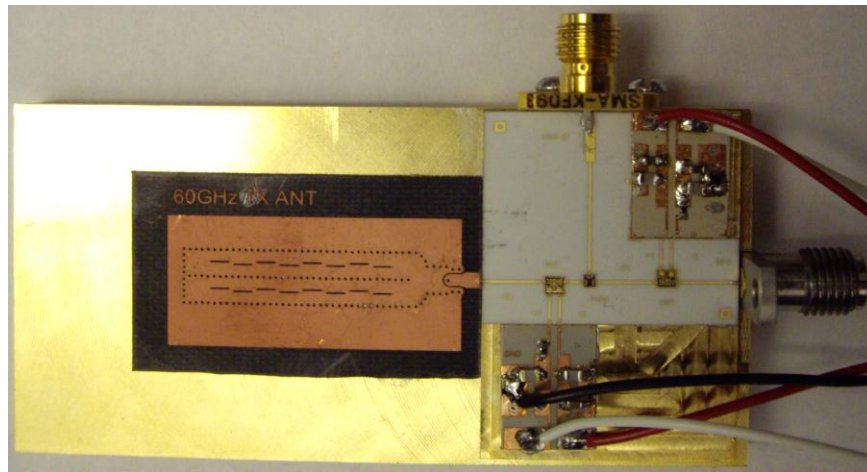
In this chapter, a 60 GHz substrate integrated transceiver system that achieves a bandwidth up to 3 GHz is presented. The proposed integration scheme of planar and non-planar structures allows the design of passive components and active devices within a single package. A complete 60

GHz wireless communication system is further analyzed and experimentally implemented for LOS transmission channels.

## 8.1 60 GHz Transceiver and Receiver Front-ends



(a) Transmitter front-end



(b) Receiver front-end

Figure 8.3: Photographs of our demonstrated 60 GHz transmitter and receiver front-ends

The photographs of our proposed 60 GHz transmitter and receiver front-ends are shown in Figure 8.3(a) and Figure 8.3(b), respectively. Based on traditional heterodyne architecture, both the transmitter and receiver front-ends are implemented with the concept of SICs that effectively combines the SIW with microstrip or CPW-based planar circuits. Currently, it is still infeasible to consider a complete monolithic approach for a 60 GHz transceiver front-end since the antenna

size is too large to be made by semiconductor wafer. This is in particular true when high-gain antennas are required that are usually made in the form of arrays. And also, certain high-Q components with highly-demanded performance such as band-pass filter are not realisable with the doped semiconductor process. In this work, an SIW-based  $2 \times 8$  slot array is designed and fabricated to achieve high gain at 60 GHz band. Thus, our proposed transceiver system is able to create the best possible scenario to obtain high density integration while preserving the required high-performances at low-cost.

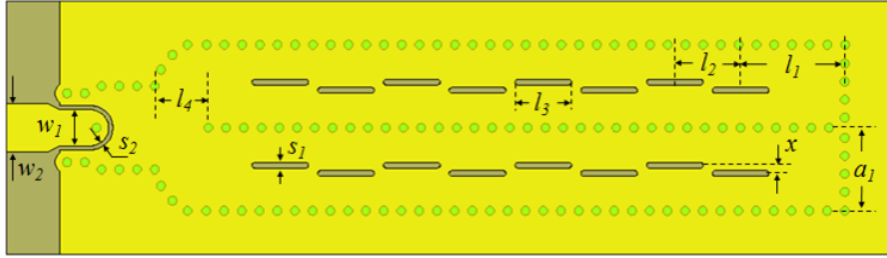


Figure 8.4: Physical dimensions of the 60 GHz SIW-based  $2 \times 8$  slot array antenna. ( $w_1 = 1.2$  mm,  $w_2 = 1.6$  mm,  $l_1 = 3.526$  mm,  $l_2 = 2.225$  mm,  $l_3 = 1.91$  mm,  $l_4 = 1.813$  mm,  $s_1 = 0.187$  mm,  $s_2 = 0.15$  mm,  $a_1 = 2.77$  mm, and  $x = 0.262$  mm)

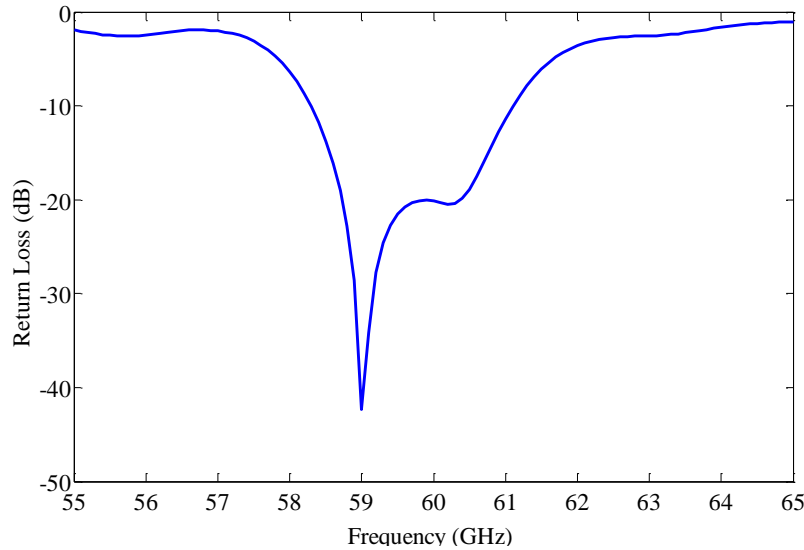


Figure 8.5: Simulated return loss of the 60 GHz  $2 \times 8$  slot array antenna



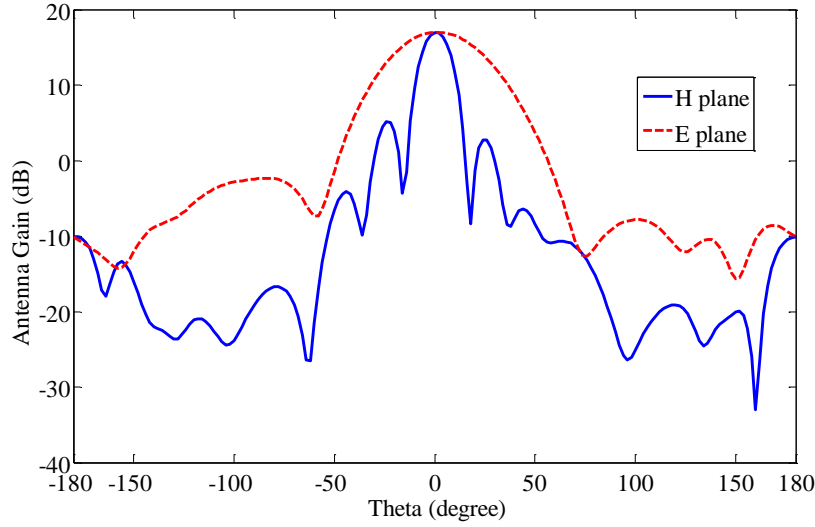


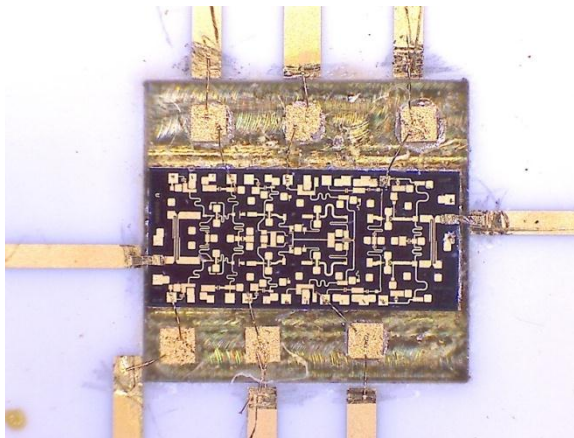
Figure 8.6: Simulated radiation pattern of the 60 GHz  $2 \times 8$  slot array antenna

The physical dimensions of the proposed 60 GHz SIW slot antenna are given in Figure 8.4. In our antenna design, the synthesis of bilateral metallic walls is made with discontinued metallised via holes in dielectric substrate, which does not allow the guidance of TM modes. The substrate used is RT5880 with dielectric constant of 2.2 and thickness of 0.508 mm. As shown in Figure 8.4, an SIW-to-microstrip transition is specifically designed for connecting the antenna with other modules of our system through wire bonding process [102]. It should be noted that the conventional SIW-to-microstrip transition is no more suitable for our design since the width of the microstrip line is comparable to that of SIW at 60 GHz.

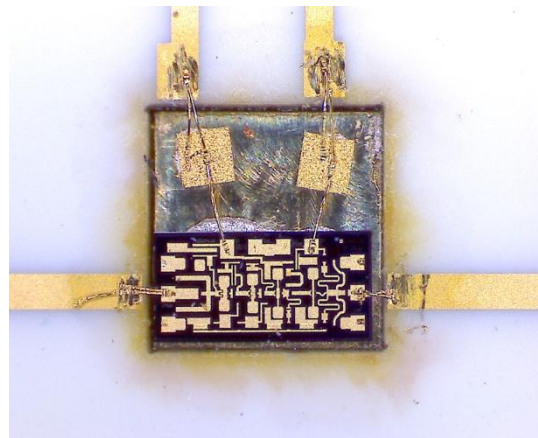
Figure 8.5 shows simulated input return loss of our designed  $2 \times 8$  slot array at 60 GHz. The antenna measurement has not been made because the facility limitation in our lab. It can be seen that our -10 dB bandwidth is roughly from 58 GHz to 61 GHz. The radiation pattern of the antenna is also plotted in Figure 8.6. It is observed that the simulated gain of our receive antenna is about 15 dBi. Therefore, a good antenna performance can be achieved for wireless communication applications.

In addition, passive circuits and antennas in our proposed system are fully integrated into the dielectric substrate. Other key components at 60 GHz band, such as LNA HMC-ALH382, power amplifier (PA) HMC-ABH241 and mixer HMC-MDB169 (i.e., up-converter and down-

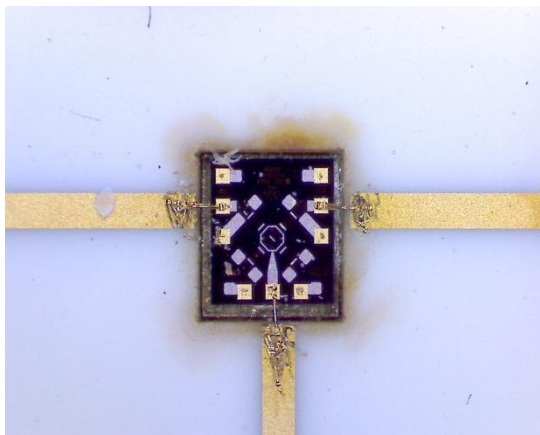
converter), are commercially available MMICs provided by Hittite. Note that our 60 GHz MMIC mixer module HMC-MDB169 requires a minimum LO driving power of +13 dBm, thus additional LNAs are assembled together with the 60 GHz mixers at the transceiver frond-end in order to obtain enough power. 50 Ohm microstrip transmission lines on 0.254 mm thick alumina thin film substrates are used for bringing RF to and from the chip. These dies are attached a 0.150 mm thick molybdenum heat spreader which is then attached to the ground plane with conductive epoxy so that the surface of the dies is coplanar with the surface of the substrate. RF bonds made with  $0.075 \text{ mm} \times 0.0125 \text{ mm}$  ribbon and DC bonds of 0.025 mm diameter, thermo-sonically bonded, are used in our circuit. Figure 8.7 shows the photographs of the wire bonding techniques with the aid of a microscope.



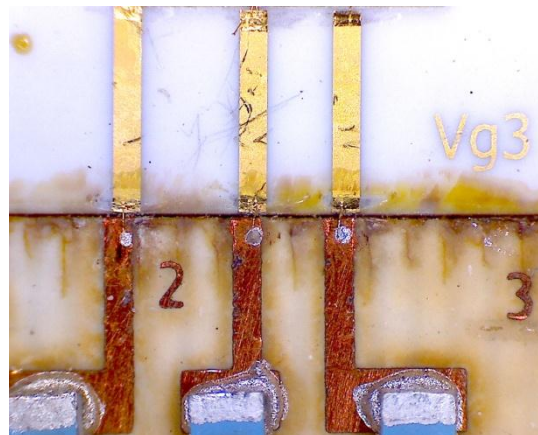
(a)



(b)



(c)



(d)

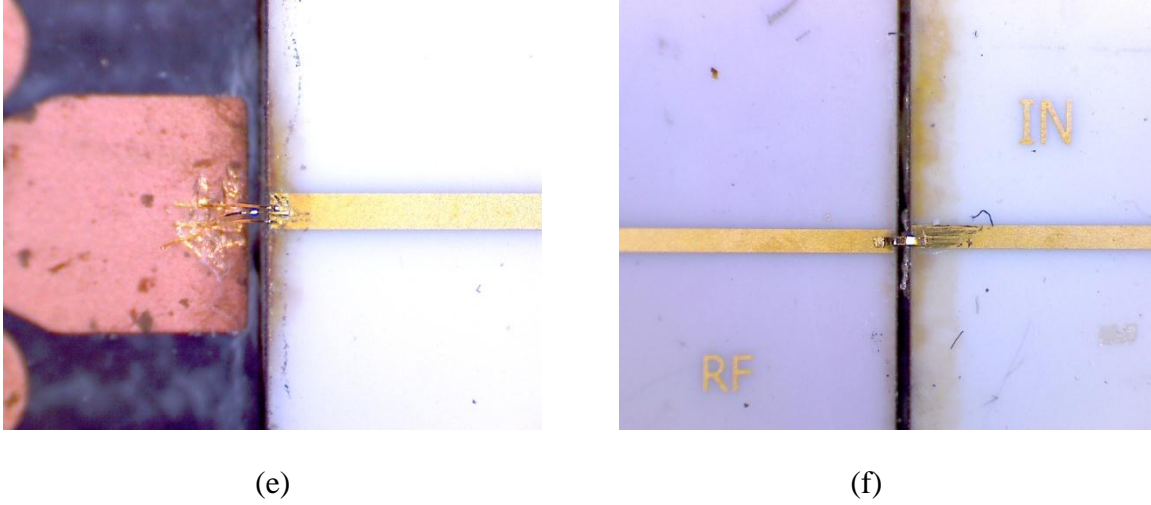


Figure 8.7: Photographs of the wire bonding techniques (a) PA HMC-ABH241, (b) LNA HMC-ALH382, (c) mixer HMC-MDB169 (up-converter and down-converter), (d) DC bias bonding, (e) RF bonding between ceramic and PCB substrates, and (f) RF bonding between ceramic substrates.

Above all, the transmitter and receiver front-end modules are tested separately with respect to their RF performances before they get interconnected with bonding wires. In brief, the designed transceiver frond-end works well in the frequency range between 58 and 61 GHz. The total gains of the transmitter front-end and receiver front-end (i.e.,  $G_{TX}$  and  $G_{RX}$ ) are measured around 8 dB and 10 dB, respectively. At the receiver, the system noise figure  $NF_s$  is about 7 dB. It is found that at millimeter-wave frequencies (e.g., 60 GHz), the discontinuity introduced by the bonding wires may affect the performance of the integrated module, as expected. However, the wire-bonding process is still an effective approach in the development of low-cost millimeter-wave hybrid integrated circuits.

## 8.2 Test setup of 60 GHz Communication Systems

Figure 8.8 depicts the block diagram of the proposed 60 GHz communication system. At the transmitter end, a PN binary sequence is modulated at IF signal with QPSK scheme by Agilent E4483C VSG. Thereafter, the QPSK modulated signal is up-converted to 60 GHz RF signal by mixer HMC-MDB169. The RF signal is then fed into PA HMC-ABH241 and the transmit antenna for transmission. At the receiver side, the received 60 GHz RF signal from antenna is sent to LNA HMC-ALH382 directly. Herein, no additional BPF is used, considering its insertion

loss at 60 GHz. The amplified RF signal is down-converted to IF signal by mixer HMC-MDB169. The IF output signal is then passed to I/Q demodulator AD8347 from Analog Devices for demodulation. The noise generated from noise source HP346C could be combined with the modulated signal at the mixer output (before demodulation) in order to control the *SNR* conditions.

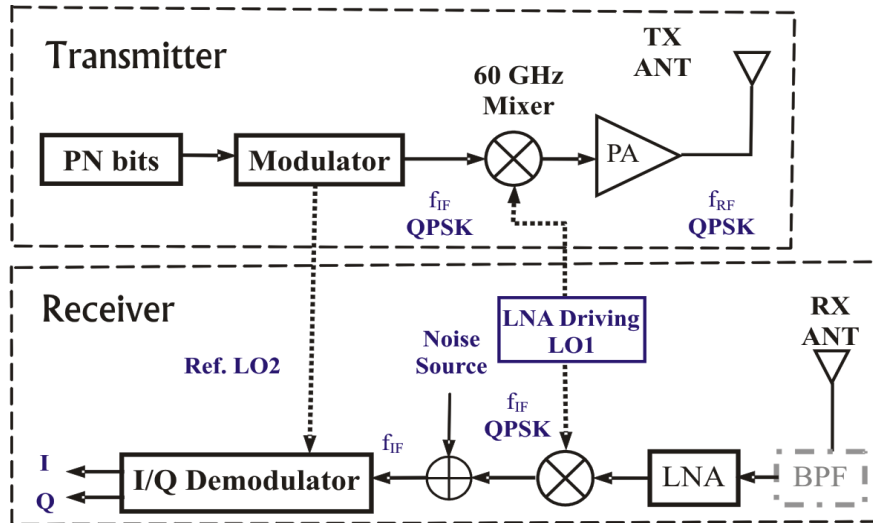


Figure 8.8: Block diagram of the 60 GHz system test setup

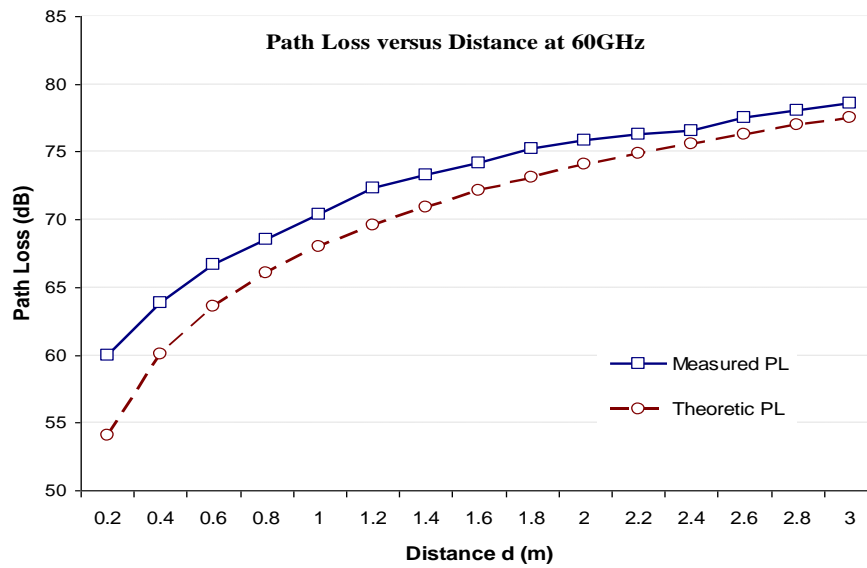


Figure 8.9: Measured and calculated *PL* at 60 GHz

Characteristics of the 60 GHz propagation channel and power budget analysis are important aspects for the 60 GHz communication systems. The LOS  $PL$  of the 60 GHz wireless channel is measured with a power meter and standard horn antennas in our laboratory environment. As shown in Figure 8.9, it can be observed that the theoretic  $PL$  calculated by (6.14) is the lower bound of the measured  $PL$  and their values are closer as the distance  $d$  increases.

The receiver sensitivity ( $P_{RX}$ ) is related to threshold signal-to-noise ratio  $SNR_{min}$ , noise figure of the system  $NF_s$ , and thermal noise power  $N_0 = kTB$ , where  $k = 1.38 \times 10^{-23}$  J/K,  $T = 290$  K,  $B$  is system bandwidth (Hz). Then, the required transmitted power ( $P_{TX}$ ) can be predicted by:

$$P_{TX} = P_{RX} - G_t - G_r + PL + \text{Fade Margin} \quad (8.1)$$

where  $G_t$  and  $G_r$  are gains of the transmit antenna and the receive antenna, respectively. *Fade Margin* represents the margin (dB) between the received signal strength level and the receiver sensitivity.

### 8.3 Measurement Results

The 60 GHz system measurement is carried out with a distance of  $d = 30$  cm between the transmitter and the receiver, which determines a  $PL$  of about 63 dB. Figure 8.10 shows the photograph of the 60 GHz system test setup as sketched in Figure 8.8. At the transmitter side, Agilent E4438C VSG generates both QPSK modulated signal and reference carrier signal  $LO_2$ . Agilent E4438C VSG is set to QPSK modulation, intermediate frequency  $f_{IF} = 1$  GHz. Note that the bandwidth of the transmitted baseband signal is limited by our VSG. If transmitted power  $P_{TX} = 10$  dBm, then the signal power at the receive antenna  $P_{RX} = -53$  dBm. Anritsu 68177 synthesized signal generator together with a millimeter-wave multiplier source module is used to generate 5 dBm 60 GHz carrier signal. Additional LNAs are assembled together with the 60 GHz mixers to obtain enough 60 GHz carrier  $LO_1$ . At the receiver side, R&S signal analyzer FSIQ40 is used to record signal spectrum. Agilent scope infiniiium DSO81204B is used to observe the demodulated I/Q signal.

To verify the 60 GHz transceiver frond-end, R&S signal analyzer FSIQ40 is used to record the modulated IF signal spectra at the input of the transmitter front-end and at the output of receiver front-end. Measuring these spectra can give added insight into the nature and origin of the error signals. For QPSK with data bit rate  $R_b = 100$  Mbps, Figures 8.11(a) and 8.11(b) compare the

measured spectra of the transmitted and the received modulated IF signals. It is observed that except for few additional unwanted noises, the received IF signal spectrum shows its similarity to transmitted IF signal spectrum ( $f_{IF} = 1$  GHz). This indicates that our transceiver frond-end can transfer the modulated signal successfully.

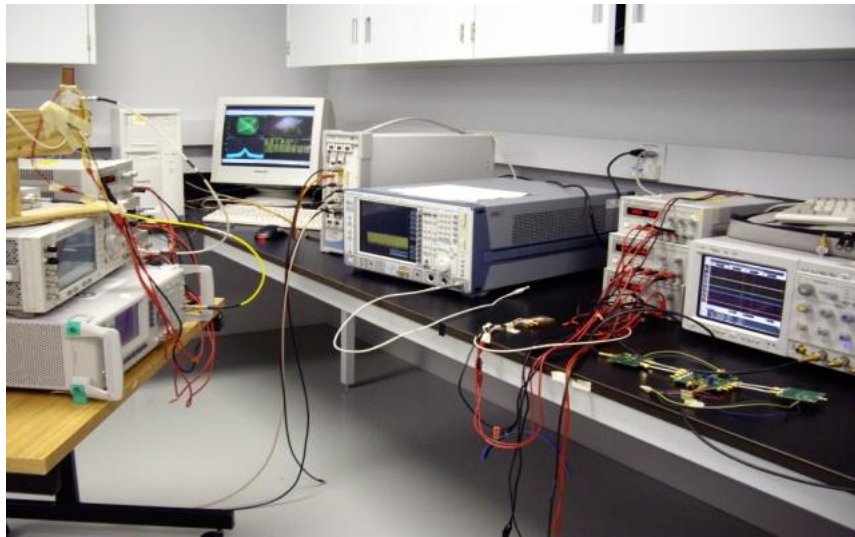
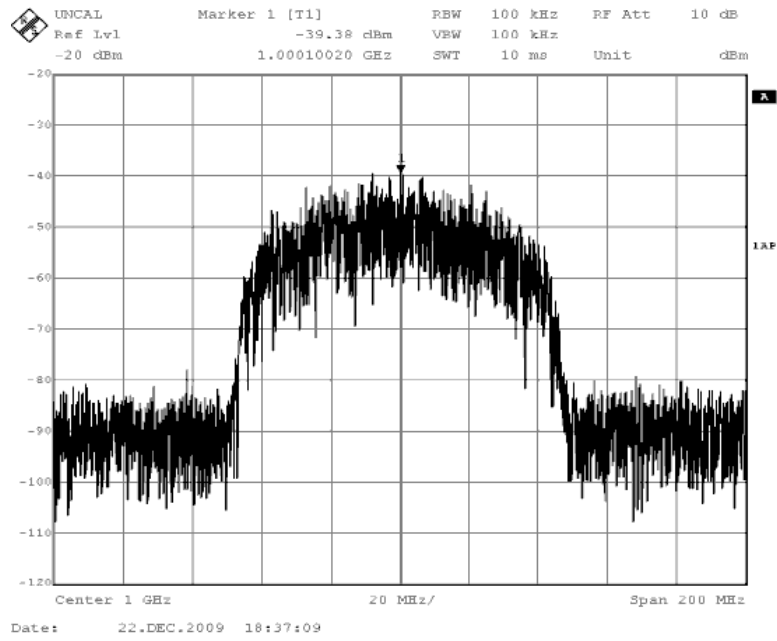
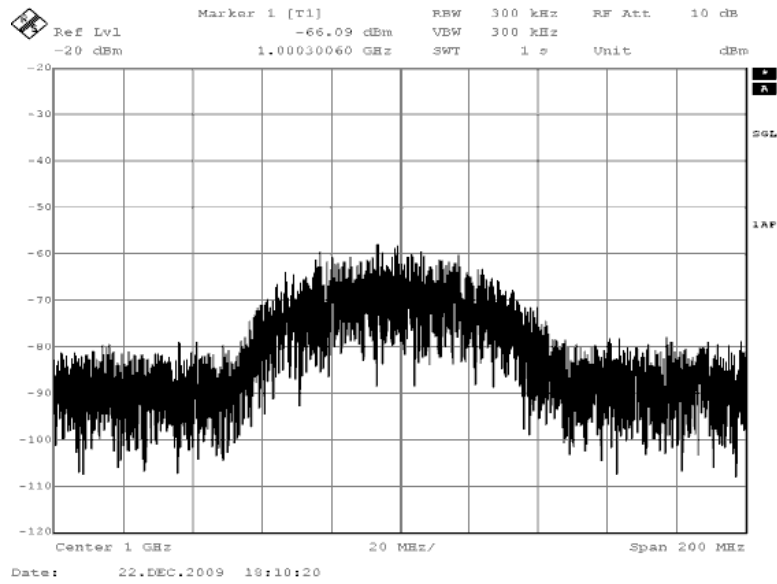


Figure 8.10: Photograph of our system test setup

Moreover, demodulator output I and Q signals are sampled by the Agilent oscilloscope infiniiium DSO81204B. Figure 8.12 plots the measured received and transmitted I/Q signal waveforms for QPSK with data rate  $R_b = 4$  Mbps. It is shown that the demodulated I/Q waveforms match well with the transmitted waveforms. That is, the modulated data signals which are transmitted and received by our 60GHz system can be demodulated triumphantly. Figure 8.13 compares measured results of the received and transmitted QPSK I/Q diagrams. The output constellation is stable and clear if the  $SNR$  has an acceptable value (e.g.,  $SNR = 20$  dB). Note that the tested data rate is limited by the baseband test bench, and the bandwidth of our 60GHz transceiver front-end system can reach up to 3 GHz.



(a)



(b)

Figure 8.11: Spectra of the (a) transmitted and (b) received modulated IF signal for QPSK,  $R_b = 100$  Mbps





Figure 8.12: Comparison of the received (1<sup>st</sup> and 2<sup>nd</sup> waveforms) and transmitted I/Q signals (3<sup>rd</sup> and 4<sup>th</sup> waveforms)

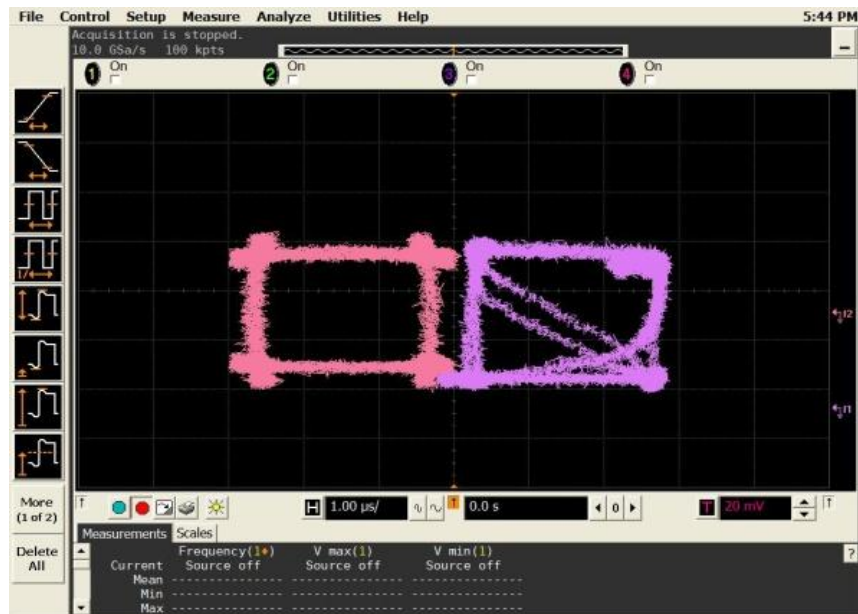


Figure 8.13: Comparison of the transmitted (left) and received (right) I/Q diagrams



## 8.4 Conclusion

In this chapter, a 60 GHz transceiver is presented as an effort to establish a compact, low cost and low profile architecture for high speed wireless communication. The proposed transceiver system is implemented with the method of SICs which has been demonstrated as an emerging platform to integrate high-gain antenna, passive components and other MMIC devices into a single package. Furthermore, the 60 GHz wireless communication system with QPSK signal is experimentally demonstrated for LOS channels. Measured results have shown that the demodulated I/Q waveforms match well with the transmitted waveforms, which indicates the good performance of our proposed system.

## **CONCLUSIONS AND FUTURE WORK**

### **Conclusions**

The scope of this dissertation focuses on the SIW devices, components, and receiver systems in millimeter-wave frequencies. Two major contributions from this work can be concluded as follows:

First, this dissertation consists of multiple highly original and innovative projects which involve the structure investigation, circuit design, practical implementation and system characterization. It is intended in discovering interesting features and establishing design and processing rules of SIW circuits at millimeter-wave frequencies through intensive theoretical and experimental research. For example, an excellent balanced geometry can be easily achieved by printing circuits on the two sides of the SIW substrate. A broadband balun and a feeding network of quasi-Yagi antennas have been proposed based on this concept. In addition, it has been reported that the SIW can be bisected with a fictitious magnetic wall and each half of the SIW becomes an HMSIW structure and the new structure can almost preserve the original field distribution. An HMSIW Wilkinson power divider and ultra-wideband QMSIW BPFs have been developed hereby for the aim of bandwidth enhancement and size reduction. Another interesting feature in connection with the SIW mixer circuits is that the SIW structure can provide very high IF-RF and IF-LO isolations as it is an inherently high-pass filter, which has been used to improve the port isolation performance of our SOM and single balanced mixer. In the framework of developing the SIW based circuits, not only the conventional SIW, but several derivative SIW structures, including Half-mode SIW and slotted SIW, have been studied in which the SIW is synthesized by using the metallic via or slot arrays to create equivalent metallic walls.

Secondly, the research work described in this dissertation has bridged a gap between SIW technology and millimeter-wave transceiver systems. It creates possible scenarios to have a high-density integration while preserving the required high-performance at low cost. The transceiver front-end architectures and commercially available diode, transistor and MMIC based substrate integration issues are particularly emphasized. With the development of passive components, active circuits such as mixers (up-converter and down-converter) and oscillators have also been studied and integrated within the same building block. This dissertation deals with two types of

substrate integrated receiver: conventional mixer based and SOM based receiver front-ends. The research outcome of the two different transceiver architectures has been studied theoretically and experimentally. System block diagram simulation is developed and accomplished with Matlab/Simulink. Generally, the most difficult design task is related to the oscillator design as the frequency stability and phase noise are crucial in the development of high-performance transceiver at millimeter-wave frequencies. In our SOM based receiver circuit, sub-harmonic techniques are investigated and deployed with the driving sources operating at much lower frequencies. To reduce the phase noise and also the structure cost, the embedded substrate integrated resonator has been applied and developed to provide a dielectric filled cavity resonator which presents a high-precision and cost free solution for the oscillator design. Furthermore, our receiver has also been upgraded with injection locking technique so that the phase noise can significantly be reduced.

In summary, our research lays the groundwork for promoting and investigating the SIW concept for the development of a broad range of millimeter-wave devices and systems. This dissertation makes an in-depth exploration in the development of future generations of high-density and mass-producible millimeter-wave circuits and systems. It establishes a unique millimeter-wave engineering research program with emphasis on the development of a new advanced theoretical and experimental platform.

## **Future Work**

Following the projects and studies described in this dissertation, a number of technical issues are still waiting to be resolved:

- When active components are integrated into SIW based systems, there are two problems breaking the integrity of SIW structures. First, the design of bias circuits becomes complicated due to the inherent DC short property of SIWs. Secondly, SIW-to-microstrip/CPW line transitions have to be used in a back-to-back formation only to provide an interface for the connection of surfaced mounted devices. The insertion loss introduced by these transitions certainly counteracts the benefits of SIW technology.
- High power handling and multi-mode accommodation are significant advantages of SIW structures. However, these beneficial features have not been successfully demonstrated in

practical applications. How to create multiple orthogonal paths for different modes in SIWs and control their mutual interactions are very interesting research topics.

- High insertion loss and poor fabrication tolerance associated with low cost PCB process poses a big technical obstacle for SIW technology in millimeter-wave applications. In particular, as frequency approaches to the extent that the skin depth is comparable with the surface roughness, conductor loss becomes a major factor determining the circuit performance. For example, in Chapter 8, we cannot manage to use a high-selectivity SIW BPF in our 60 GHz receiver system due to its high insertion loss. How to reduce the surface roughness of PCB based SIW circuits should be given substantial attention.
- The work presented in the thesis only scratch the surface of SIW technology and applications in the field of millimeter-wave communications. System evaluation carried out in Chapters 5 to 8 only demonstrated a proof of concept. Much more efforts have to been paid to accomplish a well-developed academic/industrial project.

## BIBLIOGRAPHY

- [1] R. Prasad, and L. Vandendorpe, "An overview of millimeter waves for future personal wireless communication systems," in *Proc. IEEE Int. Conf. Universal Personal Communications (ICUPC'93)*, Delft, Netherlands, 1993, pp. 885–889.
- [2] J. W. Dees, R. J. Wangler, and J. C. Wiltse, "System considerations for millimeter wave satellite communications," *IEEE Trans. Aerosp. Electron. Syst. (Supplement), Tech. Conv. Rec.*, pp. 195-213, Nov. 1966.
- [3] S. L. Johnston, "Millimeter radar," *Microwave Journal*, vol. 20, no. 11, pp. 16, 19-20, Nov. 1977.
- [4] W. J. Wilson, R. J. Howard, and A. C. Ibbot, "Millimeter-wave imaging sensor," *IEEE Trans. Microw. Theory Tech.*, vol. 34, no. 10, 1026-1035, 1986.
- [5] M. J. Lazarus, F. R. Pantoja, and M. G. Somekh, "Metallized Dielectric Horn and Waveguide Structures for Millimetre Wave Oscillator/Mixer Systems," *IEEE Trans. Microw. Theory Tech.*, vol. 29, no. 2, pp. 102-106, Feb. 1981.
- [6] R. Vahldieck, J. Bornemann, F. Arndt, and D. Grauerholz, "Optimized waveguide E-plane metal insert filters for millimeter wave applications," *IEEE Trans. Microw. Theory Tech.*, vol. 31, no. 1, pp. 65–69, Jan. 1983.
- [7] C. Svensson, and S. Gong, "System-in a-package solution for short-range wireless communications," *Applied Microwave & Wireless*, vol. 13, no. 12, pp. 78-82, Dec. 2001.
- [8] A. Shamim, M. Arsalan, L. Roy, M. Shams, and G. Tarr, "Wireless dosimeter: System-on-chip versus system-in-package for biomedical and space applications," *IEEE Trans. Circuits Syst. II*, vol. 55, no. 7, pp. 643-647, Jul. 2008.
- [9] K. Wu, D. Deslandes, and Y. Cassivi, "The Substrate Integrated Circuits – A new concept for high-frequency electronics and optoelectronics," *TELSIKS'03*, Nis, Yugoslavia, 2003, pp. P-III – P-X.
- [10] F. Xu, Y. Zhang, W. Hong, K. Wu, and T. J. Cui, "Finite-difference frequency-domain algorithm for modeling guided-wave properties of substrate integrated waveguide," *IEEE Trans. Microw. Theory Tech.*, vol. 51, no. 11, 2221–2227, 2003.

- [11] D. Deslandes, M. Bozzi, P. Arcioni and K. Wu, "Substrate Integrated Slab Waveguide (SISW) for Wideband Microwave Applications," *IEEE Int. Microwave Symp. Dig.*, 2003, pp. 1975-1978.
- [12] Y. Cassivi, and K. Wu, "Substrate Integrated NRD (SINRD) Guide on High Dielectric Constant Substrate for Millimeter Wave Circuits and Systems", *IEEE Int. Microwave Symp. Dig.*, 2004, pp. 1639-1642.
- [13] A. Patrovsky, and K. Wu, "Substrate integrated image guide (SIIG)- planar dielectric waveguide technology for millimeter-wave applications," *IEEE Trans. Microw. Theory Tech.*, vol. 54, pp. 2872-2879, June 2006.
- [14] Y. Cassivi, L. Perregrini, K. Wu, and G. Conciauro, "Low-Cost and High-Q Millimeter-Wave Resonator Using Substrate Integrated Waveguide Technique", in *Proc. 32<sup>nd</sup> Eur. Microw. Conf.*, 2002, pp. 1-4.
- [15] D. Deslandes and K. Wu, "Single-Substrate Integration Techniques for Planar circuits and Waveguide Filters", *IEEE Trans. Microw. Theory Tech.*, vol. 51, no. 2, pp. 593-596, Feb. 2003.
- [16] Y. Cassivi, D. Deslandes, and K. Wu, "Substrate Integrated Waveguide Directional Couplers", in *Proc. Asia-Pacific Microw. Conf.*, Nov. 2002, pp. 1409-1412.
- [17] S. Germain, D. Deslandes, and K. Wu, "Development of Substrate Integrated Waveguide Power Dividers", *CCECE 2003 proceedings*, pp. 1921-1924, May 2003.
- [18] W. D'Orazio, K. Wu, and J. Helszajn, "A substrate integrated waveguide degree-2 circulator," *IEEE Microw. Wireless Compon. Lett.*, vol. 14, no. 5, pp. 207-209, May 2004.
- [19] A. Petosa, A. Ittipiboon, and S. Thirakoune, "Perforated dielectric resonator antennas," *Electron. Lett.*, vol. 38, no. 24, pp. 1493-1495, Nov. 2002,
- [20] D. Deslandes, and K. Wu, "Design Considerations and Performance Analysis of Substrate Integrated Waveguide Components", in *Proc. 32<sup>nd</sup> Eur. Microw. Conf.*, 2002, pp. 881-884.
- [21] F. Xu, and K. Wu, "Guided-Wave and leakage characteristics of substrate integrated waveguide," *IEEE Trans. Microw. Theory Tech.*, vol. 53, no. 1, pp. 66-73, Jan. 2005.
- [22] D. Deslandes, and K. Wu, "Integrated microstrip and rectangular waveguide in planar form", *IEEE Microw. Wireless Compon. Lett.*, vol. 11, no. 2, Feb 2001, pp. 68-70.
- [23] D. Deslandes, and K. Wu, "Integrated Transition of Coplanar to Rectangular Waveguides", *IEEE Int. Microwave Symp. Dig.*, 2001, pp. 619-622.

- [24] D. Deslandes, and K. Wu, "Substrate integrated waveguide dual-mode filters for broadband wireless systems," *2003 IEEE Radio Wireless Conf. (RAWCON'2003)*, pp. 385-388, Aug. 10-13, Boston, USA.
- [25] S. T. Choi, K. S. Yang, K. Tokuda, and Y. H. Kim, "A V-band planar narrow bandpass filter using a new type integrated waveguide transition," *IEEE Microw. Wireless Compon. Lett.*, vol. 14, no. 12, pp. 545-547, 2004.
- [26] Y. L. Zhang, W. Hong, K. Wu, J. X. Chen, and H. J. Tang, "Novel substrate integrated waveguide cavity filter with defected ground structure," *IEEE Trans. Microw. Theory Tech.*, vol. 53, no. 4, pp. 1280-1287, Apr. 2005.
- [27] Z. C. Hao, W. Hong, J. X. Chen, X. P. Chen, and K. Wu, "Compact super wide bandpass substrate integrated waveguide filters," *IEEE Trans. Microw. Theory Tech.*, vol. 53, no. 9, pp. 2968-2977, Sep. 2005.
- [28] Z. C. Hao, W. Hong, X. P. Chen, J. X. Chen, K. Wu, and T. J. Cui, "Multilayered substrate integrated waveguide (MSIW) elliptic filter," *IEEE Microw. Wireless Compon. Lett.*, vol. 15, no. 2, pp. 95-97, Feb. 2005.
- [29] X.-P. Chen, W. Hong, T. Cui, Z. Hao, and K. Wu, "Substrate integrated waveguide elliptic filter with transmission line inserted inverter," *Electron. Lett.*, vol. 41, pp. 851-852, 2005.
- [30] D. Stephens, P. R. Young, and I. D. Robertson, "Millimeterwave substrate integrated waveguides and filters in photoimageable thick-film technology," *IEEE Trans. Microw. Theory Tech.*, vol. 53, no. 12, pp. 3832-3838, 2005.
- [31] W. Che, E. Yung, and K. Wu, "Millimeter-wave ferrite phase shifter in substrate integrated waveguide (SIW)," *IEEE Int. AP-S Symp. Dig.*, pp. 887-890, Jun. 2003.
- [32] X. Xu, R. G. Bosisio, and K. Wu, "A new six-port junction based on substrate integrated waveguide technology," *IEEE Trans. Microw. Theory Tech.*, vol. 53, no. 7, pp. 2267-2273, Jul. 2005.
- [33] F. F. He, K. Wu, W. Hong, H. J. Tang, H. B. Zhu, and J. X. Chen, "A planar magic-T using substrate integrated circuits concept," *IEEE Microw. Wireless Compon. Lett.*, vol. 18, no. 6, pp. 386-388, Feb. 2008.
- [34] L. Yan, W. Hong, G. Hua, J. Chen, K. Wu, and T. J. Cui, "Simulation and experiment on SIW slot array antennas," *IEEE Microw. Wireless Compon. Lett.*, vol. 14, no. 9, pp. 446-448, Sep. 2004.

- [35] D. Deslandes, and K. Wu, "Substrate integrated waveguide leaky-wave antenna: Concept and design considerations," in *Proc. Asia-Pacific Microw. Conf.*, Suzhou, 2005, pp. 346-349.
- [36] B. S. Izquierdo, P. R. Young, N. Grigoropoulos, J. C. Batchelor, and R. J. Langley, "Substrate integrated folded waveguide slot antenna," in *Proc. IEEE Int. Workshop Antenna Technology*, 2005, pp. 307–309.
- [37] G. Q. Luo, W. Hong, Z. -C. Hao, B. Liu, W. D. Li, J. X. Chen, H. X. Zhou, and K. Wu, "Theory and experiment of novel frequency selective surface based on substrate integrated waveguide technology," *IEEE Trans. Antennas Propagat.*, vol. 53, no. 12, pp. 4035–4043, Dec. 2005.
- [38] Y. J. Cheng, W. Hong, and K. Wu, "Design of a monopulse antenna using a dual V-type linearly tapered slot antenna (DVL TSA)," *IEEE Trans. Antennas Propagat.*, vol. 56, no. 9, pp. 2903–2909, Sep. 2008.
- [39] Y. Cassivi, and K. Wu, "Low Cost Microwave Oscillator Using Substrate Integrated Waveguide Cavity," *IEEE Microw. Wireless Compon. Lett.*, vol. 13, No. 2, pp.48-50, February 2003
- [40] C. L. Zhong, J. Xu, Z. Y. Yu, and Y. Zhu, "K<sub>a</sub>-Band Substrate Integrated Waveguide Gunn Oscillator," *IEEE Microw. Wireless Compon. Lett.*, vol. 18, no. 7, pp. 461–463, 2008.
- [41] M. Abdolhamidi, and M. Shahabadi, "X-band substrate integrated waveguide amplifier," *IEEE Microw. Wireless Compon. Lett.*, vol. 18, no. 12, pp. 815-817, Dec 2008.
- [42] H. Jin, and G. Wen, "A novel four-way K<sub>a</sub>-band spatial power combiner based on HMSIW," *IEEE Microw. Wireless Compon. Lett.*, vol. 18, no. 8, pp. 515–517, Aug. 2008.
- [43] N. Marchand, "Transmission-line conversion transformers," *Electronics*, vol. 17, no. 12, pp. 142–145, Dec. 1944.
- [44] R. Sturdivant, "Balun designs for wireless mixers, amplifiers and antennas," *Appl. Microw.*, pp. 34–44, 1993.
- [45] M. Basraoui, and S. N. Prasad, "Wideband, planar, log-periodic balun," *IEEE Int. Microwave Symp. Dig.*, 1998, pp. 785–788.
- [46] Z. Y. Zhang, Y. X. Guo, L. C. Ong, and M. Y. W. Chia, "Improved planar marchand balun with a patterned ground plane," *Int. J. RF Microw. CAE*, vol. 15, no. 3, pp. 307–316, May 2005.



- [47] S. A. Maas, *Microwave Mixer*. 2<sup>nd</sup> ed., Norwood, Artech House, 1993, pp. 219–312.
- [48] J. W. Duncan, and V. P. Minerva, “100:1 Bandwidth Balun Transformer,” *IRE Proc.*, vol. 48, pp. 156-164, 1960.
- [49] N. Kaneda, Y. Qian, and T. Itoh, “A novel Yagi-Uda dipole array fed by a microstrip-to-CPS transition,” in *Proc. Asia-Pacific Microw. Conf.*, Yokohama, Dec. 1998, pp. 1413-1416.
- [50] K. Uehara, K. Miyashita, K. I. Matsume, K. H. Hatakeyama, and K. Mizuno, “Lens-coupled imaging arrays for the millimeter and submillimeter-wave regions,” *IEEE Trans. Microw. Theory Tech.*, vol. 40, pp. 806-811. May 1992.
- [51] Y. Qian, and T. Itoh, “A broadband Uniplanar microstrip-to-CPS transition,” in *Proc. Asia-Pacific Microw. Conf.*, Dec. 1997, pp. 609-612.
- [52] N. Grigoropoulos, B. S. Izquierdo, and P. R. Young, “Substrate integrated folded waveguides (SIFW) and filters,” *IEEE Microw. Wireless Compon. Lett.*, vol. 15, no. 12, 829-831, 2005.
- [53] W. Che, L. Geng, K. Deng, and Y. L. Chow, “Analysis and experiments of compact folded substrate-integrated waveguide,” *IEEE Trans. Microw. Theory Tech.*, vol. 56, no. 1, 88-93, 2008.
- [54] B. Liu, W. Hong, Y.-Q. Wang, Q.-H. Lai, and K. Wu, “Half mode substrate integrated waveguide (HMSIW) 3-dB coupler,” *IEEE Microw. Wireless Compon. Lett.*, vol. 17, pp. 22-24, Jan 2007.
- [55] B. Liu, W. Hong, L. Tian, H.-B. Zhu, W. Jiang, and K. Wu, “Half-Mode SIW (HMSIW) Multi-Way Power Divider,” in *Proc. Asia-Pacific Microw. Conf.*, Yokohama, Dec. 2006, pp. 917-920.
- [56] Q. H. Lai, C. Fumeaux, W. Hong, and R. Vahldieck, “Characterization of the propagation properties of the half-mode substrate integrated waveguide,” *IEEE Trans. Microw. Theory Tech.*, vol. 57, no. 8, pp. 1996-2004, Aug. 2009.
- [57] E. Wilkinson, “An N-Way Hybrid Power Divider,” *IRE Trans. Microw. Theory Tech.*, vol. 8, pp. 116-118, Jan 1960.
- [58] X. Chen, W. Hong, T. Cui, J. Chen, and K. Wu, “Substrate integrated waveguide (SIW) linear phase filter,” *IEEE Microw. Wireless Compon. Lett.*, vol. 15, pp. 787-789, Nov 2005.

- [59] G. L. Mattaei, L. Young, and E. M. T. Jones, *Microwave Filters, Impedance-Matching Network, and Coupling Structures*, Norwood, MA: Artech House, 1980.
- [60] B. M. Schiffman, "A new class of broad-band microwave 90-degree phase shifters," *IRE Trans. Microw. Theory Tech.*, vol. 6, no. 4, pp. 232–237, Apr. 1958.
- [61] B. Schiek, and J. Kohler, "A method for broad-band matching of microstrip differential phase shifters," *IEEE Trans. Microw. Theory Tech.*, vol. 25, no. 8, pp. 666–671, Aug. 1977.
- [62] G. N. Tsandoulas, D. H. Temme, and F. G. Willwerth, "Longitudinal section mode analysis of dielectrically loaded rectangular waveguides with application to phase shifter design," *IEEE Trans. Microw. Theory Tech.*, vol. 18, pp. 88-95, Feb. 1970.
- [63] F. Arndt, U. Tucholke, and T. Wriedt, "Broadband dual-depth E-plane corrugated square waveguide polarizer," *Electron. Lett.*, vol. 20, pp. 458–459, May 1984.
- [64] F. Arndt, A. Frye, M. Wellnitz, and R. Wirsing, "Double dielectric-slab-filled waveguide phase shifter," *IEEE Trans. Microw. Theory Tech.*, vol. 33, pp. 373-381, May. 1985.
- [65] K. Sellal, L. Talbi, T. Denidni, and J. Lebel, "A new substrate integrated waveguide phase shifter," in *Proc. 36<sup>th</sup> Europ. Microwave Conf.*, Sept. 2006, pp. 72-75.
- [66] B. Liu, W. Hong, Z. C. Hao, and K. Wu, "Substrate integrated waveguide 180-degree narrow-wall directional coupler," in *Proc. Asia-Pacific Microwave Conf.*, Dec. 2006, pp. 559-561.
- [67] Y. J. Chen, W. Hong, and K. Wu, "Novel Substrate Integrated Waveguide fixed phase shifter for 180-degree Directional Coupler," *IEEE Int. Microwave Symp. Dig.*, 2007, pp. 189 - 192.
- [68] A. Patrovsky, M. Daigle, and K. Wu, "Coupling mechanism in hybrid SIW-CPW forward couplers for millimeter wave substrate integrated circuits," *IEEE Trans. Microw. Theory Tech.*, vol. 56, no. 11, pp. 2594-2601, Nov. 2008.
- [69] F. Stevenson, "Theory of slots in rectangular wave-guides," *Journal of Applied Physics*, Vol. 19, Jan 1948, pp. 24-38.
- [70] R. S. Elliott, *Antenna Theory and Design*, Englewood Cliffs, Prentice-Hall, 1981.
- [71] A. A. Oliner, "The impedance properties of narrow radiating slots in the broad face of rectangular waveguide," *IEEE Trans. Antennas Propagat.*, pp. 4-20, Jan 1957.
- [72] P. A. Rizzi, *Microwave Engineering- Passive Circuits*, Prentice Hall, New Jersey, 1988.
- [73] D. H. Evans, "A millimeter-wave self-oscillating mixer using a GaAs FET harmonic-mode oscillator," *IEEE Int. Microwave Symp. Dig.*, 1986, pp. 601- 604.

- [74] M. Sironen, Y. Qian, and T. Itoh, "A subharmonic self-oscillating mixer with integrated antenna for 60-GHz wireless application," *IEEE Trans. Microw. Theory Tech.*, vol. 49, pp.442-450, March 2001.
- [75] J. Xu, and K. Wu, "A subharmonic self-oscillating mixer using substrate integrated waveguide cavity for millimeter-wave application," *IEEE Int. Microwave Symp. Dig.*, 2005, pp. 2019 - 2022.
- [76] L. Chiu, T. Y. Yum, T. F. Cheng, Q. Xue, and C. H. Chan, "An injection locked subharmonic self-oscillating mixer for multi-band operation," *Micro. Opt. Tech. Lett.*, vol. 42, pp. 415-419, Sept. 2004.
- [77] S. A. Winkler, K. Wu, and A. Stelzer, "Integrated receiver based on a high-order subharmonic self-oscillating mixer," *IEEE Trans. Microw. Theory Tech.*, vol. 55, pp. 1398-1404, June 2007.
- [78] A. Gopinath, "Losses in coplanar waveguides," *IEEE Trans. Microw. Theory Tech.*, vol. 30, pp.1101-1104, July 1982.
- [79] K. C. Gupta, R. Garg, and I. J. Bahl, *Microstrip Lines and Slot Lines*, Dedham, MA: Artech House, 1979.
- [80] G. Gonzalez, *Microwave Transistor Amplifiers, Analysis and Design*, 2nd ed. Englewood Cliffs, NJ: Prentice-Hall, 1997.
- [81] W. C. Lindsey, and M. K. Simon, *Telecommunication Systems Engineering*, Englewood Cliffs, N.J., Prentice-Hall, 1973.
- [82] H. Daembkes, B. Adelseck, L. P. Schmidt, and J. Schroth, "GaAs MMIC based components and frontends for millimeterwave communication and sensor systems," in *Proceedings of IEEE Microwave Systems Conference (NTC '95)*, pp. 83–86, Orlando, FL, USA, May 1995.
- [83] H. Shigematsu, T. Hirose, F. Brewer, and M. Rodwell, "Millimeterwave CMOS circuit design," *IEEE Trans. Microw. Theory Tech.*, vol. 53, no. 2, pp. 472–477, Feb. 2005.
- [84] M. Sato, T. Hirose, and K. Mizuno, "Advanced MMIC receiver for 94-GHz band passive millimeter-wave imager," *IEICE Trans. Electron.*, vol. E92-C, no. 9, pp. 1124-1129, Sept. 2009.
- [85] S. A. Maas, *Microwave Mixers*, 2<sup>nd</sup> ed. Boston: Artech House, 1993.

- [86] C. -H. Lien, C. -H. Wang, C. -S. Lin, P. -S. Wu, K. -Y. Lin, and H. Wang, "Analysis and design of reduced-size Marchand rat-race hybrid for millimeter-wave compact balanced mixers in 130-nm CMOS process," *IEEE Trans. Microw. Theory Tech.*, vol. 57, pp. 1966-1977, Aug. 2009.
- [87] F. Ellinger, L. C. Rodoni, G. Sialm, C. Kromer, G. V. Buren, M. L. Schmatz, C. Menolfi, T. Toifl, T. Morf, M. Kossel, and H. Jackel, "30–40-GHz drain-pumped passive-mixer MMIC fabricated on VLSI SOI CMOS technology," *IEEE Trans. Microw. Theory Tech.*, vol. 52, no. 5, pp. 1382–1391, May 2004.
- [88] S. A. Maas and K. W. Chang, "A broadband planar, doubly balanced monolithic K<sub>a</sub>-band diode mixers," *IEEE Trans. Microw. Theory Tech.*, vol. 41, no. 12, pp. 2330–2335, Dec. 1993.
- [89] H. Arslan, and H. A. Mahmoud, "Error vector magnitude to SNR conversion for nondata aided receivers," *IEEE Trans. Wireless Commun.*, vol. 8, pp. 2694-2704, May 2009.
- [90] Z. Q. Chen, and F. F. Dai, "Effects of LO phase and amplitude imbalances and phase noise on M-QAM transceiver performance," *IEEE Trans. Industrial Electronics*, vol. 57, pp.1505 – 1517, May 2010.
- [91] R. S. Elliott, and W. R. O'Loughlin, "The Design of Slot Arrays Including Internal Mutual Coupling," *IEEE Trans. Antennas and Propagat.*, vol. 34, no. 9, September 1986.
- [92] R. A. Shafik, M. S. Rahman, and A. H. M. R. Islam, "On the extended relationships among EVM, BER and SNR as performance metrics," in *Proc. ICECE'06*, Bangladesh, pp. 408–411, Dec. 2006.
- [93] Z. Y. Zhang, and K. Wu, "Sub-harmonic self-oscillating mixer design using dual-mode substrate integrated waveguide cavity," in *Proc. 39<sup>th</sup> Eur. Microw. Conf.*, Sept. 2009, pp.196 – 199.
- [94] M. C. Sanchez, E. Martin, and J. M. Zamarro, "Unified and simplified treatment of techniques for characterising transmission, reflection or absorption resonators," *IEE Proc. Microw., Antennas Propagat.*, vol. 137, no. 4, pp. 209–212, Aug. 1990.
- [95] K. Kurokawa, "Injection locking of microwave solid-state oscillators," *Proc. IEEE*, vol. 61, pp. 1386-1410, Oct. 1973.
- [96] P. Smulders, "Exploiting the 60 GHz band for local wireless multimedia access: Prospects and future directions," *IEEE Commun. Mag.*, vol. 40, no. 1, pp. 140 - 147, 2002.

- [97] C. H. Doan, S. Emami, D. A. Sobel, A. M. Niknejad, and R. W. Brodersen, "Design considerations for 60 GHz CMOS radios," *IEEE Commun. Mag.*, vol. 42, no. 12, pp. 132–140, 2004.
- [98] S. E. Gunnarsson, C. Karnfelt, H. Zirath, R. Kozhuharov, D. Kuylenskierna, C. Fager, M. Ferndahl, B. Hansson, A. Alping, and P. Hallbjorner, "60 GHz single-chip front-end MMICs and systems for multi-Gb/s wireless communication," *IEEE Journal of Solid-State Circuits*, vol. 42, pp. 1143–1157, May 2007.
- [99] K. K. Samanta, D. Stephens, and I. D. Robertson, "Design and performance of a 60-GHz multi-chip module receiver employing substrate integrated waveguides," *IET Microw. Antennas Propagat.*, vol. 1, pp. 961–967, 2007.
- [100] K. S. Yang, S. T. Choi, Y. H. Kim, S. Nishi, S. Shimizu, and K. Tokuda, "60 GHz small mobile transceiver (SMT) with integrated IF modem for millimeter-wave over fiber communication system," in *Proceedings of International Conference on Consumer Electronics (ICCE '05)* pp. 351–352, Jan. 2005.
- [101] S. E. Gunnarsson, C. Stoj, C. Karnfelt, H. Zirath, R. Kozhuharov, D. Kuylenskierna, R. Christoffersen, and E. Stoj, "A generic, multi-purpose, and small-size 60 GHz transmit/receive module used for secure WLAN communication," in *Proc. Asia-Pacific Microw. Conf.*, Dec. 2008, pp. 1–4.
- [102] S. Lee, S. Jung, and H. Y. Lee, "Ultra-Wideband CPW-to-Substrate Integrated Waveguide Transition Using an Elevated-CPW Section," *IEEE Microw. Wireless Compon. Lett.*, vol. 18, pp. 746–748, 2008.

## LIST OF PUBLICATIONS

- [1] **Zhen-Yu Zhang**, and K. Wu, "A broadband substrate integrated waveguide (SIW) planar balun," IEEE Microwave and Wireless Component Letter, vol. 17, pp.843-845, Dec, 2007.
- [2] **Zhen-Yu Zhang**, K. Wu, and N. Yang, "Broadband millimeter-wave quasi-yagi antenna using substrate integrated waveguide technique," IEEE Radio and Wireless Symposium incorporating WAMICON, pp. 671-674, Jan, 2008, Orlando, U.S.A.
- [3] **Zhen-Yu Zhang**, and K. Wu, "Broadband half-mode substrate integrated waveguide (HMSIW) wilkinson power divider," IEEE MTT-S International Microwave Symposium, pp. 879-882, June, 2008, Atlanta, U.S.A.
- [4] **Zhen-Yu Zhang**, N. Yang, and K. Wu, "5-GHz bandpass filter demonstration using quarter-mode substrate integrated waveguide cavity for wireless systems," IEEE Radio and Wireless Symposium incorporating WAMICON, pp. 95-98, Jan, 2009, San Diego, U.S.A.
- [5] **Zhen-Yu Zhang**, and K. Wu, "Sub-harmonic self-oscillating mixer design using dual-mode substrate integrated waveguide cavity," Proceedings of the 39<sup>th</sup> European Microwave conference (EuMIC ) pp.196 – 199, Sept, 2009, Rome, Italy.
- [6] **Zhen-Yu Zhang**, K. Wu, and N. Yang, "A millimeter-wave sub-harmonic self-oscillating mixer using dual-mode substrate integrated waveguide cavity," IEEE Transactions on Microwave Theory and Techniques, vol. 58, pp. 1151-1158, May, 2010.
- [7] **Zhenyu Zhang**, Y. R. Wei, and K. Wu, "Millimeter-wave wireless communication systems integrated with a novel receiver front-end," IEEE MTT-S International Microwave Symposium, pp. 1612-1615, May, 2010, Anaheim, U.S.A.
- [8] **Zhenyu Zhang**, Y. R. Wei, and K. Wu, "60 GHz transceiver architectures deploying substrate integrated circuits (SICs) technique," 40<sup>th</sup> European Microwave conference, pp. 33-36, Sept, 2010, Paris, France.
- [9] **Zhenyu Zhang**, K. Wu, and Y. R. Wei, "180-degree substrate integrated waveguide hybrid and its application to broadband millimeter-wave single balanced mixer design," Asia-pacific Microwave conference, Dec, 2010, Yokohama, Japan.

- [10] **Zhenyu Zhang**, K. Wu, and Y. R. Wei, "Broadband delay compensation phase shifter using slotted substrate integrated waveguide structure," IEEE MTT-S International Microwave Symposium, pp. 1-4, June, 2011, Baltimore, U.S.A.
- [11] **Zhen-Yu Zhang**, Y. R. Wei, and K. Wu, "Broadband millimeter-wave single balanced mixer and its applications to substrate integrated wireless systems," accepted by IEEE Transactions on Microwave Theory and Techniques.
- [12] **Zhen-Yu Zhang**, Y. R. Wei, and K. Wu, "Millimeter-wave receiver front-end using injection-locked sub-harmonic self-oscillating mixer," submitted to IEEE Transactions on Microwave Theory and Techniques.